NASA
Technical
Paper
3238

August 1992

Lewis Icing Research Tunnel Test of the Aerodynamic Effects of Aircraft Ground Deicing/Anti-Icing Fluids

L. James Runyan,
Thomas A. Zierten,
Eugene G. Hill,
and Harold E. Addy, Jr.

NASA

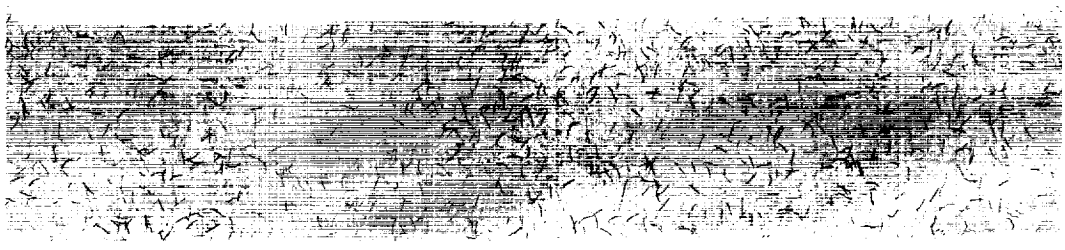

NASA Technical Paper 3238

1992

Lewis Icing Research Tunnel Test of the Aerodynamic Effects of Aircraft Ground Deicing/Anti-Icing Fluids

L. James Runyan,
Thomas A. Zierten,
and Eugene G. Hill
Boeing Commercial Airplanes
Seattle, Washington

Harold E. Addy, Jr.
Lewis Research Center
Cleveland, Ohio

NASA
National Aeronautics and Space Administration
Office of Management
Scientific and Technical Information Program

Contents

Summary

A wind tunnel test was conducted in the NASA Lewis Research Center Icing Research Tunnel to investigate the aerodynamic effects of aircraft ground deicing and anti-icing fluids. Both a three-dimensional half model and a two-dimensional model were tested. Test temperatures ranged from 10 to −29 °C (50 to −20 °F). Fluids tested included three commercial fluids available for use during the 1987–88 winter season, one discontinued commercial fluid that was tested to allow comparison with previous test data, and eight new experimental fluids provided by four fluid manufacturers. The models were instrumented with balances to measure forces and moments, and an ultraviolet photographic technique was used to study fluid film thickness distribution. Boundary-layer data were taken on the two-dimensional model for selected cases. The test results showed significant lift loss, drag increase, and pitching moment increase caused by incomplete flow-off of the fluids. For the three-dimensional half model, the lift loss at $C_{L,\max}$ was significantly higher that at operational angles of attack. The new experimental fluids resulted in significantly lower lift losses than the baseline type II fluids. Good correlation was obtained between results on the two-dimensional model and results on the three-dimensional half-model. Results from testing with distributed solid roughness (simulated frost) showed that the magnitude of the lift loss at $C_{L,\max}$ was highly sensitive to the roughness on the wing in the forward 30 percent of the chord. At operational angles of attack, lift loss due to distributed solid roughness was comparable with that of the baseline type II fluid at low temperatures. At $C_{L,\max}$ lift loss due to distributed solid roughness was approximately two to three times as large (depending on configuration) as that of the baseline type II fluid at low temperatures. Correlation of boundary-layer measurements and fluid surface aerodynamic data indicated that the adverse aerodynamic effects of the fluids result from fluid roughness and the resulting thickening of the boundary layer.

Introduction

A comprehensive test of the aerodynamic effects of aircraft ground deicing and anti-icing fluids has been conducted in the NASA Lewis Icing Research Tunnel. The test was conducted in conjunction with a flight test program on a 737-200ADV airplane. This allowed the validity of the wind tunnel results on small scale models to be assessed by comparing them with the flight test data.

The question of the aerodynamic effects of aircraft deicing and anti-icing fluids has been a subject of increasing interest in recent years. Wind tunnel tests conducted by Boeing in 1982 (ref. 1) showed that these fluids do cause a significant lift loss and drag increase after liftoff. However, those tests suffered from several drawbacks, including testing in an uncooled wind tunnel with artificially thickened fluids and using small scale models. After the Boeing small scale tests, the von Karman Institute for Fluid Dynamics, in collaboration with the Association of European Airlines (AEA), performed wind tunnel tests of a large-scale airfoil at operational temperatures using unadulterated fluids. Results of this later testing tended to verify earlier Boeing test results and established the impetus for full-scale measurement of the fluid's aerodynamic effects and the wind tunnel test described in this paper.

Both a three-dimensional half model of the 737-200ADV and a two-dimensional model were tested. A wide range of temperatures (10 to −29 °C (50 to −20 °F)) and several fluids and high-lift configurations were investigated. Besides measuring the aerodynamic effects of the fluids using force balances on both models, the two-dimensional model was instrumented with a boundary-layer rake to measure data that might be useful in understanding the physical mechanism behind the fluid effects. Also, an ultraviolet fluorescence photographic technique was used to determine the fluid depth and roughness characteristics on both models.

This paper first describes the background of fluid testing that preceded the present investigation, including the associated flight test. A description of the present test is then given, followed by a presentation of the test results for the three-dimensional half model and the two-dimensional model and a discussion of the physical mechanism of the fluid effects. Finally, specific conclusions regarding the aerodynamic effects of deicing and anti-icing fluids are drawn based on the results of this test.

Symbols

$b/2$	three-dimensional half-model span
C_D	airplane drag coefficient
$C_{D,P}$	parasite drag coefficient
$C_{D,SA}$	drag coefficient in stability axes

C_F	skin friction coefficient
C_L	airplane lift coefficient
$C_{L,SA}$	lift coefficient in stability axes
$C_{L,SAC}$	sectional lift coefficient in stability axes
C_M	airplane pitching moment
C_N	normal force coefficient
$C_{0.25\bar{c}}$	pitching moment about quarter chord of mean aerodynamic chord in stability axes
c_l	sectional lift coefficient
$c_{l,SA}$	sectional lift coefficient in stability axes
c_m	sectional pitching moment coefficient
c_{2D}	two-dimensional model chord length
c_{3D}	mean aerodynamic chord of three-dimensional half model
h	height
k	average fluid wave height
L	length
N	normal force
O	oleo-strut
P	total pressure
q	dynamic pressure
S_{ref}	reference wing area (= 8.1154/2 ft for three-dimensional half model)
T	temperature
t	time
V	velocity
W	width
X_{NF}	center of pressure location
Y	height above model surface
α	angle of attack
α_B	angle of attack of body waterline
α_W	angle of attack of wing chord plane of two-dimensional model
δ_A	aileron angle, deg
σ	standard deviation

Subscripts:

B	body
max	maximum
min,u	minimum unstick
ref	reference
SA	stability axes
0	initial value
1	condition 1
2	condition 2

Background

Early Boeing Tests

The aerodynamic effects of aircraft ground deicing and anti-icing fluids were first investigated in the wind tunnel by Boeing in 1982 (ref. 1). This early test series included fluid flow behavior evaluations on a truncated Boeing 767 slat in the 38- by 50-cm (15 by 20 in.) Boeing Icing Wind Tunnel (BIWT), and two-dimensional airfoil tests in the 1.52- by 2.43-m (5 by 8 ft) Boeing Research Wind Tunnel (BRWT) and in BIWT. Force data were measured only in the BRWT test. Since the BRWT is uncooled, it was necessary to modify the fluids that were tested to have low-temperature viscosity characteristics at the warm tunnel temperatures. The results of the BRWT test indicated that the fluids may cause a measurable lift loss and drag increase. However, the modification of the fluids, and the small model scale (0.24) decreased confidence in the validity of those results.

Association of European Airlines Tests

In 1984 the Association of European Airlines (AEA) undertook a follow-up to the Boeing investigation. In collaboration with Professor Mario Carbonaro and the von Karman Institute for Fluid Dynamics, the AEA undertook a research program to evaluate deicing and anti-icing fluids for their aerodynamic effects on a large-scale model using unadulterated fluids at operational cold temperatures. In their phase I (ref. 2) various fluids were tested on a flat plate to assess the effect of test temperature and initial fluid thickness. In phases II and III (refs. 3 and 4) aerodynamic data were obtained on a 1.5-m chord two-dimensional airfoil model designed to represent the 66-percent-span location of the 737-200ADV airplane. These tests were conducted in the 2.2- by 2.4-m (7.2 by 7.9 ft) cold wind tunnel of the Bundesversuchs-und Forschungsanstalt Arsenal in Vienna, Austria. Results from these tests showed measurable lift losses and drag increases due to the fluids. However, these tests still did not overcome all the drawbacks of the early Boeing tests. The model scale, though much larger, was still only 0.59, and it was only a two-dimensional model. This still left some question about scale effects and three-dimensional effects. Also, no data were obtained on the effect of the fluids on the maximum lift coefficient.

Flight Tests

To minimize questions raised by scale effects and three-dimensional effects, Boeing and the AEA conducted a flight test in January of 1988 in Kuopio, Finland, on a 737-200ADV airplane. The airplane was fully instrumented (ref. 5) so that the fluid effects on lift and drag could be determined. The AEA provided the test airplane and hosted the testing at the European test site. Boeing installed the instrumentation on the airplane, planned and conducted the flight test, and analyzed the data. Four deicing and anti-icing fluids commercially

available during or before 1988 were tested. The results showed that the fluids cause a measurable lift loss and drag increase (ref. 6). However, there were also drawbacks to the flight test. For safety reasons, the effect of the fluids on lift loss at $C_{L,max}$ was not investigated since that would have required stalling the airplane near the ground. Also, because of the high cost of flight testing and the limitations imposed by the ambient temperatures during the flight test, only a limited range of temperatures, fluids, and airplane configurations could be investigated. Providing complementary data to overcome these limitations was the impetus for the present wind tunnel investigation. Even though it was conducted with small scale models, the availability of full-scale data for comparison gave this test an advantage that all the earlier wind tunnel tests lacked.

Test Description

Participants

This test was a joint effort of the Boeing Co., NASA Lewis Research Center, and the Association of European Airlines. Four fluid manufacturers assisted in the test by providing fluids. Boeing built, instrumented, and installed the models; planned and conducted the test; and analyzed the data. NASA Lewis provided and operated the Icing Research Tunnel and assisted in the model installation, the conduct of the test, and the recording of the data. The AEA monitored the test to help maintain continuity with the AEA fluids research program.

Objectives

The primary objective of the test was to obtain data that would contribute to understanding the aerodynamic effects of deicing and anti-icing fluids on aircraft. As discussed earlier, the wind tunnel test was conducted after the flight test. This allowed use of the flight test results to verify that the wind tunnel results on the small scale models were reasonable for the corresponding angle of attack conditions investigated. However, the effect of fluids on the maximum lift coefficient could not be investigated in flight because that would have required the airplane to be stalled near the ground. Therefore, determination of the effect of the fluids on the maximum lift coefficient was one of the most important objectives of the wind tunnel test. Also, because of the lower cost of the wind tunnel test, compared with flight test, and because of the ability to control the test temperature, a larger range of temperatures, high-lift configurations, and fluid formulations could be tested. By measuring boundary-layer data and fluid surface roughness characteristics, it was hoped that a better understanding of the lift loss mechanism would be achieved. Finally, it was hoped that the results of this test would contribute to a data base for establishing aerodynamic acceptance standards for aircraft ground deicing and anti-icing fluids.

Icing Wind Tunnel Description

The test was conducted in the NASA Lewis Icing Research Tunnel (IRT). The IRT is a closed circuit, single return, closed throat wind tunnel. It has a heat exchanger and refrigeration system that allows the tunnel to operate at temperatures from −29 to 27 °C (−20 to 80 °F). The IRT also has a water spray system that generates an icing cloud. The spray system, however, was not used for these tests.

The test section is a rectangle that is 1.8 m (6 ft) high, 2.7 m (9 ft) wide, and 6.1 m (20 ft) long. Test section airspeeds can be set up to 134 m/s (300 mph). The turbulence level without the spray system operating is approximately 0.5 percent. The maximum Reynolds number is 1.1×10^7/m (3.3×10^6/ft). The stagnation pressure in the IRT is atmospheric, and the dynamic pressure varies from 0 to 11 kPa (230 lb/ft^2). An overview of the IRT is shown in figure 1 (p. 13).

The variation in velocity across the test section is ±0.67 m/s (±1.5 mi/hr) outside the boundary layer for all tunnel operating speeds and operating temperatures. An example of the variation in velocity is shown in figure 2. The boundary-layer thickness at the model location in the test section is between 0.06 and 0.13 m (2.5 and 5.1 in.) along the walls.

For this test, variation in temperature, both spatially across the tunnel and temporally as the fan is accelerated, was of concern. The spatial variation in temperature across the test section of the tunnel is ±3.0 °C (±5.5 °F). However, this variation is due to the presence of several localized warm or cool spots that are located near the walls of the tunnel. A region of relatively constant temperature (±0.5 °C or ±1.0 °F) exists at or near the center of the test section, as indicated by the dashed rectangle in figure 3. The figure shows lines of constant temperature in the test section at the model location for an airspeed of 45 m/s (100 mph) and a tunnel operating temperature of −18 °C (0 °F). The dashed rectangle encloses a region within which the temperature variation is no more than ±0.6 °C (1.0 °F). This region covered the entire three-dimensional half model and most of the two-dimensional model. Additionally, measurements taken downstream of the heat exchanger during fan acceleration indicate that the average temperature over a cross section in the tunnel varied at most ±1.1 °C (±2.0 °F) during the fan accelerations.

Models and Installation

Both a three-dimensional half model and a two-dimensional model were tested. The details of the three-dimensional half model are shown in figure 4 (p. 15). It was a 0.091 scale model of the 737-200ADV, with an average chord of 0.30 m (1 ft) and a semispan of 1.28 m (4.2 ft). The slats could be tested in either the extended, sealed configuration or the fully extended, gapped configuration. Flap configurations tested were flaps 5 and 15. These flap configurations for the two-dimensional model, which are conceptually the same for the three-dimensional model, are shown in figure 8. Deflected ailerons were also tested. As shown in the figure 4, the model was mounted on a splitter wall, which housed the turntable and force balance. The model was

TABLE I.—FLUIDS TESTED

Fluid number	Type of fluid	Latest winter[a] of commercial availability	Holdover time in freezing rain, min	Source
1	Newtonian deicing	1987-88	2-5	U of Quebec, Chicoutimi
2	Nonnewtonian anti-icing	Pre-1987	>30	--------
3	↓	1987-88	>30	Hoechst Lab
4	↓	1987-88	21	U of Quebec, Chicoutimi
2.1	↓	Experimental	---	--------
2.2	↓	↓	33	Kilfrost Lab
3.1	↓	↓	---	--------
3.2	↓	↓	32	Hoechst Lab
4.1	↓	↓	>30	U of Quebec, Chicoutimi
4.2	↓	↓	---	--------
5.1	↓	↓	32	SPCA Tech. Rept. on AD104
5.2	↓	↓	---	--------

[a]As of winter of 1987-88.

tested both with and without the ground plane shown in figure 5. A photograph of the model in the presence of the ground plane is shown in figure 6 (p. 15).

Details of the two-dimensional model are summarized in figure 7 (p. 16). The airfoil is based on a cut at the 65-percent-span station of the 737-200ADV. The model scale was 0.18, and the chord was 0.457 m (1.5 ft). Based on commonly accepted wind tunnel practices, the chord length was limited to one-quarter of the 1.83-m (6-ft) tunnel height. The model span was 1.52 m (5 ft). The slats could be tested in either the extended, sealed configuration or the fully extended, gapped configuration. The flap configurations tested were flaps 5 and 15. The model was mounted between two splitter walls, which housed the turntables and the force balances. Figure 8 shows the two-dimensional model configurations that were tested. Figure 9 (p. 17) shows the two-dimensional model installed between the splitter walls.

Data System

The characteristics of the data system are summarized in figure 10. The heart of the data acquisition system was a Hewlett-Packard 9845 computer. Output from this computer was fed directly to a Digital Equipment Corp. MicroVAX for data analysis. This system provided the capability to get online data plots within about 10 min of the completion of the run and final plots within an hour. A typical online data plot is shown in figure 11.

Fluids

The two basic fluid types tested were newtonian deicing fluids and non-Newtonian anti-icing fluids. Newtonian deicing fluids have a high glycol content (minimum 80 percent) with the balance consisting of water and inhibitors. The viscosity of these fluids is a function of temperature only and is relatively low except at very cold winter temperatures. These fluids provide limited protection against refreezing. Ethylene glycol based Newtonian fluids are the principal type of fluid used in the United States at this time. Non-Newtonian anti-icing fluids typically have a lower glycol content (minimum 50 percent) with the balance consisting primarily of water (usually a minimum of 45 percent), thickeners, and inhibitors. They provide good protection against refreezing and are used extensively in Europe. Their use in the United States is increasing. They are highly viscous at low shear stress levels, and their viscosity decreases rapidly as shear stress increases.

The four fluids tested in the 1988 flight test were also tested in the wind tunnel. Fluid 1 was a nonethylene-glycol-based, Newtonian deicing fluid. Fluid 2 was a pre-1987 (obsolete) non-Newtonian anti-icing fluid. It is typical of 1980-era non-Newtonian fluids, and is no longer commercially available. It was tested to allow comparison with results from earlier wind tunnel tests. Fluids 3 and 4 were 1987 non-Newtonian anti-icing fluids. Fluid 3 was the baseline fluid for the test because, at the time of the test, it was representative of the most widely used non-Newtonian anti-icing fluids.

Besides testing the four fluids described above, all of which were commercially available during or before 1987, eight experimental fluids developed by the four participating fluid manufacturers were tested. These were all non-Newtonian fluids. The fluid manufacturers were Hoechst AG, Kilfrost Ltd., SPCA, and Union Carbide Corp. All the fluids tested are summarized in table I.

The fluid rheological characteristics (viscosity versus shear stress) and water content are given in appendix A. These data are based on samples of each fluid tested by Boeing Materials Technology after the test. Also included are the holdover times for the four basic fluids and for four of the experimental fluids. These four experimental fluids are the ones chosen for commercial production by the fluid manufacturers after the test.

Data Measurements

The principal data measurements were the model force data from internal balances on both the two-dimensional model and the three-dimensional half model. These measurements allowed lift, drag, and pitching moment to be determined on both models. On the three-dimensional half model, rolling moment could also be determined.

Another data measurement was fluid depth. Two measurements of fluid depth were made. The first was a gap gauge measurement of initial fluid depth before each run. The measurement was made at approximately the 50 percent chord location at three spanwise stations. The second measurement of fluid depth was made using an ultraviolet fluorescence photographic technique. The fluids were dyed with Rhodamine 6G fluorescent dye (0.005 percent concentration). Photographs were taken by the light of an ultraviolet strobe lamp every 2 sec during each run. A calibration plate having grooves of various depths was filled with fluid and photographed before each run. After the test a scanning microdensitometer was used to analyze the negatives. This allowed fluid depth (including waves) to be determined as a function of chordwise location based on the correlation of brightness and fluid depth from the calibration photograph. Dyeing the fluid also made it possible to use a video camera to make continuous recordings of the fluid flow-off characteristics. This was done for all runs on both models.

As an aid in understanding the physical mechanism of the fluid aerodynamic effects, the two-dimensional model was instrumented to measure boundary-layer total pressure profiles. This was done using a 10-probe rake mounted just forward of the flaps.

Test Parameters

The test matrix for the three-dimensional half model is summarized in table II. The table shows the configurations and temperatures tested for each fluid and for the dry baseline. The table also indicates that flow visualization runs and simulated frost (distributed solid roughness) runs were made for the flaps 5, sealed-slat configuration. The flow visualization runs consisted of china clay runs to show the airflow patterns over the wing at various angles of attack and naphthalene sublimation runs to show the location of transition from laminar to turbulent flow on the wing with and without trip strips. These flow visualization techniques will be discussed later. The simulated frost runs consisted of applying grit to the wing surface. This was done to provide solid roughness data to correlate with the fluid roughness effects. None of the experimental fluids were tested on the three-dimensional half model because of the limited tunnel testing time.

The test matrix for the two-dimensional model is shown in table III. Flow visualization runs and simulated frost runs for this model were similar to those described above for the three-dimensional half model. All eight of the experimental fluids were tested on this model.

Test Procedures

The basic test procedures were established to simulate field application of the fluids. The basic test procedures were as follows:

(1) Wipe the wing clean with dry rags.
(2) Wipe on a thin film of 50 percent water, 50 percent fluid 1 mixture.
(3) Pour the fluid to be tested on the wing.
(4) Use a fluid scraper to get the desired fluid depth (usually 0.5 mm).
(5) Run the tunnel at idle (6.2 m/sec (12 keas)) for 5 min.
(6) Linearly increase the tunnel speed to 69.4 m/sec (135 keas) in 30 sec.
(7) At $t = 25$ sec, rotate the model from 0 to the desired attitude at 3/sec.
(8) Continue the run for 30 sec past the end of rotation.

The tunnel acceleration is compared with a typical airplane flight test ground roll acceleration in figure 12 (p. 18). The match is good, except for the first few seconds. This early mismatch was a result of the characteristics of the tunnel motor control system, which increases the tunnel speed from idle (about 6.2 m/sec (12 keas)) to about 12.3 m/sec (24 keas) (for about 3 sec) before starting the linear acceleration to 69.4 m/sec (135 keas). Because of the low velocities and short times involved, this early mismatch probably has no measurable effect on the data.

Test Limitations

The primary limitations of this test are related to the small scale of the models tested and the resulting questions concerning scale effects. The corrections applied to the data to account for the presence of the wind tunnel floor and ceiling lose their validity at high lift conditions if the ratio of the model chord to the tunnel height exceeds about four. Thus, the tunnel test section height of 1.83 m (6 ft) limited the maximum model chord length for the two-dimensional model to 0.457 m (1.5 ft). The three-dimensional half model was an existing Boeing model which had about the right span for the test section. Thus, both models had short chords. This results in shorter fluid flow distances in the wind tunnel than on the full-scale airplane. Another effect of the short chords is a lower chord Reynolds number in the wind tunnel, which results in higher shearing stress at a given percentage of the chord at a given velocity than is present on the full-scale airplane. We realized before the test that these differences would raise questions about the validity of the wind tunnel results. However, having flight data available for comparison with the wind tunnel data allowed the magnitude of these effects to be determined. It also provided the possibility, if it had been found necessary, of adjusting the wind tunnel test parameters, such as fluid depth, tunnel speed, and velocity at rotation, to provide a better match with flight data. A parametric study was conducted of these variables, and adjustments were found to be unnecessary.

TABLE II.—THREE-DIMENSIONAL HALF MODEL TEST MATRIX

	Flow vis	Simulated frost	Fluid 1	Fluid 2	Fluid 3	Fluid 4	Dry baseline
Flaps 5, sealed slat configuration; ground plane in:							
Temperature—							
0 °C					✓		✓
−5 °C						✓	✓
−10 °C			✓	✓	✓	✓	✓
−20 °C			✓		✓	✓	✓
q_{LOF} (for T = −10 °C)					✓		✓
Fluid thickness (T = −10 °C)					✓		✓
Flaps 5, sealed slat configuration; free air:							
T = +10 °C	✓	✓					
−20 °C					✓		✓
Flaps 5, sealed slat configuration; free air + aileron:							
T = −20 °C					✓		✓
Flaps 5, gapped slat configuration; free air:							
T = −20 °C					✓		✓
Flaps 15, gapped slat configuration; ground plane in:							
T = −5 °C						✓	✓
−10 °C			✓	✓	✓		✓
−20 °C			✓		✓	✓	✓
Flaps 15, gapped slat configuration; free air:							
T = −20 °C					✓		✓

✓ Indicates conditions included in flight test.

TABLE III.—TWO-DIMENSIONAL MODEL TEST MATRIX

	Flow vis	Simulated frost	Fluid 1	Fluid 2	Fluid 3	Fluid 4	Dry baseline	New fluids
Flaps 5, sealed slat configuration:								
T = +10 °C	✓	✓			✓		✓	
0 °C					✓		✓	✓
−5 °C						✓	✓	
−10 °C			✓	✓	✓	✓	✓	✓
−20 °C			✓	✓	✓	✓	✓	✓
−29 °C			✓		✓		✓	
Time to lift off								
T = −20 °C					✓		✓	
q_{LOF} (T = −20 °C)					✓		✓	
Fluid thickness:								
(T = −20 °C)					✓		✓	
Flaps 5, gapped slat configuration:								
T = −20 °C					✓		✓	
Flaps 15, gapped slat configuration:								
T = −10 °C			✓	✓	✓	✓	✓	
−20 °C			✓	✓	✓	✓	✓	
Flaps 15, cruise leading edge:								
T = 0 °C					✓		✓	
−10 °C					✓		✓	
−20 °C					✓		✓	

✓ Indicates conditions included in flight test.

Results

Three-Dimensional Half Model

Flow visualization.—Flow visualization runs were made at various angles of attack at the beginning of the test to determine the flow quality on the wing surface without fluid. China clay, which is a mixture of kaolin powder and kerosene, was applied to the wing surface. The tunnel was then brought up to a designated speed with the model at a constant pitch angle. The kerosene subsequently evaporated, leaving a signature of the wing surface airflow. The results are shown in figure 13 (p. 18). At an angle of attack of 7°, the dark area at the trailing edge of the aft flap segment is the only local area of separation. At an angle of attack of 11°, which is only 2° below $C_{L,max}$, the outboard wing in the vicinity of the aileron is separated. At an angle of attack of 14°, which is 1° above stall, the entire outboard half of the wing is separated. The dark circle near the midspan of the wing indicates a vortex at that location, caused by the separation.

Sublimation runs were made to determine the extent of laminar flow on the three-dimensional half model. A solution of naphthalene crystals dissolved in Freon TMC was sprayed onto the model surface around the wing leading edge. The tunnel was then brought up to speed with the model at a constant pitch angle. The naphthalene remained on the model in areas of laminar boundary-layer flow and sublimated in areas of turbulent flow. Figure 14(a) (p. 19) shows the outboard leading-edge region of the wing with no trip strips after a sublimation run. Laminar flow (the white areas) extends at least to the end of the slat in all areas and beyond that in some areas.

To assure that turbulent flow existed on as much of the wing as possible and to better simulate the shear stress to which the fluid is subjected in full-scale flight, a trip strip was applied near the wing leading edge. It consisted of No. 80 microbeads and was applied with a 50–50 solution of Duco cement and acetone using a striping brush. The results of a flow sublimation run with the trip strip are shown in figure 14(b). The boundary layer is turbulent behind the trip strip in most areas. However, to assure that the flow would be tripped everywhere, the final trip strip used consisted of No. 50 microbeads.

Effect of test parameters.—The effect of the small model scale on the aerodynamic effects of the fluids was not well understood. Therefore, the early part of the test was devoted to investigating the effect of certain test parameters on the fluid aerodynamic effects. The plan was to vary the test parameters, as necessary, to achieve a good match between the lift loss due to fluid 3 (which was considered to be the baseline fluid) and that measured in the flight test at a similar condition.

The test parameters investigated were the velocity at rotation, the time to rotation, and the fluid thickness. Figure 15 (p. 20) shows the effect of varying these parameters on the lift coefficient. These results are shown for a body attitude of 7. This attitude results in a lift coefficient that is about 75 percent of $C_{L,max}$. It was chosen because, on the full-scale airplane, the takeoff safety speed condition (one-engine-out climb) corresponds to about 75 percent of $C_{L,max}$.

As shown in figure 15, velocity at rotation has an effect on the lift coefficient with fluid on the wing. A typical full-scale 737-200ADV airplane velocity at rotation is 61.7 to 64.3 m/sec (120 to 125 keas). Two runs were made to investigate the effect of time to rotation. The velocity at rotation was held constant for both runs by changing the tunnel acceleration. The results shown in figure 15 indicate no significant effect of changing the time to rotation from 23 to 46 sec.

To investigate the effect of fluid thickness, thickness was varied from 2 to 0.5 mm (0.08 to 0.02 in.). Figure 15 shows that there is no discernable trend to the data and that the data scatter is only slightly larger than the 1 percent estimated data accuracy. Therefore, there does not appear to be a significant effect of initial fluid thickness.

Using a time to rotation and a velocity at rotation in the wind tunnel that were similar to those of the flight test (25 sec and 61.7 to 64.3 m/sec (120 to 125 keas), respectively) resulted in reasonably good agreement between the lift losses due to the fluids in the wind tunnel and those measured in the flight test. Therefore, these were the values that were used throughout the test, except for specific runs.

Figure 16 shows the effect of the same test parameters on the drag increase due to fluid 3 at the same condition for which the lift effect was shown. The effect of velocity at rotation was significant, and the effect of time to rotation was small. Initial fluid thickness apparently does not affect drag increase.

Test technique verification.—The original test plan called for rotating the model to a fixed attitude and holding that attitude for the duration of the run. The attitude would be changed from run to run to define points on the lift curve. The purpose of this approach was to match the procedures of the Kuopio flight test, where the airplane was rotated to a fixed attitude and then held at that attitude until liftoff. However, during the test it was determined that, unlike the flight test, it was possible to determine the entire lift curve during a single run by rotating the model continuously to an attitude above that corresponding to $C_{L,max}$. Figure 17 shows the results of a series of runs in which the model was rotated to various fixed attitudes, including an attitude above stall. Each symbol on the lift curve indicates the highest attitude of a given run. All of the points, both for the dry wing case and for the fluid case, lie on a single curve, with only a small amount of data scatter. Therefore, we concluded that all the required data could be obtained in a single run in which the model is rotated to an attitude above stall. In fact, this approach probably resulted in more well-defined curves, with less data scatter than would have occurred with the original approach.

Typical three-component data.—A typical set of force data for the three-dimensional half model is shown in figure 18 (p. 21). This figure shows lift coefficient versus body angle of attack, drag coefficient, and pitching moment coefficient. Three dry baseline runs and a single fluid run are shown. The effect of the fluid on lift, drag, and pitching moment is very evident.

Plots similar to figure 18 for all four of the basic fluids at various temperatures and on various three-dimensional half model high-lift configurations are contained in appendix B.

Effect of fluids on lift.—A summary of the lift losses due to the fluids for the flaps 5, sealed-slat configuration in ground effect is shown in figure 19(a) for an angle of attack of 7° and at $C_{L,max}$. The lift loss for the baseline, fluid (fluid 3) at −20 °C is almost 9 percent. The lift loss is even higher for fluid 2. Fluid 1 even has a lift loss of almost 7 percent at T = −20 °C; for fluid 4 the lift loss is about 5 percent at that temperature. An important conclusion that can be drawn from these results is that the lift loss, in most cases, is higher than that at $\alpha = 7°$. This was one of the primary results desired from the wind tunnel test. In most cases the lift loss increases as the temperature decreases.

At the takeoff safety speed condition (the attitude corresponding to 75 percent of maximum lift), the agreement between the fluid lift losses in the wind tunnel and those measured in the flight test (not shown) is within the estimated accuracy of the data for all fluids except fluid 2. This overall agreement is sufficiently good to allow the direct use of the three-dimensional half model results at full-scale conditions. The agreement with the flight test data for the flaps 15 configuration is similar to that of the flaps 5 configuration.

The effect of gaping the slat on the lift loss due to the fluid for the flaps 5 configuration is shown in figure 20. The flaps 5 configuration does not normally have a gapped slat, but was tested specifically to allow comparison of lift losses for both configurations. At $\alpha = 7°$, the effect of the fluid on the lift was similar. However, at $C_{L,max}$ the lift loss is much larger for the gapped slat than for the sealed slat. In spite of this, gaping the slat with fluid on the wing restores the maximum lift capability to that of the sealed slat, dry wing configuration.

In the flight test, when fluid was applied to the airplane wing, the leading-edge slats and the trailing edge flaps were in the up position. They were extended immediately after departure from the terminal area. In the wind tunnel tests of the gapped-slat configuration, the slat was in the extended position when the fluid was applied. This allowed some of the fluid to get on the underside of the slat and on that portion of the wing leading edge that would be covered by the slat when it was in the up position. To determine how this affected the lift loss due to the fluid, a run was made in which these regions were carefully cleaned after the fluid was applied. Results from this run (run 225) are compared in figure 21(a) (p. 22) with those for a normal run in which these regions were not cleaned. Lift increases significantly, particularly at $C_{L,max}$, when these regions are cleaned. The flight case is probably somewhere between the two cases, since some fluid will run down onto the dry wing leading edge after the slat is extended during the taxi.

Figure 19(b) shows the lift loss due to the fluids for the flaps 15, gapped-slat configuration. These losses are significantly higher than for the flaps 5, sealed-slat configuration. For fluid 3 the lift loss at $C_{L,max}$ at −20 °C is about 13 percent compared with less than 9 percent for the flaps 5, sealed- slat configuration. We believe this increased lift loss to result, in part, from a large secondary fluid wave that moves back from the leading edge after rotation on the flaps 15 configuration. Secondary fluid waves were also observed on the flaps 5 configuration, but they were not as large. Figure 22 (p. 23) is a photograph of the flaps 15 configuration with fluid 3 on it taken just after rotation. The secondary wave is evident in this photograph. As discussed later in the section "Distributed Solid Roughness", the loss in maximum lift caused by the fluid is highly dependent on the presence of fluid in the first 30 percent of the chord. Therefore, it appears that the secondary wave, by replenishing the fluid in that key part of the wing after rotation, plays an important part in determining the loss in maximum lift caused by the fluid.

The effect of cleaning the slat lower surface and the portion of the wing that would be covered by the slat in the retracted position (surface 1) is shown in figure 21(b) for the flaps 15 configuration. As was the case for the flaps 5, gapped-slat configuration, the lift loss at $C_{L,max}$ decreases significantly when these regions are cleaned. Unlike the flaps 5 configuration, cleaning these regions has no effect at the lower angles of attack. Again, we believe that for the actual full-scale airplane, the lift loss will be somewhere between the clean case and the uncleaned case. None of the these regions were cleaned for the flaps 15, gapped-slat configuration shown in this paper, unless there is a specific note to the contrary.

Effect of fluids on drag.—The drag increase due to the fluids 15 sec after the start of tunnel acceleration is shown in figure 23(a). This time corresponds, approximately, to the time during the airplane ground roll at which the average takeoff acceleration drag occurs. Interestingly, the fluids that have the smallest lift loss do not necessarily have the smallest drag increase. In particular, fluid 4 has a larger drag increase than fluid 3 at $T = -20$ °C even though, as was seen previously, it has a much smaller lift loss. Drag increase data for the flaps 15, gapped-slat configuration are shown in figure 23(b).

The drag increase due to the fluids at the takeoff safety speed condition (at a model body attitude of 7°) is shown in figure 24(a) (p. 24) for the flaps 5, sealed-slat configuration and in figure 24(b) for the flaps 15 configuration. For most cases the drag increases are larger for the flaps 15 configuration. For the baseline fluid (fluid 3) the drag increase at $T = -20$ °C for flaps 5 is about 11 percent, compared with about 25 percent for flaps 15.

The effect of time from brake release to liftoff (time from start of tunnel acceleration to end of rotation) and time after liftoff (time after the end of rotation) on the drag increase due to the fluid is shown in figure 25. The drag increment due to the fluid decreases with increasing time from brake release to liftoff and decreases with time after liftoff. After 1 min the drag increase for both flap configurations has dropped to about 10 percent of its initial value after liftoff.

Effect of fluids on pitching moment.—The effect of the fluids on the pitching moment about the quarter mean aerodynamic chord is shown in figure 26(a) for the flaps 5, sealed-slat configuration. At 7° the dry wing pitching moment coefficient is negative. The fluids cause a positive (nose-up) pitching moment increment. This is a result of both decreased lift and a small forward movement in the location of the center of lift, as shown in figure 27. At $C_{L,max}$ the dry-wing pitching moment is positive, indicating that lift is being lost on the aft part of the wing or on the outboard part of the wing, or both, compared with the lift at 7°. Figure 26(a) also shows that the fluids result in a negative pitching moment increment at $C_{L,max}$. This negative increment is due both to the lower lift and to an aft movement in the center of lift, as shown in figure 27.

The effect of the fluids on the pitching moment for the flaps 15, gapped-slat configuration is shown in figure 26(b). The pitching moments for the dry wing are more negative than those for the flaps 5 case, indicating that the loading has been moved aft. At 7° the fluids result in a positive pitching moment increment, similar to the flaps 5 data. This is due both to a reduction in lift and to a forward movement in the center of lift (fig. 27). At $C_{L,max}$ the fluids again result in a positive pitching moment increment. This is primarily because of the decrease in lift due to the fluid, since there is very little movement of the center of lift (fig. 27).

Effect of fluids on rolling moment.—The effect of the fluids on the rolling moment for the flaps 5 configuration is shown in figure 28(a) (p. 25). These results on the half model simulate the case of an airplane with fluid on the left wing only. All of the fluids result in a negative rolling moment increment (left wing down), as expected, since they cause a lift loss. The negative rolling moment increments are larger for the flaps 15 case.

The change in rolling moment, together with the change in lift, was used to determine the change in the spanwise center of lift. The results are shown in figure 29. An inboard shift in the center of lift increment at $C_{L,max}$ for $\alpha = 7°$, indicates that, as $C_{L,max}$ is approached, relatively more lift is being lost due to the fluid outboard than to fluid inboard. The effect is small, however, because a 1 percent change in (Y center of lift)/(b/2) is only a 0.5 in. shift, at model scale.

Effect of fluids on aileron power.—The effect of fluid 3 on the aileron power is shown in figure 30. These results are for a 20° trailing-edge down aileron deflection. They indicate that aileron power is increased with the fluid on the wing.

Two-Dimensional Model

Flow visualization.—Flow visualization runs were made at the beginning of the two-dimensional model testing to assess the quality of flow on the model upper surface at the junction with the turntable and to assess the two dimensionality of the flow over the model. No boundary-layer blowing or suction was used on the splitter wall or turntable.

Figure 31 (p. 26) shows the results of a china clay run at an angle of attack of 13°, which is about 1° below stall. Even at this angle of attack, the only areas of flow separation are the small, dark, triangular areas on the midflap and aft flap segments at the wall. Also, except very near the wall, the streamlines are all parallel to the direction of the undisturbed flow, indicating that the flow is highly two dimensional. Thus, the flow quality on the model was judged to be satisfactory.

Figure 32(a) (p. 27) shows the results of a naphthalene sublimation run made to determine the location of natural transition from laminar to turbulent flow on the model upper surface at $\alpha = 8°$. Transition, as indicated by the end of the white region, is occurring either at or slightly aft of the end of the slat. Figure 32(b) shows the sublimation results after application of a 2.5-mm (0.1-in.) wide trip strip of No. 50 microbeads located 8 mm (0.3 in.) behind the slat leading edge. A small amount of the white naphthalene can be seen ahead of the trip strip, and none behind, indicating that the trip strip is working.

Typical three-component data.—A typical set of three-component data for the two-dimensional model is shown in figure 33 (p. 28) for three dry baseline runs and a single fluid run shown. The effect of the fluid is, again, evident. This type of data was generated for all runs and analyzed to determine the fluid effects on the two-dimensional model, as discussed in the next sections. The complete set of two-dimensional model force data is contained in appendix C.

Effect of fluids on lift.—A summary of the lift losses due to the fluids for the flaps 5, sealed-slat configuration is shown in figure 34(a) for $\alpha = 8°$ and at $c_{l,max}$, where c_l is the sectional lift coefficient. The 8° angle of attack represents the takeoff safety speed condition for the two-dimensional model, corresponding to about 75 percent of $c_{l,max}$. Note that for the two-dimensional model the angle of attack of the wing chord plane is used and for the three-dimensional model the angle of attack of a body water line is used. On the 737-200ADV the wing chord plane angle of attack is 1° higher than that of the body. These results show that, in many cases, the lift loss at $c_{l,max}$ is lower than at 8°. This indicates the importance of the three-dimensional effects on the three-dimensional half model, since it had higher lift losses at $C_{L,max}$ than at 7° for almost all cases. It is interesting to note that, at a temperature of 29 °C, the lift loss for fluid 1, which is about 13 percent at $c_{l,max}$, is significantly higher than that of fluid 3, which is only about 9 percent. At warmer temperatures, fluid 1 has lower lift losses than fluid 3. Note that these two-dimensional results are useful for determining the relative fluid-to-fluid lift losses at a given temperature and temperature-to-temperature lift losses for a given fluid. However, since these are two-dimensional data, they cannot be used directly to estimate lift losses on the airplane.

Lift losses on the two-dimensional model with the flaps 15, gapped-slat configuration are shown in figure 34(b). These losses are much larger than those for the flaps 5, sealed-slat configuration. Secondary fluid waves were observed at both

flap settings on the two-dimensional model immediately after rotation, just as had been observed on the three-dimensional half model. The secondary waves were, again, larger for the flaps 15 configuration than for the flaps 5 configuration.

A most important result of the test was the significant reduction in lift loss for the experimental fluids as compared with the 1987 baseline non-Newtonian fluid (fluid 3). The experimental fluids were tested only on the two-dimensional model and only on the flaps 5, sealed-slat configuration. The lift loss results at −20 °C are shown in figure 35 along with the results for fluids 1 and 3, for comparison. The lift loss varies from fluid to fluid, but in most cases, it is about 40 percent lower for the experimental fluids than for fluid 3, both at $\alpha = 8°$ and at $c_{l,\max}$. The effect of temperature on the lift losses of four of the experimental fluids is shown in figure 36 (p. 29). Note that at a temperature of 0 °C the lift loss at $c_{l,\max}$ for fluids 3.1, 4.1, and 5.1 is negligible, whereas, for fluid 3 it is about 6 percent. This is a very significant improvement.

Effect of fluids on drag.—The increase in drag caused by the fluids during the simulated takeoff acceleration (the period during which the tunnel was accelerated before model rotation) is shown as a function of time in figure 37 for the four basic fluids, and in figures 38 to 40 for the experimental fluids. Note that the relationships between the fluids change with time.

The takeoff acceleration drag at a time of 15 sec after the start of tunnel acceleration corresponds roughly to the average takeoff acceleration drag. It is shown in figure 41 for the experimental fluids and for fluids 1 and 3. Even though all the experimental fluids had lower lift losses than fluid 3, some result in larger takeoff acceleration drag increases.

The drag increase at the takeoff safety speed condition due to the four basic fluids is shown in figure 42 (p. 30) for the flaps 5, sealed-slat configuration. At $T = -20$ °C the drag increase varies from about 20 percent for fluid 4 to about 94 percent for fluid 2. Again, it is important to remember that these two-dimensional model data are useful for making fluid-to-fluid comparisons and temperature-to-temperature comparisons, but not for estimating absolute drag increments on a full-scale airplane. Note, also, that these data correspond to the end of rotation (time of liftoff) and that the drag increment due to the fluid drops rapidly with time after liftoff, as was shown for the three-dimensional half model in figure 25. The large percentage drag increases are a result of the low dry-wing drag level of the two-dimensional model (no body drag, induced drag, etc.).

Figure 43 shows the effect of temperature on the fluid 3 drag increment at the takeoff safety speed. The drag increase varies from 21 percent at 10 °C to about 70 percent at −29 °C.

The drag increases at the takeoff safety speed for the experimental fluids are compared with those for fluids 1 and 3 in figure 44 (p. 31). Note that the experimental fluids show lower drag increases than fluid 3 at all three temperatures.

Drag increases at the takeoff safety speed condition for the four basic fluids on the flaps 15, gapped-slat configuration are shown in figure 45. They tend to be slightly smaller than those for the flaps 5, sealed-slat configuration.

Configuration with no leading-edge device.—To investigate fluid effects on a configuration without a leading-edge high-lift device, several runs were made with a flaps 15, cruise leading-edge configuration. Since this configuration is more typical of a smaller, slower airplane, the tunnel acceleration scheme was changed to increase from 11.3 to 46.3 m/sec (22 to 90 keas) in about 22 sec, with rotation at 18 sec at a speed of about 41.2 m/sec (80 keas). The results are shown in figure 46 for fluid 3. For this configuration the takeoff safety speed condition (75 percent of $c_{l,\max}$) corresponds to an angle of attack of 2°. The lift loss is measurable at this condition, but it is very small at $c_{l,\max}$. This may be due to the large velocities and resulting high shearing stresses that occur at the leading edge without the slat. This would result in a cleaner leading edge and a lower lift loss at $c_{l,\max}$ than for a configuration with a deflected slat. This cleaner leading edge was indicated by the lack of a noticeable secondary wave for this configuration. The importance of a clean leading edge is discussed in the next section.

Distributed Solid Roughness

Boeing had previously obtained flight test data on the effects of simulated frost on several airplanes, including the 737-200ADV (ref. 7). As a possible aid in the extrapolation of the wind tunnel results to full-scale flight Reynolds numbers, several runs were made to test the effects of distributed solid roughness. Figure 47 (p. 32) shows the effect of various grit sizes on lift, drag, and pitching moment for the three-dimensional half model. Note that the lift loss at $C_{L,\max}$ is approximately 20 to 25 percent. As expected, the lift loss is higher for the larger grit sizes. In these runs the solid roughness was put on the entire upper surface from the leading edge of the slat to the trailing edge of the aft flap, except for those regions that were not exposed when the slat and flaps were retracted. This results in the proper simulation of frost on the wing surface. The data obtained using number 100 grit size most closely matched the incremental lift loss of the flight test data. To determine the region of the wing chord that is most important in determining the aerodynamic effects of the roughness, two additional No. 100 grit runs were made with the roughness on only the aft 70 percent and on the aft 40 percent of the chord. As shown in figure 48, most of the lift loss at $C_{L,\max}$ is caused by the roughness in the first 30 percent of the chord, since there is a large decrease in lift loss when grit is applied to only the aft 70 percent of the chord and only a very slight additional decrease in lift loss when only the aft 40 percent is covered.

Figure 49 (p. 33) shows how the fluid 3 results at $T = -20$ °C compare with the No. 100 grit results with various coverages. The fluid lift loss is similar to that of the 100 percent coverage solid roughness at the lower angle of attack, but at $C_{L,\max}$ the lift loss is closer to the aft 70 percent coverage case. This may indicate that, unlike the solid roughness, the fluid is being cleaned off in the forward portion of the chord as the model

is rotated. Some fluid roughness still remains in the forward 30 percent at the $C_{L,max}$ condition, however. This results in higher lift loss than for the solid roughness case with only aft 70 percent coverage.

Effect of Fluid Chordwise Coverage

In order to investigate the effect of fluid chordwise coverage, two runs were made with the three-dimensional half model in which no fluid was applied forward of a specified chord location. Figure 50 shows that the fluid lift loss at $C_{L,max}$ is greatly reduced, as it was proportionately so for the solid roughness, if no fluid is applied in the first 30 percent chord. Again, very little additional decrease occurs in the lift loss if only the aft 40 percent is covered. The effect on drag is also highly dependent on whether fluid present in the first 30 percent chord. The critical nature of the leading-edge area may be due to the very thin boundary layer in that area and the resulting higher ratio of fluid wave height to boundary-layer thickness.

Fluid Surface Waves and Roughness

An ultraviolet fluorescence photographic technique was used to measure and record fluid depth and surface waves as a function of chordwise location. The fluids were dyed with Rhodamine 6G fluorescent dye, and photographs were taken every 2 sec during each run, simultaneously with the flash of an ultraviolet strobe light. The method is described more fully in an earlier section (see "Data Measurements"). Results for the four basic fluids on the two-dimensional model are shown in figures 51 to 54 (pp. 34–37). In each figure a photograph and the fluid depth as a function of chord location are shown at three times. The first time is fairly early in the run. The second time corresponds, approximately, to the beginning of rotation. The third time corresponds, roughly, to an angle of attack of about 8°. Similar data for a wide range of fluids, temperatures, and model configurations are shown in appendix D.

To characterize the fluid roughness in each case by a single number, the mean height of the waves in the region from 50 to 55 percent chord was determined for each case. This location was chosen as representative of a typical wave height for each case. Although the first 30 percent of the chord was shown in the previous section to be the most important region in determining the fluid effects, the fluid wave heights near the leading edge were very close to the noise level of the measurement technique, which was estimated to be about 0.1 mm (0.004 in.). Thus, the more aft location was chosen. This average roughness was determined for the four cases shown and also for a number of additional cases, including the experimental fluids. It was then normalized by the chord of the model and correlated with the drag increase at 8°. The results indicate a definite trend of increasing drag increment with increasing fluid roughness (fig. 55, p. 38). The curve corresponds to the solid roughness skin friction drag increase, from an arbitrarily chosen base value corresponding to a k/c of 0.0001, for a fully rough surface (ref. 8). The reasonably good fit of the fluid data by this curve is an indication that fluid aerodynamic effects vary with fluid roughness height in a manner similar to the variation of the aerodynamic effects of solid roughness with solid roughness size.

Boundary-Layer Data

A boundary-layer rake was mounted on the two-dimensional model just forward of the flap (fig. 56(a)). The rake had 10 total pressure probes ranging from a height of 0.5 mm (0.02 in.) to 40.6 mm (1.60 in.). Total pressure profiles were measured for each of the four basic fluids and for the dry wing, as shown. The profiles measured with fluid on the wing do not go below a height of 5.1 mm (0.2 in.) above the model surface because fluid clogged the two probes below this height. The effect of the fluids on the profiles is very clear and includes not only the effect of the fluid roughness on the boundary layer, but also the displacement effect of the fluid itself. Figure 56(b) shows how the fluid 3 total pressure profile varies with time. After 90 sec, the fluid effect has almost totally disappeared. As shown in figure 57 (p. 39), the correlation is fair between the lift loss due to a given fluid and the height above the model surface at which the total pressure is 99 percent of the reference free stream value.

Discussion

Aerodynamic Effects of Fluids

The results show that deicing and anti-icing fluids remain on the wing after liftoff and cause a measurable lift loss and drag increase. These effects are dependent on the fluid, the high-lift configuration, and the temperature. For a high-lift configuration with leading-edge devices, the fluid effect is largest at the maximum lift condition. In most cases the fluid aerodynamic effects increase as the temperature decreases. The transitory nature of the fluid effects is indicated by the 90 percent decrease in fluid-caused drag within the first minute after liftoff. The eight experimental fluids that were tested show a significant reduction in aerodynamic effects compared with the earlier-generation fluids. The reasonably good agreement that was found between measured fluid effects in the wind tunnel and those measured in flight (refs. 5 and 6) indicates that scale effects are not large for the configurations tested.

Physical Mechanism Hypothesis

Based on the fluid roughness data and the boundary-layer measurements, the following physical mechanism for the fluid aerodynamic effects is hypothesized. The fluid surface roughness thickens the boundary layer in a manner similar to solid roughness. The fluid in the first 30 percent of the chord is the most critical because the boundary layer is thinnest in this area. The secondary wave that flows back from near the leading edge immediately after rotation replenishes the fluid in this critical region and is a key factor in determining the

magnitude of the lift loss. The thickened boundary layer (on the upper surface only), plus the effect of the fluid thickness itself, results in an effective decambering of the airfoil, causing reduced lift at angles of attack below stall. At $C_{L,\max}$, lift is reduced because the energy loss suffered by the boundary layer (which includes the energy required to move the fluid off the wing) makes it less able to withstand adverse pressure gradients, resulting in earlier separation. The extraction of energy from the boundary layer by the fluid (due to its roughness) also results in increased drag.

Conclusions

The wind tunnel test described in this paper has resulted in an improved understanding of the effects of deicing and anti-icing fluids on the aerodynamics of aircraft. A significant finding is that the newly developed (experimental at the time of the test) non-Newtonian anti-icing fluids have significantly smaller effects on aerodynamic characteristics than the previous generations of non-Newtonian anti-icing fluids. Three of these fluids are no longer experimental and are now commercially available. They provide airlines the benefit extended protection times without any larger aerodynamic effects than would result from a typical Newtonian deicing fluid. Additional important conclusions are as follows:

1. All the fluids tested cause a measurable lift loss and drag increase.

2. On the three-dimensional half model, the lift loss at $C_{L,\max}$ is higher than at the lower angle of attack conditions.

3. The lift losses measured in the wind tunnel show fair agreement with those measured in the associated flight test for all fluids except fluid 2, the pre-1987 (obsolete) non-Newtonian fluid.

4. The lift loss is higher with a gapped slat than with a sealed slat.

5. The lift loss due to fluid at $C_{L,\max}$ was greatly reduced for a configuration without a leading-edge slat.

6. At a temperature of -29 °C, the lift loss due to the newtonian deicing fluid (fluid 1), is larger than that of the baseline non-Newtonian anti-icing fluid (fluid 3).

7. A key element of the physical mechanism of the fluid aerodynamic effects appears to be the effect of the fluid roughness on the boundary layer, together with the displacement effect of the fluid itself. In particular, the fluid roughness in the forward 30 percent of the chord has a large influence on the lift loss at $C_{L,\max}$. Fluid aerodynamic effects appear to depend on the fluid surface roughness in a manner similar to the relationship between skin friction and solid roughness.

8. A secondary fluid wave flows aft from the leading edge immediately after rotation. It appears to be caused by the scrubbing action of the increased shearing stress occurring in the leading-edge region as the angle of attack increases. It replenishes the fluid in the forward 30 percent of the chord just before liftoff and appears to be a key factor in determining the magnitude of the loss in maximum lift.

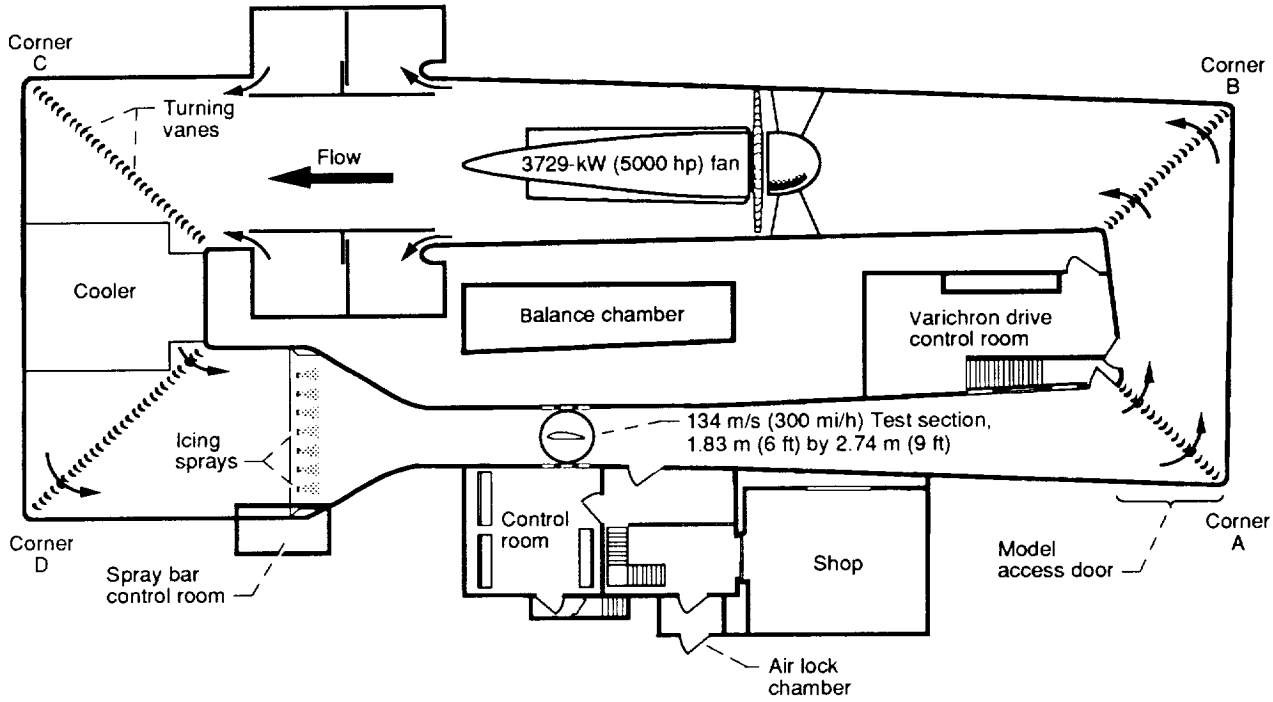

Figure 1.—NASA Lewis Icing Research tunnel.

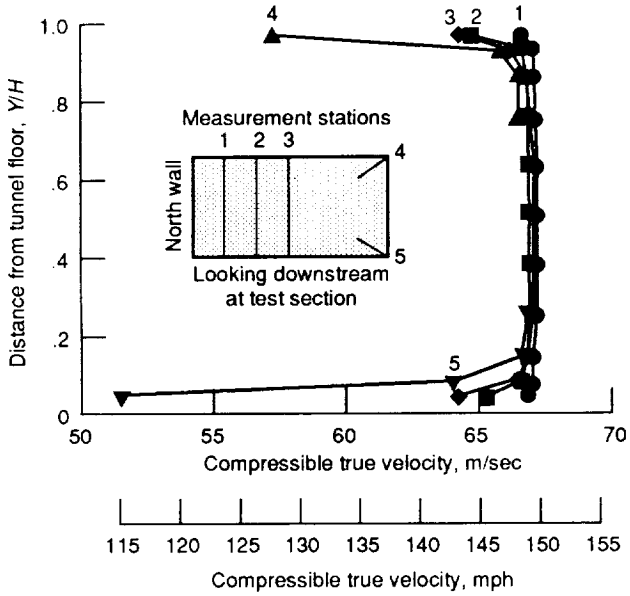

Figure 2.—Test section velocity variation. Air temperature, −18 °C; tunnel height, 1.83 m (6.0 ft).

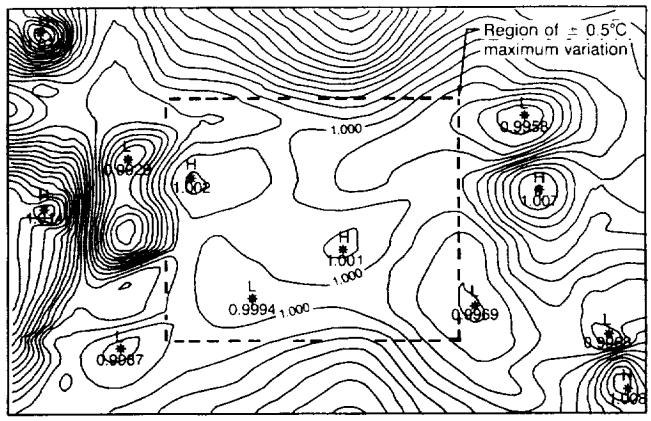

Figure 3.—IRT temperature contours in test section. Velocity 44.7 m/sec (100 mph); fluid temperature, −18 °C.

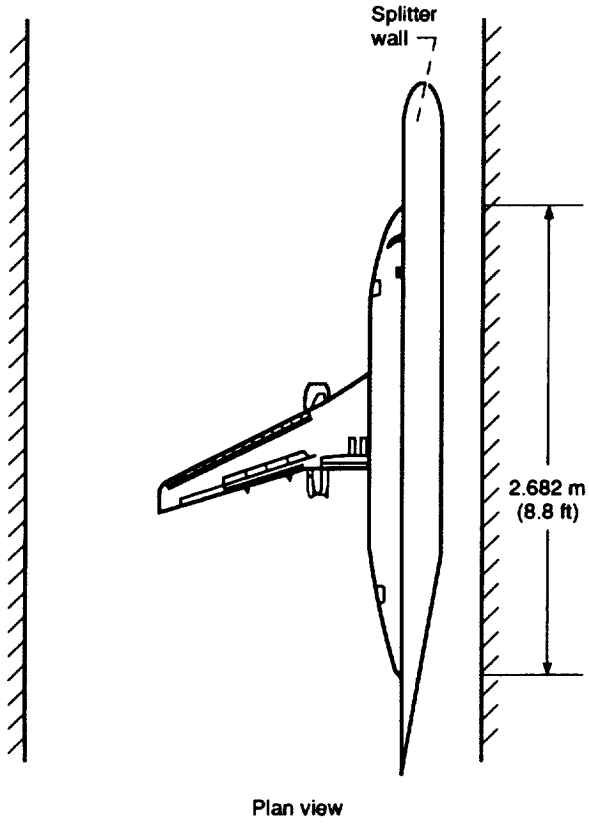

Figure 4.—Three-dimensional model (737-200ADV). Scale, 0.091; average chord, 0.305 m (1 ft). Tested with and without ground plane, with slat gapped and sealed, and with ailerons in flaps 5 and 15 configurations.

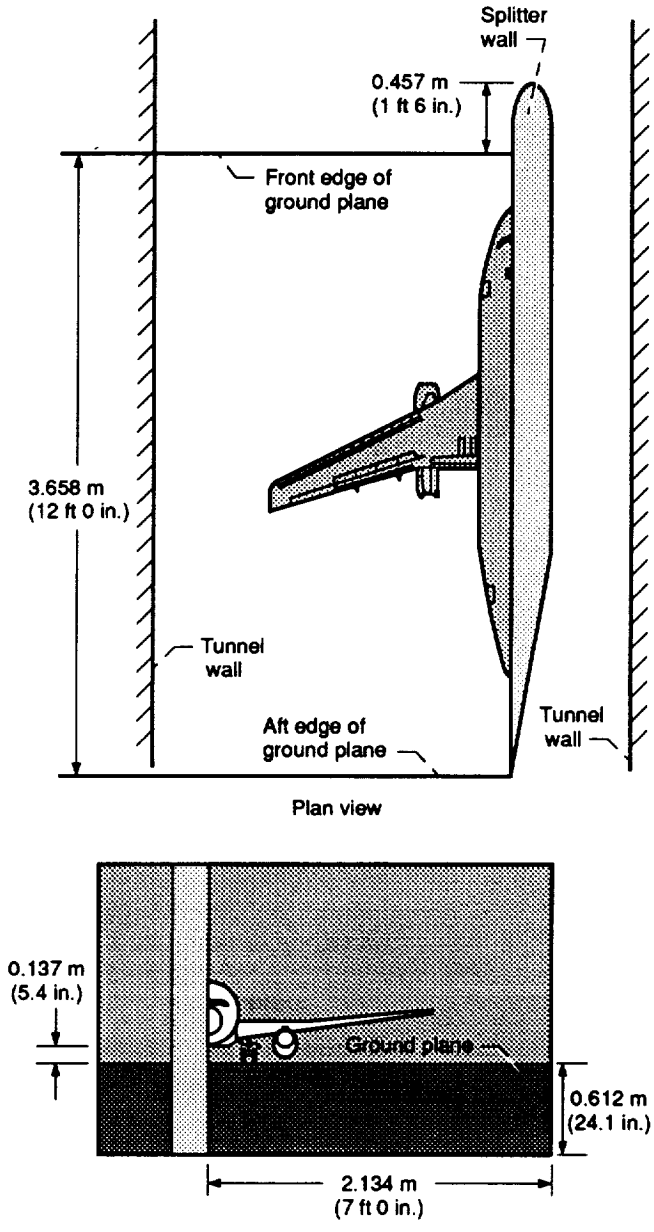

Figure 5.—Ground plane. Ground plane height corresponds to $V_{min,u}$ condition (oleo extended).

ORIGINAL PAGE
BLACK AND WHITE PHOTOGRAPH

Figure 6.—Three-dimensional half model with ground plane.

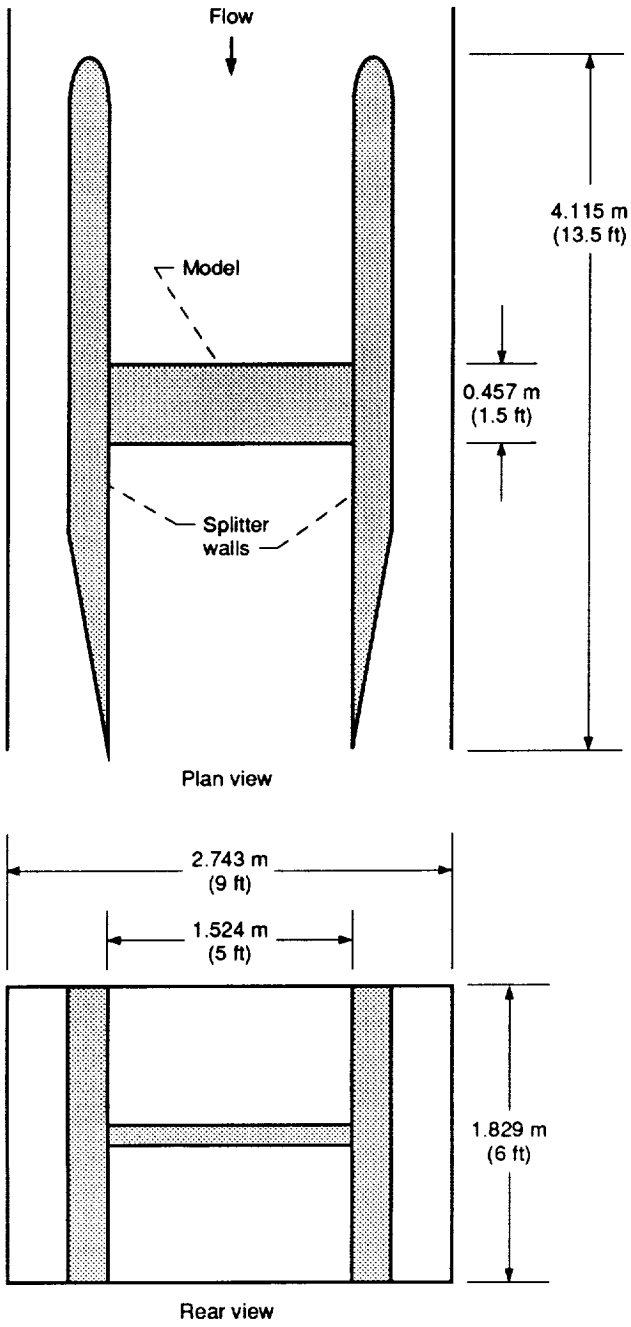

Figure 7.—Two-dimensional model. Airfoil of 737-200ADV at 65 percent span; scale, 0.18. Tested with slat retracted, sealed, or gapped in configurations flaps 5 and 15.

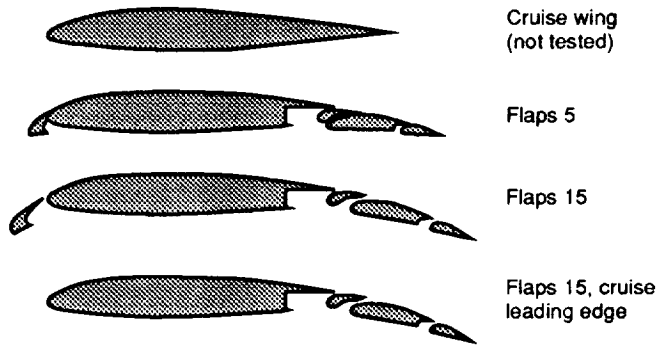

Figure 8.—Two-dimensional model flaps configurations.

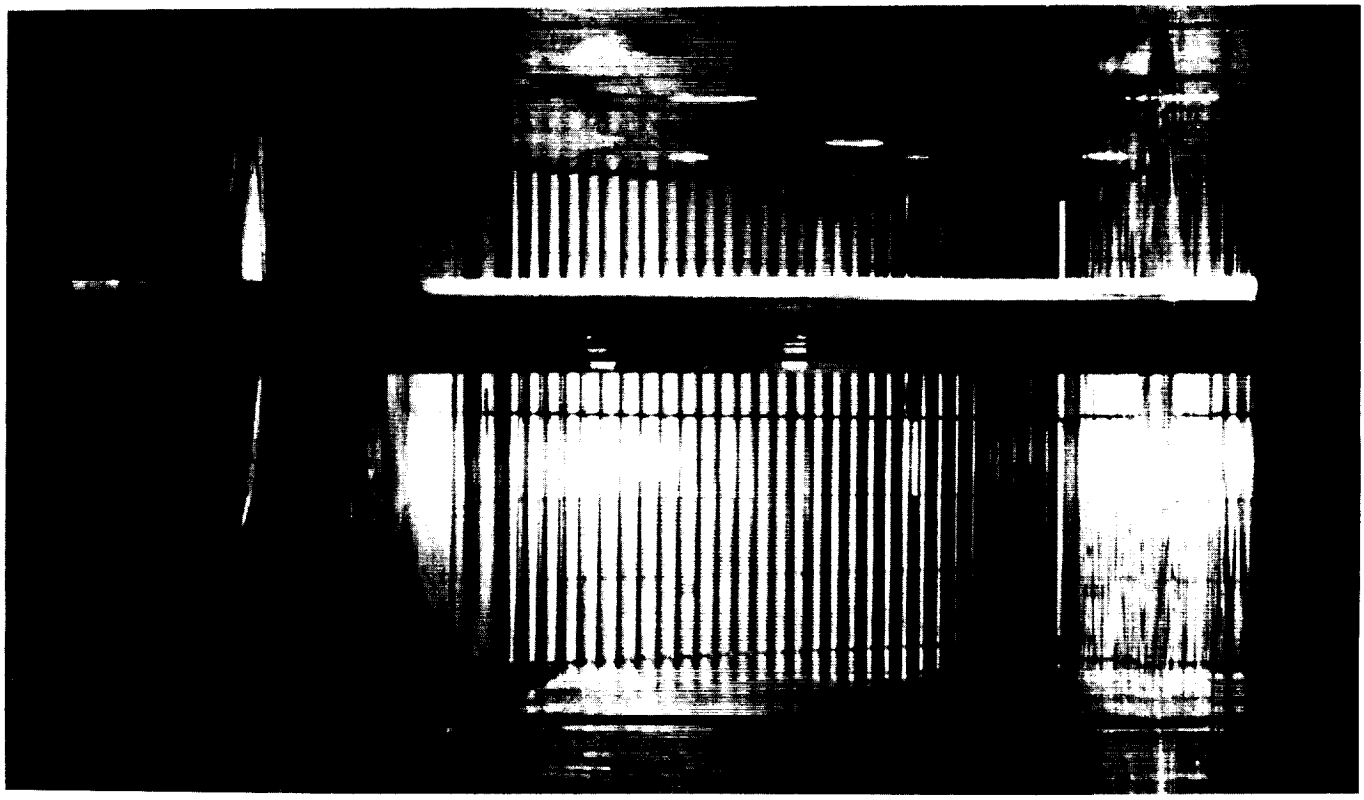

Figure 9.—Front view of two-dimensional model installed between splitter walls.

- Each channel sampled digitally four times per second
  - Balance forces and moments
  - Balance temperatures
  - Pressure transducers
  - Angle and temperature signals from accelerometer
- Online data plots on laser paper
- Final plotted and tabulated data 1 h after acquisition
- Final data tape for use on PDP 11/70

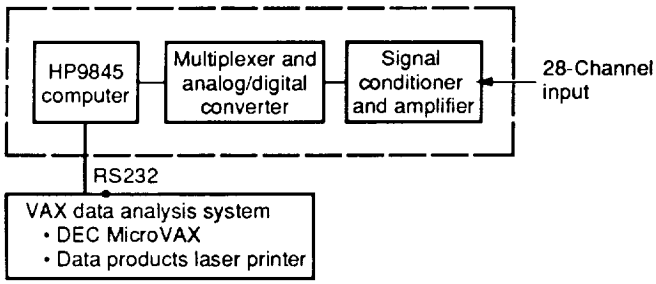

Figure 10.—Data system.

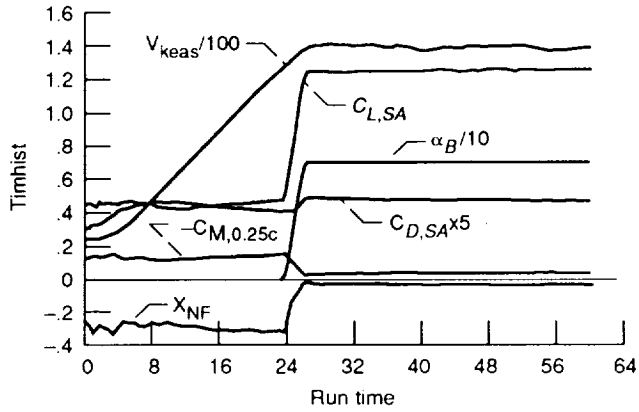

Figure 11.—Typical online data plot.

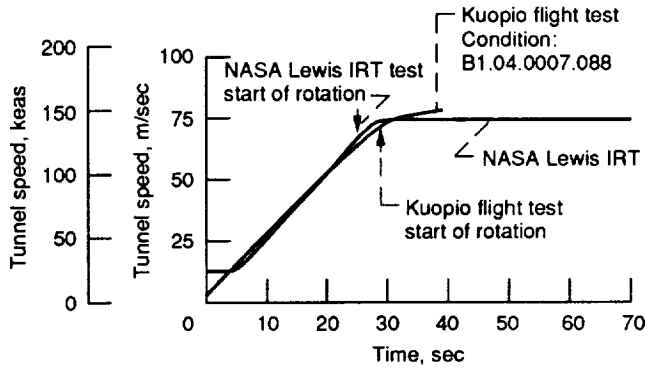

Figure 12.—Takeoff acceleration simulation.

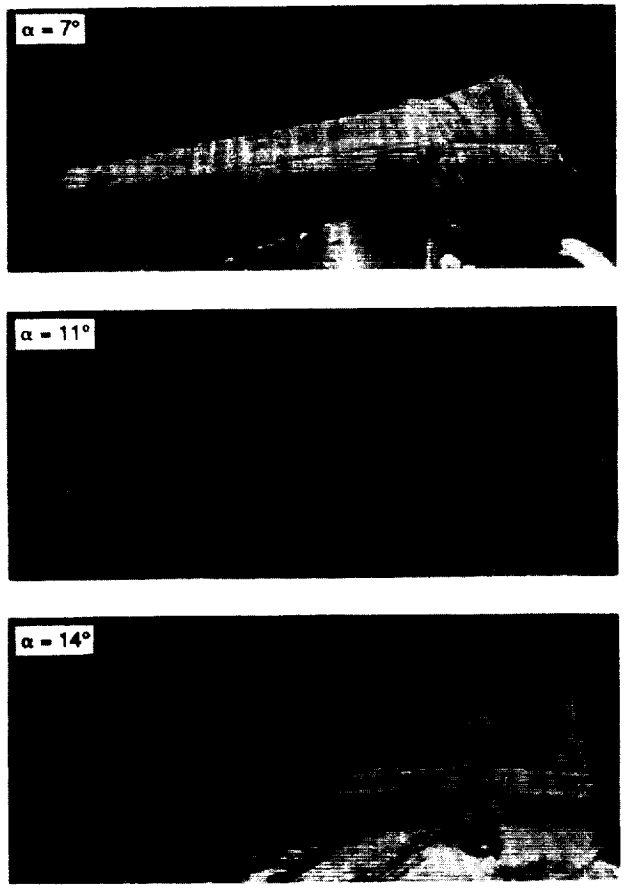

Figure 13.—China clay runs for three-dimensional half model in flaps 5, sealed-slat configuration. Ground plane in; tunnel airspeed, 69.4 m/sec (135 keas).

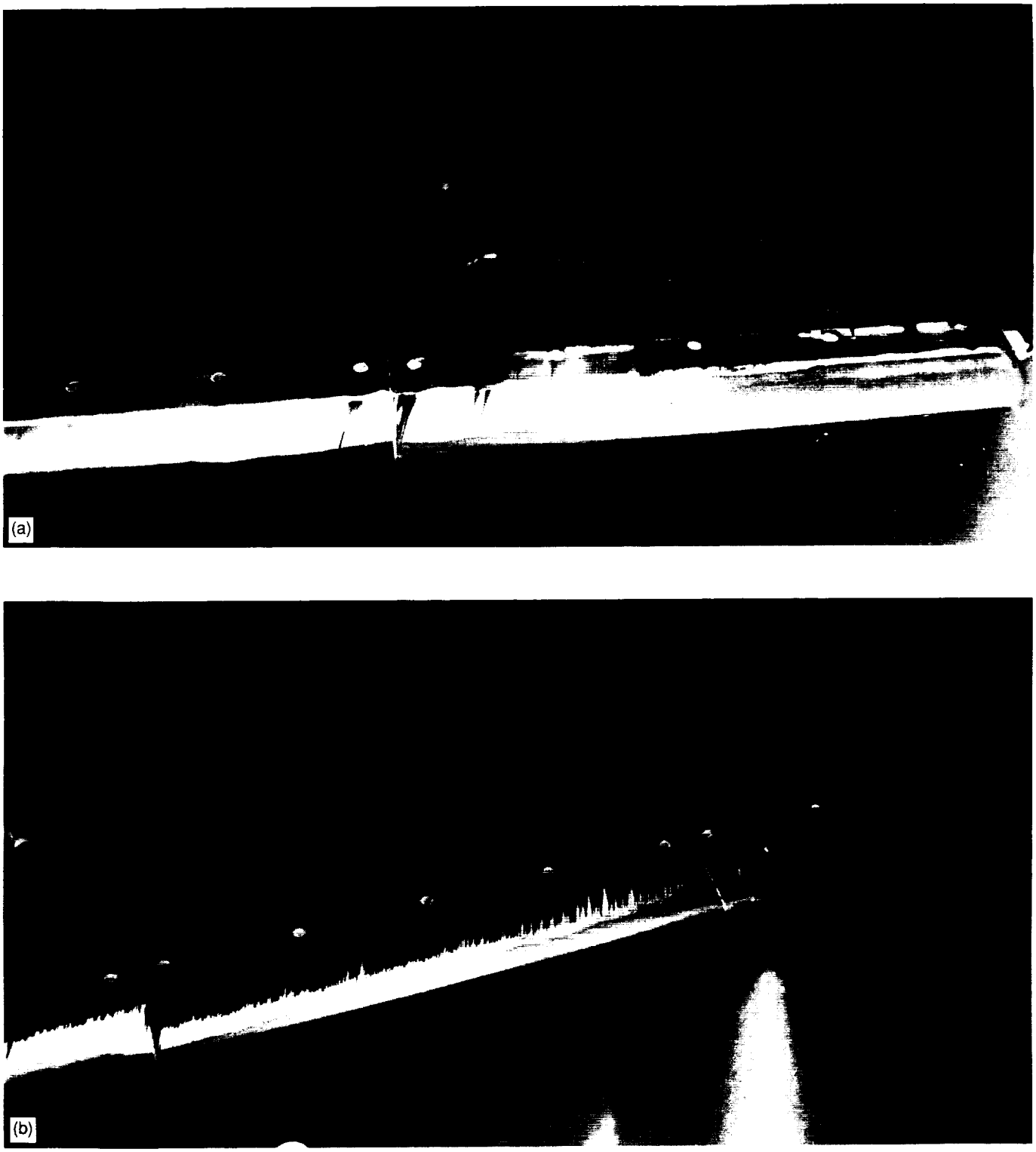

(a) Outboard wing, no trip.
(b) Outboard wing with No. 80 microbead trip.

Figure 14.—Sublimation run for three-dimensional half model in flaps 5, sealed-slat configuration. Ground plane in; $\alpha = 7°$ tunnel maximum velocity, 69.4 m/sec (135 keas); air temperature, –20°C.

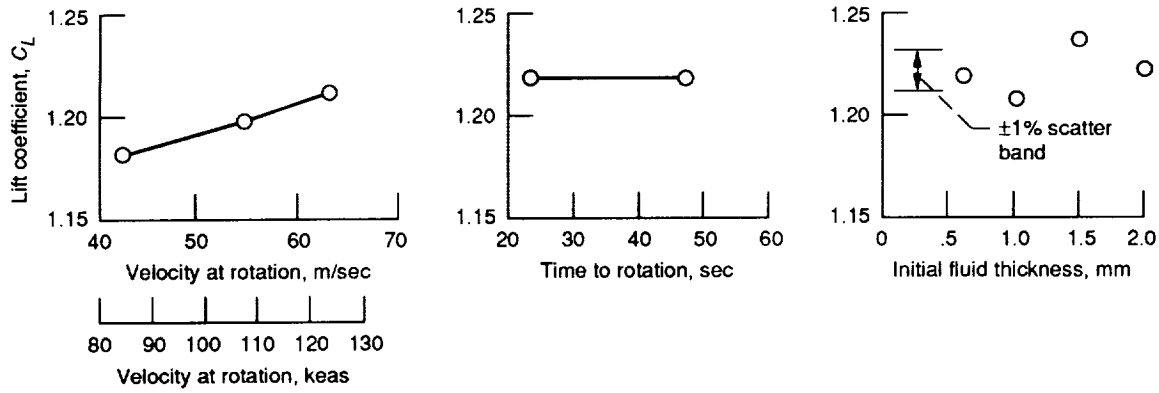

Figure 15.—Effect of test parameters on lift decrease due to fluids. Three-dimensional half model in flaps 5, sealed-slat configuration; fluid 3; air temperature, –10 °C; ground plane in; α = 7°.

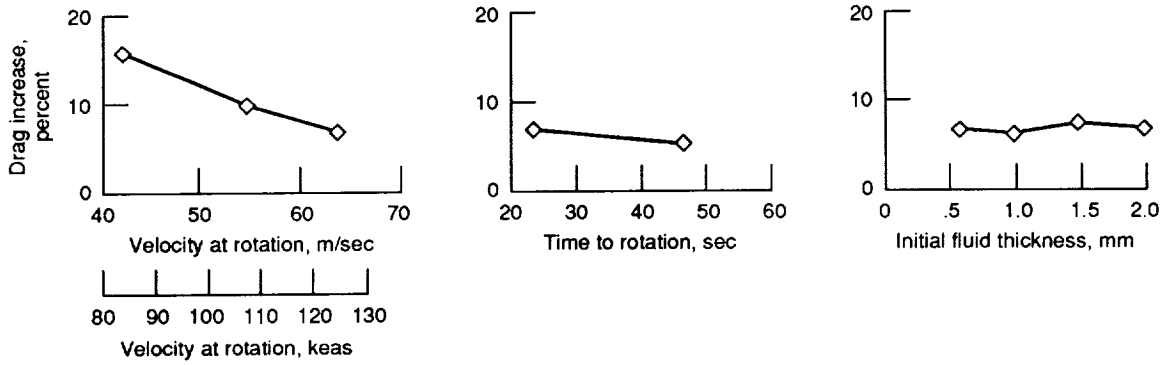

Figure 16.—Effect of test parameters on drag increase due to fluid at takeoff safety speed. Three-dimensional model in flaps 5, sealed slat configuration; fluid 3; air temperature, –10 °C; ground plane in; α_B = 7°.

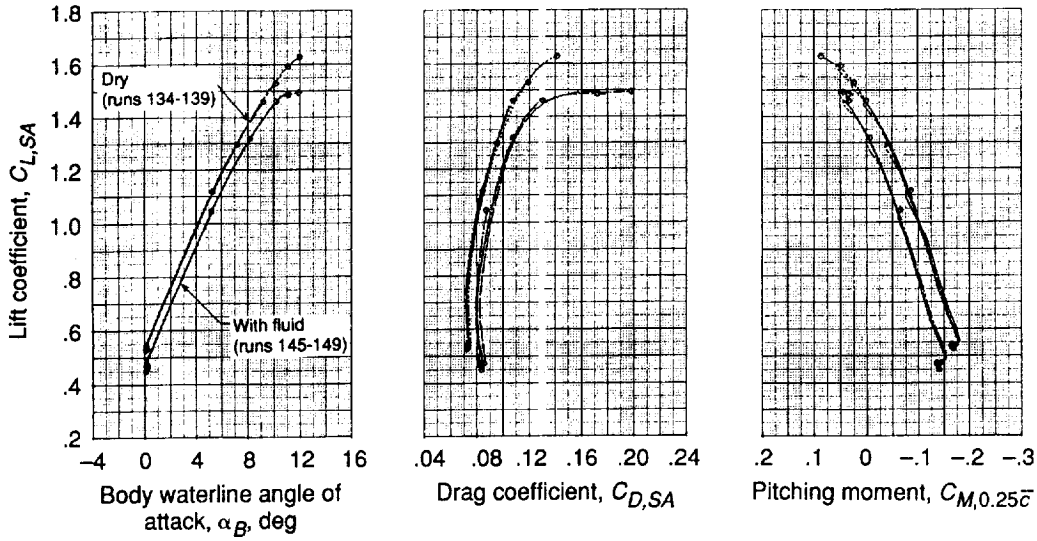

Figure 17.—Test technique verification. Three-dimensional half model in flaps 5, sealed-slat configuration; fluid 3; air temperature, –20 °C; ground plane in. Symbols indicate highest α_B point of a given run.

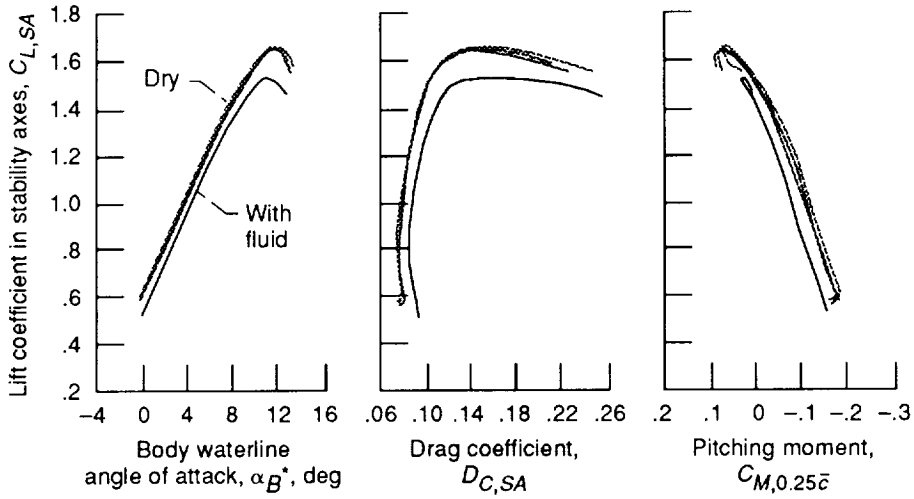

Figure 18.—Typical three-component data for three-dimensional half model in flaps 5, sealed-slat configuration; fluid 3; air temperature, −20 °C; ground plane in.

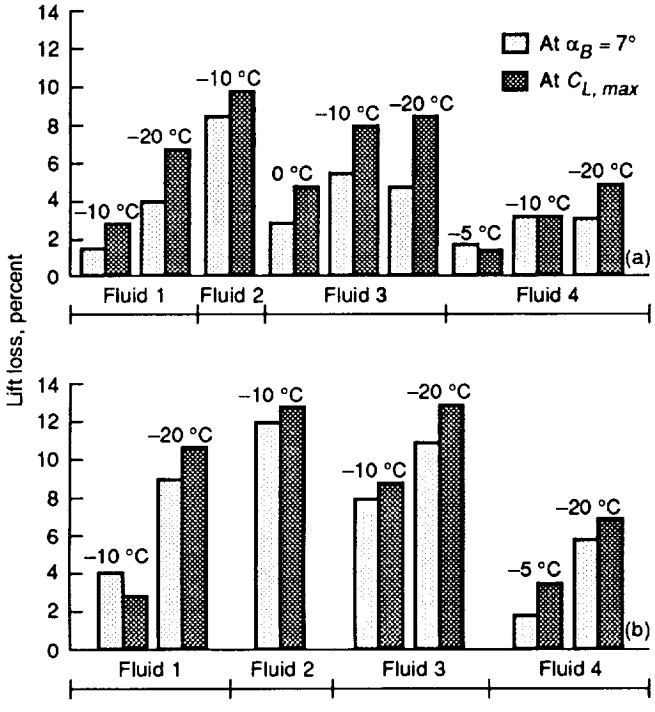

(a) Flaps 5, sealed-slat configuration.
(b) Flaps 15, gapped-slat configuration.

Figure 19.—Lift losses due to fluid. Three-dimensional half model; ground plane in.

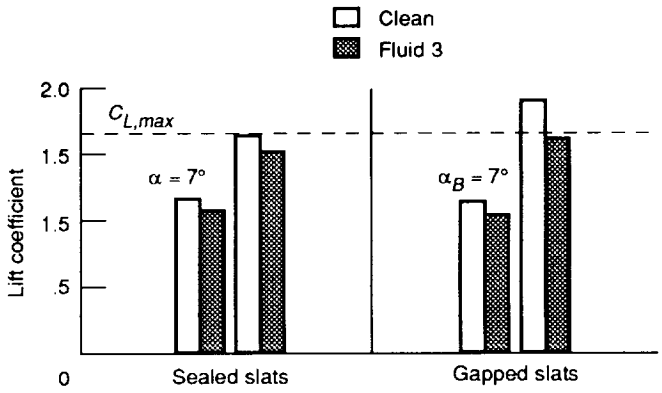

Figure 20.—Effect of gapped slat on lift with and without fluid. Three-dimensional half model in flaps 5 configuration; air temperatue, −20 °C; free air.

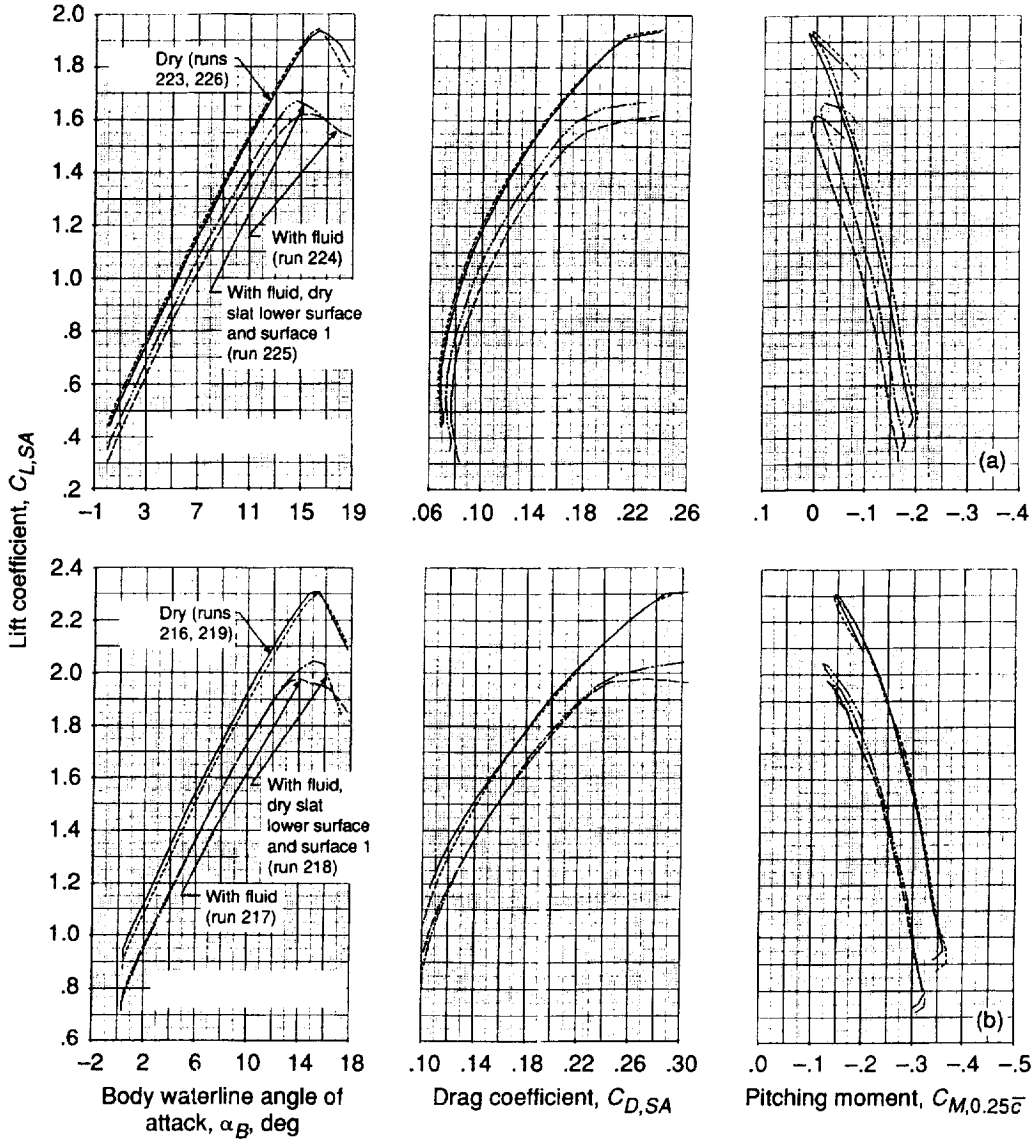

(a) Flaps 5, gapped-slat configuration.
(b) Flaps 15, gapped-slat configuraton.

Figure 21.— Effect of cleaning slat lower surface and surface 1. Three-dimensional half model; fluid 3; air temperature, –20 °C; free air.

ORIGINAL PAGE
BLACK AND WHITE PHOTOGRAPH

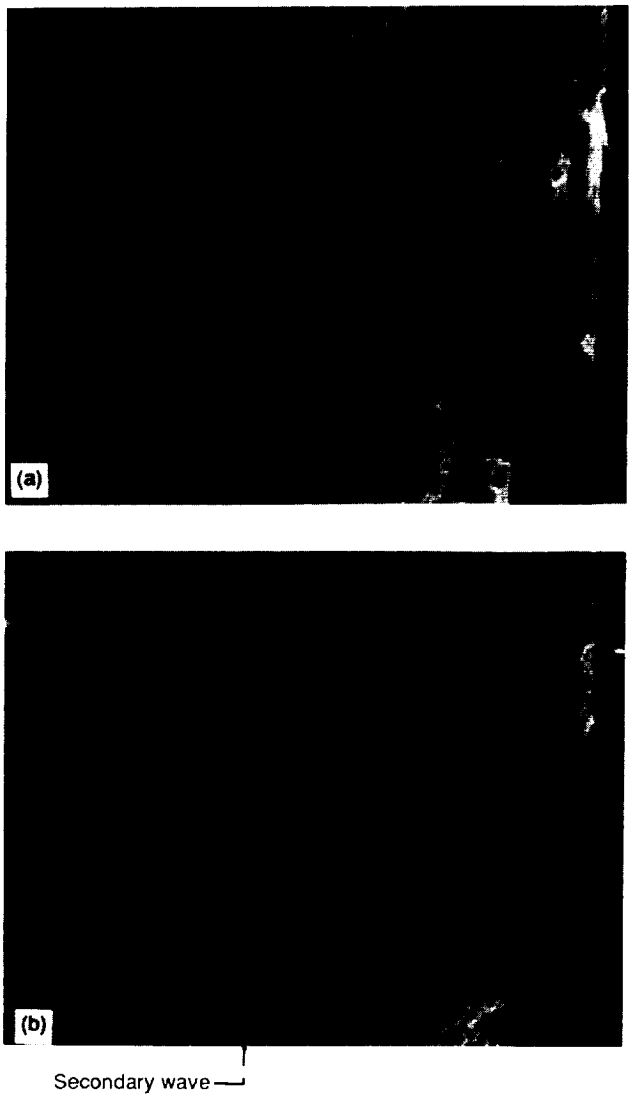

(a) At start of rotation. Elapsed time, 20 sec; airspeed, 56.5 m/sec (110 keas); α_B, 0.1°.
(b) 2 seconds after start of rotation. Elapsed time, 22 sec; airspeed, 61.7 m/sec (120 keas); α_B, 6.1°.

Figure 22.—Secondary fluid wave on three-dimensional model in flaps 15, gapped-slat configuration. Fluid 3; air temperature, −20 °C; initial fluid depth, 0.500 mm.

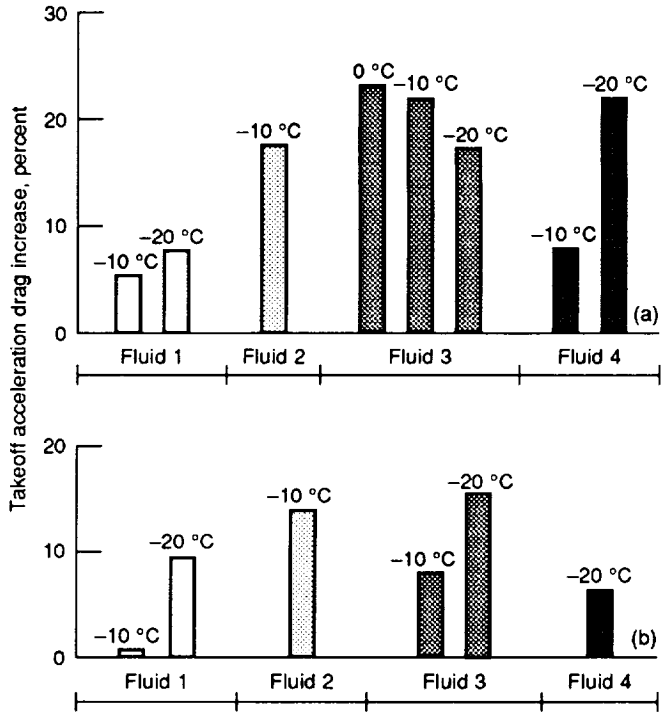

(a) Flaps 5, sealed-slat configuration.
(b) Flaps 15, gapped-slat configuration.

Figure 23.—Takeoff acceleration drag increase due to fluids. Three-dimensional half model; elapsed time, 15 sec; ground plane in.

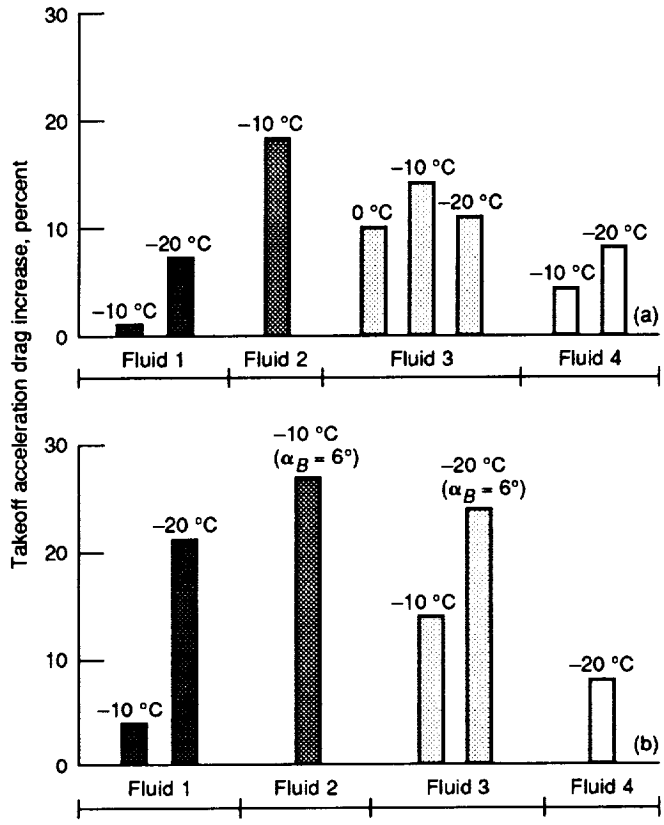

(a) Flaps 5, sealed-slat configuration.
(b) Flaps 15, gapped-slat configuration.

Figure 24.—Drag increase due to fluids at takeoff safety speed. Three-dimensional half model; ground plane in; C_L corresponding to clean wing $\alpha_B = 7°$, except as noted.

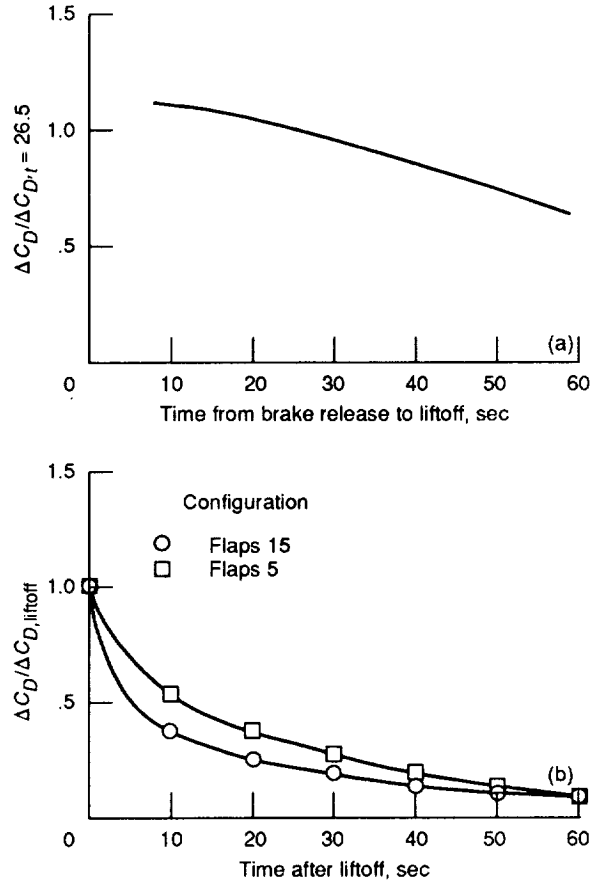

(a) Air temperature, −10 °C; flaps 5 configuration; $\alpha_B = 7°$.
(b) Air temperature, −20 °C.

Figure 25.—Drag increase due to fluids at takeoff safety speed versus time. Three-dimensional half model; fluid 3; air temperature, $\Delta C_D = C_{D,w/fluid} - C_{D,dry}$.

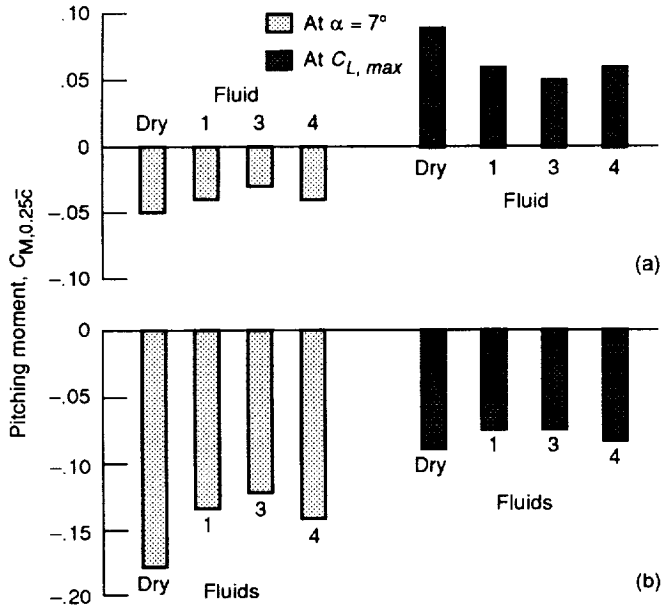

(a) Flaps 5, sealed-slat configuration.
(b) Flaps 15, gapped-slat configuration.

Figure 26.—Effect of fluid on pitching moment. Three-dimensional half model; air temperature, −20 °C; ground plane in.

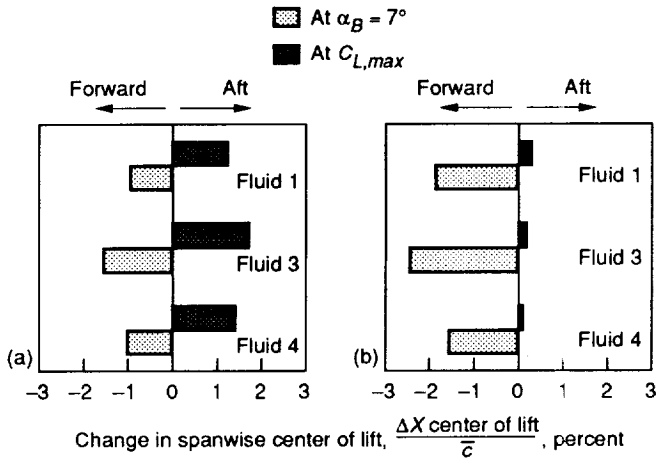

(a) Flaps 5 configuration.
(b) Flaps 15 configuration.

Figure 27.—Effect of fluid on chordwise center of lift. Three-dimensional half model; fluid 3; air temperature, −20 °C; ground plane in.

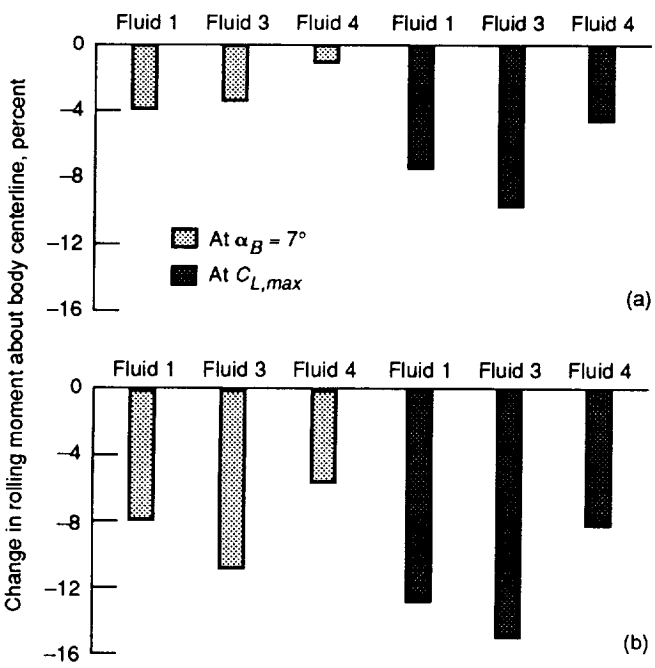

(a) Flaps 5, sealed-slat configuration.
(b) Flaps 15, gapped-slat configuration.

Figure 28.—Effect of fluid on rolling moment. Three-dimensional half model; air temperature, −20 °C; ground plane in. Simulates case of airplane with fluid on left wing only.

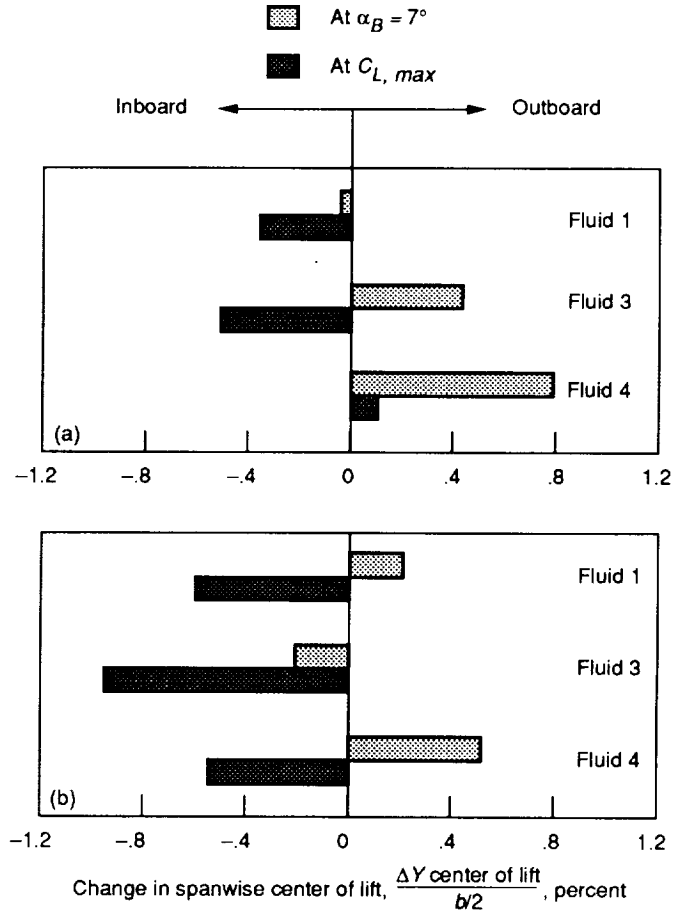

(a) Flaps 5 configuration.
(b) Flaps 15 configuration.

Figure 29.—Effect of fluid on spanwise center of lift. Three-dimensional half model; fluid 3; air temperature, −20 °C; ground plane in.

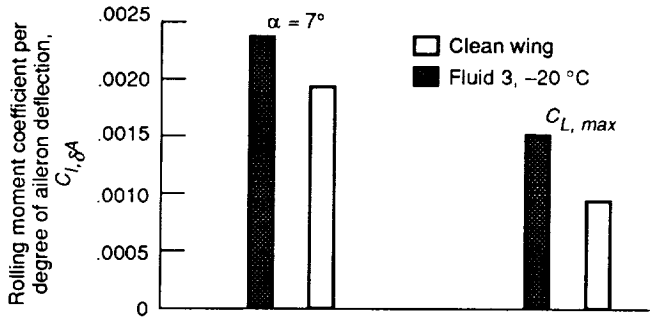

Figure 30.—Effect of fluid on aileron power (based on full-scale equivalent). Three-dimensional half model; flaps 5, sealed-slat configuration; $\delta_A = 20°$; free air. Rolling moment base on 20° trailing-edge-sown aileron deflection.

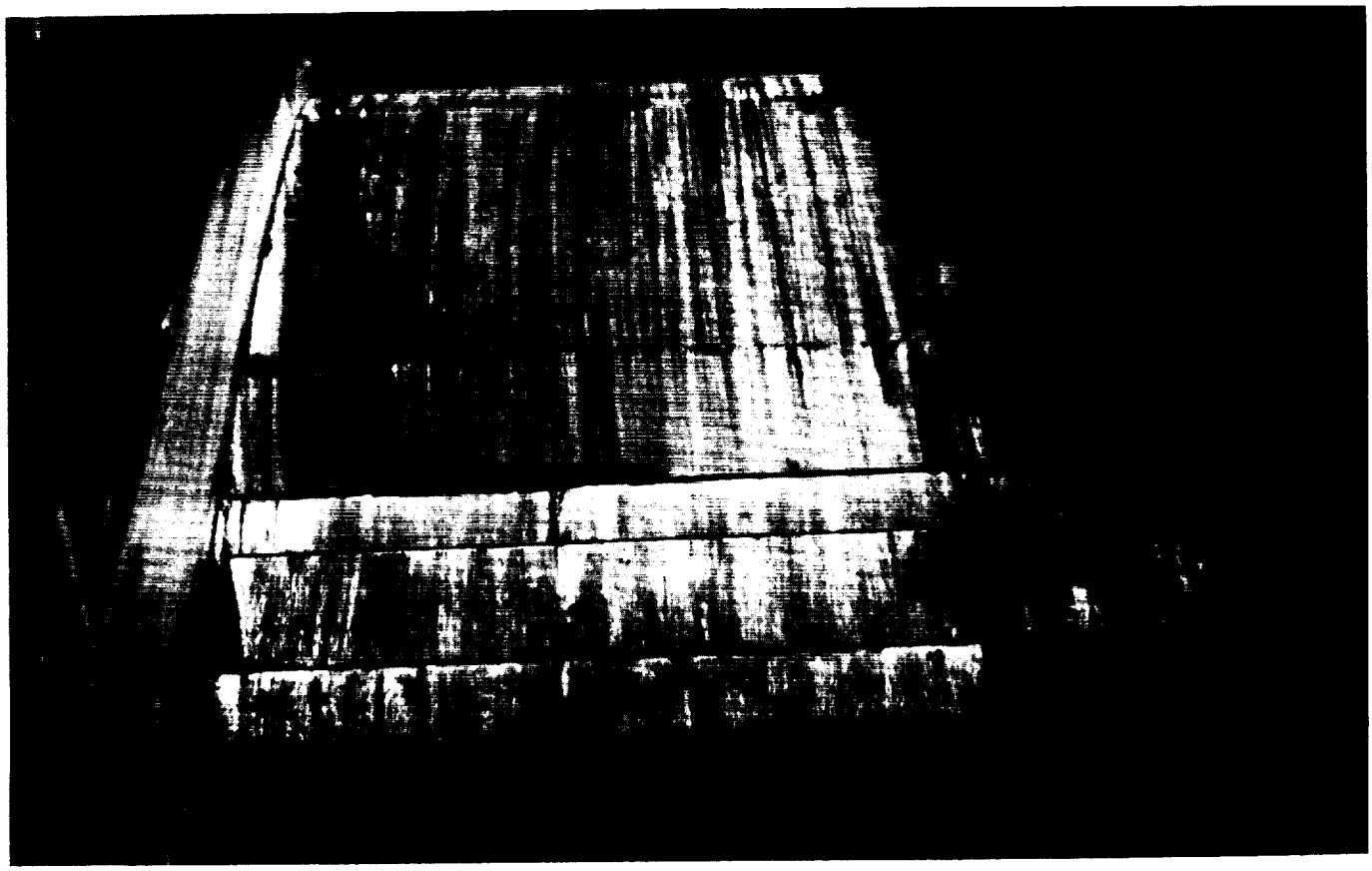

(a) No trip.
(b) With trip; No. 50 microbeads in 0.3 in aft of slat leading edge.

Figure 31.—Two-dimensional model china clay run in flaps 5, sealed-slat configuration. Velocity, 69.4 m/sec (135 keas); $\alpha_w = 13°$.

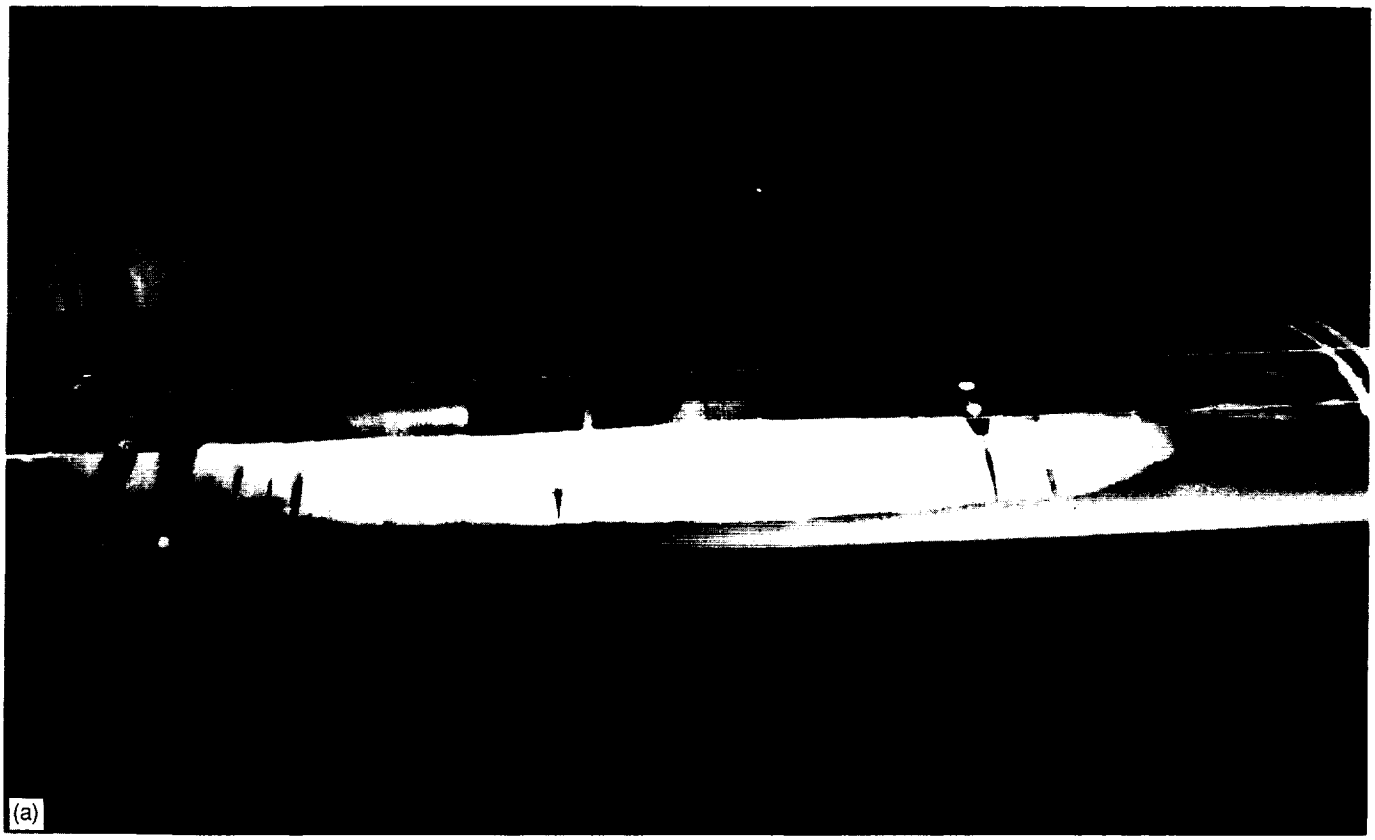

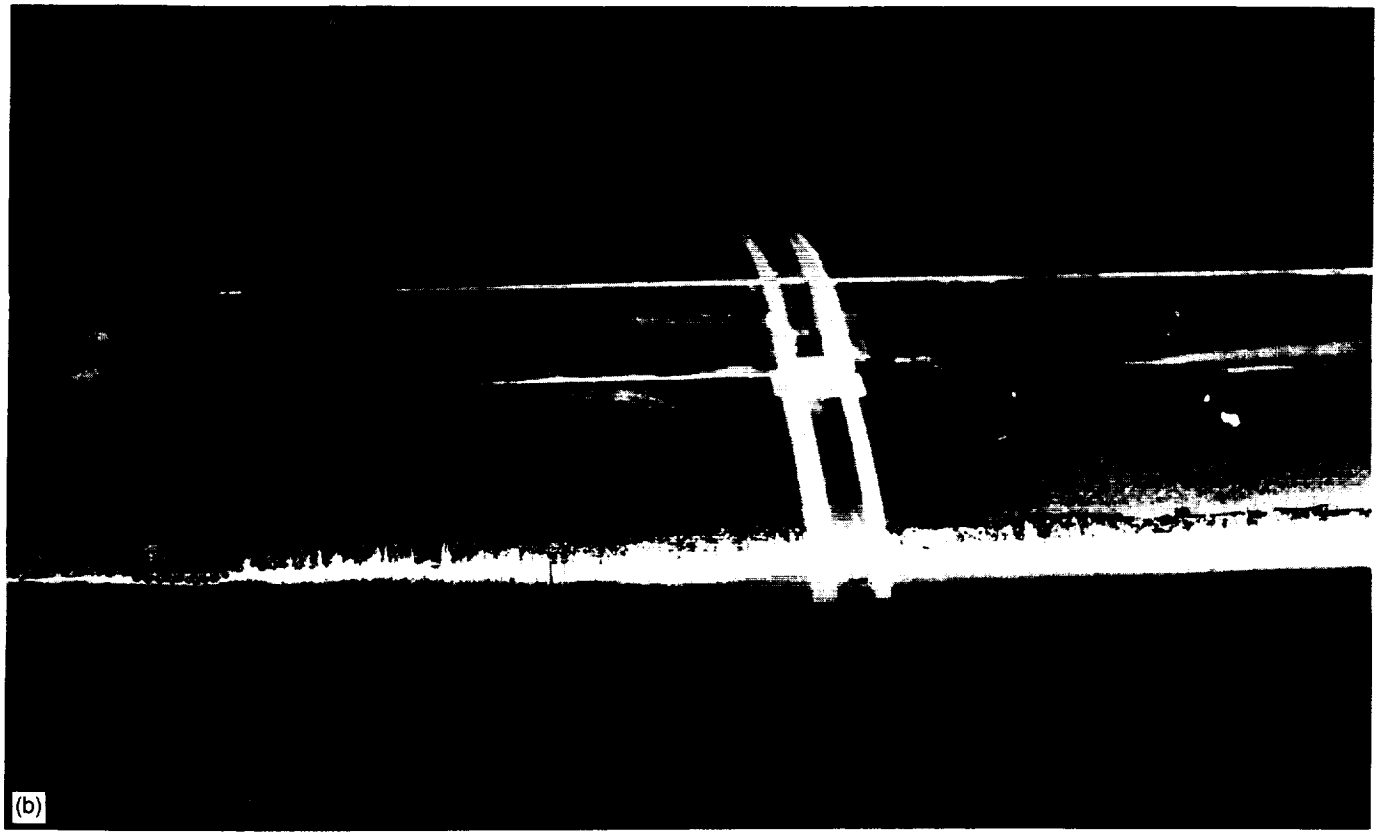

Figure 32.—Two-dimensional model sublimation run. Flaps 5, sealed-slat configuration; velocity, 6904 m/sec (135 keas); $\alpha_w = 8°$.

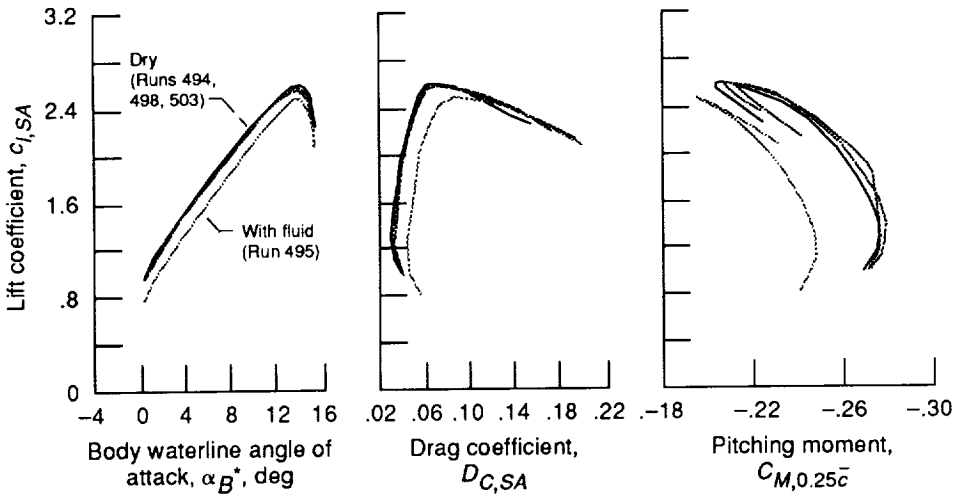

Figure 33.—Typical three-component force data for two-dimensional model. Flaps 5, sealed-slat configuration; fluid 3; air temperature, −20 °C; 65 percent span section. Data corrected for dynamic q effects.

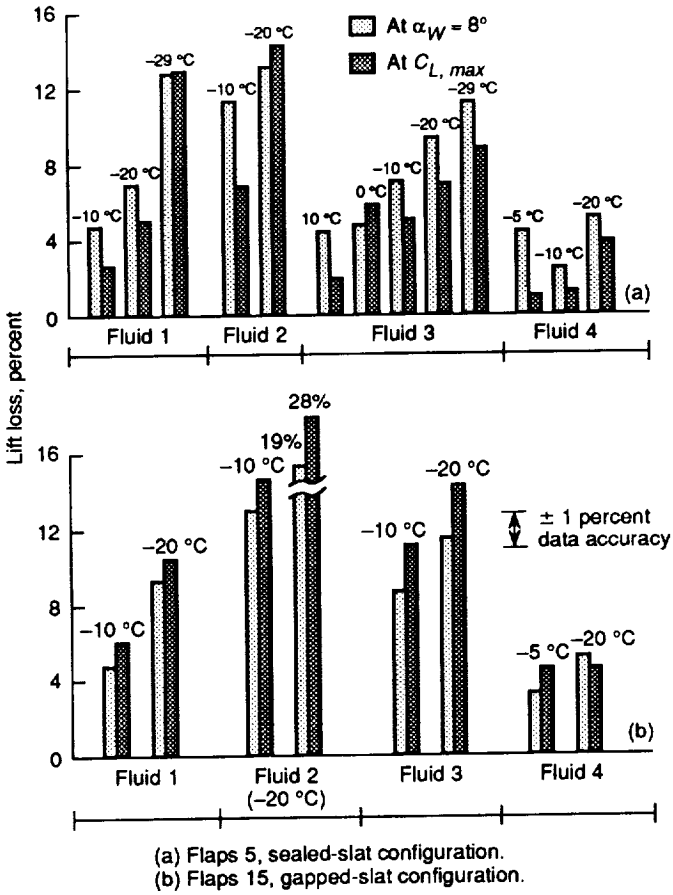

(a) Flaps 5, sealed-slat configuration.
(b) Flaps 15, gapped-slat configuration.

Figure 34.—Lift loss due to fluid. Two-dimensional half model.

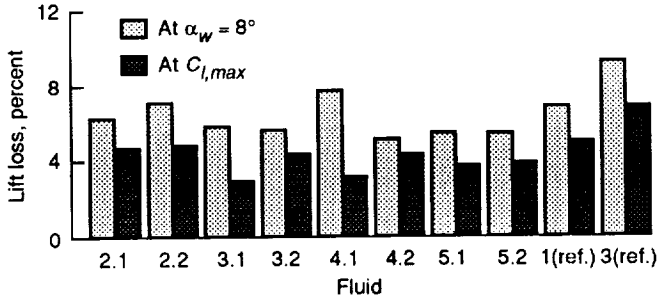

Figure 35.—Lift loss due to experimental fluids. Two-dimensional model in flaps 5, sealed-slat configuration; air temperature, −20 °C.

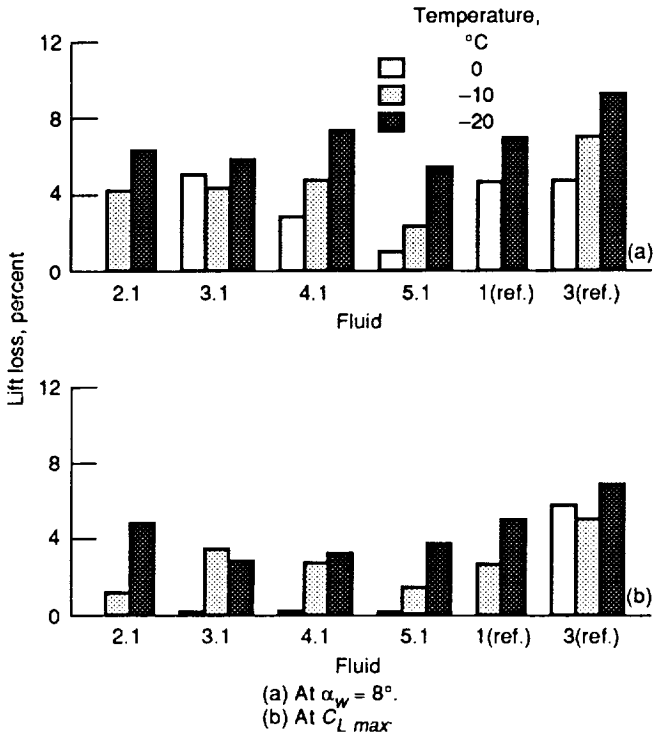

(a) At $\alpha_w = 8°$.
(b) At $C_{L\ max}$.

Figure 36.—Temperature sensitivity of lift loss due to experimental fluids. Two-dimensional model in flaps 5, sealed-slat configuration.

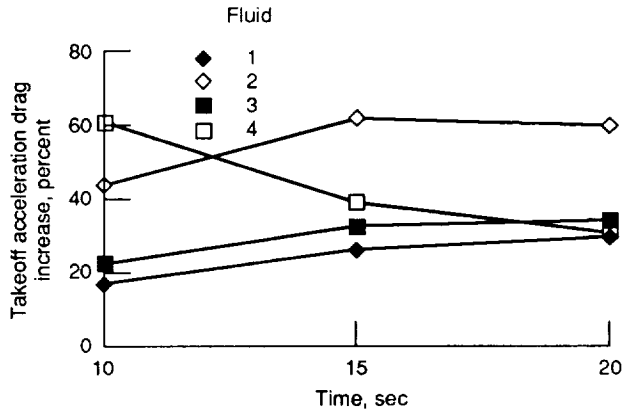

Figure 37.—Takeoff acceleration drag increase due to fluids. Two-dimensional model in flaps 5, sealed-slat configuration. Air temperature, −20 °C; $\alpha_w = 0$.

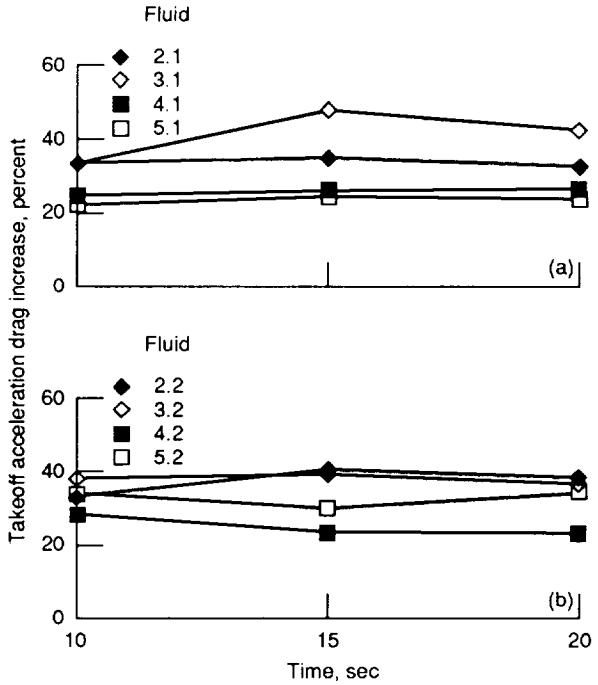

(a) Fluids 2.1 to 5.1.
(b) Fluids 2.2 to 5.2.

Figure 38.—Takeoff acceleration drag increase due to experimental fluids. Two-dimensional model in flaps 5, sealed-slat configuration. Air temperature, −20 °C; $\alpha_w = 0$.

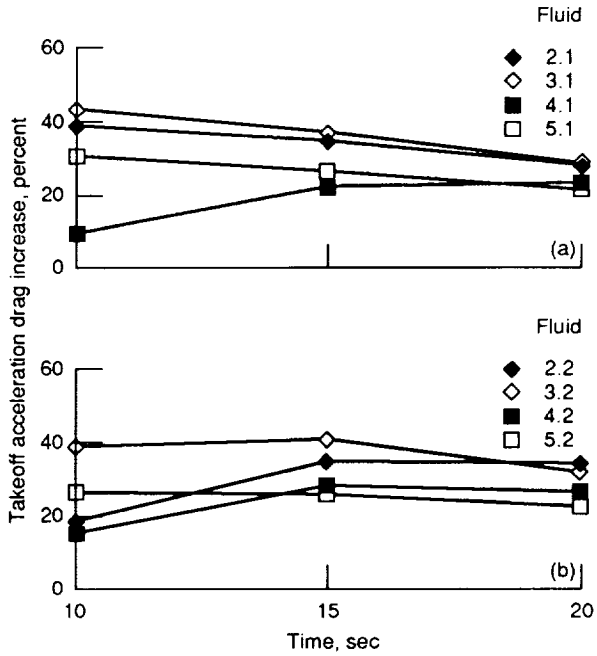

(a) Fluids 2.1 to 5.1.
(b) Fluids 2.2 to 5.2.

Figure 39.—Takeoff acceleration drag increase due to experimental fluids. Two-dimensional model in flaps 5, sealed-slat configuration. Air temperature, −10 °C; $\alpha_w = 0$.

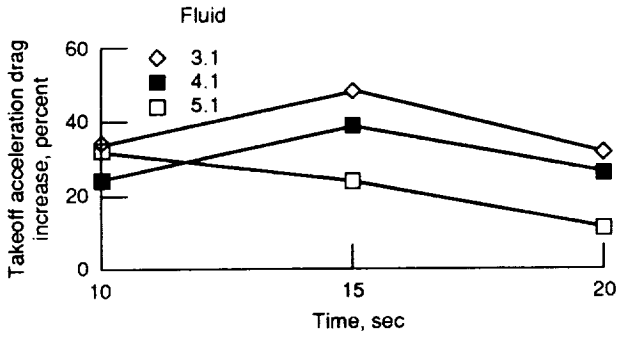

Figure 40.—Takeoff acceleration drag increase due to experimental fluids (no data for fluid 2.1). Two-dimensional model in flaps 5, sealed-slat configuration. Air temperature, –20 °C; α_w = 0; elapsed time, 15 sec.

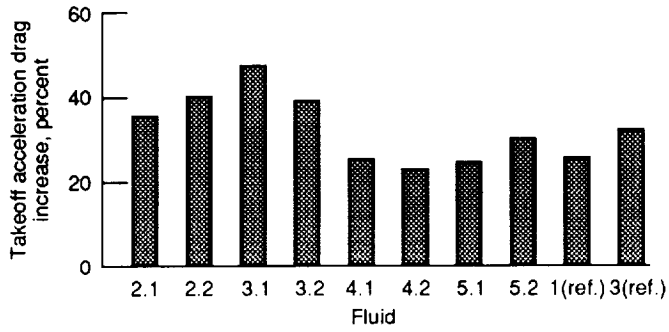

Figure 41.—Summary of takeoff acceleration drag increase due to experimental fluids. Two-dimensional model in flaps 5, sealed-slat configuration. Air temperature, –20 °C: α_w = 0; elapsed time, 15 sec.

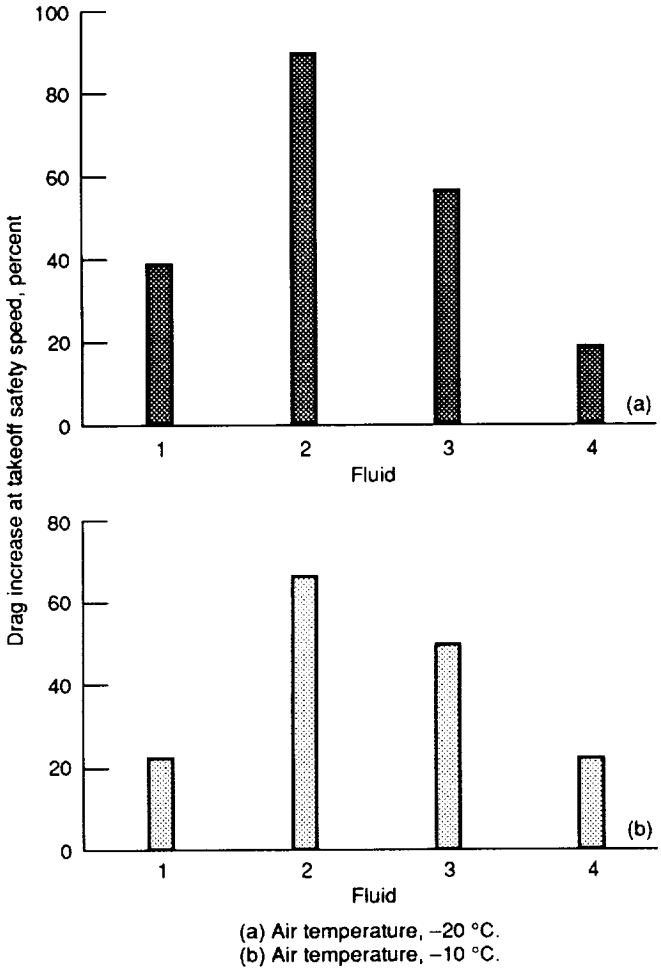

(a) Air temperature, –20 °C.
(b) Air temperature, –10 °C.

Figure 42.—Drag increase at takeoff safety speed due to fluids. Two-dimensional model in flaps 5, sealed-slat configuration. Elapsed time, 25 sec; c_1 corresponding to clean wing α_w = 6.5°, except for fluid 2 where α_w = 3.5°.

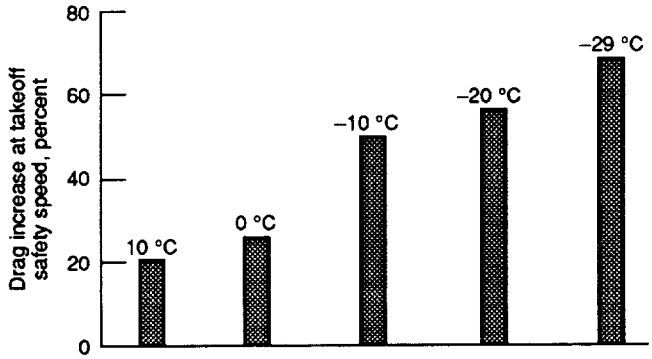

Figure 43.—Effect of temperature on drag increase due to fluid 3. Two-dimensional model in flaps 5, sealed-slat configuration. Elapsed time, 25 sec; c_l corresponding to clean wing α_w = 6.5, except for fluid 2 where α_w = 3.5°.

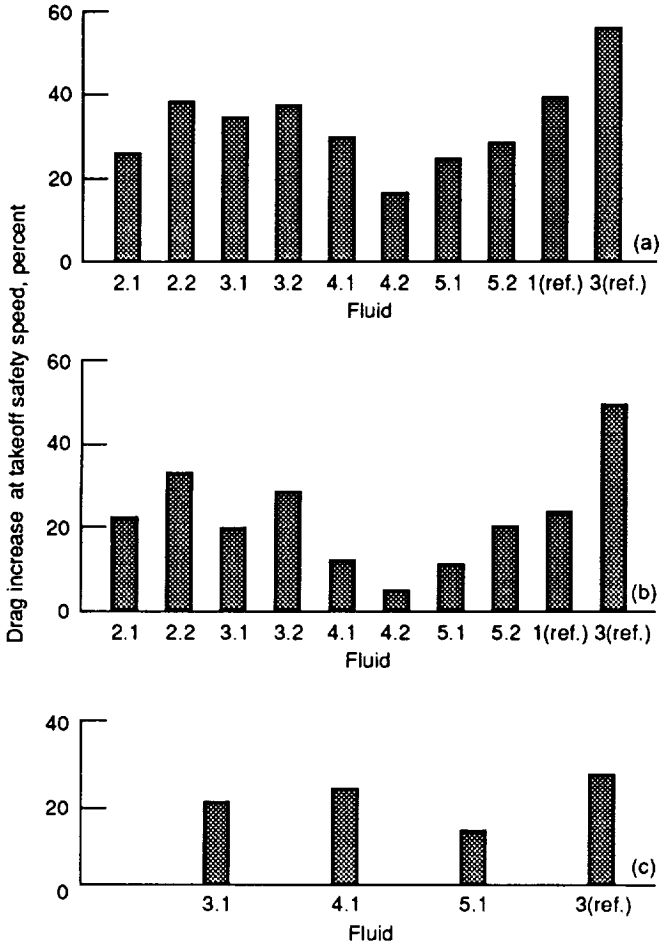

(a) Fluid temperature, –20 °C.
(b) Fluid temperature, –10 °C.
(c) Fluid temperature, 0 °C.

Figure 44.—Drag increase at takeoff safety speed due to experimental fluids. Two-dimensional model in flaps 5, sealed-slat configuration. Elapsed time, 25 sec; c_l corresponding to clean wing $\alpha_w = 6.5$ °.

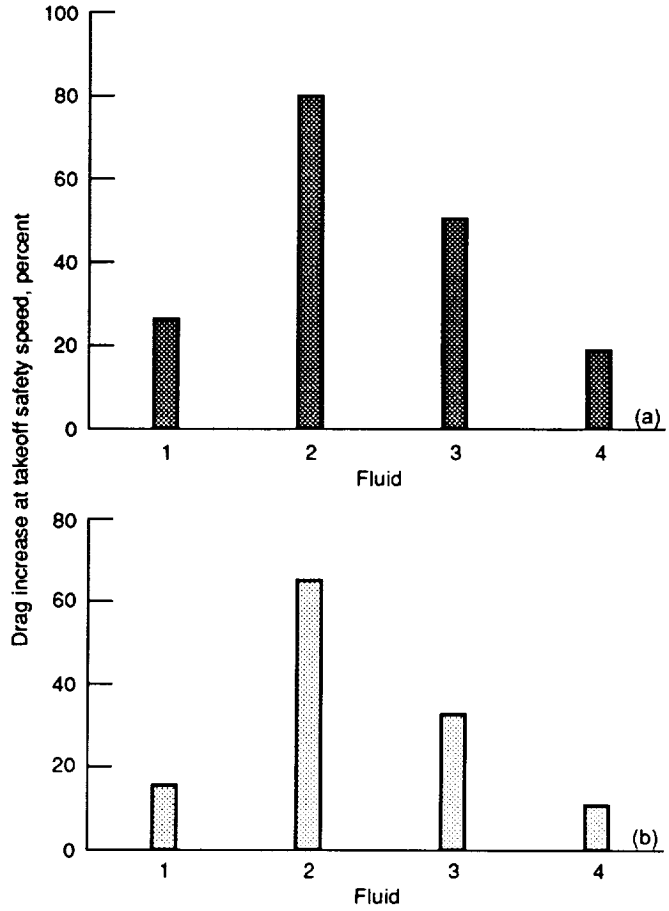

(a) Fluid temperature, –20 °C.
(b) Fluid temperature, –10 °C.

Figure 45.—Drag increase at takeoff safety speed due to experimental fluids. Two-dimensional model in flaps 15, gapped-slat configuration. Elapsed time, 25 sec; c_l corresponding to clean wing $\alpha_w = 6.5°$, except for fluid 2 where $\alpha_w = 3.5°$.

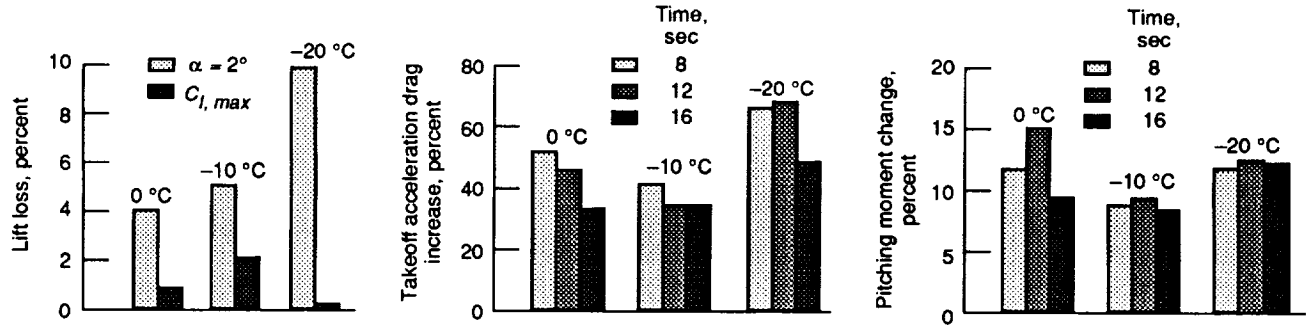

Figure 46.— Fluid aerodynamic effects without leading-edge high-lift device. Two-dimensional model in flaps 15, cruise leading-edge configuration. Fluid 3; velocity at rotation, 156 m/sec (80 keas).

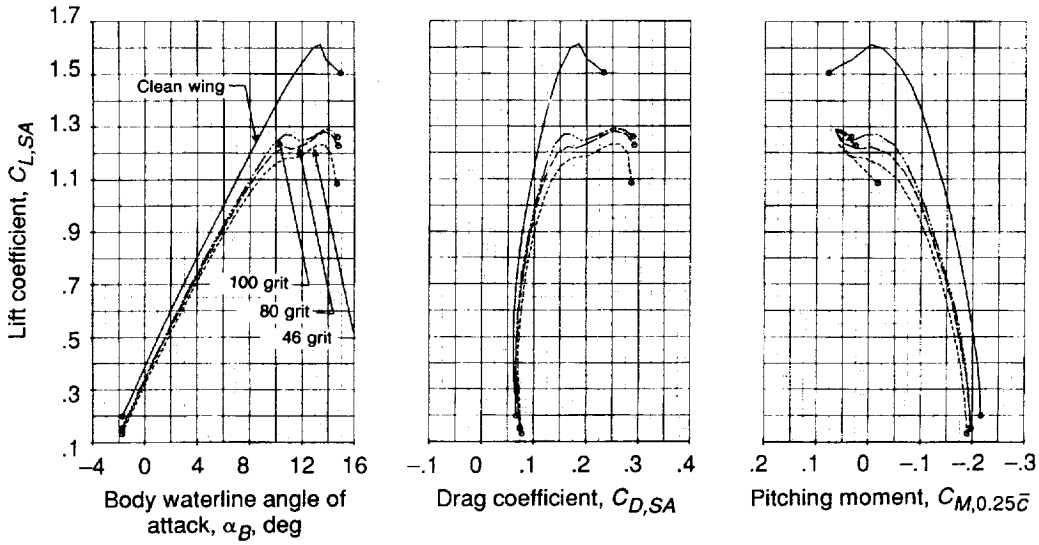

Figure 47.—Effect of simulated frost grit size on aerodynamic effects. Three-dimensional half model in flaps 5, sealed-slat configuration; ambient temperature; free air.

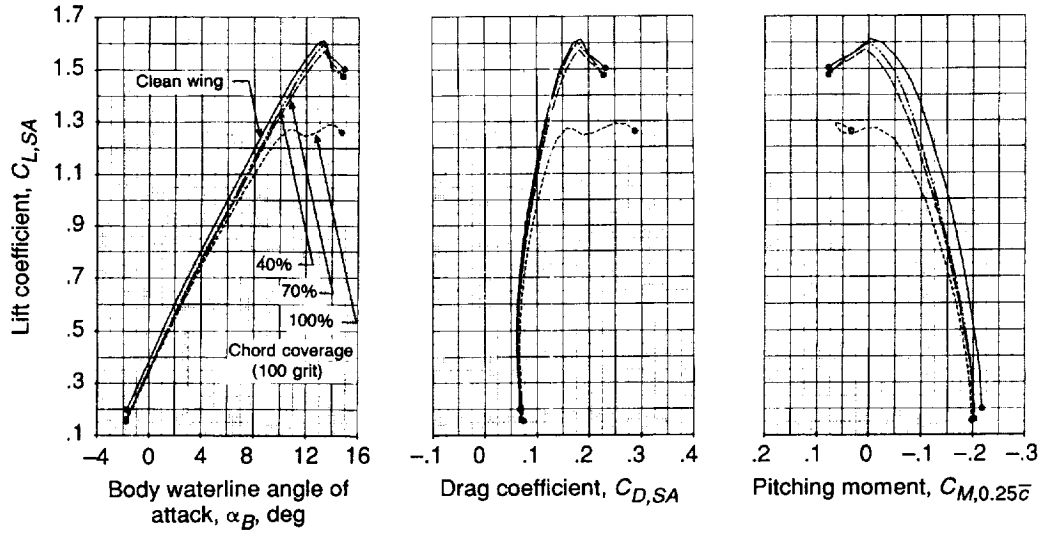

Figure 48.—Effect of simulated frost chord coverage on aerodynamic effects. Three-dimensional half model in flaps 5, sealed-slat configuration; ambient temperature; free air.

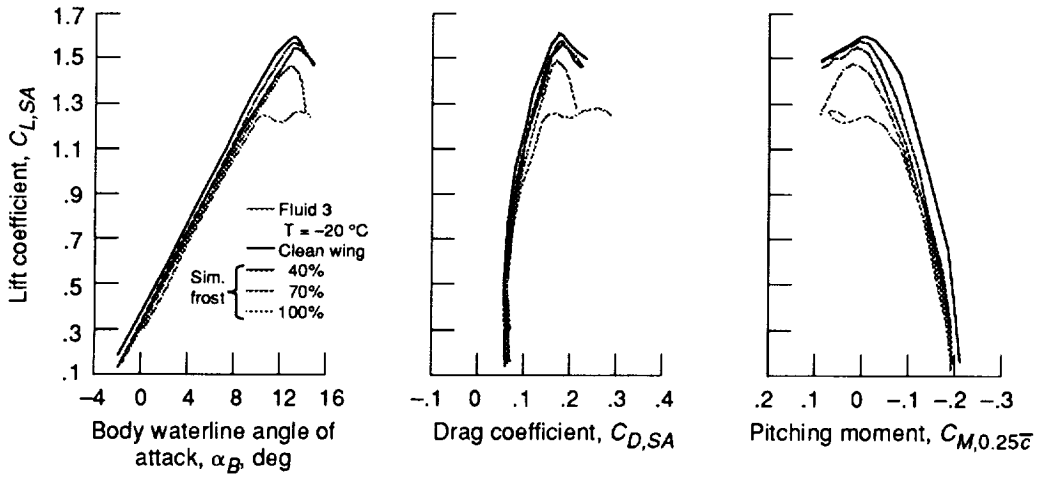

Figure 49.—Comparison of aerodynamic effects of fluid 3 and simulated frost. Three-dimensional half model in flaps 5, sealed-slat configuration; free air.

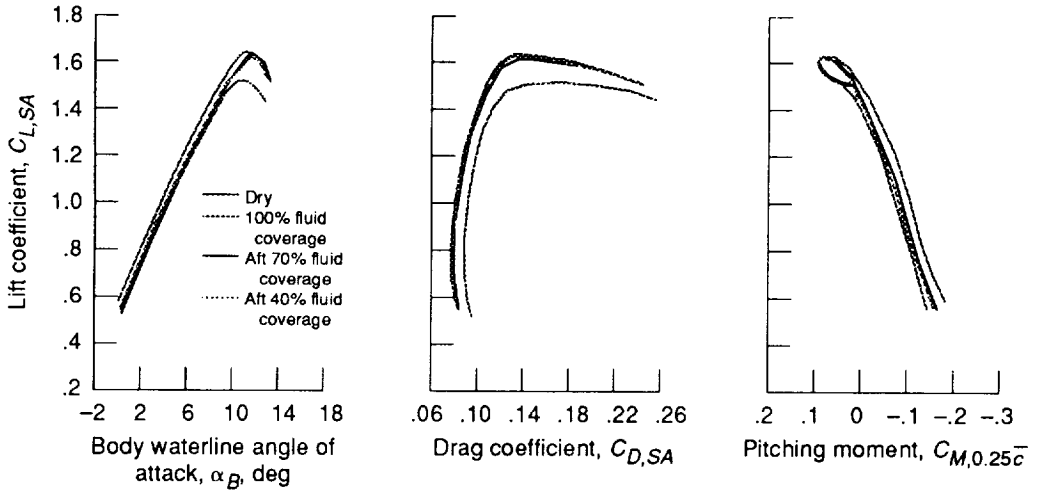

Figure 50.—Effect of chordwise coverage on fluid aerodynamic effects. Three-dimensional half model in flaps 5, sealed-slat configuration; fluid 3; air temperature, −10 °C; ground plane in.

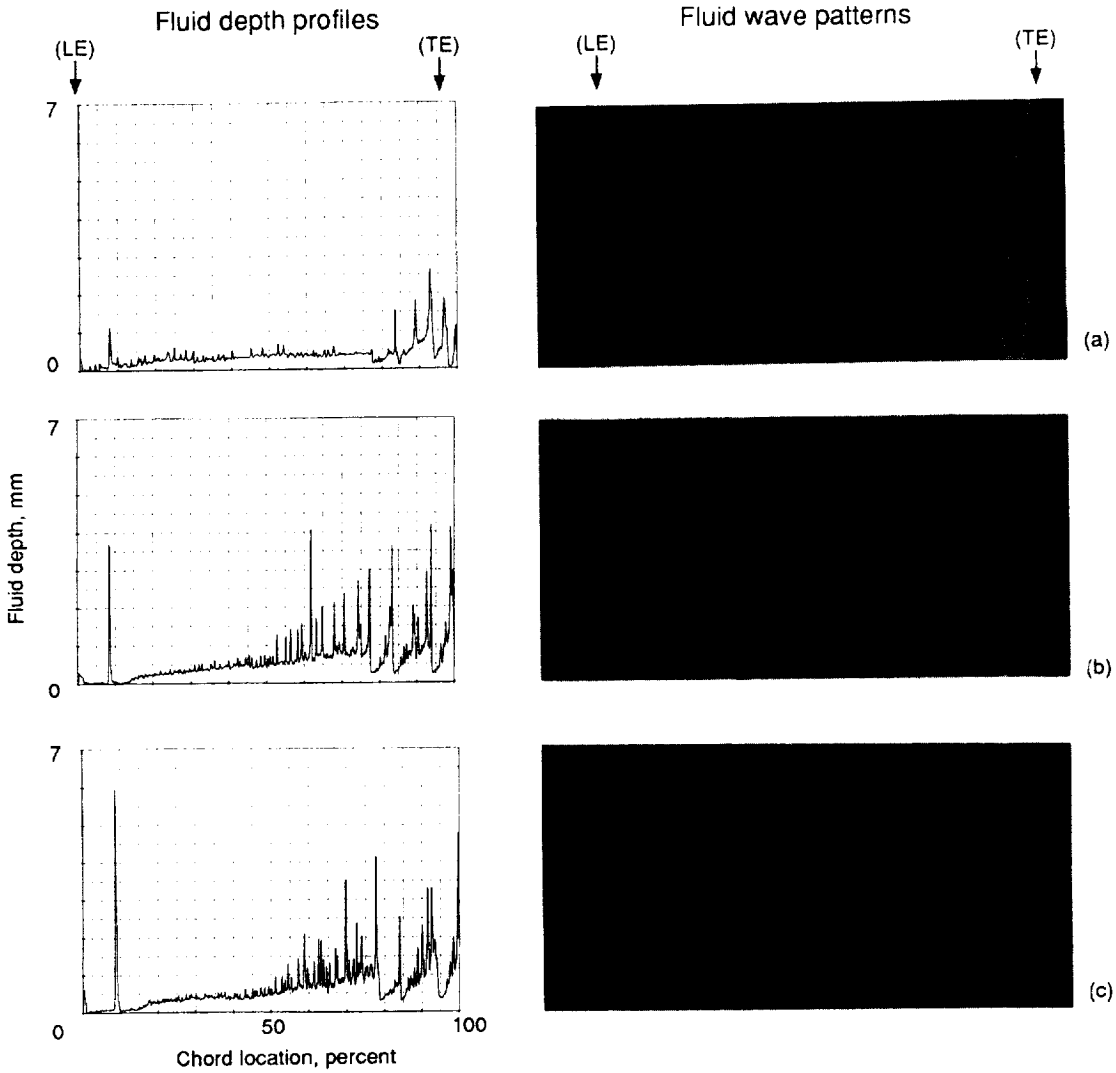

(a) Elapsed time, 10 sec; airspeed, 24.2 m/sec (47 keas); $\alpha_W = 0$.

(b) Elapsed time, 24 sec; airspeed, 61.2 m/sec (119 keas); $\alpha_W = 0.1°$.

(c) Elapsed time, 26 sec; airspeed, 66.3 m/sec (129 keas); $\alpha_W = 4.3°$.

Figure 51.—Fluid 1 depth profiles and wave patterns. Initial fluid depth 0.75 mm; air temperature, –20 °C; two-dimensional model in flaps 5 configuration; run 344.

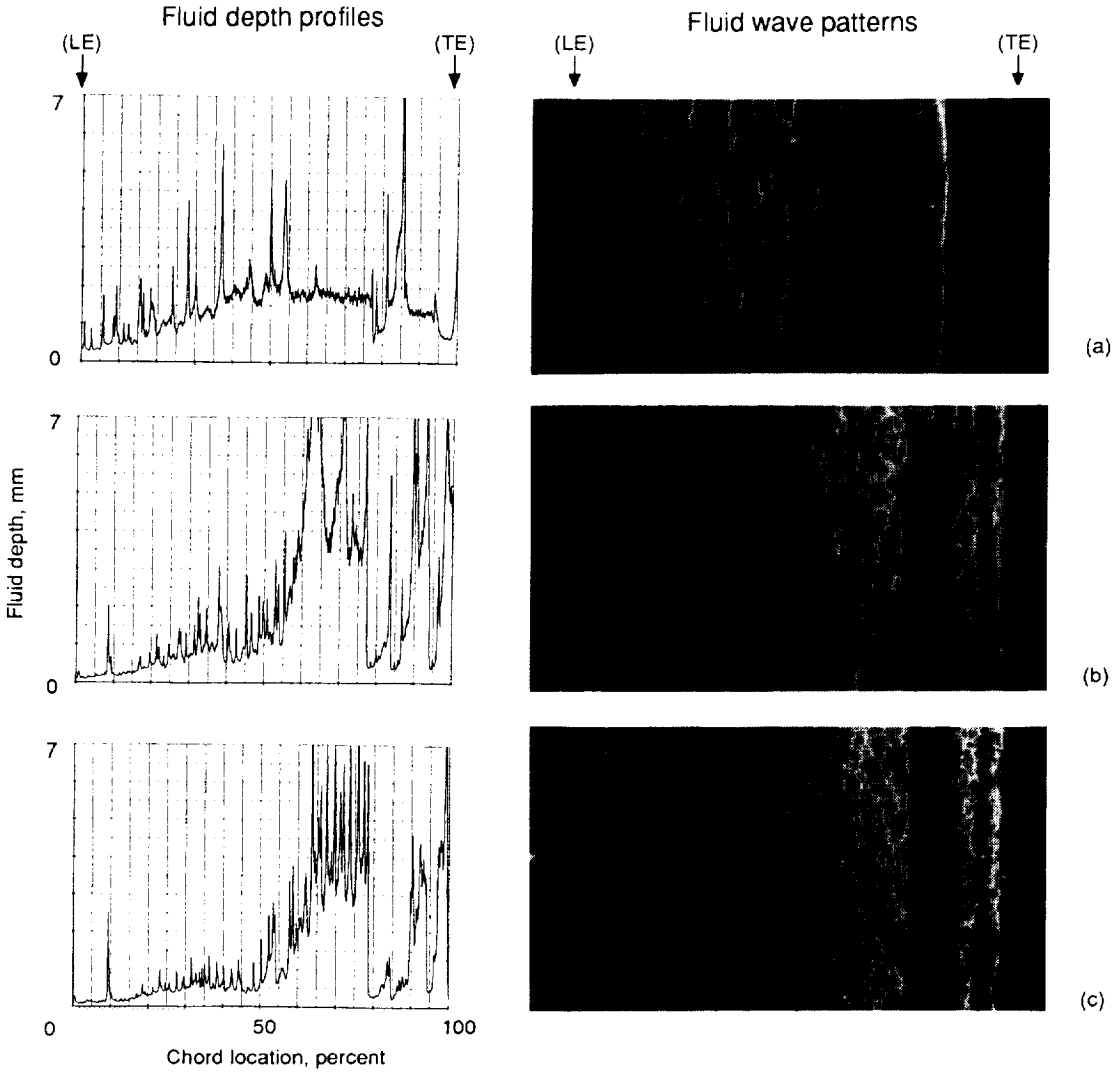

(a) Elapsed time, 10 sec; airspeed, 25.2 m/sec (49 keas); $\alpha_W = 0$.

(b) Elapsed time, 22 sec; airspeed, 57.6 m/sec (112 keas); $\alpha_W = -0.1°$.

(c) Elapsed time, 26 sec; airspeed, 67.9 m/sec (132 keas); $\alpha_W = 8.7°$.

Figure 52.—Fluid 2 depth profiles and wave patterns. Initial fluid depth 1.0 mm; air temperature, –20 °C; two-dimensional model in flaps 5 configuration; run 342.

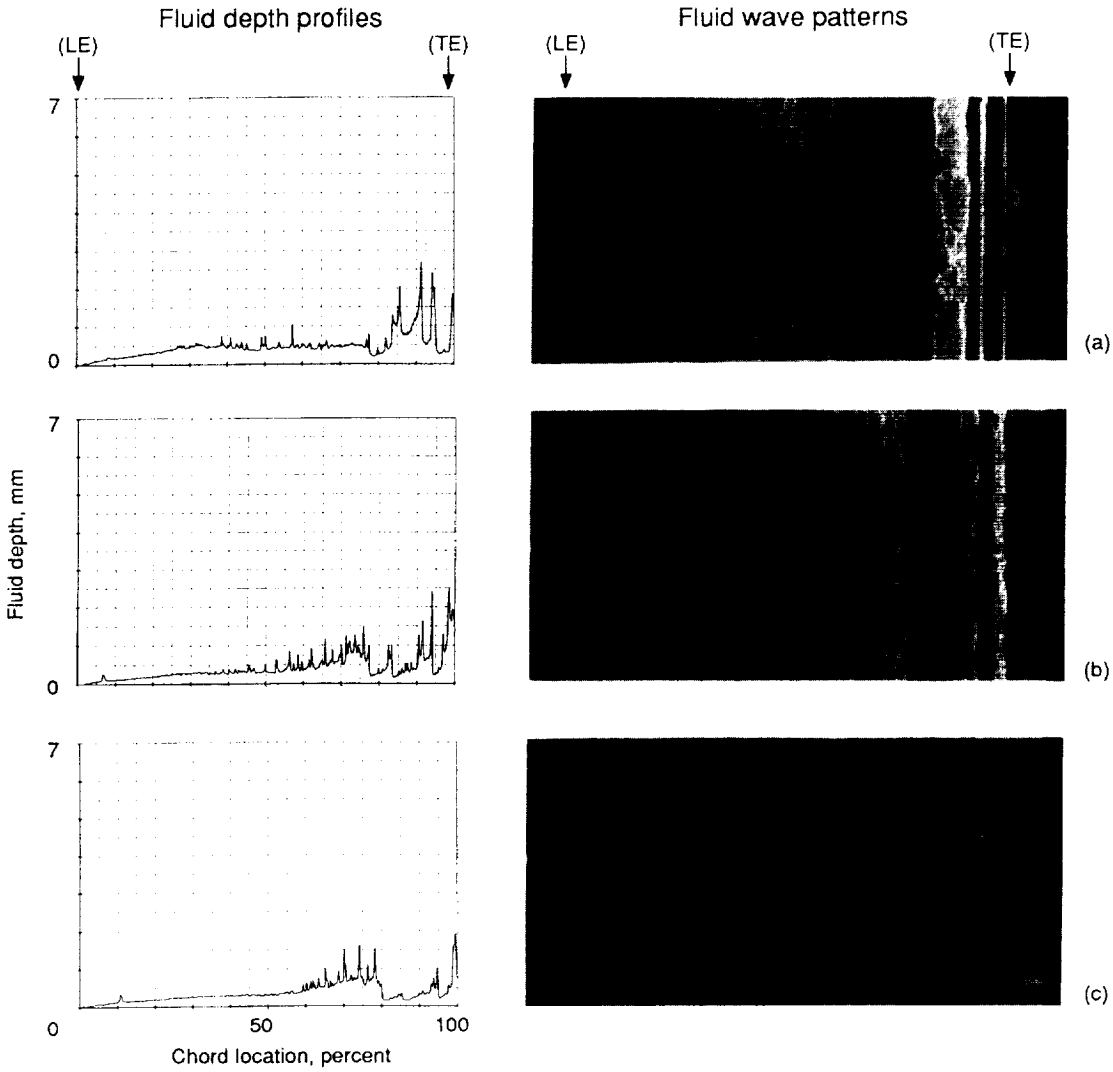

(a) Elapsed time, 10 sec; airspeed, 25.2 m/sec (49 keas); $\alpha_W = 0.1°$.

(b) Elapsed time, 22 sec; airspeed, 57.1 m/sec (111 keas); $\alpha_W = 0.1°$.

(c) Elapsed time, 26 sec; airspeed, 67.3 m/sec (131 keas); $\alpha_W = 12.1°$.

Figure 53.—Fluid 3 depth profiles and wave patterns. Initial fluid depth, 0.525 mm; air temperature, –20 °C; two-dimensional model in flaps 5 configuration; run 329.

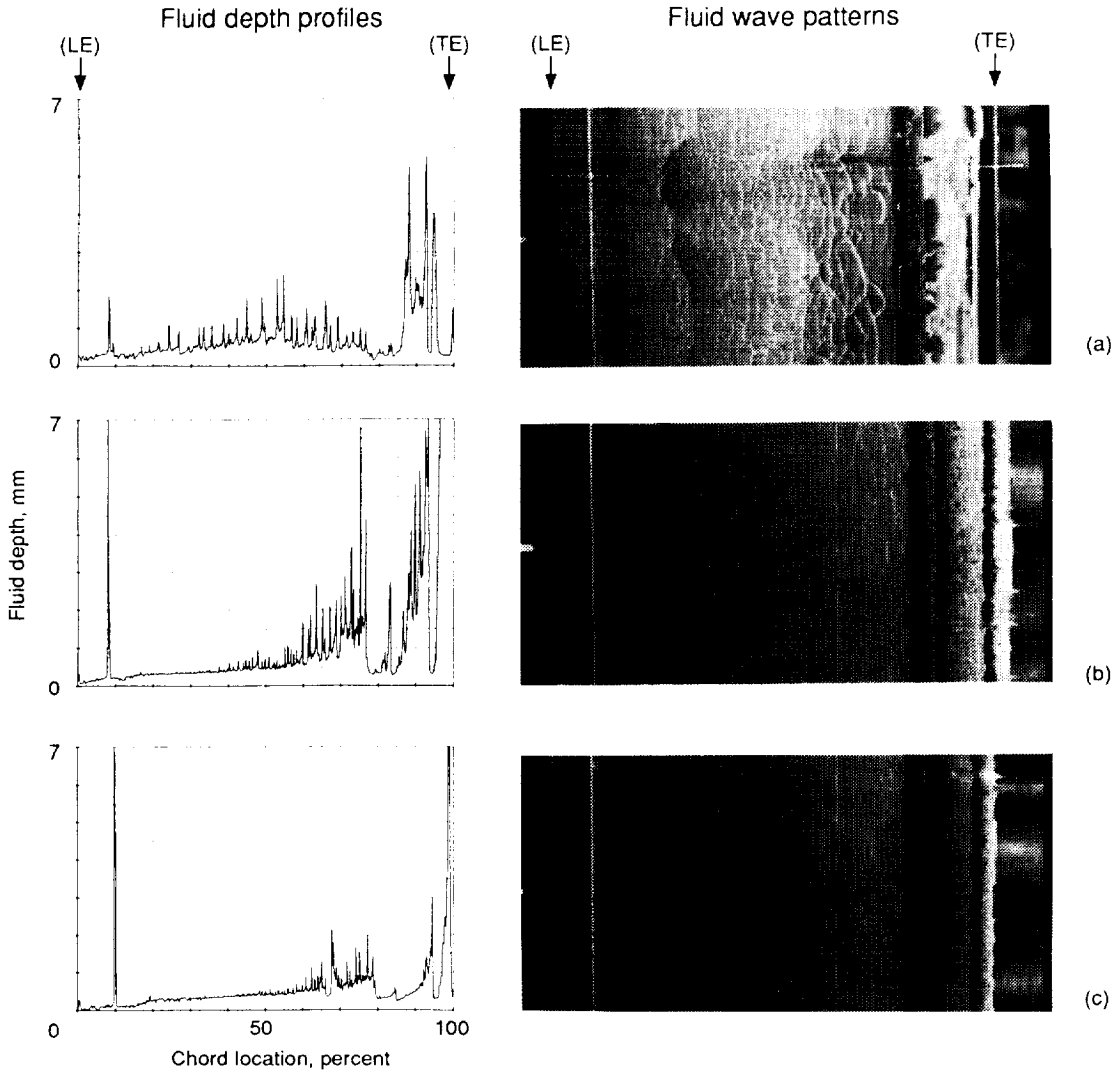

(a) Elapsed time, 10 sec; airspeed, 24.7 m/sec (48 keas); $\alpha_W = 0°$.

(b) Elapsed time, 22 sec; airspeed, 56.5 m/sec (110 keas); $\alpha_W = -0.1°$.

(c) Elapsed time, 26 sec; airspeed, 66.8 m/sec (130 keas); $\alpha_W = 8.3°$.

Figure 54.—Fluid 4 depth profiles and wave patterns. Initial fluid depth, 0.81 mm; air temperature, –20 °C; two-dimensional model in flaps 5 configuration; run 346.

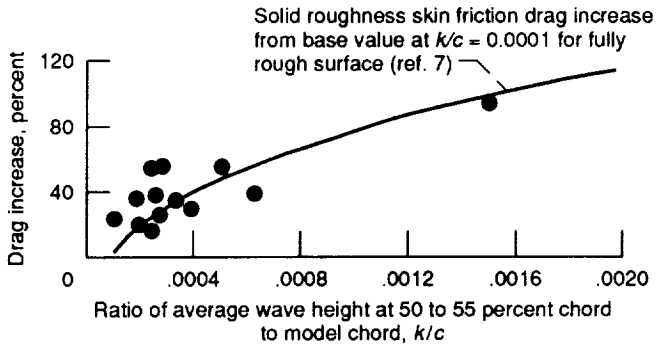

Figure 55.—Correlation between drag increase due to fluid and fluid roughness. Two-dimensional model in flaps 5, sealed-slat configuration. Air temperature, –20 °C; α_w = 8°.

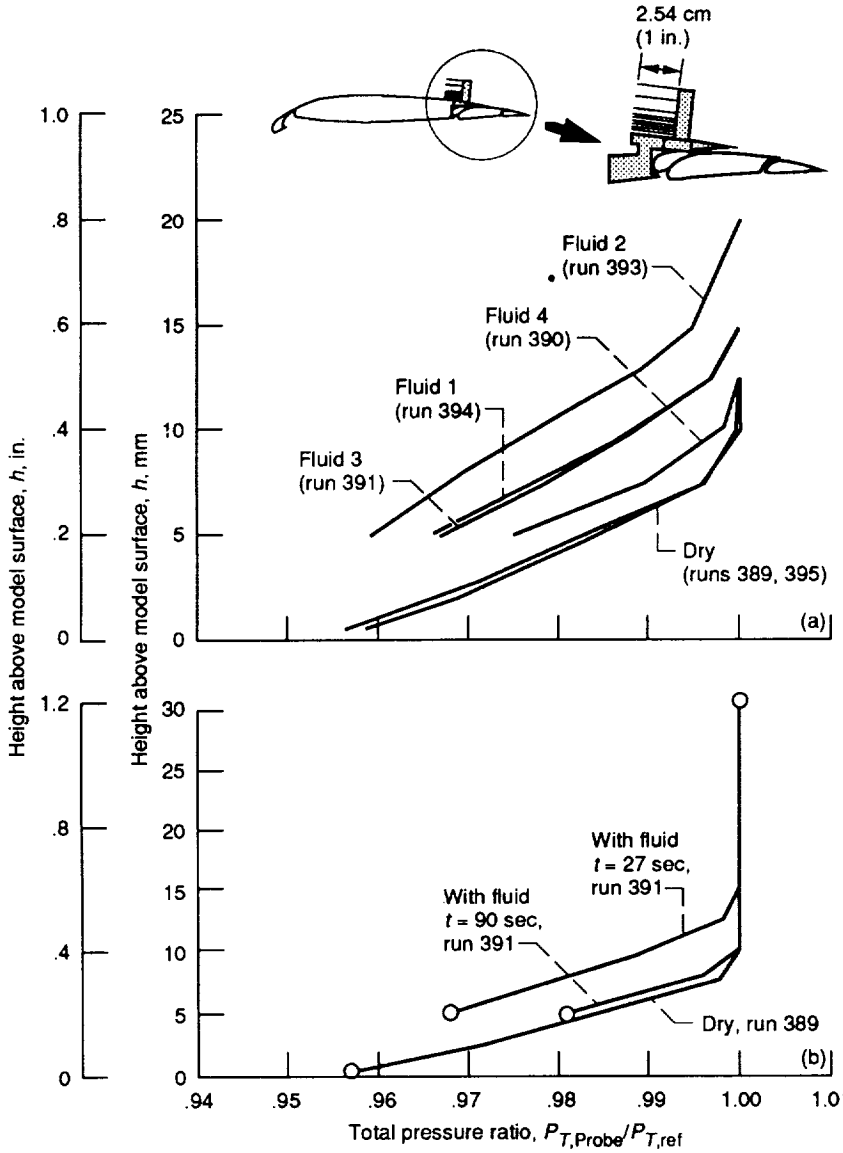

Probe	h	
	mm	in.
1	0.51	0.02
2	2.54	0.10
3	5.08	0.20
4	7.62	0.30
5	10.16	0.40
6	12.70	0.50
7	15.24	0.60
8	20.32	0.80
9	30.48	1.20
10	40.64	1.60

(a) For fluids 1 to 4; elapsed time, 27 sec.
(b) For fluid 3 at two elapsed times.

Figure 56.—Boundary layer rake data. Two-dimensional model in flaps 5, sealed-slat configuration. Air temperature, –20 °C; α_w = 8°. Span location is 38.1 cm (15 in.) from left splitter wall.

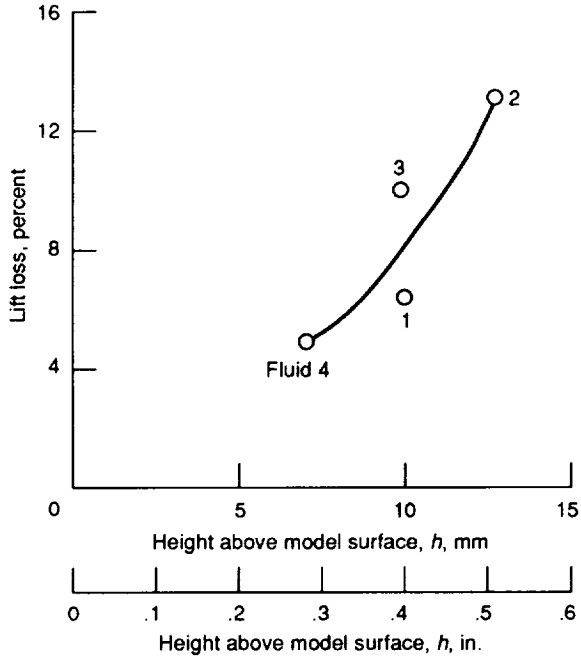

Figure 57.—Correlation of lift losses due to fluid and height at which total pressure ratio is 0.99. Two-dimensional model in flaps 5, sealed-slat configuration. Air temperature, –20 °C; elapsed time, 27 sec; $\alpha_w = 8°$.

Appendix A

Fluid Holdover Time, Rheological Properties, and Water Content

This appendix contains rheological properties and water content for all fluids tested. The rheological properties and water content were determined by Boeing Materials Technology. The fluid holdover times were determined by various sources, as noted in the section below.

Fluid Holdover Time

The fluid holdover times in freezing rain are shown in table I (p. 4). The data sources are also noted in that table. Holdover times are shown for the four basic fluids (fluids 1, 2, 3, and 4). Holdover times are also shown for the four experimental fluids that were chosen for commercial production (fluids 2.2, 3.2, 4.1, and 5.1). The AEA freezing rain endurance test (ref. 9) was used in all cases.

Fluid Rheological Properties

The fluid rheological properties were determined by Boeing Materials Technology from samples taken during the wind tunnel test. Viscosities were determined for each fluid at 20 °C, 0 °C, −10 °C, and −25 °C. A Brookfield viscometer (Model LVT DV-II), a small sample adaptor, and test spindles SCR4-18/13R (fluid 1 at all temperatures and fluid 4.2 at 0 °C) and SCR4-34/13R (all fluids except fluid 1 and fluid 4.2 at 0 °C) were used to determine the fluid viscosities. Temperature control was maintained using Brookfield EX-200 and Neslab coolers. Data were recorded using the Brookfield DV Gather software program.

Tables IV to XV contain the rheological data for all of the fluids. Some of these data at −10 °C are shown in the plots of viscosity versus shear stress of figure 58. The four basic fluids (fluids 1, 2, 3, and 4) are shown in figure 58(a). The eight experimental fluids are shown in figures 58(b) and (c).

Fluid Water Content

The water contents of all 12 fluids tested are shown in table XVI. These results were determined by Boeing Materials Technology from samples taken during the wind tunnel test.

TABLE IV.—FLUID 1 RHEOLOGICAL PROPERTIES

Item	Velocity at rotation, rpm	Torque, percent	Viscosity, cP	Shear stress, dyne/cm^2	Shear rate, sec^{-1}
Temperature, −25 °C					
01	0.3	7.1	711	2.81	0.3
02	.6	14.8	741	5.86	.7
03	1.5	37.5	748	14.80	1.9
04	3.0	74.9	752	29.70	3.9
05	1.5	38.4	768	15.20	1.9
06	.6	15.8	792	6.26	.7
07	.3	8.2	818	3.23	.3
Temperature, −10 °C					
01	0.3	1.4	140	0.55	0.3
02	.6	3.3	166	1.31	.7
03	1.5	9.4	189	3.72	1.9
04	3.0	19.4	194	7.68	3.9
05	6.0	39.1	195	15.40	7.8
06	12.0	79.1	197	31.30	15.8
07	6.0	40.3	202	16.00	7.9
08	3.0	20.2	202	7.99	3.9
09	1.5	10.4	209	4.12	1.9
10	.6	4.5	225	1.78	.7
11	.3	2.0	200	.79	.3
Temperature, 0 °C					
01	0.3	0.6	60.1	0.23	0.3
02	.6	1.6	80.2	.63	.7
03	1.5	5.0	100.0	1.98	1.9
04	3.0	9.6	96.2	3.80	3.9
05	6.0	18.8	94.2	7.44	7.8
06	12.0	37.8	94.4	14.90	15.7
07	30.0	95.1	95.2	37.60	39.4
08	12.0	38.1	95.2	15.10	15.8
09	6.0	19.5	97.7	7.72	7.9
10	3.0	9.4	94.2	3.72	3.9
11	1.5	5.4	108.0	2.14	1.9
12	.6	1.5	75.2	.59	.7
13	.3	.9	90.2	.35	.3
Temperature, 20 °C					
01	0.3	0.2	20.0	0.07	0.3
02	.6	.8	40.1	.31	.7
03	1.5	1.8	36.1	.71	1.9
04	3.0	3.4	34.1	1.35	3.9
05	6.0	6.1	30.6	2.42	7.9
06	12.0	11.7	29.2	4.62	15.8
07	30.0	28.7	28.7	11.30	39.3
08	60.0	57.2	28.6	22.60	79.0
09	30.0	28.8	28.9	11.30	39.4
10	12.0	11.8	29.6	4.67	15.7
11	6.0	6.2	31.1	2.46	7.9
12	3.0	3.4	34.1	1.35	3.9
13	1.5	1.8	36.1	.71	1.9
14	.6	.7	35.1	.27	.7
15	.3	.4	40.1	.15	.3

TABLE V.—FLUID 2 RHEOLOGICAL PROPERTIES

Item	Velocity at rotation, rpm	Torque, percent	Viscosity, cP	Shear stress, dyne/cm^2	Shear rate, sec^{-1}
Temperature, −25 °C					
01	0.6	39.1	39 100	65.5	0.1
02	1.5	60.7	24 400	102.0	.4
03	3.0	86.4	17 400	145.0	.8
04	3.0	86.7	17 400	146.0	.8
05	1.5	60.9	24 400	102.0	.4
06	.6	39.8	39 900	66.9	.1
Temperature, −10 °C					
01	0.6	21.4	21 400	35.8	0.1
02	1.5	31.6	12 600	52.9	.4
03	3.0	43.8	8 750	73.4	.8
04	6.0	61.6	6 160	103.0	1.6
05	12.0	88.4	4 430	148.0	3.3
06	6.0	62.3	6 250	105.0	1.6
07	3.0	44.5	8 920	74.8	.8
08	1.5	32.4	13 000	54.3	.4
09	.6	22.2	22 200	37.2	.1
Temperature, 0 °C					
01	0.6	15.3	15 300	25.7	0.1
02	1.5	22.2	8 880	37.2	.4
03	3.0	30.5	6 110	51.2	.8
04	6.0	42.4	4 240	71.1	1.6
05	12.0	60.1	3 020	101.0	3.3
06	30.0	98.1	1 970	165.0	8.3
07	12.0	60.4	3 040	102.0	3.3
08	6.0	42.7	4 280	71.7	1.6
09	3.0	30.7	6 180	51.8	.8
10	1.5	22.8	9 150	38.4	.4
11	.6	15.6	15 600	26.2	.1
Temperature, 20 °C					
01	0.6	7.4	7 410	12.4	0.1
02	1.5	10.1	4 040	16.9	.4
03	3.0	13.9	2 790	23.4	.8
04	6.0	19.4	1 940	32.5	1.6
05	12.0	27.3	1 370	45.9	3.3
06	30.0	44.3	885	74.2	8.3
07	60.0	65.3	655	110.0	16.7
08	30.0	44.5	892	74.8	8.3
09	12.0	27.5	1 380	46.2	3.3
10	6.0	19.5	1 950	32.8	1.6
11	3.0	14.0	2 810	23.5	.8
12	1.5	10.4	4 170	17.5	.4
13	.6	7.1	7 100	11.9	.1

TABLE VI.—FLUID 3 RHEOLOGICAL PROPERTIES

Item	Velocity at rotation, rpm	Torque, percent	Viscosity, cP	Shear stress, dyne/cm^2	Shear rate, sec^{-1}
Temperature, −25 °C					
01	0.3	1.1	2 200	1.85	0
02	.6	2.2	2 200	3.70	.1
03	1.5	4.7	1 890	7.90	.4
04	3.0	8.3	1 660	13.90	.8
05	6.0	14.3	1 430	24.00	1.6
06	12.0	25.0	1 250	42.00	3.3
07	30.0	51.5	1 030	86.50	8.3
08	60.0	89.1	892	150.00	16.8
09	30.0	51.8	1 040	87.10	8.3
10	12.0	25.4	1 280	42.80	3.3
11	6.0	14.8	1 480	24.80	1.6
12	3.0	8.4	1 690	14.10	.8
13	1.5	4.8	1 920	8.06	.4
14	.6	2.2	2 200	3.70	.1
15	.3	1.2	2 400	2.02	0
Temperature, −10 °C					
01	0.3	1.2	2 400	2.02	0
02	.6	2.1	2 100	3.53	.1
03	1.5	4.2	1 690	7.06	.4
04	3.0	6.8	1 360	11.40	.8
05	6.0	11.1	1 110	18.60	1.6
06	12.0	18.3	918	30.80	3.3
07	30.0	35.3	708	59.40	8.3
08	60.0	58.2	585	98.00	16.7
09	30.0	35.6	715	59.90	8.3
10	12.0	18.6	927	31.10	3.3
11	6.0	11.5	1 150	19.30	1.6
12	3.0	7.0	1 400	11.80	.8
13	1.5	4.4	1 770	7.39	.4
14	.6	2.3	2 300	3.86	.1
15	.3	1.6	3 190	2.68	0
Temperature, 0 °C					
01	0.3	2.2	4 410	3.70	0
02	.6	3.3	3 310	5.54	.1
03	1.5	5.6	2 240	9.38	.4
04	3.0	8.6	1 720	14.40	.8
05	6.0	12.9	1 290	21.70	1.6
06	12.0	19.9	994	33.30	3.3
07	30.0	35.7	715	59.90	8.3
08	60.0	56.3	563	94.40	16.7
09	30.0	35.8	718	60.20	8.3
10	12.0	20.0	1 000	33.60	3.3
11	6.0	13.0	1 300	21.80	1.6
12	3.0	8.5	1 700	14.30	.8
13	1.5	5.9	2 370	9.91	.4
14	.6	3.5	3 510	5.88	.1
15	.3	2.2	4 410	3.70	0
Temperature, 20 °C					
01	0.3	2.0	4 010	3.36	0
02	.6	2.9	2 910	4.87	.1
03	1.5	4.5	1 800	7.56	.4
04	3.0	6.5	1 300	10.90	.8
05	6.0	9.4	942	15.80	1.6
06	12.0	14.0	701	23.50	3.3
07	30.0	23.9	478	40.00	8.3
08	60.0	36.3	362	60.80	16.7
09	30.0	24.0	481	40.30	8.3
10	12.0	14.1	705	23.70	3.3
11	6.0	9.6	960	16.10	1.6
12	3.0	6.5	1 300	10.90	.8
13	1.5	4.7	1 890	7.90	.4
14	.6	2.9	2 910	4.87	.1
15	.3	2.2	4 410	3.70	0

TABLE VII.—FLUID 4 RHEOLOGICAL PROPERTIES

Item	Velocity at rotation, rpm	Torque, percent	Viscosity, cP	Shear stress, dyne/cm^2	Shear rate, sec^{-1}
Temperature, −25 °C					
01	0.6	6.4	6 410	10.7	0.1
02	1.5	8.0	3 210	13.4	.4
03	3.0	11.0	2 200	18.5	.8
04	6.0	15.1	1 510	25.3	1.6
05	12.0	20.4	1 030	34.4	3.3
06	30.0	32.3	648	54.3	8.3
07	60.0	47.5	476	79.8	16.7
08	30.0	32.0	641	53.8	8.3
09	12.0	20.2	1 010	33.9	3.3
10	6.0	14.9	1 490	25.0	1.6
11	3.0	10.7	2 140	18.0	.8
12	1.5	8.5	3 410	14.3	.4
13	.6	5.0	5 010	8.4	.1
Temperature, −10 °C					
01	0.6	4.6	4 590	7.70	0.1
02	1.5	6.0	2 400	10.10	.4
03	3.0	7.9	1 580	13.30	.8
04	6.0	10.2	1 020	17.10	1.6
05	12.0	13.6	680	22.80	3.3
06	30.0	20.5	411	34.40	8.3
07	60.0	28.8	287	48.20	16.7
08	30.0	20.2	404	33.90	8.3
09	12.0	13.3	665	22.30	3.3
10	6.0	9.8	982	16.50	1.6
11	3.0	7.4	1 480	12.40	.8
12	1.5	5.4	2 170	9.07	.4
13	.6	3.5	3 510	5.88	.1
Temperature, 0 °C					
01	0.6	3.0	3 010	5.04	0.1
02	1.5	4.4	1 770	7.39	.4
03	3.0	5.9	1 180	9.91	.8
04	6.0	8.2	822	13.80	1.6
05	12.0	10.8	539	18.10	3.3
06	30.0	16.2	326	27.30	8.3
07	60.0	22.4	224	37.50	16.7
08	30.0	16.0	319	26.80	8.4
09	12.0	10.5	526	17.60	3.3
10	6.0	7.8	782	13.10	1.6
11	3.0	5.6	1 120	9.38	.8
12	1.5	4.0	1 600	6.72	.4
13	.6	2.5	2 500	4.20	.1
Temperature, 20 °C					
01	0.6	1.2	1 200	2.02	0.1
02	1.5	2.1	842	3.53	.4
03	3.0	3.1	621	5.21	.8
04	6.0	4.6	459	7.70	1.6
05	12.0	6.7	336	11.30	3.3
06	30.0	10.5	210	17.60	8.3
07	60.0	14.6	146	24.50	16.7
08	30.0	10.4	209	17.50	8.3
09	12.0	6.8	341	11.40	3.3
10	6.0	4.7	471	7.90	1.6
11	3.0	3.2	641	5.38	0.8
12	1.5	2.1	842	3.53	.4
13	.6	1.3	1 300	2.18	.1

TABLE VIII.—FLUID 2.1 RHEOLOGICAL PROPERTIES

Item	Velocity at rotation, rpm	Torque, percent	Viscosity, cP	Shear stress, dyne/cm^2	Shear rate, sec^{-1}
Temperature, -25 °C					
01	0.6	1.8	1 800	3.02	0.1
02	1.5	4.6	1 840	7.70	.4
03	3.0	7.4	1 480	12.40	.8
04	6.0	12.9	1 290	21.70	1.6
05	12.0	23.2	1 170	39.20	3.3
06	30.0	49.1	982	82.30	8.3
07	60.0	85.7	858	144.00	16.7
08	30.0	49.3	985	82.60	8.3
09	12.0	23.2	1 170	39.20	3.3
10	6.0	12.6	1 260	21.10	1.6
11	3.0	7.4	1 480	12.40	.8
12	1.5	4.0	1 600	6.72	.4
13	.6	2.2	2 200	3.70	.1
Temperature, -10 °C					
01	0.6	3.2	3 210	5.38	0.1
02	1.5	5.9	2 370	9.91	.4
03	3.0	9.8	1 970	16.50	.8
04	6.0	15.8	1 580	26.50	1.6
05	12.0	25.9	1 300	43.70	3.3
06	30.0	49.3	985	82.60	8.3
07	60.0	80.9	810	136.00	16.7
08	30.0	51.4	1 030	86.20	8.3
09	12.0	27.8	1 390	46.80	3.3
10	6.0	17.2	1 720	28.80	1.6
11	3.0	10.5	2 100	17.60	.8
12	1.5	6.6	2 640	11.10	.4
13	.6	3.5	3 510	5.88	.1
Temperature, 0 °C					
01	0.6	2.4	2 200	4.03	0.1
02	1.5	4.7	1 890	7.90	.4
03	3.0	7.5	1 500	12.60	.8
04	6.0	12.1	1 210	20.30	1.6
05	12.0	20.8	1 040	35.00	3.3
06	30.0	36.4	728	61.00	8.3
07	60.0	57.9	581	97.40	16.7
08	30.0	36.5	731	61.30	8.3
09	12.0	19.7	985	33.00	3.3
10	6.0	12.2	1 220	20.50	1.6
11	3.0	7.6	1 520	12.70	.8
12	1.5	4.9	1 970	8.23	.4
13	.6	2.7	2 700	4.54	.1
Temperature, 20 °C					
01	0.6	0.9	902	1.51	0.1
02	1.5	1.8	721	3.02	.4
03	3.0	2.9	581	4.87	.8
04	6.0	4.8	481	8.06	1.6
05	12.0	7.9	396	13.30	3.3
06	30.0	15.2	304	25.50	8.3
07	60.0	24.8	249	41.70	16.7
08	30.0	15.2	304	25.50	8.3
09	12.0	7.9	396	13.30	3.3
10	6.0	4.8	481	8.06	1.6
11	3.0	2.9	581	4.87	.8
12	1.5	1.8	721	3.02	.4
13	.6	.9	902	1.51	.1

TABLE IX.—FLUID 2.2 RHEOLOGICAL PROPERTIES

Item	Velocity at rotation, rpm	Torque, percent	Viscosity, cP	Shear stress, dyne/cm^2	Shear rate, sec^{-1}
Temperature, -25 °C					
01	0.6	2.3	2 300	3.86	0.1
02	3.0	8.0	1 600	13.40	.8
03	6.0	13.9	1 390	23.40	1.6
04	12.0	24.9	1 240	41.70	3.3
05	30.0	52.3	1 050	87.90	8.3
06	60.0	91.6	917	154.00	16.7
07	30.0	52.5	1 050	88.20	8.4
08	12.0	24.8	1 240	41.70	3.3
09	6.0	13.8	1 380	23.20	1.6
10	3.0	8.0	1 600	13.40	.8
11	1.5	4.4	1 770	7.39	.4
12	.6	1.6	1 600	2.68	.1
Temperature, -10 °C					
01	0.6	6.8	6 810	11.4	0.1
02	1.5	11.8	4 730	19.8	.4
03	3.0	18.1	3 640	30.5	.8
04	6.0	28.0	2 810	47.0	1.6
05	12.0	43.8	2 190	73.4	3.3
06	30.0	81.0	1 620	136.0	8.3
07	12.0	47.3	2 370	79.5	3.3
08	6.0	30.7	3 090	51.8	1.6
09	3.0	19.8	3 970	33.3	.8
10	1.5	13.0	5 210	21.8	.4
11	.6	7.2	7 210	12.1	.1
Temperature, 0 °C					
01	0.6	6.0	6 010	10.1	0.1
02	1.5	10.2	4 090	17.1	.4
03	3.0	15.4	3 090	25.9	.8
04	6.0	23.5	2 350	39.5	1.6
05	12.0	36.1	1 800	60.5	3.3
06	30.0	63.2	1 270	106.0	8.3
07	60.0	98.0	982	165.0	16.8
08	30.0	64.7	1 300	109.0	8.3
09	12.0	37.2	1 850	62.4	3.3
10	6.0	24.4	2 440	40.9	1.6
11	3.0	15.9	3 190	26.8	.8
12	1.5	10.7	4 290	18.0	.4
13	.6	7.3	7 310	12.3	.1
Temperature, 20 °C					
01	0.6	2.7	2 700	4.54	0.1
02	1.5	4.7	1 890	7.90	.4
03	3.0	7.1	1 420	11.90	.8
04	6.0	10.7	1 070	18.00	1.6
05	12.0	16.6	830	27.80	3.3
06	30.0	29.4	588	49.30	8.3
07	60.0	45.3	454	76.20	16.7
08	30.0	29.4	588	49.30	8.3
09	12.0	16.6	830	27.80	3.3
10	6.0	10.8	1 080	18.10	1.6
11	3.0	7.1	1 420	11.90	.8
12	1.5	4.8	1 920	8.06	.4
13	.6	2.9	2 910	4.87	.1

TABLE X.—FLUID 3.1 RHEOLOGICAL PROPERTIES

Item	Velocity at rotation, rpm	Torque, percent	Viscosity, cP	Shear stress, dyne/cm^2	Shear rate, sec^{-1}
Temperature, −25 °C					
01	0.3	1.1	2 200	1.85	0
02	.6	2.0	2 000	3.36	.1
03	1.5	4.4	1 770	7.39	.4
04	3.0	7.5	1 500	12.60	.8
05	6.0	12.9	1 290	21.70	1.6
06	12.0	22.4	1 120	37.50	3.3
07	30.0	46.2	925	77.60	8.3
08	60.0	80.0	802	134.00	16.7
09	30.0	46.2	925	77.60	8.3
10	12.0	22.5	1 130	37.80	3.3
11	6.0	13.1	1 310	22.00	1.6
12	3.0	7.5	1 500	12.60	.8
13	1.5	4.4	1 770	7.39	.4
14	.6	2.0	2 000	3.36	.1
15	.3	1.3	2 610	2.18	0
Temperature, −10 °C					
01	0.3	2.4	4 810	4.03	0
02	.6	3.4	3 410	5.71	.1
03	1.5	6.1	2 440	10.20	.4
04	3.0	9.6	1 920	16.10	.8
05	6.0	14.9	1 490	25.00	1.6
06	12.0	23.5	1 180	39.50	3.3
07	30.0	43.5	868	72.80	8.3
08	60.0	70.1	703	118.00	16.7
09	30.0	43.7	875	73.40	8.3
10	12.0	23.7	1 190	39.80	3.3
11	6.0	15.2	1 520	25.50	1.6
12	3.0	9.7	1 940	16.30	.8
13	1.5	6.3	2 520	10.60	.4
14	.6	3.4	3 410	5.71	.1
15	.3	2.3	4 610	3.86	0
Temperature, 0 °C					
01	0.3	3.4	6 810	5.71	0
02	.6	4.8	4 810	8.06	.1
03	1.5	7.8	3 120	13.1	.4
04	3.0	11.3	2 250	19.0	.8
05	6.0	16.6	1 660	27.8	1.6
06	12.0	24.8	1 240	41.7	3.3
07	30.0	43.1	865	72.5	8.3
08	60.0	66.2	663	111.0	16.7
09	30.0	43.1	865	72.5	8.3
10	12.0	25.0	1 250	42.0	3.3
11	6.0	16.7	1 670	28.0	1.6
12	3.0	11.3	2 250	19.0	.8
13	1.5	7.9	3 170	13.3	.4
14	.6	5.2	5 210	8.74	.1
15	.3	3.6	7 210	6.05	0
Temperature, 20 °C					
01	0.3	2.7	5 410	4.54	0
02	.6	3.7	3 710	6.22	.1
03	1.5	5.8	2 320	9.74	.4
04	3.0	8.0	1 600	13.40	.8
05	6.0	11.4	1 140	19.20	1.6
06	12.0	16.5	830	27.80	3.3
07	30.0	27.4	548	45.90	8.3
08	60.0	40.8	409	68.60	16.7
09	30.0	27.4	548	45.90	8.3
10	12.0	16.5	930	27.80	3.3
11	6.0	11.5	1 150	19.30	1.6
12	3.0	8.0	1 600	13.40	.8
13	1.5	5.8	2 320	9.74	.4
14	.6	3.8	3 810	6.38	.1
15	.3	2.7	5 410	4.54	0

TABLE XI.—FLUID 3.2 RHEOLOGICAL PROPERTIES

Item	Velocity at rotation, rpm	Torque, percent	Viscosity, cP	Shear stress, dyne/cm^2	Shear rate, sec^{-1}
Temperature, −25 °C					
01	0.3	0.9	1 800	1.51	0
02	.6	1.8	1 800	3.02	.1
03	1.5	3.8	1 520	6.38	.4
04	3.0	6.9	1 380	11.60	.8
05	6.0	12.4	1 240	20.80	1.6
06	12.0	22.0	1 100	37.00	3.3
07	30.0	46.8	935	78.40	8.3
08	60.0	82.3	825	138.00	16.7
09	30.0	46.8	939	78.70	8.3
10	12.0	22.3	1 120	37.50	3.3
11	6.0	12.6	1 260	21.10	1.6
12	3.0	7.0	1 400	11.80	.8
13	1.5	4.0	1 600	6.72	.4
14	.6	1.7	1 700	2.86	.1
15	.3	1.0	2 000	1.68	0
Temperature, −10 °C					
01	0.3	1.7	3 410	2.86	0
02	.6	2.8	2 810	4.70	.1
03	1.5	5.4	2 170	9.07	.4
04	3.0	8.7	1 740	14.60	.8
05	6.0	14.0	1 400	23.50	1.6
06	12.0	22.8	1 140	38.40	3.3
07	30.0	43.4	868	72.80	8.3
08	60.0	70.5	706	118.00	16.7
09	30.0	43.5	868	72.80	8.3
10	12.0	23.0	1 150	38.60	3.3
11	6.0	14.3	1 430	24.00	1.6
12	3.0	8.7	1 740	14.60	.8
13	1.5	5.7	2 290	9.58	.4
14	.6	2.7	2 700	4.54	.1
15	.3	2.1	4 210	3.53	0
Temperature, 0 °C					
01	0.3	3.3	6 610	5.54	0
02	.6	4.8	4 810	8.06	.1
03	1.5	8.0	3 210	13.40	.4
04	3.0	11.8	2 350	19.80	.8
05	6.0	17.6	1 770	29.70	1.6
06	12.0	26.7	1 340	44.80	3.3
07	30.0	46.9	939	78.70	8.3
08	60.0	72.3	725	121.00	16.7
09	30.0	46.9	939	78.70	8.3
10	12.0	26.9	1 340	45.10	3.3
11	6.0	17.9	1 800	30.20	1.6
12	3.0	11.8	2 350	19.80	.8
13	1.5	8.4	3 370	14.10	.4
14	.6	4.7	4 710	7.90	.1
15	.3	3.3	6 610	5.54	0
Temperature, 20 °C					
01	0.3	3.1	6 210	5.21	0
02	.6	4.5	4 510	7.56	.1
03	1.5	6.9	2 770	11.60	.4
04	3.0	9.6	1 920	16.10	.8
05	6.0	13.8	1 380	23.20	1.6
06	12.0	20.0	1 000	33.60	3.3
07	30.0	33.2	665	55.70	8.3
08	60.0	49.3	493	82.60	16.7
09	30.0	33.1	665	55.70	8.3
10	12.0	19.9	994	33.30	3.3
11	6.0	13.7	1 370	23.00	1.6
12	3.0	9.6	1 920	16.10	.8
13	1.5	6.8	2 720	11.40	.4
14	.6	4.4	4 410	7.39	.1
15	.3	3.4	6 810	5.71	0

TABLE XII.—FLUID 4.1 RHEOLOGICAL PROPERTIES

Item	Velocity at rotation, rpm	Torque, percent	Viscosity, cP	Shear stress, dyne/cm^2	Shear rate, sec^{-1}
Temperature, −25 °C					
01	0.3	9.9	19 900	16.6	0
02	.6	12.7	12 700	21.3	.1
03	1.5	17.6	7 080	29.7	.4
04	3.0	22.5	4 510	37.8	.8
05	6.0	30.1	3 020	50.7	1.6
06	12.0	42.8	2 140	72.0	3.3
07	30.0	75.6	1 510	127.0	8.4
08	12.0	44.5	2 240	74.8	3.3
09	6.0	30.0	3 010	50.4	1.6
10	3.0	21.3	4 240	35.6	.8
11	1.5	15.7	6 260	26.2	.4
12	.6	11.4	11 400	19.2	.1
13	.3	8.8	17 700	14.8	0
Temperature, −10 °C					
01	0.3	9.8	19 700	16.50	0
02	.6	8.9	8 920	15.00	.1
03	1.5	11.6	4 620	19.50	.4
04	3.0	14.4	2 890	24.20	.8
05	6.0	18.6	1 850	31.10	1.6
06	12.0	24.3	1 220	40.90	3.3
07	30.0	37.6	755	63.30	8.3
08	60.0	62.1	621	104.00	16.7
09	30.0	40.3	808	67.80	8.3
10	12.0	24.6	1 230	41.20	3.3
11	6.0	18.0	1 800	30.20	1.6
12	3.0	13.6	2 720	22.80	.8
13	1.5	10.4	4 170	17.50	.4
14	.6	7.1	7 100	11.90	.1
15	.3	5.8	11 600	9.74	0
Temperature, 0 °C					
01	0.3	6.1	12 200	10.20	0
02	.6	7.4	7 410	12.40	.1
03	1.5	9.6	3 840	16.10	.4
04	3.0	11.7	2 340	19.70	.8
05	6.0	14.8	1 408	24.80	1.6
06	12.0	18.7	935	31.40	3.3
07	30.0	27.6	554	46.50	8.3
08	60.0	42.3	424	71.10	16.7
09	30.0	28.5	571	47.90	8.3
10	12.0	18.8	935	31.40	3.3
11	6.0	14.3	1 430	24.00	1.6
12	3.0	11.2	2 240	18.80	.8
13	1.5	8.8	3 520	14.80	.4
14	.6	6.5	6 510	10.90	.1
15	.3	4.9	9 820	8.23	0
Temperature, 20 °C					
01	0.3	4.7	9 420	7.90	0
02	.6	5.2	5 210	8.74	.1
03	1.5	7.1	2 840	11.90	.4
04	3.0	8.6	1 720	14.40	.8
05	6.0	10.6	1 060	17.80	1.6
06	12.0	13.2	661	22.20	3.3
07	30.0	18.3	367	30.80	8.3
08	60.0	25.2	252	42.30	16.7
09	30.0	18.6	371	31.10	8.3
10	12.0	13.1	656	22.00	3.3
11	6.0	10.3	1 030	17.30	1.6
12	3.0	8.2	1 640	13.80	.8
13	1.5	6.5	2 610	10.90	.4
14	.6	4.6	4 590	7.70	.1
15	.3	3.6	7 210	6.05	0

TABLE XIII.—FLUID 4.2 RHEOLOGICAL PROPERTIES

Item	Velocity at rotation, rpm	Torque, percent	Viscosity, cP	Shear stress, dyne/cm^2	Shear rate, sec^{-1}
Temperature, −25 °C					
01	0.3	3.1	6 210	5.21	0
02	.6	4.9	4 910	8.23	.1
03	1.5	8.4	3 370	14.10	.4
04	3.0	13.7	2 740	23.00	.8
05	6.0	20.0	2 000	33.60	1.6
06	12.0	30.5	1 530	51.20	3.3
07	30.0	52.7	1 060	88.50	8.3
08	60.0	80.7	808	136.00	16.8
09	30.0	48.0	962	80.60	8.3
10	12.0	25.5	1 280	42.80	3.3
11	6.0	16.1	1 610	27.00	1.6
12	3.0	10.4	2 090	17.50	.8
13	1.5	6.9	2 770	11.60	.4
14	.6	4.0	4 010	6.72	.1
15	.3	2.9	5 810	4.87	0
Temperature, −10 °C					
01	0.3	1.8	3 610	3.02	0
02	.6	2.5	2 500	4.20	.1
03	1.5	4.2	1 690	7.06	.4
04	3.0	6.1	1 220	10.20	.8
05	6.0	8.9	892	15.00	1.6
06	12.0	12.9	646	21.70	3.3
07	30.0	23.0	461	38.60	8.3
08	60.0	37.0	371	62.20	16.7
09	30.0	23.3	468	39.20	8.3
10	12.0	12.9	646	21.70	3.3
11	6.0	8.4	842	14.10	1.6
12	3.0	5.5	1 100	9.24	.8
13	1.5	3.8	1 520	6.38	.4
14	.6	2.2	2 200	3.70	.1
15	.3	1.5	3 010	2.52	0
Temperature, 0 °C					
01	0.3	12.3	1 230	4.87	0.3
02	.6	16.3	817	6.45	.7
03	1.5	26.7	534	10.60	1.9
04	3.0	37.0	371	14.70	3.9
05	6.0	55.2	277	21.90	7.9
06	12.0	85.9	215	34.10	15.8
07	6.0	52.8	264	20.90	7.9
08	3.0	33.6	334	13.20	3.9
09	1.5	22.4	449	8.87	1.9
10	.6	11.6	581	4.59	.7
11	.3	7.6	762	3.01	.3
Temperature, 20 °C					
01	0.3	0.5	1 000	0.84	0
02	.6	.8	802	1.34	.1
03	1.5	1.5	601	2.52	.4
04	3.0	2.3	461	3.86	.8
05	6.0	3.5	351	5.88	1.6
06	12.0	5.3	265	8.90	3.3
07	30.0	9.3	187	15.60	8.3
08	60.0	14.4	144	24.20	16.8
09	30.0	9.4	189	15.80	8.3
10	12.0	5.5	276	9.24	3.3
11	6.0	3.7	371	6.22	1.6
12	3.0	2.4	481	4.03	.8
13	1.5	1.7	681	2.86	.4
14	.6	1.0	1 000	1.68	.1
15	.3	.7	1 400	1.18	0

TABLE XIV.—FLUID 5.1 RHEOLOGICAL PROPERTIES

Item	Velocity at rotation, rpm	Torque, percent	Viscosity, cP	Shear stress, dyne/cm^2	Shear rate, sec^{-1}
Temperature, −25 °C					
01	0.3	0.5	1 000	0.84	0
02	.6	1.1	1 100	1.85	.1
03	1.5	2.1	842	3.53	.4
04	3.0	3.8	762	6.38	.8
05	6.0	7.2	721	12.10	1.6
06	12.0	13.1	656	22.00	3.3
07	30.0	28.9	578	48.40	8.3
08	60.0	52.1	521	87.40	16.7
09	30.0	29.0	581	48.70	8.3
10	12.0	3.2	661	22.20	3.3
11	6.0	7.1	710	11.90	1.6
12	3.0	3.9	782	6.55	.8
13	1.5	2.1	842	3.53	.4
14	.6	1.1	1 100	1.85	.1
15	.3	.5	1 000	.84	0
Temperature, −10 °C					
01	0.3	0.3	601	0.50	0
02	.6	.6	601	1.01	.1
03	1.5	1.3	521	2.18	.4
04	3.0	2.4	481	4.03	.8
05	6.0	4.4	441	7.39	1.6
06	12.0	7.8	391	13.10	3.3
07	30.0	16.6	332	27.80	8.3
08	60.0	28.7	287	48.20	16.7
09	30.0	16.6	332	27.80	8.3
10	12.0	7.9	396	13.30	3.3
11	6.0	4.5	451	7.56	1.6
12	3.0	2.5	501	4.20	.8
13	1.5	1.4	561	2.35	.4
14	.6	.6	601	1.01	.1
15	.3	.3	601	.50	0
Temperature, 0 °C					
01	0.3	0.3	601	0.50	0
02	.6	.7	701	1.18	.1
03	1.5	1.4	561	2.35	.4
04	3.0	2.3	461	3.86	.8
05	6.0	3.9	391	6.55	1.6
06	12.0	6.7	336	11.30	3.3
07	30.0	13.4	269	22.50	8.3
08	60.0	22.6	227	38.10	16.7
09	30.0	13.4	269	22.50	8.3
10	12.0	6.7	336	11.30	3.3
11	6.0	3.9	391	6.55	1.6
12	3.0	2.3	461	3.86	.8
13	1.5	1.4	561	2.35	.4
14	.6	.8	802	1.34	.1
15	.3	.5	1 000	.84	0
Temperature, 20 °C					
01	0.3	0.3	601	0.50	0
02	.6	.6	601	1.01	.1
03	1.5	1.0	401	1.68	.4
04	3.0	1.7	341	2.86	.8
05	6.0	2.8	281	4.70	1.6
06	12.0	4.5	225	7.56	3.3
07	30.0	8.7	174	14.60	8.3
08	60.0	14.3	143	24.00	16.7
09	30.0	8.7	174	14.60	8.3
10	12.0	4.5	225	7.56	3.3
11	6.0	2.7	270	4.54	1.6
12	3.0	1.7	341	2.86	.8
13	1.5	1.0	401	1.68	.4
14	.6	.6	601	1.01	.1
15	.3	.3	601	.50	0

TABLE XV.—FLUID 5.2 RHEOLOGICAL PROPERTIES

Item	Velocity at rotation, rpm	Torque, percent	Viscosity, cP	Shear stress, dyne/cm^2	Shear rate, sec^{-1}
Temperature, −25 °C					
01	0.3	0.9	1 800	1.51	0
02	.6	1.3	1 300	2.18	.1
03	1.5	3.0	1 200	5.04	.4
04	3.0	5.2	1 040	8.74	.8
05	6.0	9.1	910	15.30	1.6
06	12.0	16.1	807	27.00	3.3
07	30.0	34.4	688	57.70	8.3
08	60.0	61.7	618	104.00	16.8
09	30.0	35.8	718	60.20	8.3
10	12.0	17.4	868	29.10	3.3
11	6.0	10.1	1 010	16.90	1.6
12	3.0	5.8	1 160	9.74	.8
13	1.5	3.3	1 320	5.54	.4
14	.6	1.8	1 800	3.02	.1
15	.3	1.2	2 400	2.02	0
Temperature, −10 °C					
01	0.3	0.7	1 400	1.18	0
02	.6	1.1	1 100	1.85	.1
03	1.5	2.2	882	3.70	.4
04	3.0	3.8	762	6.38	.8
05	6.0	6.3	631	10.60	1.6
06	12.0	10.6	529	17.80	3.3
07	30.0	21.3	424	35.60	8.3
08	60.0	36.0	361	60.50	16.7
09	30.0	21.9	438	36.70	8.3
10	12.0	11.3	566	19.00	3.3
11	6.0	6.8	681	11.40	1.6
12	3.0	4.1	818	6.86	.8
13	1.5	2.6	1 040	4.37	.4
14	.6	1.4	1 400	2.35	.1
15	.3	.8	1 600	1.34	0
Temperature, 0 °C					
01	0.3	1.0	2 000	1.68	0
02	.6	1.3	1 300	2.18	.1
03	1.5	2.4	962	4.03	.4
04	3.0	3.8	762	6.38	.8
05	6.0	5.9	591	9.91	1.6
06	12.0	9.3	466	15.60	3.3
07	30.0	17.4	347	29.10	8.3
08	60.0	28.2	284	47.60	16.7
09	30.0	17.6	354	29.70	8.3
10	12.0	9.5	476	16.00	3.3
11	6.0	6.1	610	10.20	1.6
12	3.0	3.8	762	6.38	.8
13	1.5	2.6	1 040	4.37	.4
14	.6	1.6	1 600	2.68	.1
15	.3	1.0	2 000	1.68	0
Temperature, 20 °C					
01	0.3	1.0	2 000	1.68	0
02	.6	1.3	1 300	2.18	.1
03	1.5	2.1	842	3.53	.4
04	3.0	3.0	601	5.04	.8
05	6.0	4.5	451	7.56	1.6
06	12.0	6.7	336	11.30	3.3
07	30.0	11.8	235	19.80	8.3
08	60.0	18.3	184	30.80	16.7
09	30.0	11.8	235	19.80	8.4
10	12.0	6.8	341	11.40	3.3
11	6.0	4.5	451	7.56	1.6
12	3.0	3.0	601	5.04	.8
13	1.5	2.1	842	3.53	.4
14	.6	1.3	1 300	2.18	.1
15	.3	.9	1 800	1.51	0

TABLE XVI.—WATER CONTENT OF DEICING AND ANTI-ICING FLUIDS

Fluid	Water content, percent (a)
1	9.9
2	46.7
2.1	45.8
2.2	44.4
3	43.9
3.1	42.3
3.2	42.3
4	43.0
4.1	36.4
4.2	42.0
5.1	49.0
5.2	48.6

[a]Average of three runs.

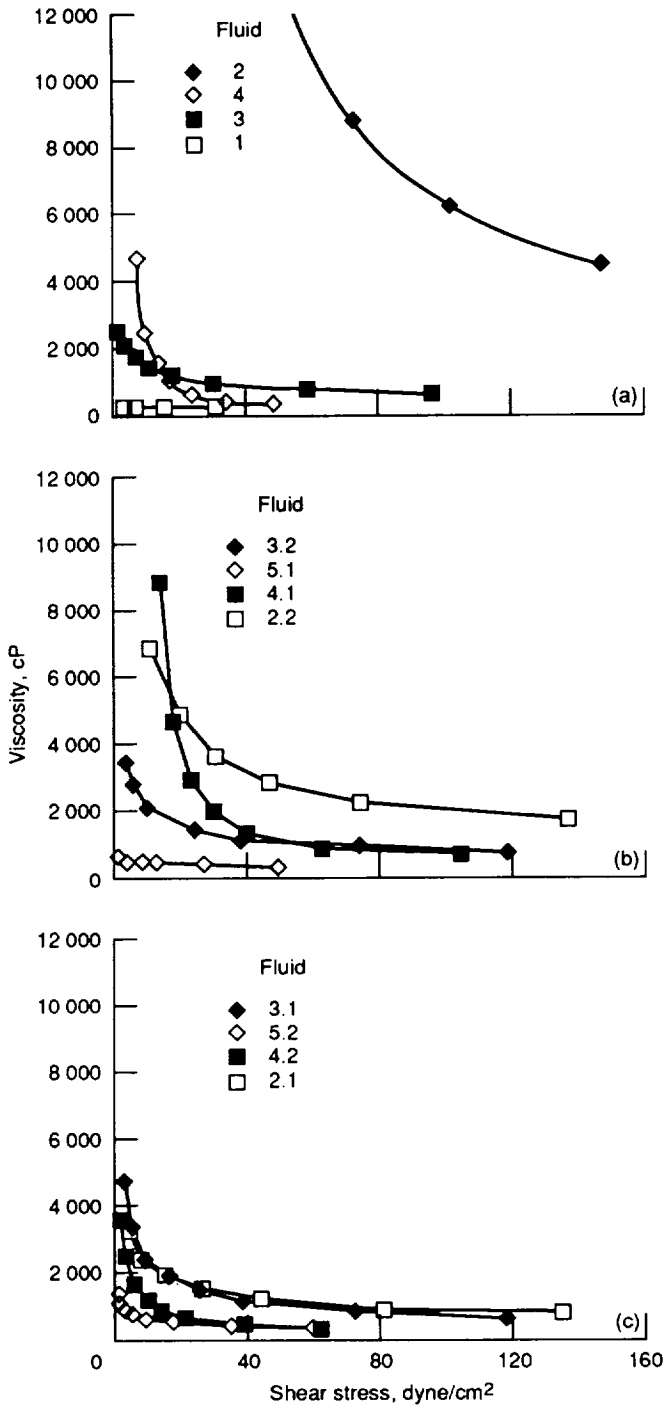

Figure 58.—Fluid viscosity versus shear stress. Fluid temperature, −10 °C.

Appendix B

Three-Dimensional Half Model Force Data

This appendix contains the three-dimensional model force data. The data are divided into the following categories: (1) data in ground effect (ground plane in); (2) data in free air (ground plane out); (3) effect of miscellaneous parameters; and (4) test technique verification. Some lift data are adjusted for initial balance offset, which is present due to balance drift from the applicable wind off zero. This correction to the data is explained in appendix E.

Data in Ground Effect

Because the ground acts as a reflection plane, the aerodynamics of the airplane are different near the ground than they are in free air. Therefore, to properly simulate this effect, most of the three-dimensional half model testing was done with the ground plane in. The ground plane was described earlier in this report (see "Models and Installation").

Flaps 5, sealed slats.—The three-dimensional half model configuration that was investigated most extensively was the flaps 5, sealed slat. This is the most common takeoff flap setting used on the 737-200ADV. All four of the basic fluids were tested on this configuration. The range of temperatures tested varied from fluid to fluid. For some of the fluids two sets of data were taken at a given temperature. These repeat runs were usually separated by a large number of runs. In these cases, both the dry baseline and the fluid runs were repeated to account for any long-term balance shifts that might have occurred. The data are shown in figures 59 to 62. For each fluid the data are arranged in order of decreasing temperature.

Flaps 15, gapped slats.—Data were obtained for all four of the basic fluids on this configuration. These results are shown in figures 63 to 66.

Free-Air Data

After the airplane lifts off and begins to climb, it very quickly moves out of ground effect. It then is considered to be in free air. Since both the flight data and the results from this test show that there is still fluid left on the wing during the early portion of the climbout, it is important to understand the fluid effects under these free air conditions. Therefore, runs were made with the ground plane removed for both the flaps 5 and flaps 15 configurations. This was done only for fluid 3 at 20 °C. The results are shown in figure 67.

Effect of Miscellaneous Parameters

The effects of miscellaneous parameters such as initial fluid depth, final velocity, fluid chordwise coverage, gaping the slat on the flaps 5 configuration, aileron deflection, and cleaning the underside of the slat after application of the fluid are shown in figures 68 to 73. The effect of initial fluid depth (fig. 68) was investigated early in the test when the model was being rotated to a particular fixed angle of attack on each run. That is why the data shown in these two figures only go to 7°. The same explanation applies to the data on the effect of final velocity (fig. 69).

Test Technique Verification

As discussed earlier (see "Test technique verification" section in the main text), the original test plan called for rotating the model to a fixed attitude and holding that attitude for the duration of the run. The attitude would be changed from run to run in order to define points on the lift curve. The purpose of this approach was to match the procedures of the Kuopio flight test. However, as noted previously, it was determined during testing that it was possible to obtain the entire lift curve during a single run by rotating the model continuously to an attitude above that corresponding to $C_{L,\max}$. Figure 74 show the results of runs made to verify that this test technique worked for each of the four basic fluids. In these figures the symbols indicate the maximum angle of attack for a given run. However, data are taken continuously as the model is rotated so that data are obtained at all angles of attack up to the maximum for a given run. Each of the runs trace out essentially the same curve up to the maximum angle of attack for a given run. Thus, by rotating the model to an angle of attack beyond stall, all of the data can be obtained in a single run.

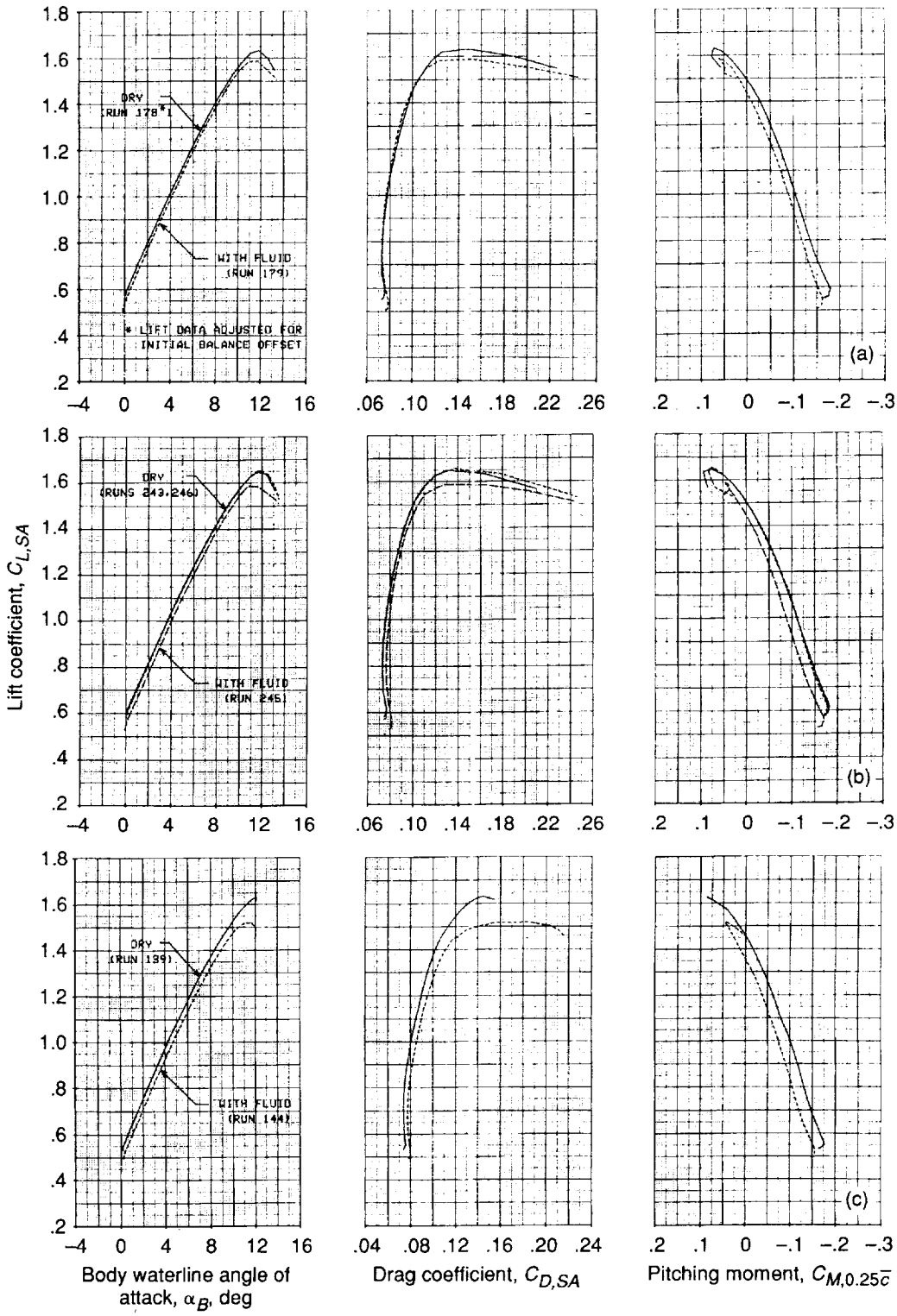

(a) Air temperature, –10 °C; early run.

(b) Air temperature, –10 °C; later run.

(c) Air temperature, –20 °C.

Figure 59.—Aerodynamic effects of fluid 1 on three-dimensional half model in flaps 5, sealed-slat configuration. Ground plane in.

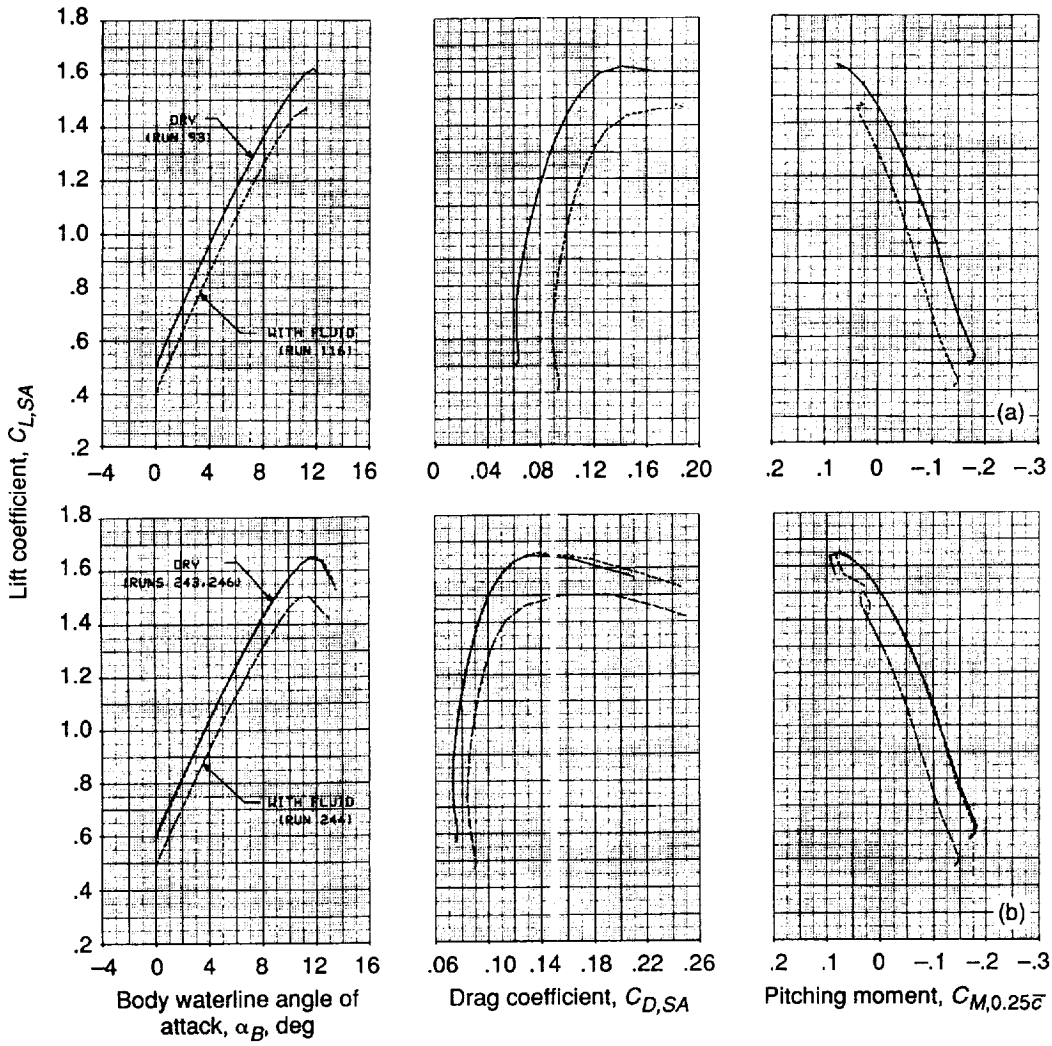

(a) Air temperature, −10 °C; early run.

(b) Air temperature, −10 °C; later run.

Figure 60.—Aerodynamic effects of fluid 2 on three-dimensional half model in flaps 5, sealed-slat configuration. Ground plane in.

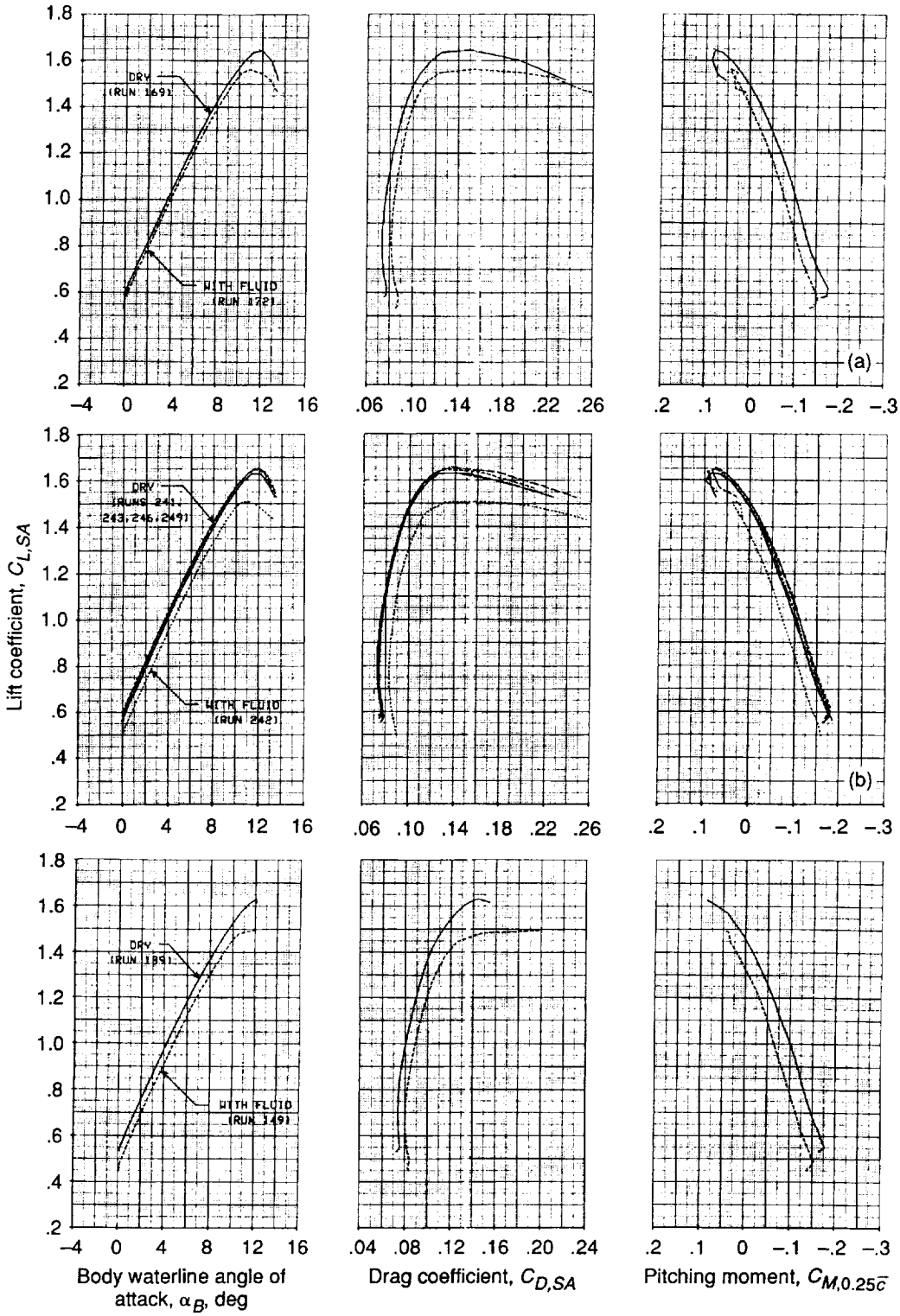

(a) Air temperature, 0 °C. Lift data adjusted for initial balance offset.

(b) Air temperature, –10 °C.

(c) Air temperature, –20 °C.

Figure 61.—Aerodynamic effects of fluid 3 on three-dimensional half model in flaps 5, sealed-slat configuration. Ground plane in.

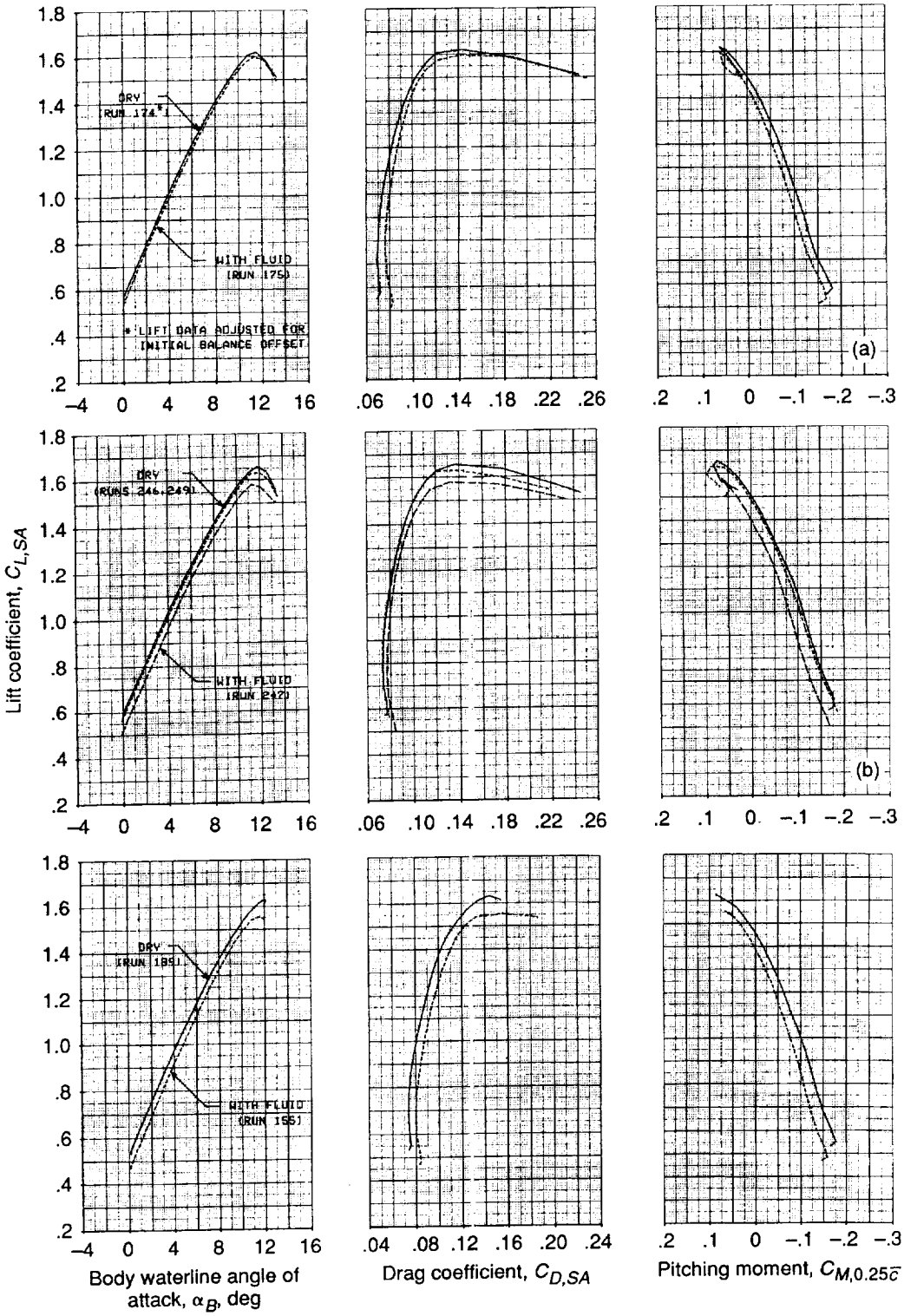

(a) Air temperature, –5 °C. Dry lift data adjusted for initial balance offset.

(b) Air temperature, –10 °C.

(c) Air temperature, –20 °C.

Figure 62.—Aerodynamic effects of fluid 4 on three-dimensional half model in flaps 5, sealed-slat configuration. Ground plane in.

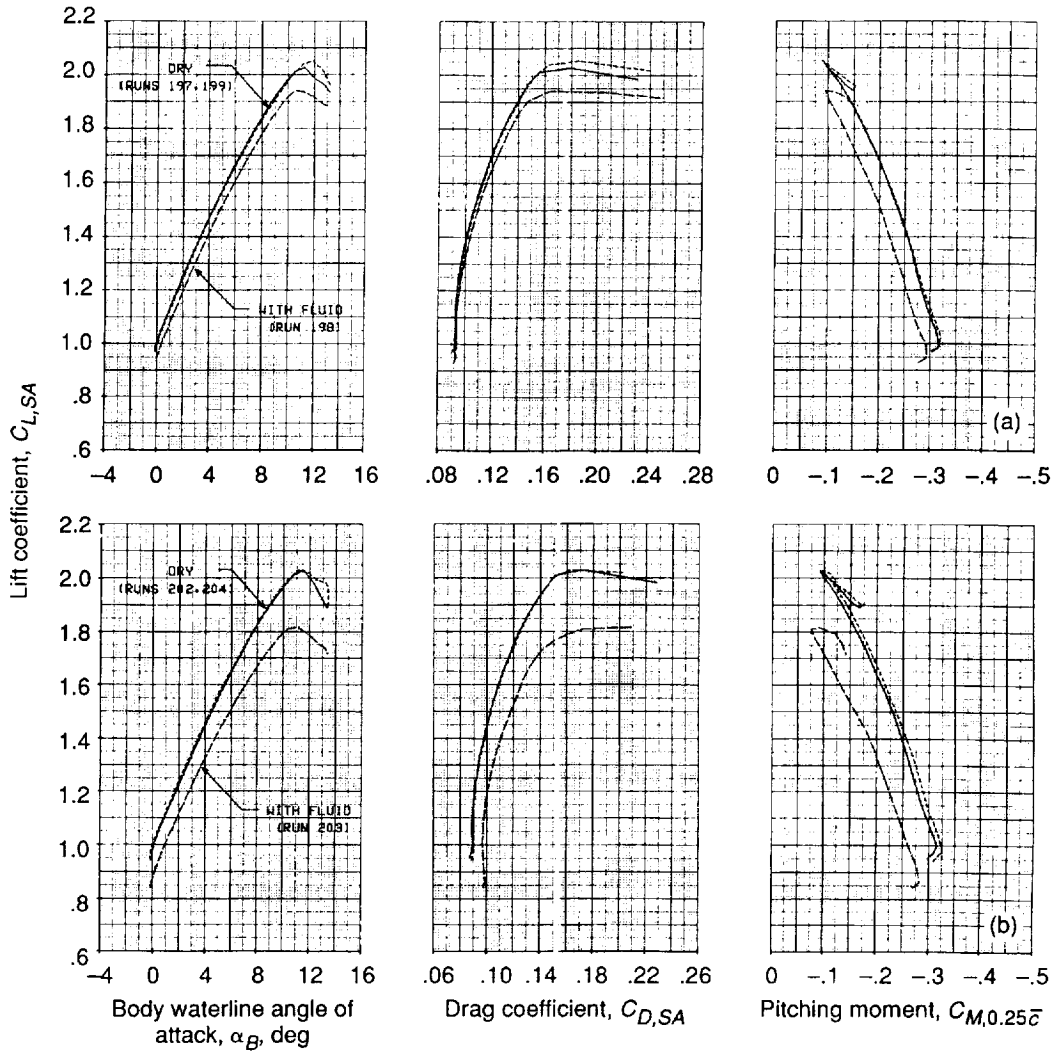

(a) Air temperature, –10 °C.

(b) Air temperature, –20 °C.

Figure 63.—Aerodynamic effects of fluid 1 on three-dimensional half model in flaps 15, gapped-slat configuration. Ground plane in.

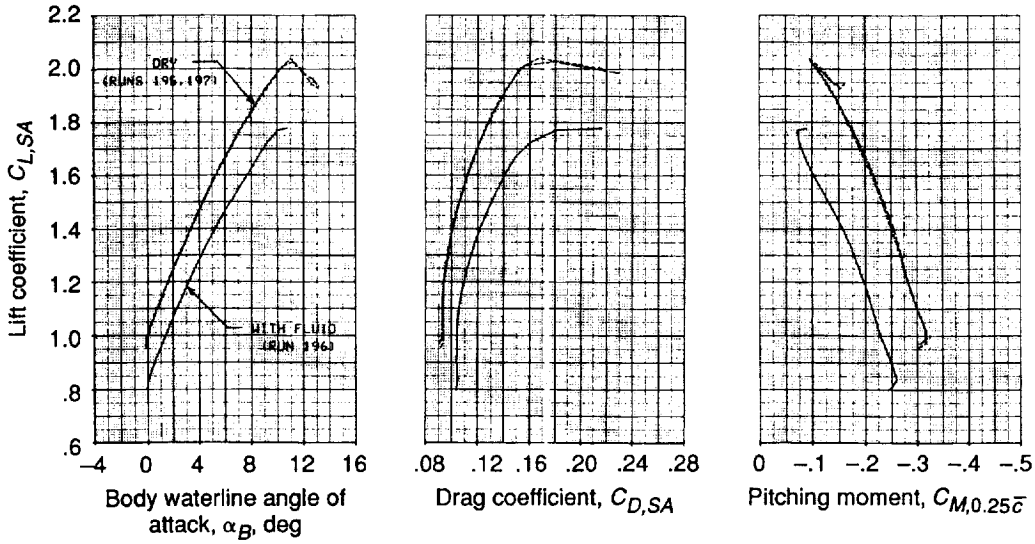

Figure 64.—Aerodynamic effects of fluid 2 on three-dimensional half model in flaps 15, gapped-slat configuration. Ground plane in; air temperature, –10 °C.

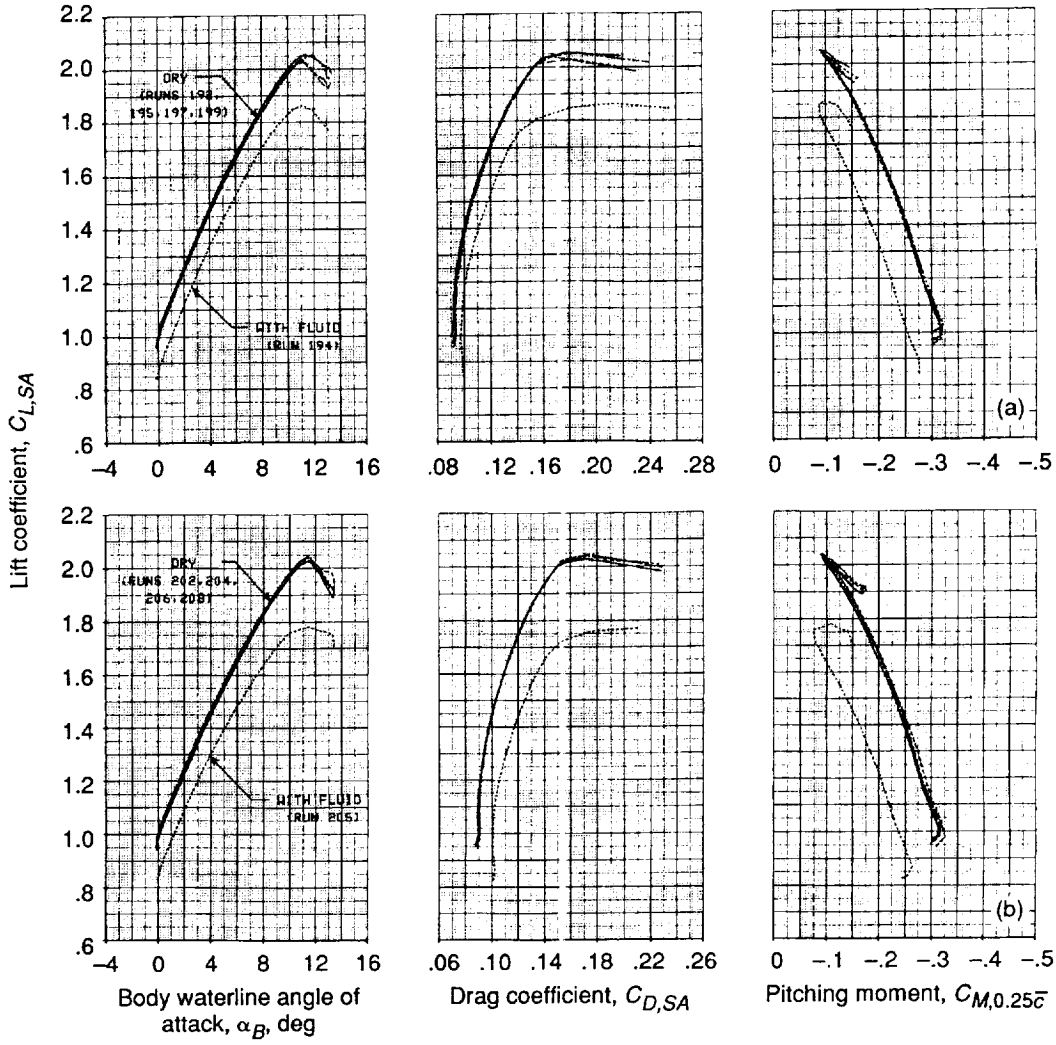

(a) Air temperature, –10 °C.

(b) Air temperature, –20 °C.

Figure 65.—Aerodynamic effects of fluid 3 on three-dimensional half model in flaps 15, gapped-slat configuration. Ground plane in.

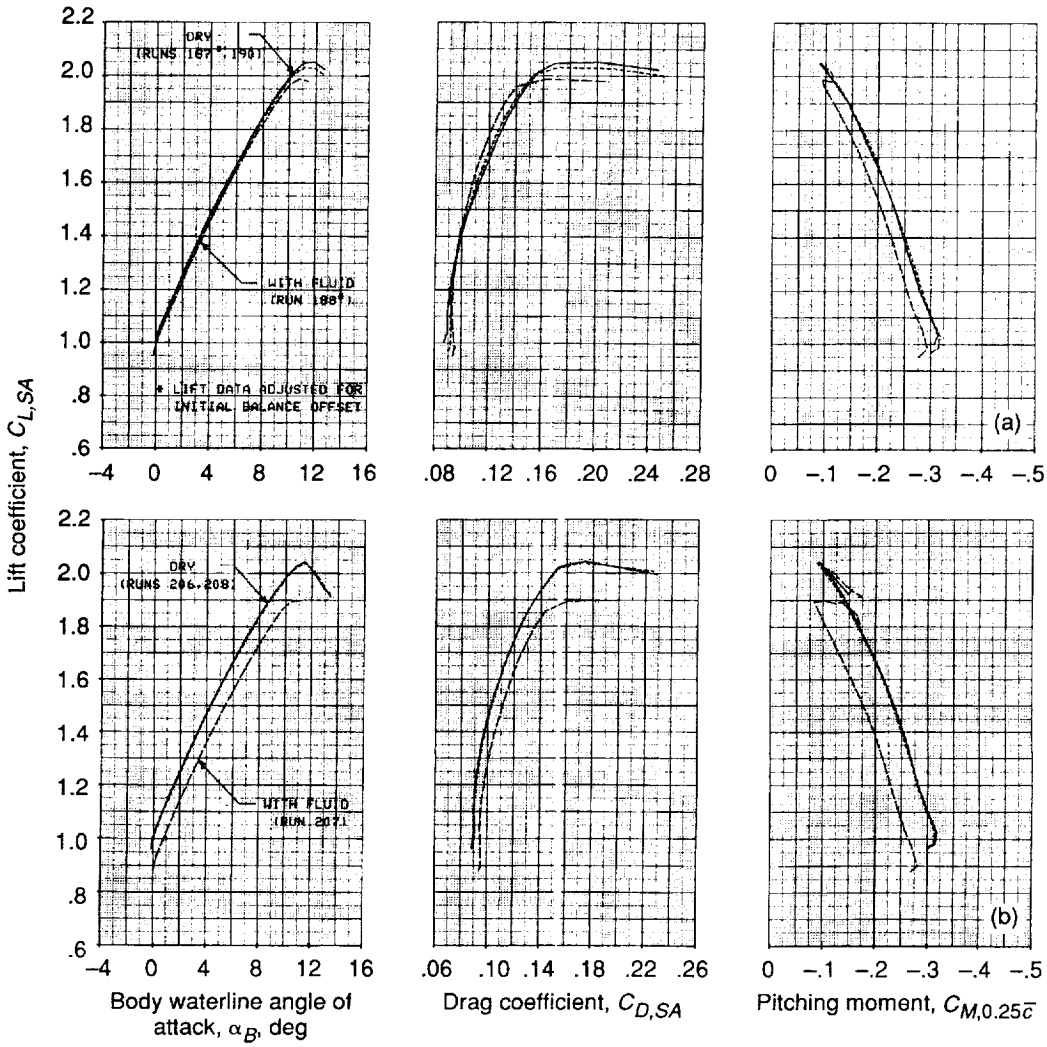

(a) Air temperature, −5 °C.

(b) Air temperature, −20 °C.

Figure 66.—Aerodynamic effects of fluid 4 on three-dimensional half model in flaps 15, gapped-slat configuration. Ground plane in.

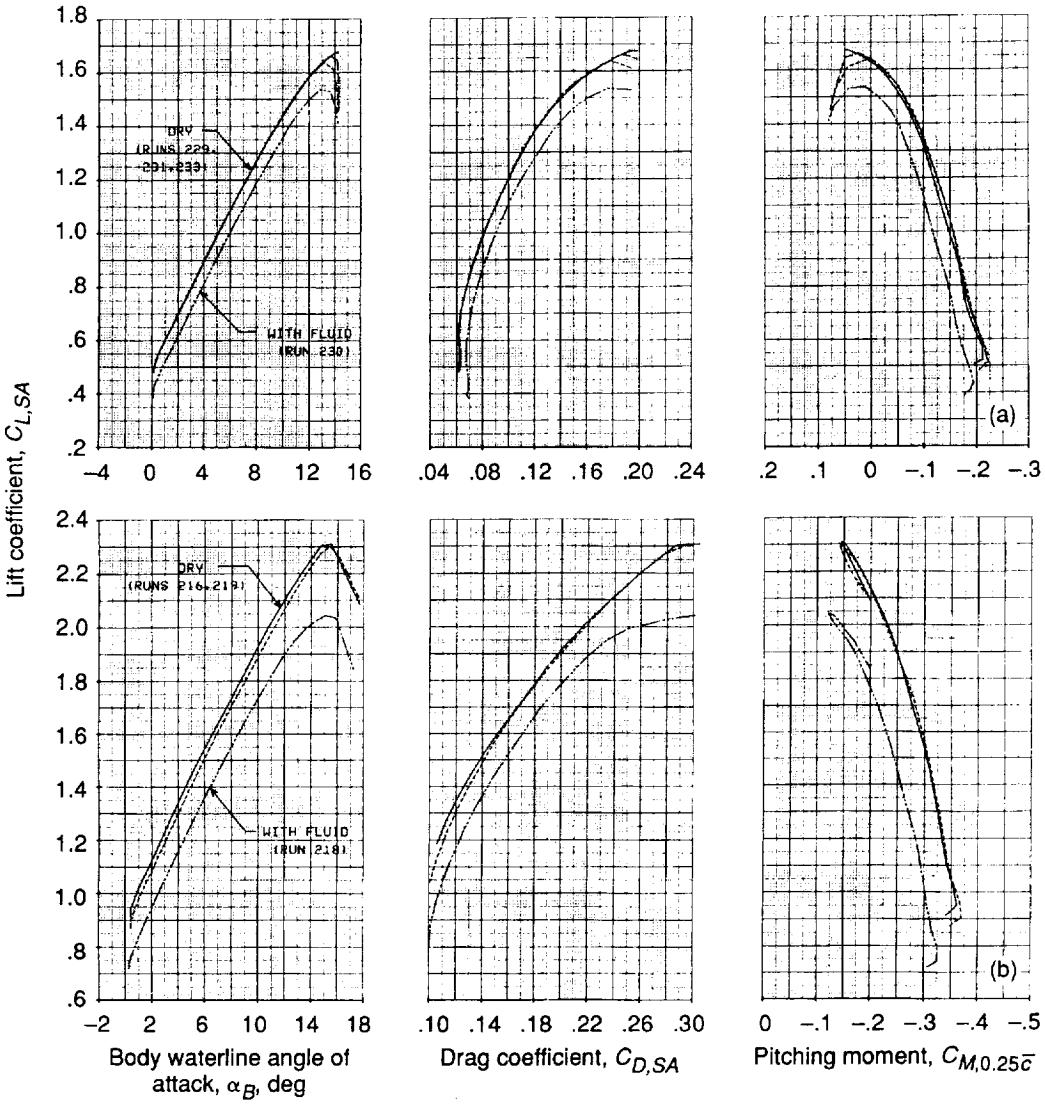

(a) In flaps 5, sealed-slat configuration.

(b) In flaps 15, gapped slat configuration.

Figure 67.—Aerodynamic effects of fluid 3 on three-dimensional half model in flaps 15, gapped-slat configuration. Free air; temperature, –20 °C.

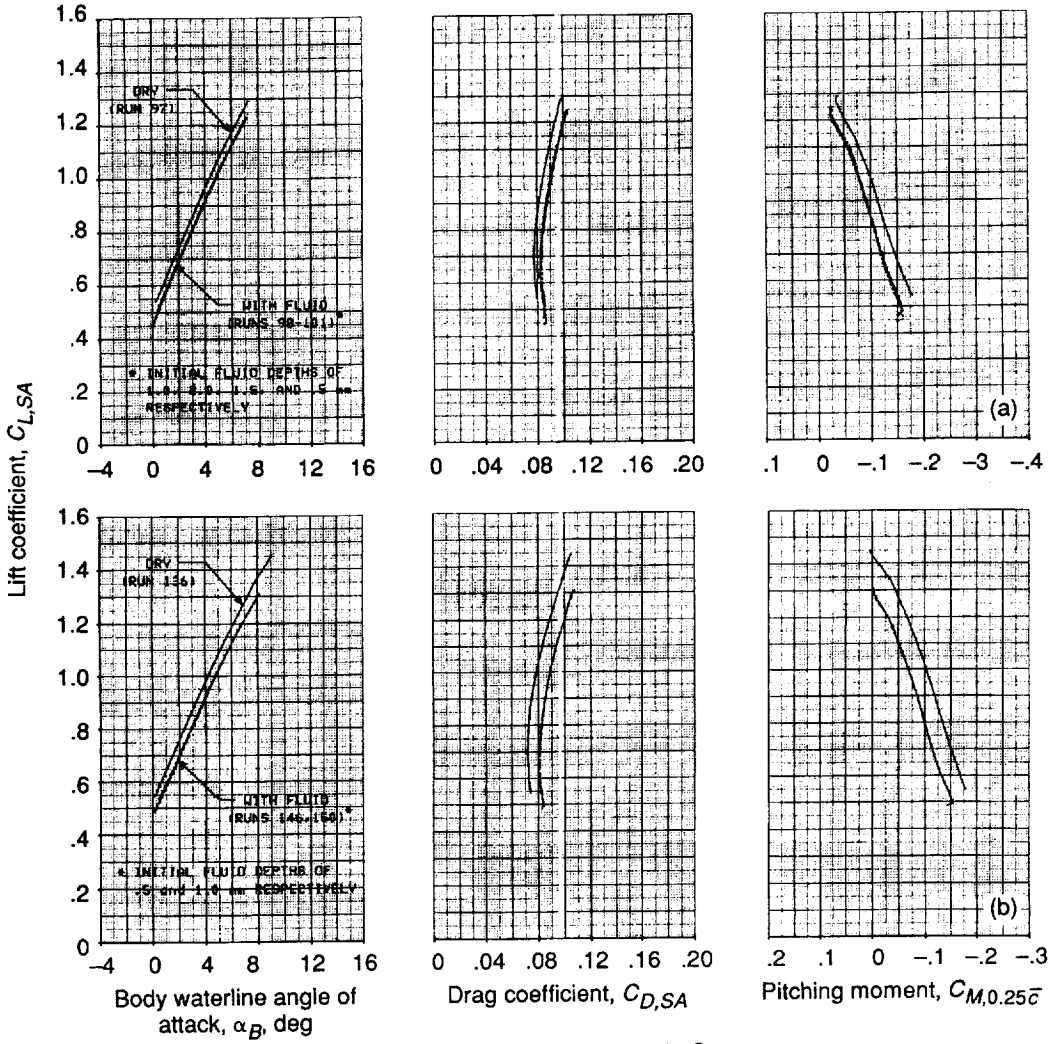

(a) Air temperature, −10 °C.

(b) Air temperature, −20 °C.

Figure 68.—Effect of initial fluid depth on aerodynamic effects of fluid 3 on three-dimensional half model in flaps 5, sealed-slat configuration. Ground plane in.

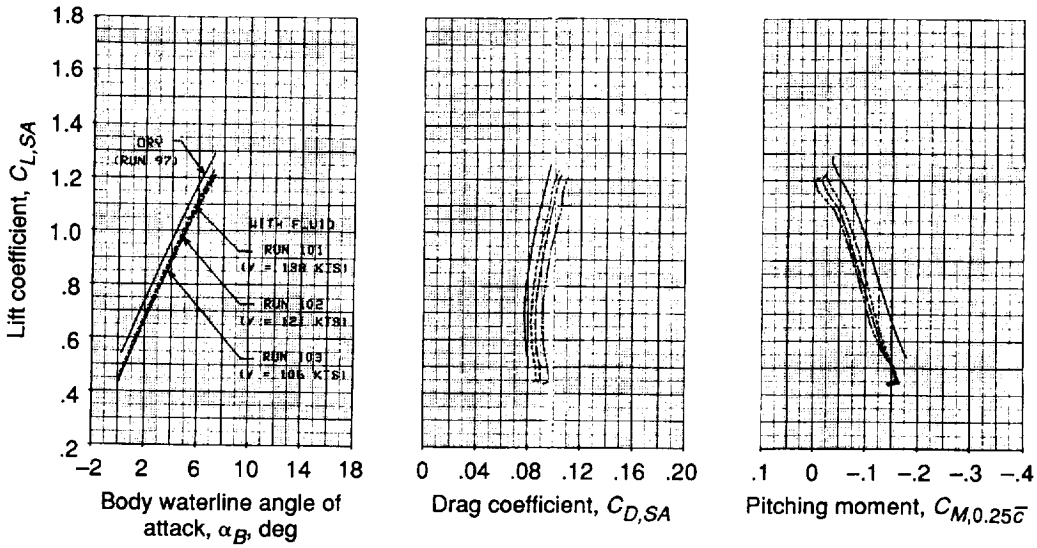

Figure 69.—Effect of final velocity on aerodynamic effects of fluid 3 on three-dimensional half model in flaps 5, sealed-slat configuration. Ground plane in; air temperature, −10 °C.

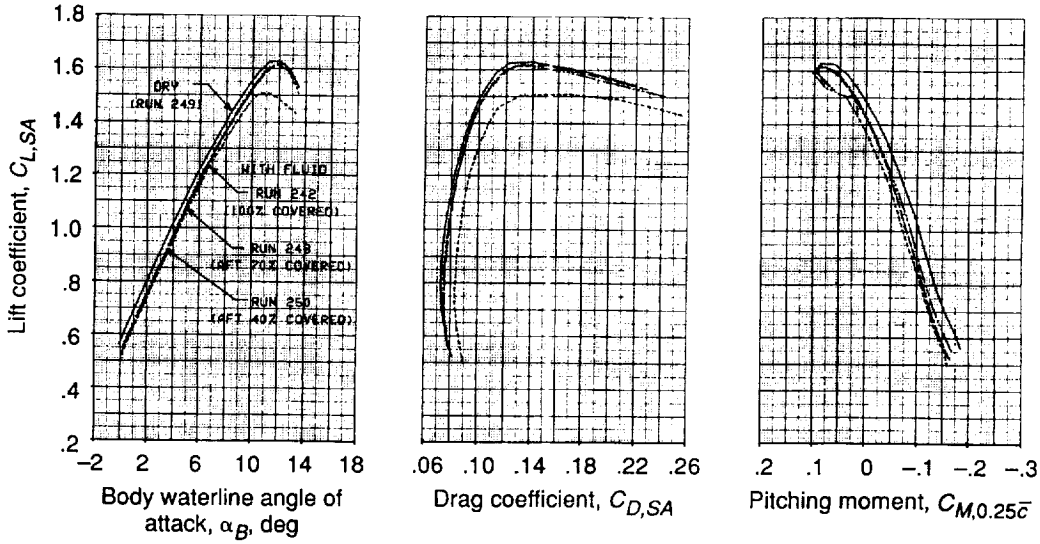

Figure 70.—Effect of fluid coverage on aerodynamic effects of fluid 3 on three-dimensional half model in flaps 5, sealed-slat configuration. Ground plane in; air temperature, −10 °C.

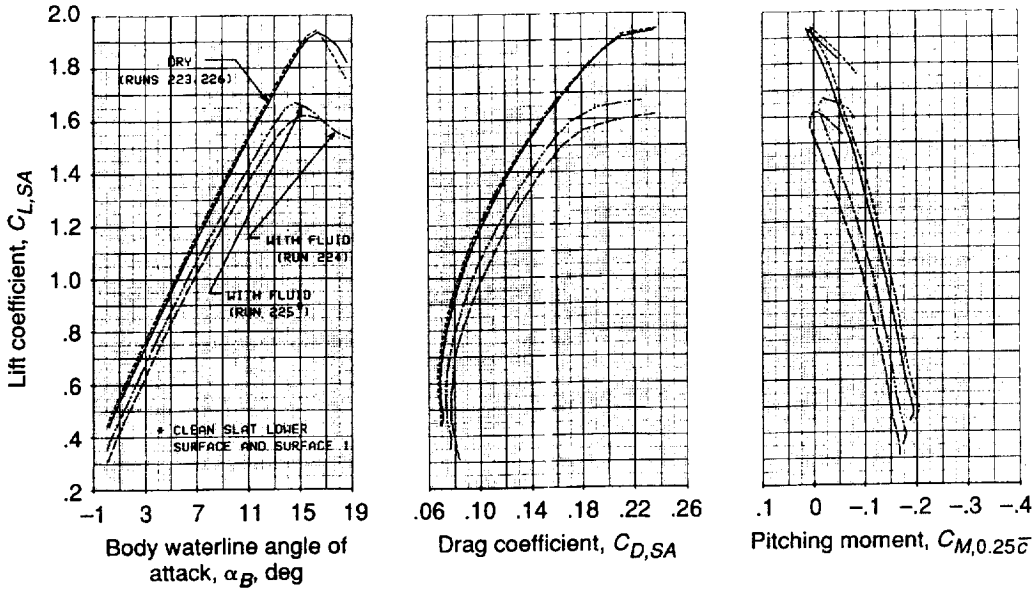

Figure 71.—Aerodynamic effects of fluid 3 on three-dimensional half model in flaps 5, gapped-slat configuration. Free air; temperature, –20 °C

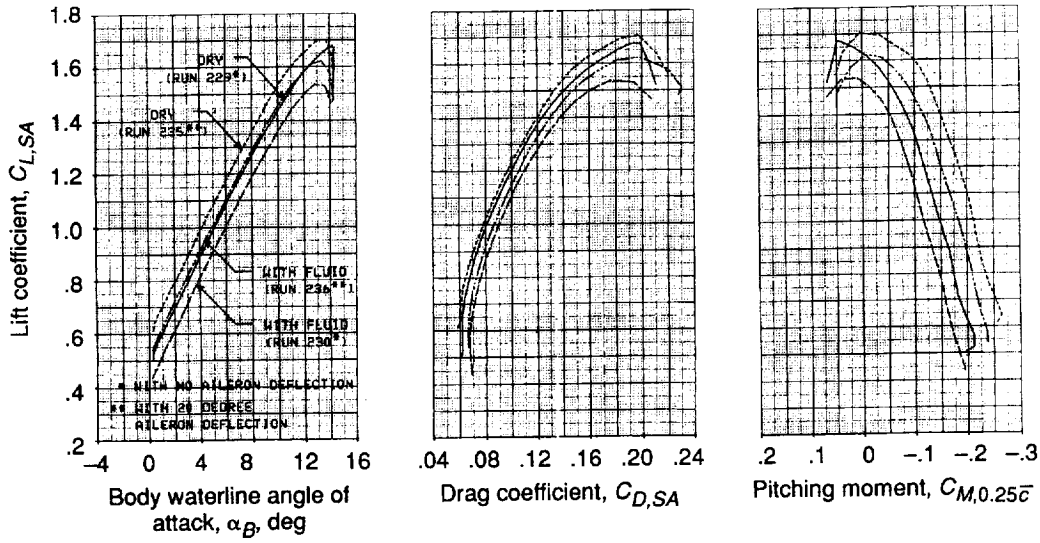

Figure 72.—Aerodynamic effects of fluid 3 on three-dimensional half model in flaps 5, gapped-slat configuration. Comparison of 0 and 20° aileron deflections. Free air; temperature, –20 °C.

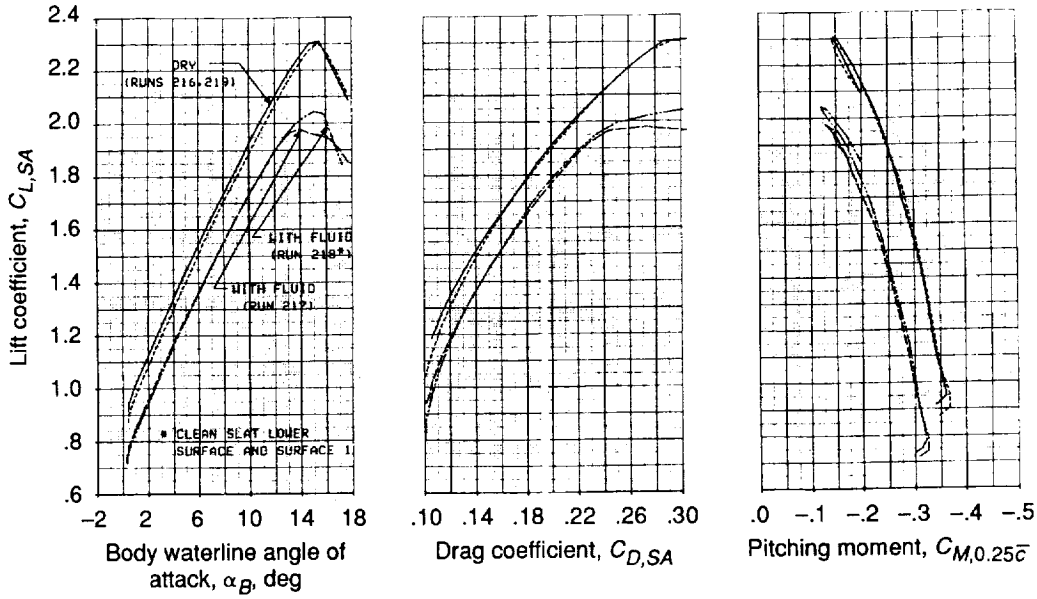

Figure 73.— Aerodynamic effects of fluid 3 on three-dimensional half model in flaps 15, gapped-slat configuration. Free air; temperature, –20 °C.

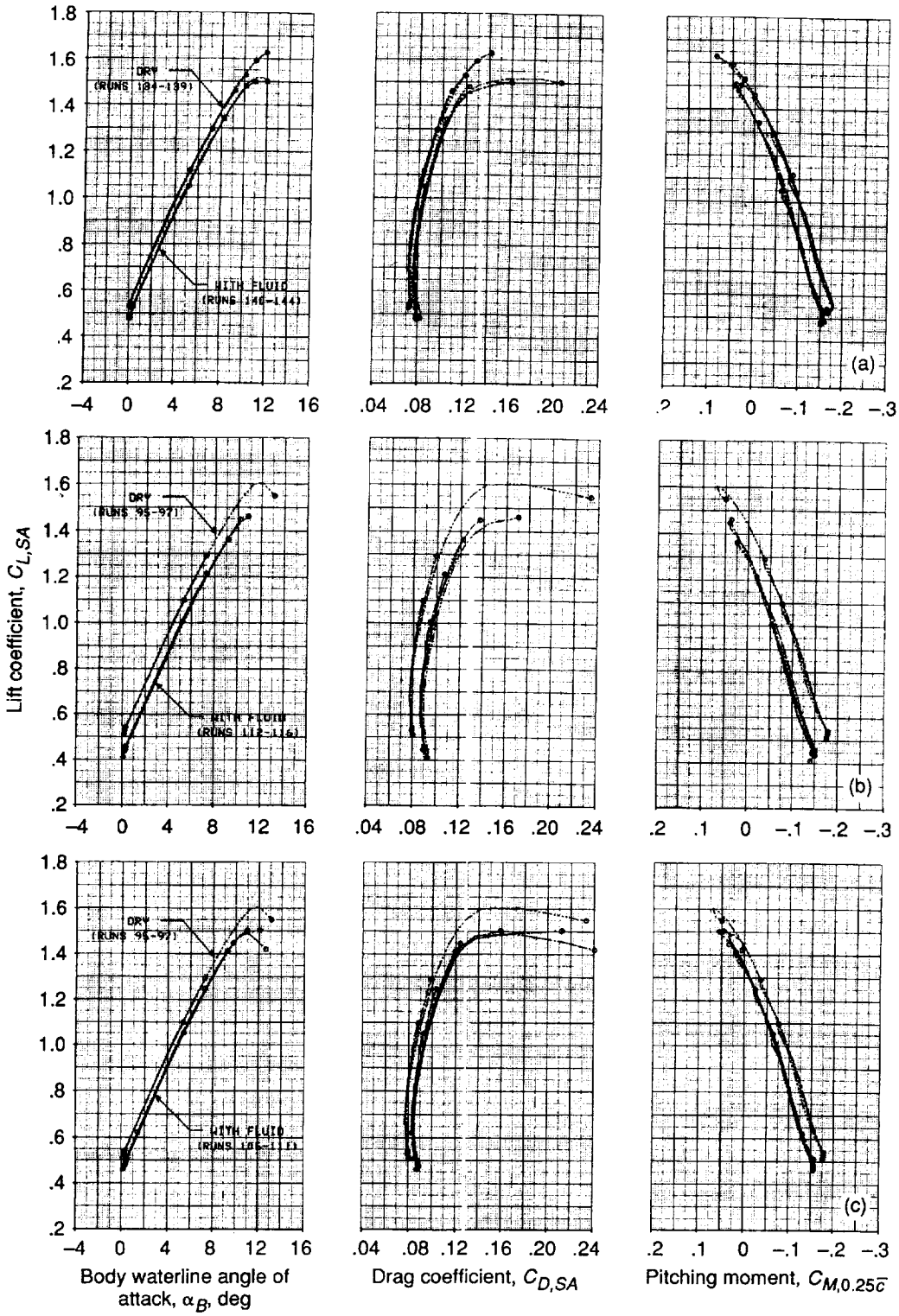

(a) Fluid 1, temperature, –20 °C.

(b) Fluid 2, temperature, –10 °C.

(c) Fluid 3, temperature, –10 °C.

Figure 74.—Test technique verification for three-dimensional half model in flaps 5, sealed-slat configuration. Symbols indicate highest α_B point of a given run.

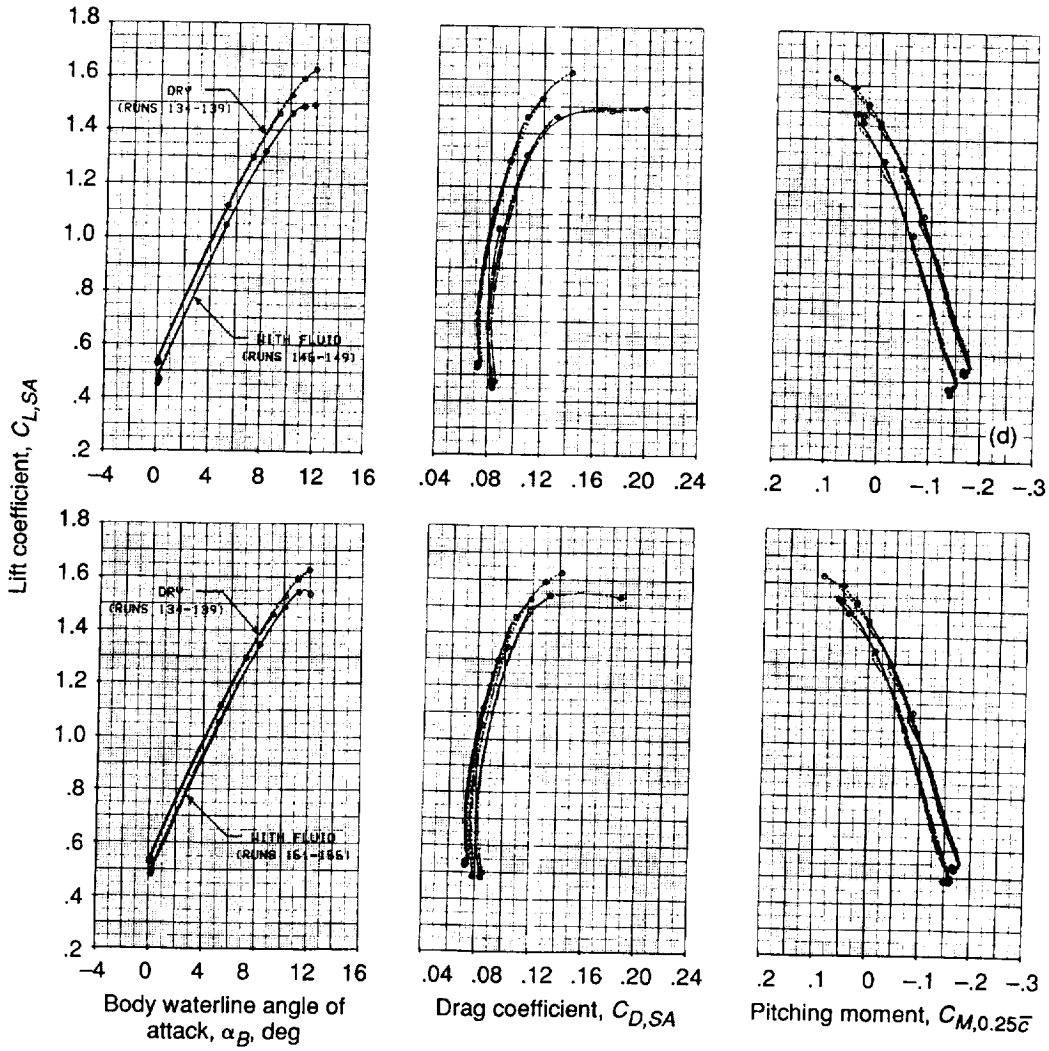

(d) Fluid 3, temperature, −20 °C.

(e) Fluid 4, temperature, −20 °C.

Figure 74.—Concluded.

Appendix C

Two-Dimensional Model Force Data

This appendix contains the two-dimensional model force data. The data are divided into the following categories: (1) effects of basic fluids (fluids 1 to 4), (2) effects of experimental fluids, (3) effects of miscellaneous parameters, and (4) test technique verification. Most of these data were corrected for dynamic pressure q effects. This correction is explained in appendix E.

Basic Fluid Data

Flaps 5, sealed slats.—Figures 75 to 78 show lift drag and pitching moment data arranged by fluid. For a given fluid, the data are arranged in order of decreasing temperature.

Flaps 15, gapped slats.—These results are shown in figures 79 to 82. Because of a balance problem that existed when this configuration was being tested, there are no drag data at most conditions.

Flaps 15, cruise leading edge.—To investigate fluid effects on a configuration without a leading edge high lift device, several runs were made with a flaps 15, cruise leading-edge configuration. Since this configuration is more typical of a smaller, slower airplane, the tunnel acceleration was changed to increase from 11.3 to 46.3 m/sec (22 to 90 keas) in about 22 sec, with rotation at 18 sec at a speed of about 41.1 m/sec (80 keas). The results are shown in figure 83.

Experimental Fluid Data

Lift, drag, and pitching moment data for the experimental fluids on the flaps 5, sealed-slat configuration are shown in figures 84 to 91. The data are arranged by fluid. For a given fluid, the data are arranged in order of decreasing temperature.

Miscellaneous Data

Figure 92 to 96 show data for the following: (1) effect of initial fluid depth; (2) effect of time to rotation (fig. 93), (3) effect of rotation velocity; (4) gapped-slat data for the flaps 5 configuration; and (6) simulated frost data.

Test Technique Verification

Figure 97 shows results from runs made to verify the test technique of obtaining data over the entire angle of attack range in a single run. This was done for both the flaps 5, sealed-slat configuration and the flaps 15, gapped-slat configuration.

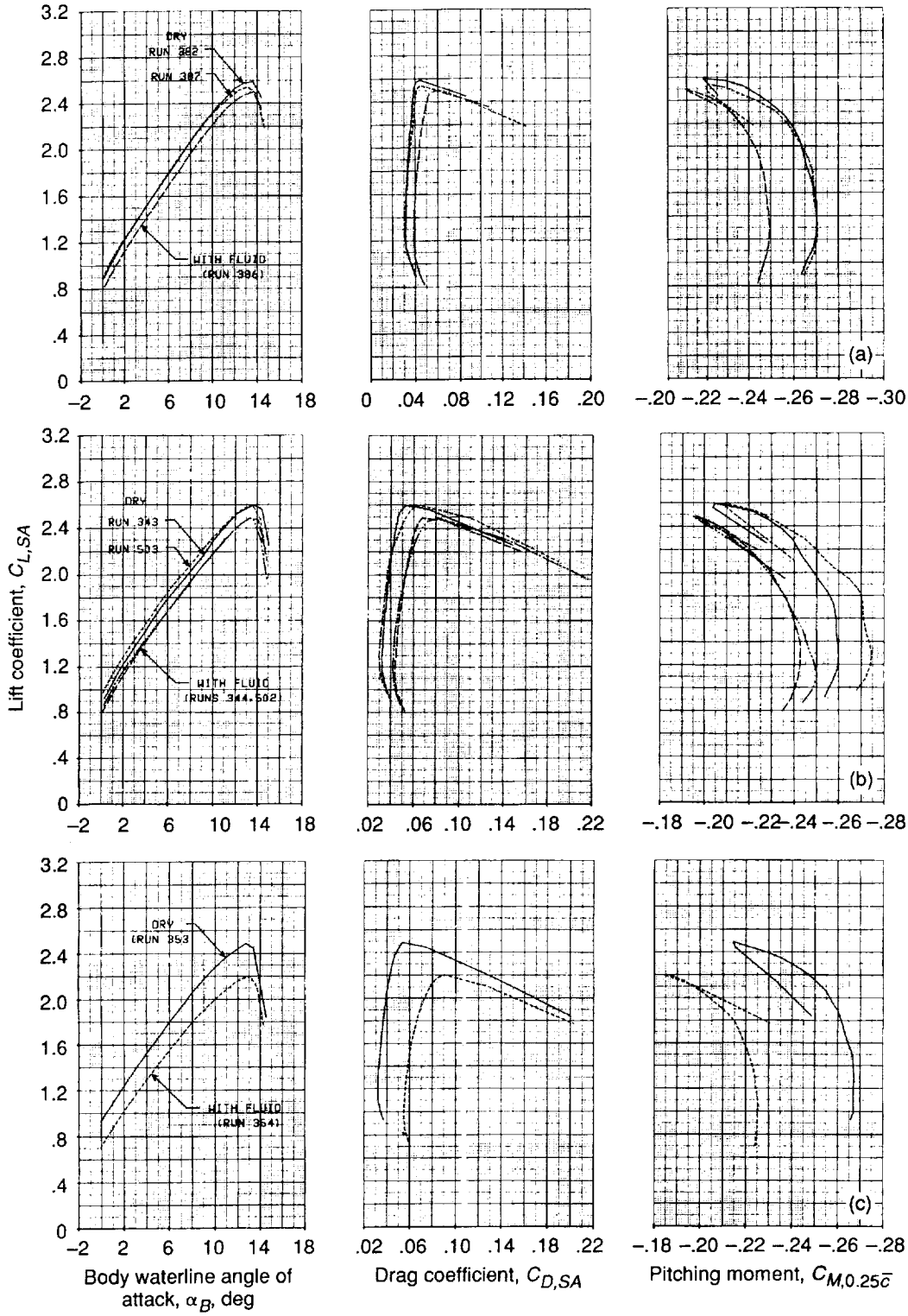

(a) Air temperature, –10 °C.

(b) Air temperature, –20 °C.

(c) Air temperature, –29 °C.

Figure 75.—Aerodynamic effects of fluid 1 on two-dimensional half model in flaps 5, sealed-slat configuration. Data corrected for dynamic q effects

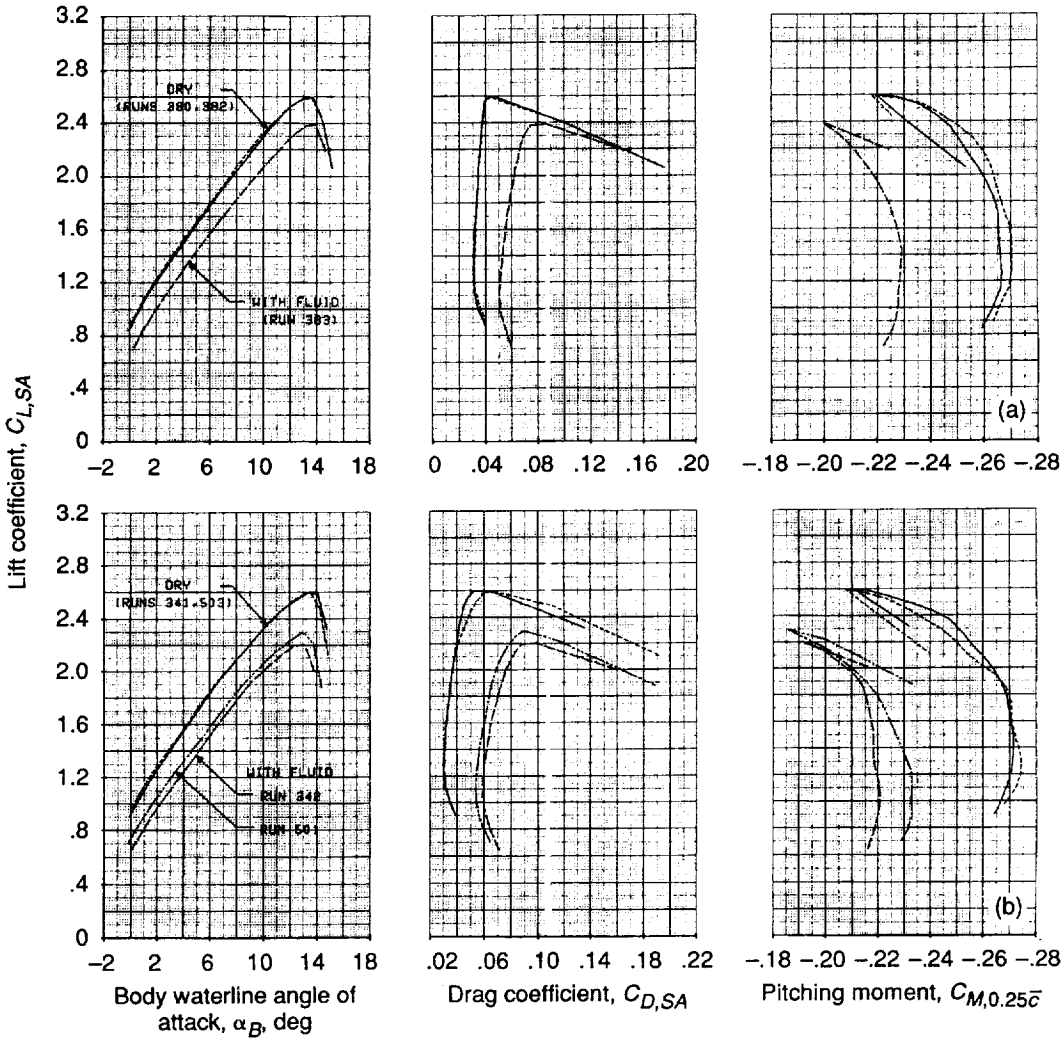

(a) Air temperature, –10 °C.

(b) Air temperature, –20 °C.

Figure 76.—Aerodynamic effects of fluid 2 on two-dimensional model in flaps 5, sealed-slat configuration. Data corrected for dynamic q effects.

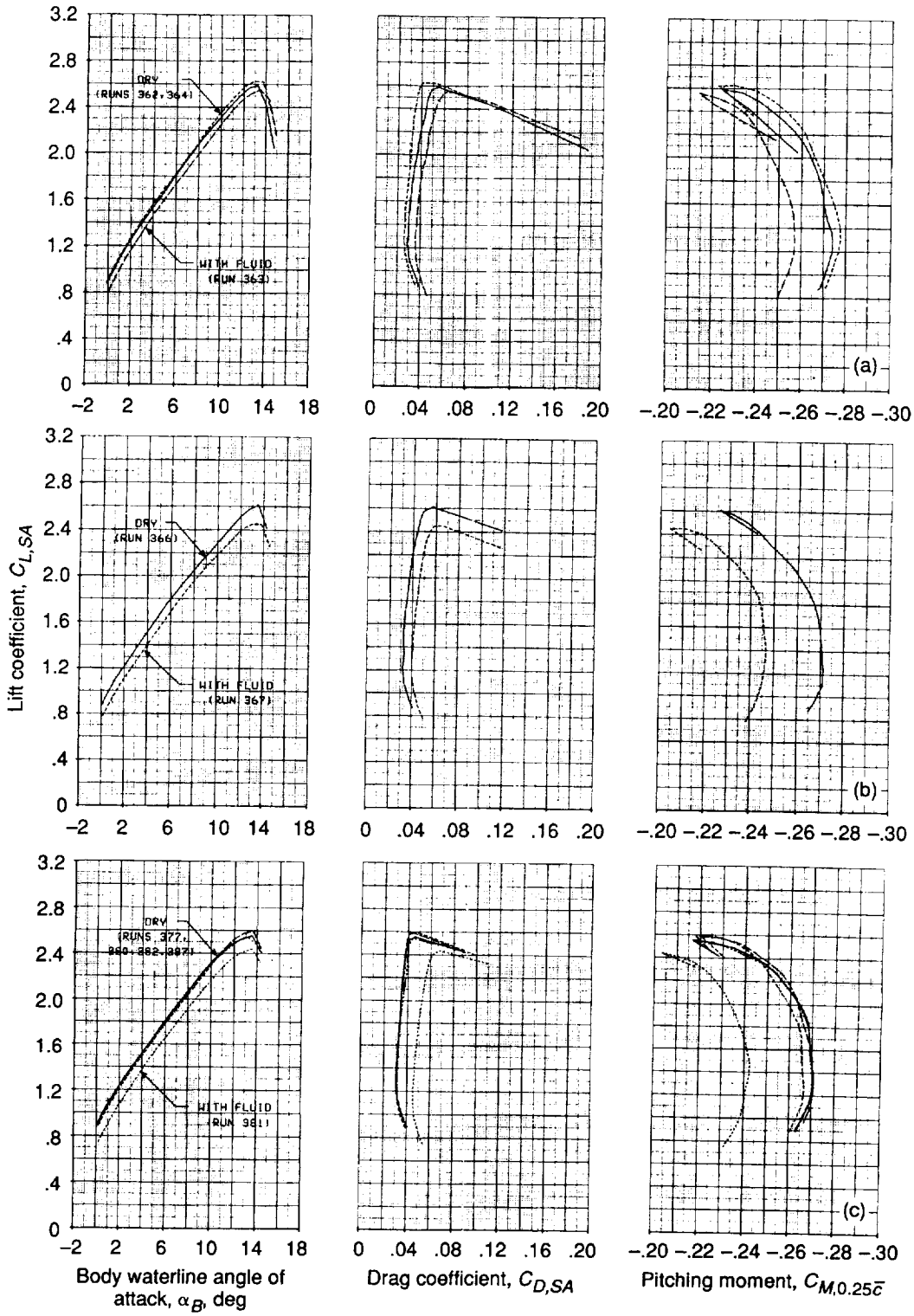

(a) Air temperature, −10 °C.

(b) Air temperature, 0 °C.

(c) Air temperature, −10 °C.

Figure 77.—Aerodynamic effects of fluid 3 on two-dimensional model in flaps 5, sealed-slat configuration. Data corrected for dynamic q effects

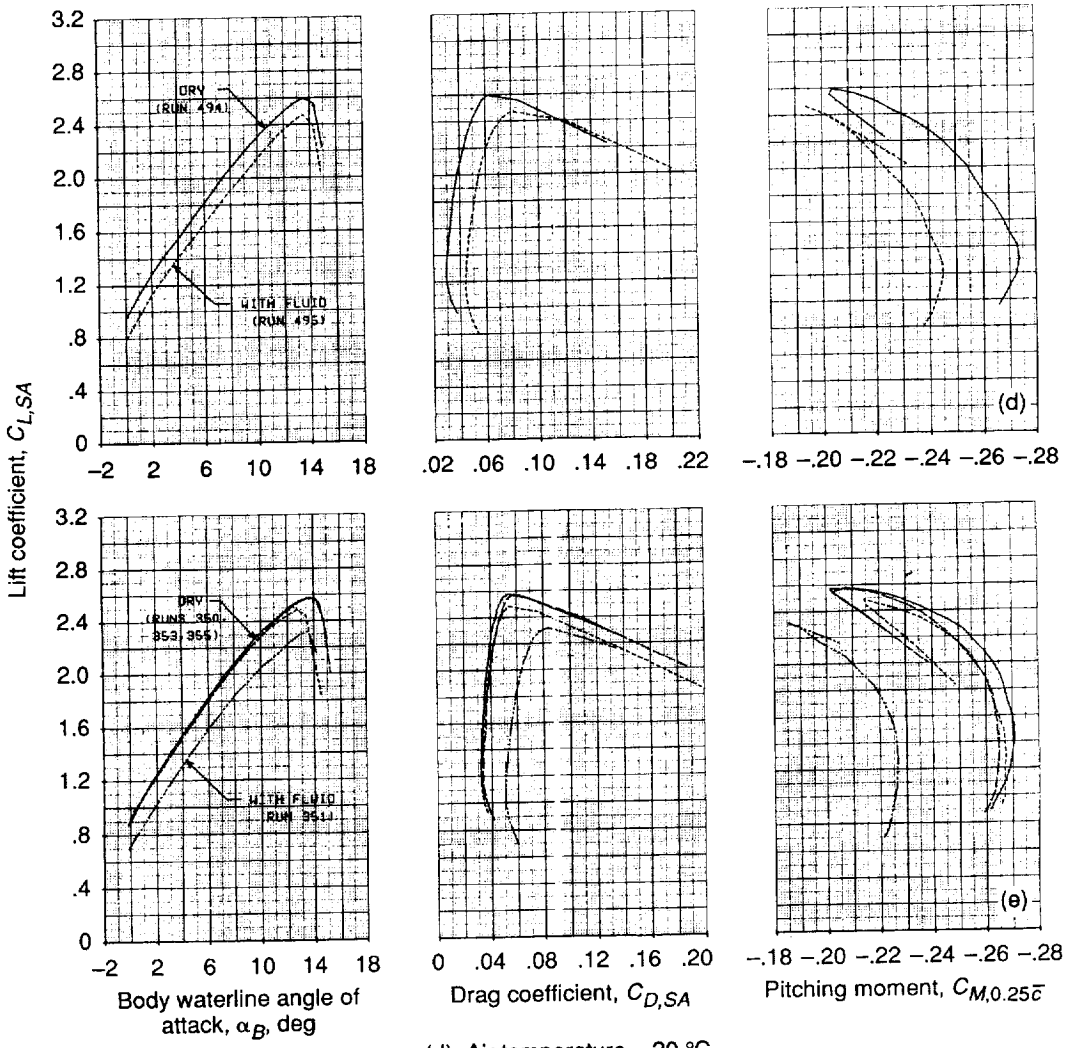

(d) Air temperature, –20 °C.

(e) Air temperature, –29 °C.

Figure 77.—Concluded.

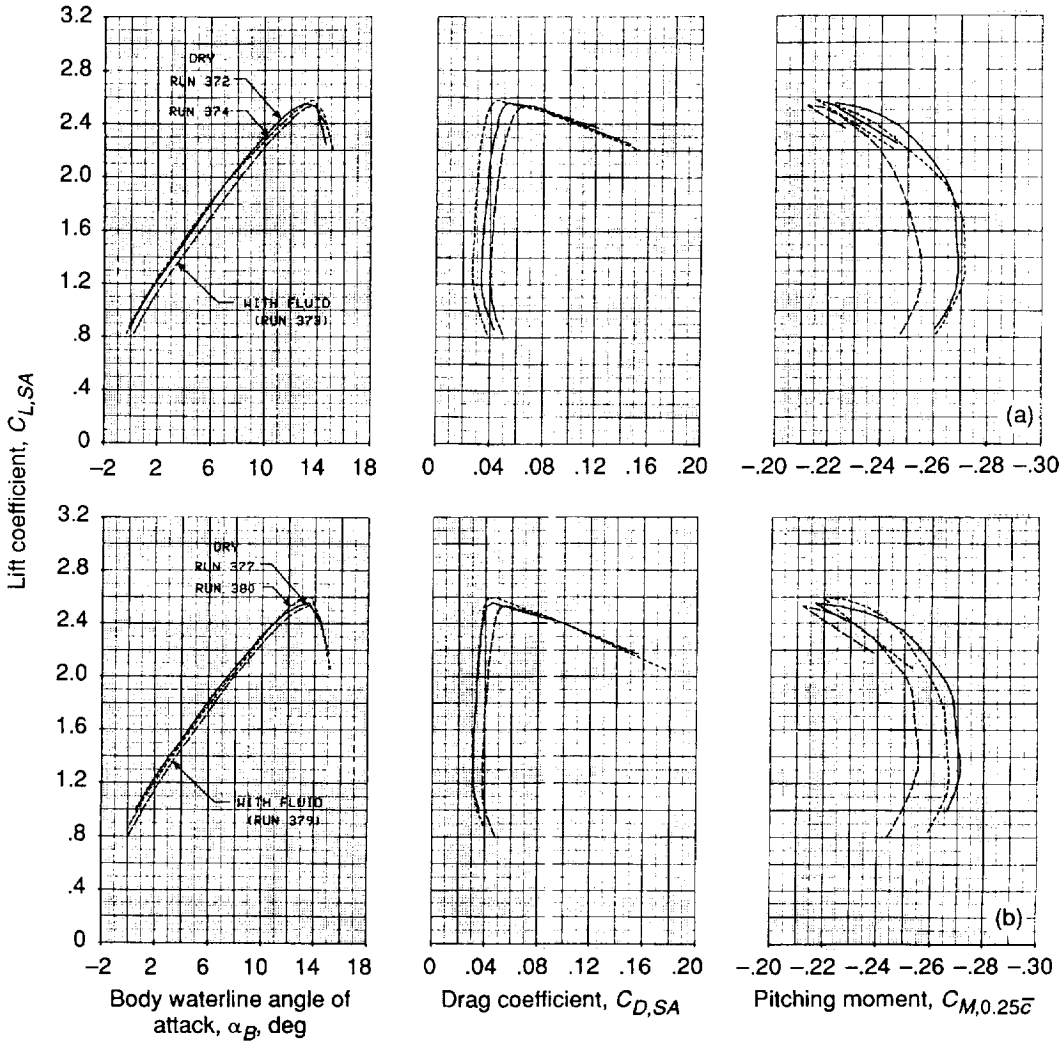

(a) Air temperature, –5 °C.

(b) Air temperature, –10 °C.

Figure 78.—Aerodynamic effects of fluid 4 on two-dimensional model in flaps 5, sealed-slat configuration. Data corrected for dynamic q effects.

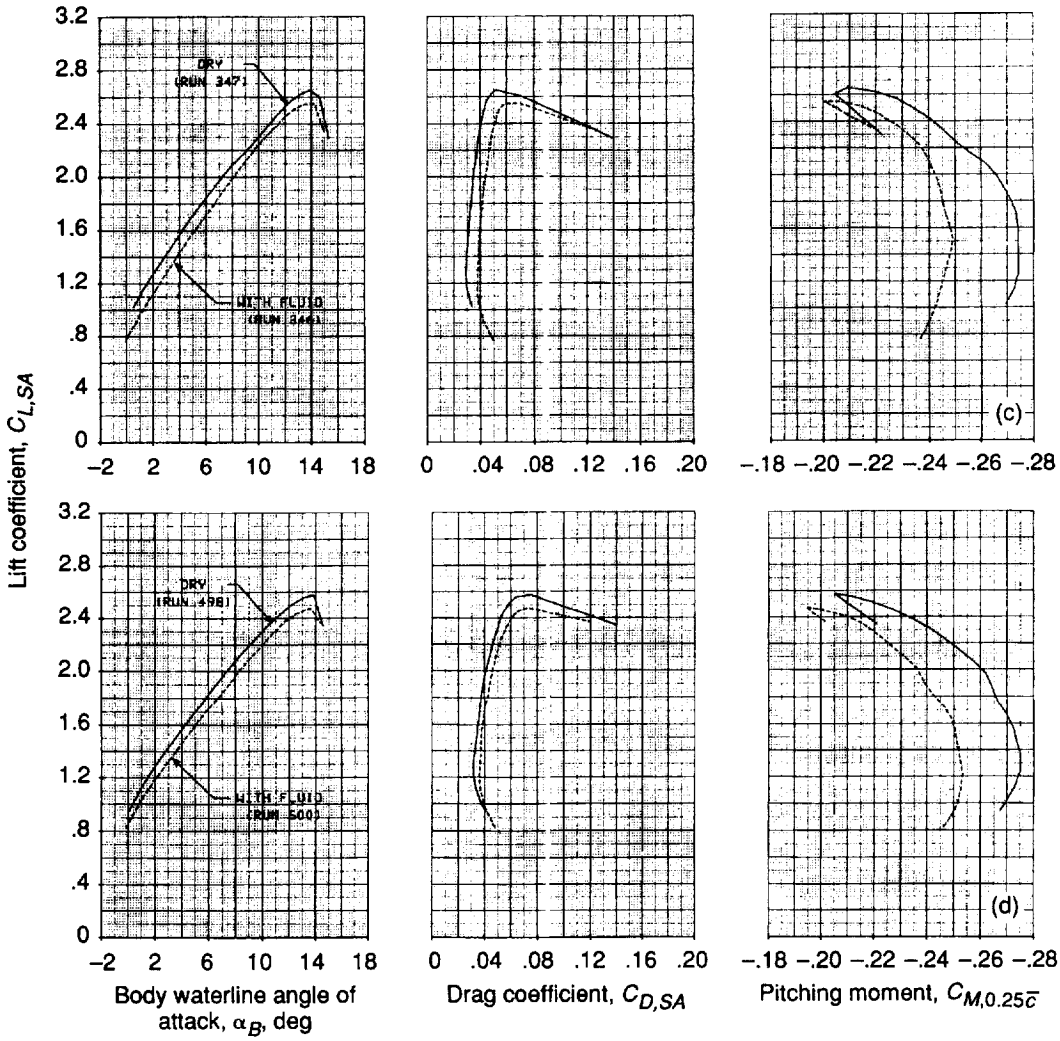

(c) Air temperature, –20 °C; runs 346 and 347.

(d) Air temperature, –20 °C; runs 498 and 500.

Figure 78.—Concluded.

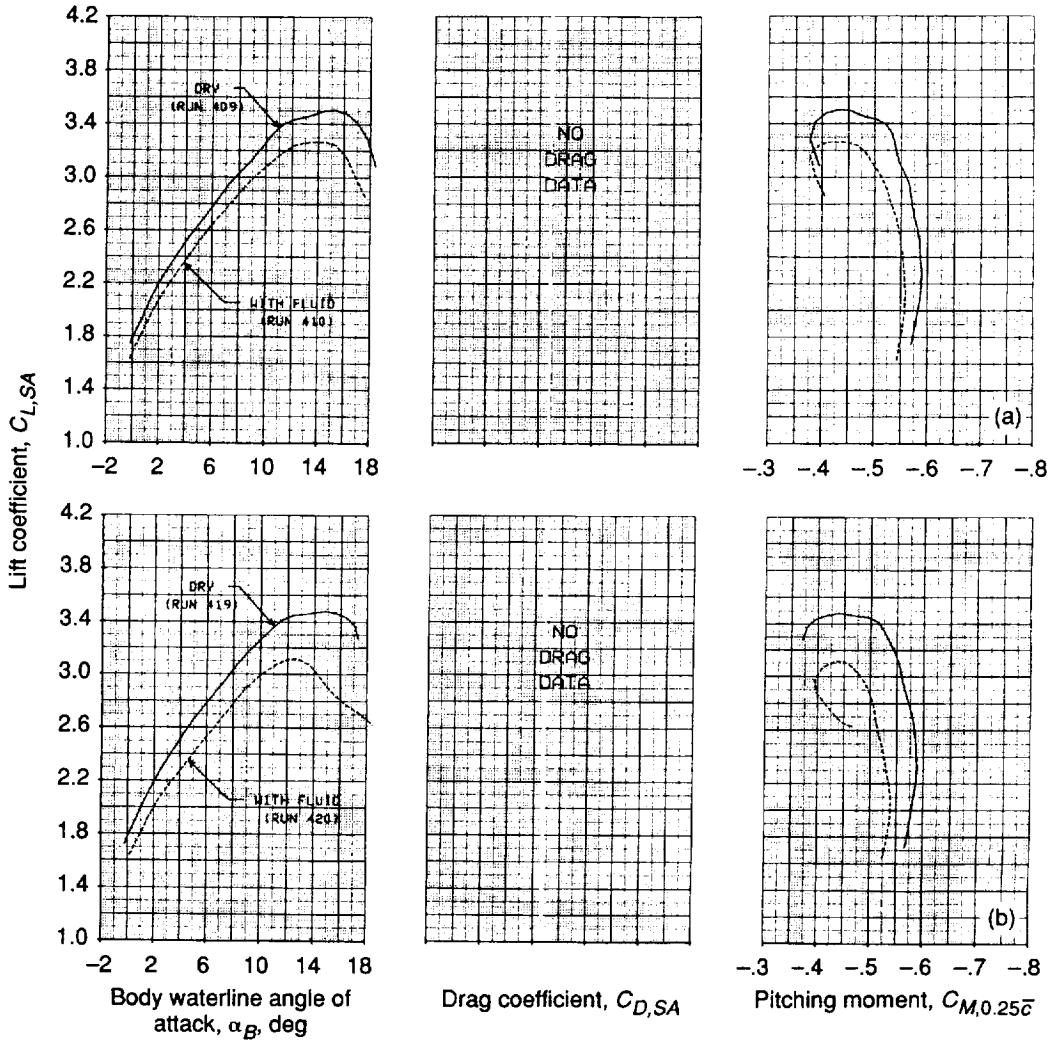

(a) Air temperature, −10 °C.

(b) Air temperature, −20 °C.

Figure 79.—Aerodynamic effects of fluid 1 on two-dimensional model in flaps 15, gapped-slat configuration. Data corrected for dynamic q effects.

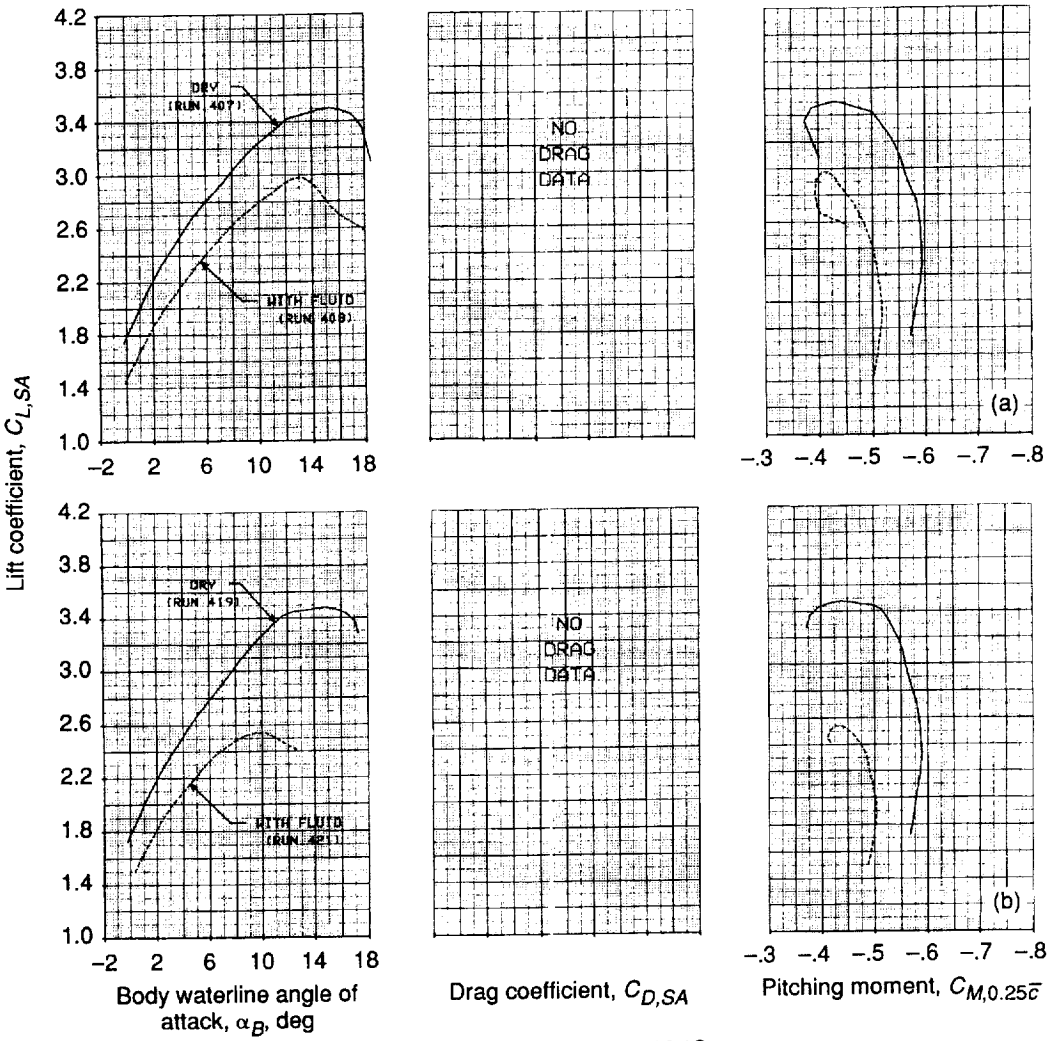

(a) Air temperature, −10 °C.

(b) Air temperature, −20 °C.

Figure 80.—Aerodynamic effects of fluid 2 on two-dimensional model in flaps 15, gapped-slat configuration. Data corrected for dynamic q effects.

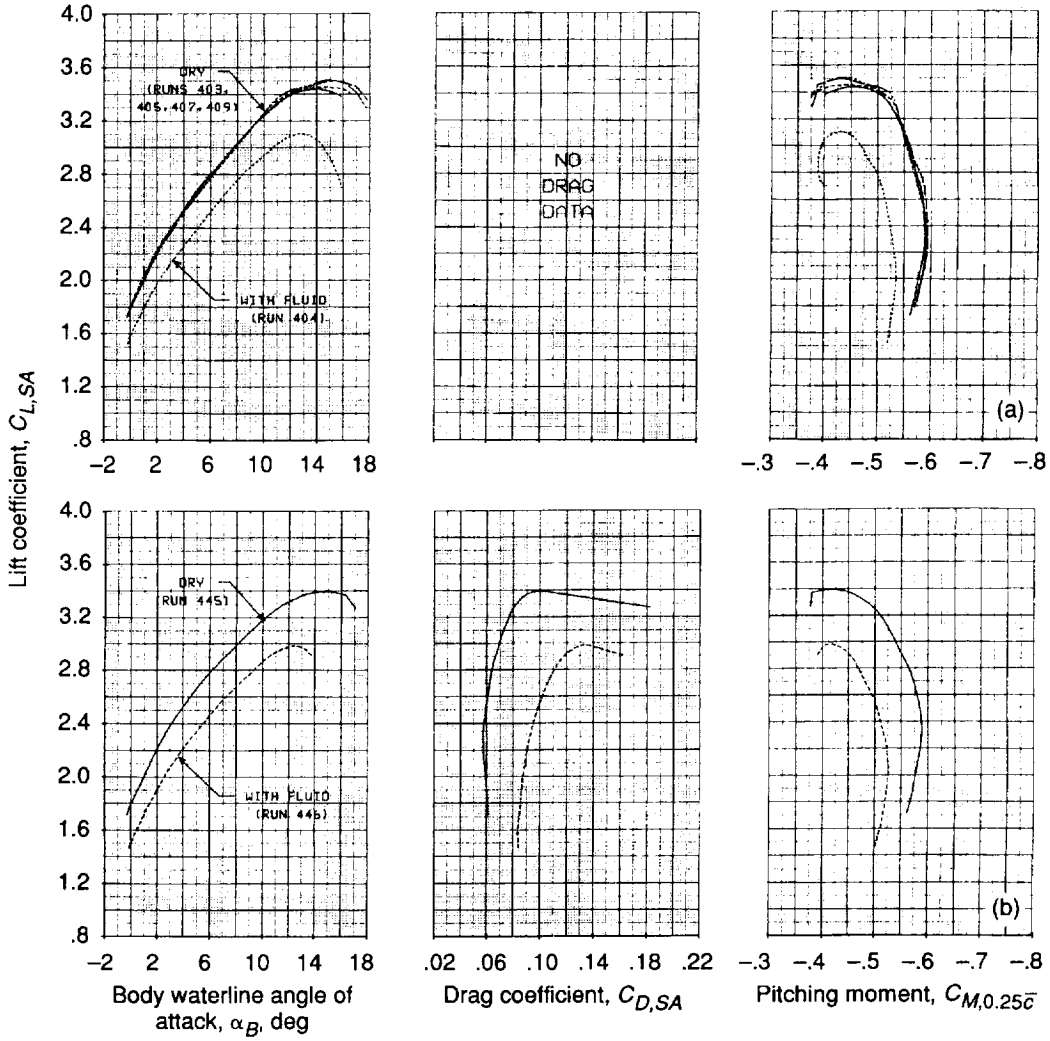

(a) Air temperature, −10 °C.

(b) Air temperature, −20 °C.

Figure 81.—Aerodynamic effects of fluid 3 on two-dimensional model in flaps 15, gapped-slat configuration. Data corrected for dynamic q effects.

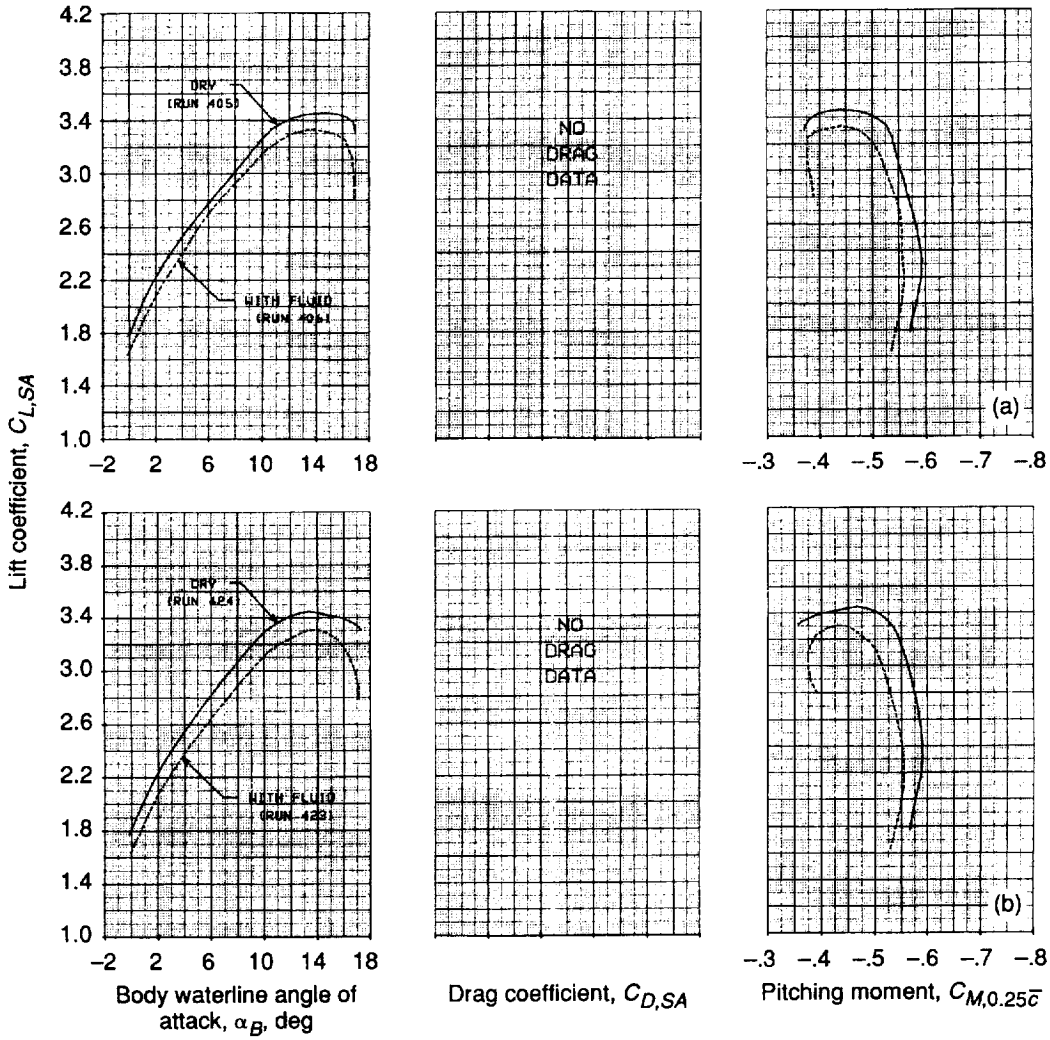

(a) Air temperature, −10 °C.

(b) Air temperature, −20 °C.

Figure 82.—Aerodynamic effects of fluid 4 on two-dimensional model in flaps 15, gapped-slat configuration. Data corrected for dynamic q effects.

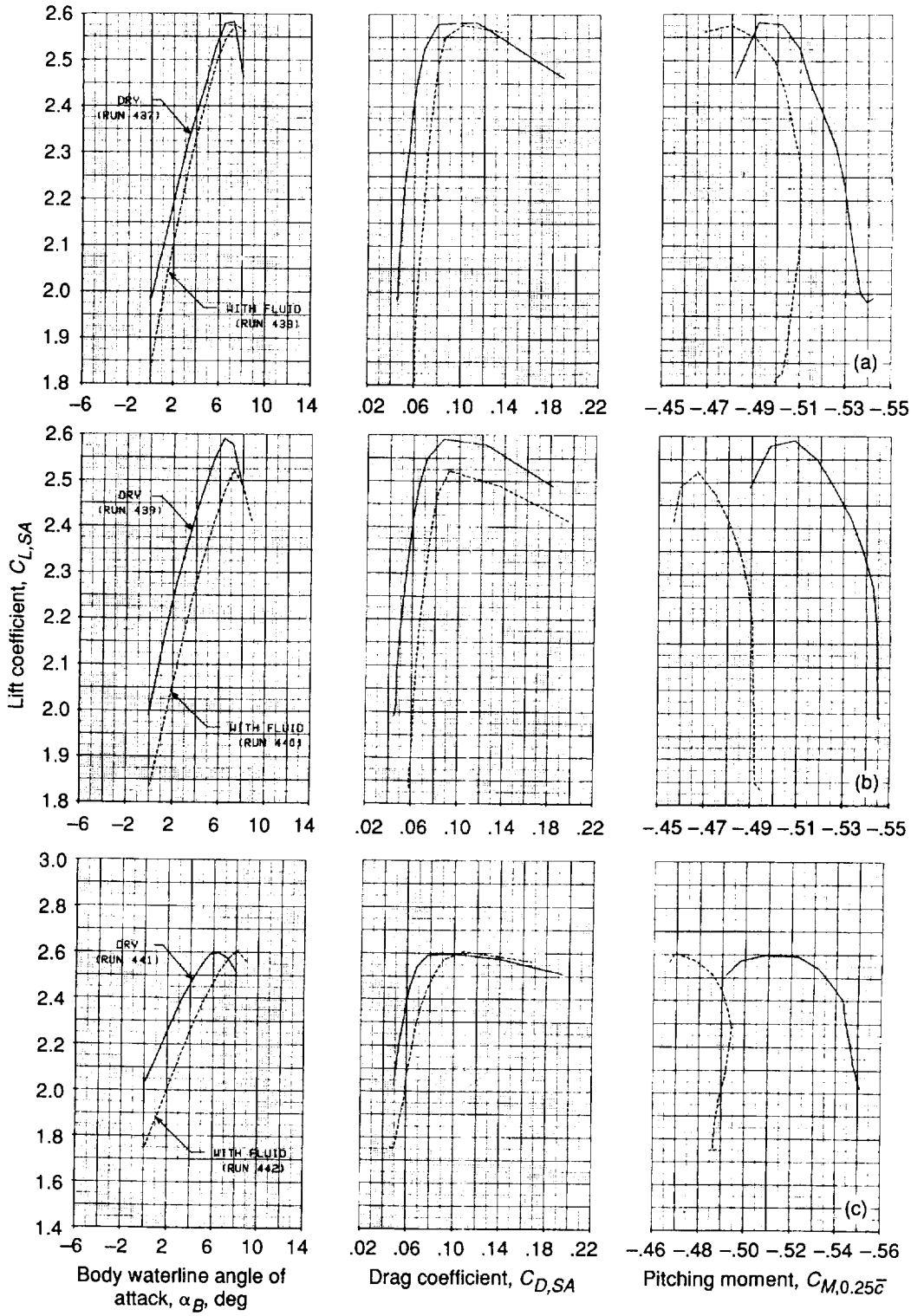

(a) Air temperature, 0 °C.

(b) Air temperature, –10 °C.

(c) Air temperature, –20 °C.

Figure 83.—Aerodynamic effects of fluid 3 on two-dimensional model in flaps 15, cruise leading-edge configuration. Data corrected for dynamic q effects

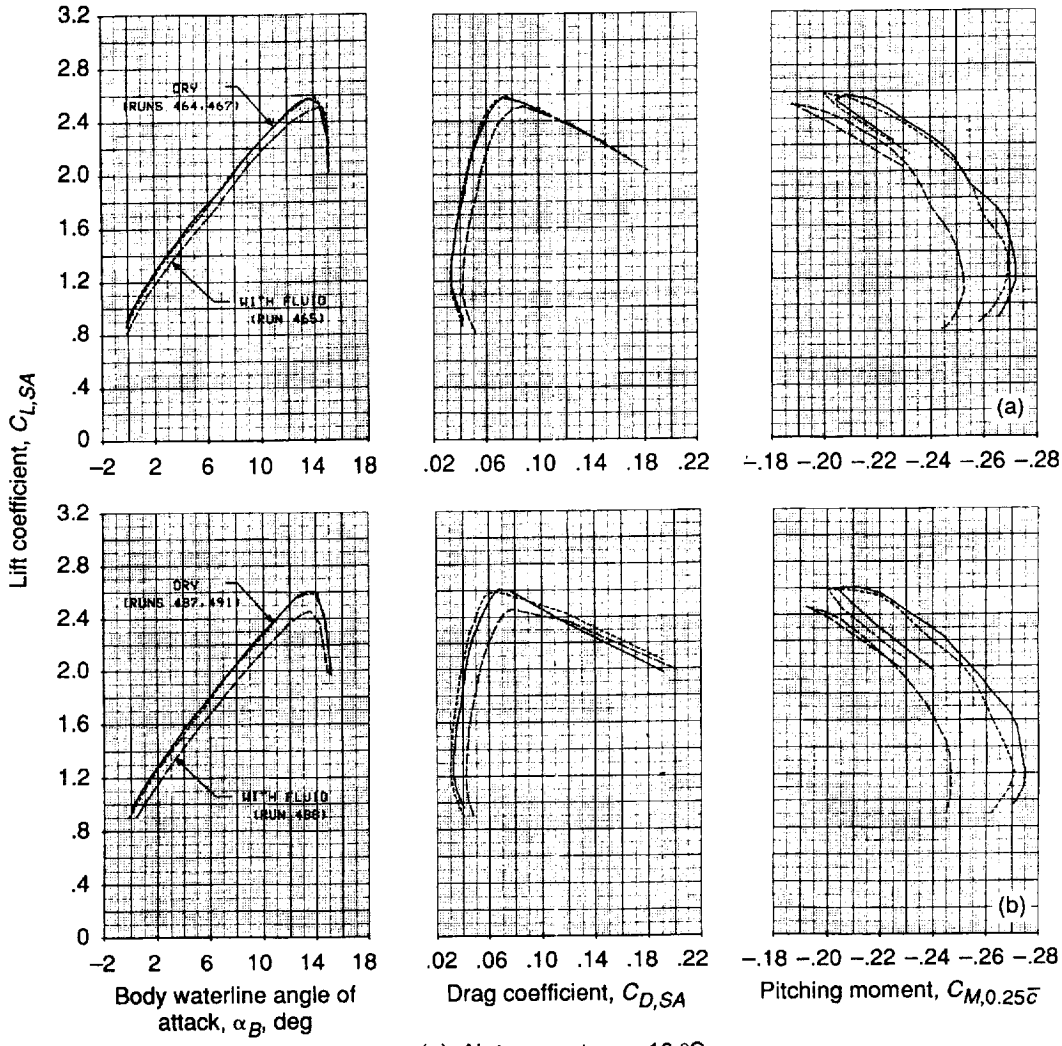

(a) Air temperature, –10 °C.

(b) Air temperature, –20 °C.

Figure 84.—Aerodynamic effects of fluid 2.1 on two-dimensional model in flaps 5, sealed-slat configuration. Data corrected for dynamic q effects.

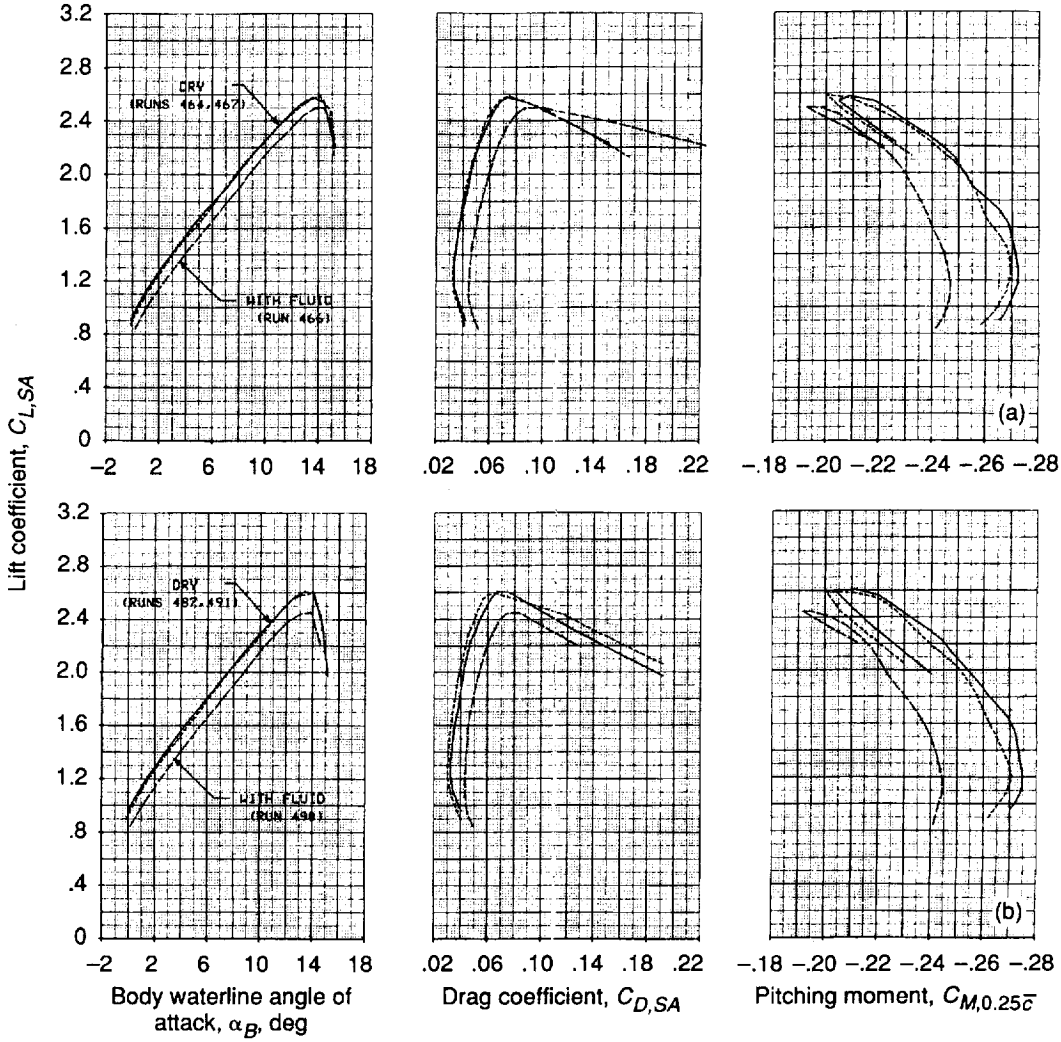

(a) Air temperature, –10 °C.

(b) Air temperature, –20 °C.

Figure 85.—Aerodynamic effects of fluid 2.2 on two-dimensional model in flaps 5, sealed-slat configuration. Data corrected for dynamic q effects.

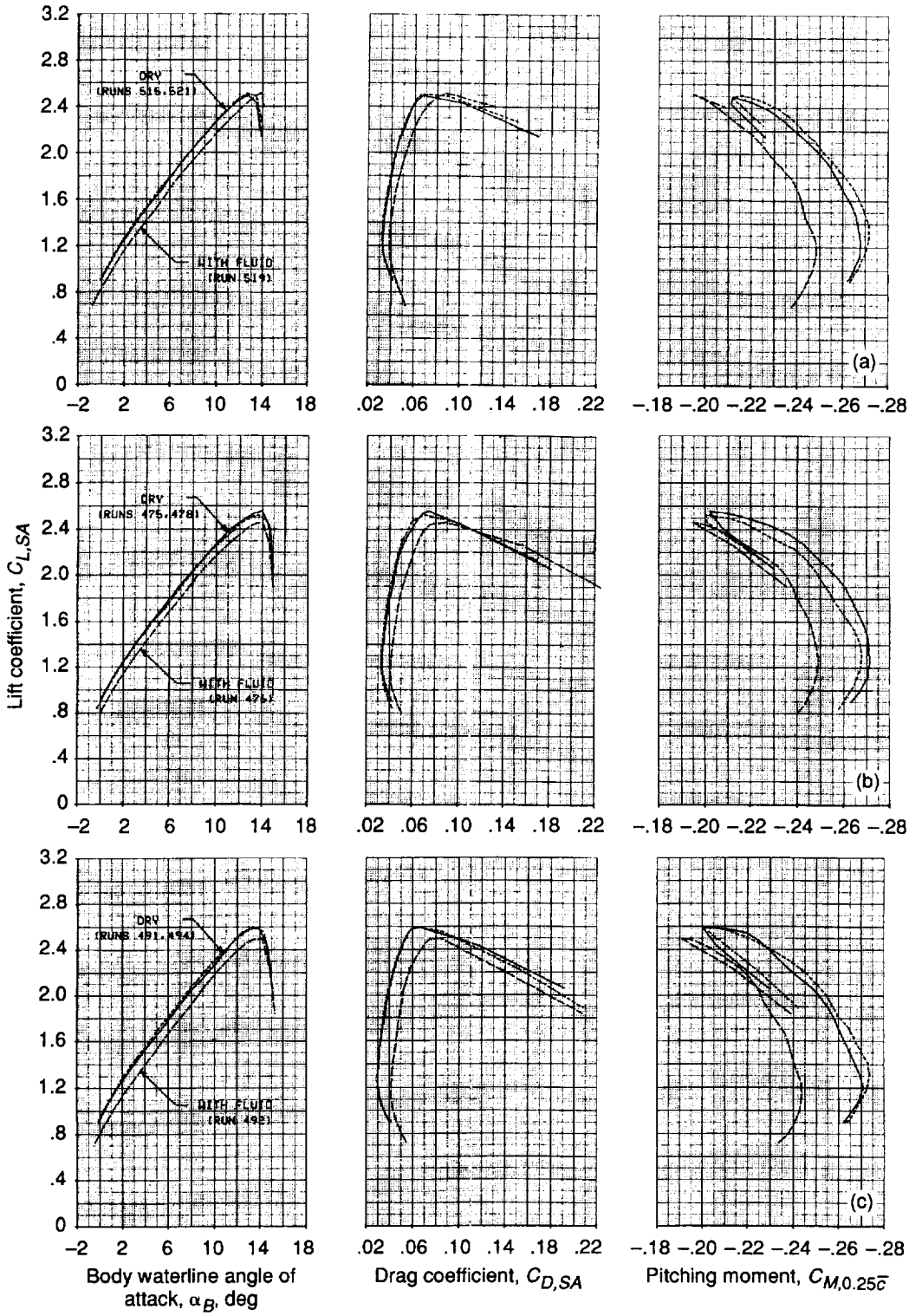

(a) Air temperature, 0 °C.
(b) Air temperature, −10 °C.
(c) Air temperature, −20 °C.

Figure 86.—Aerodynamic effects of fluid 3.1 on two-dimensional model in flaps 5, sealed-slat configuration. Data corrected for dynamic q effects.

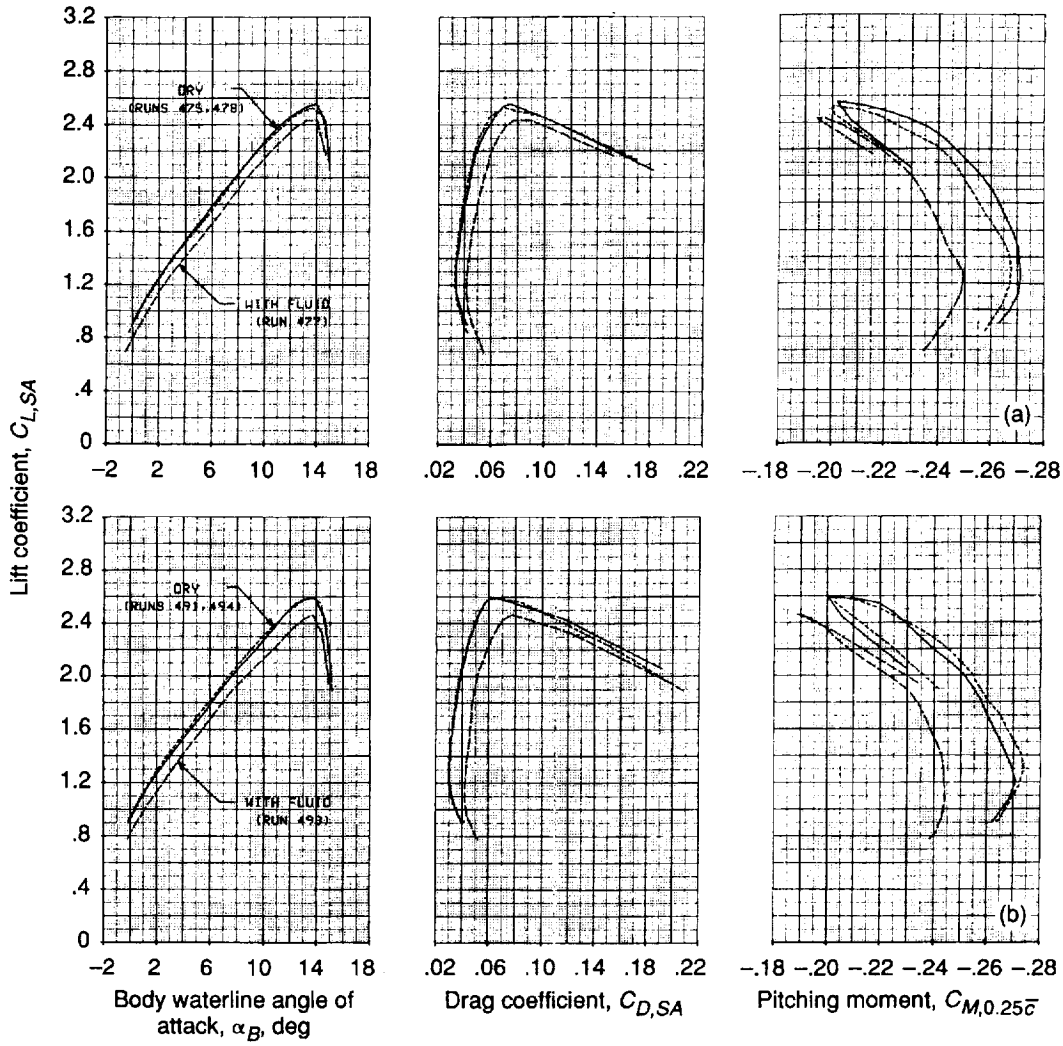

(a) Air temperature, −10 °C.

(b) Air temperature, −20 °C.

Figure 87.—Aerodynamic effects of fluid 3.2 on two-dimensional model in flaps 5, sealed-slat configuration. Data corrected for dynamic q effects.

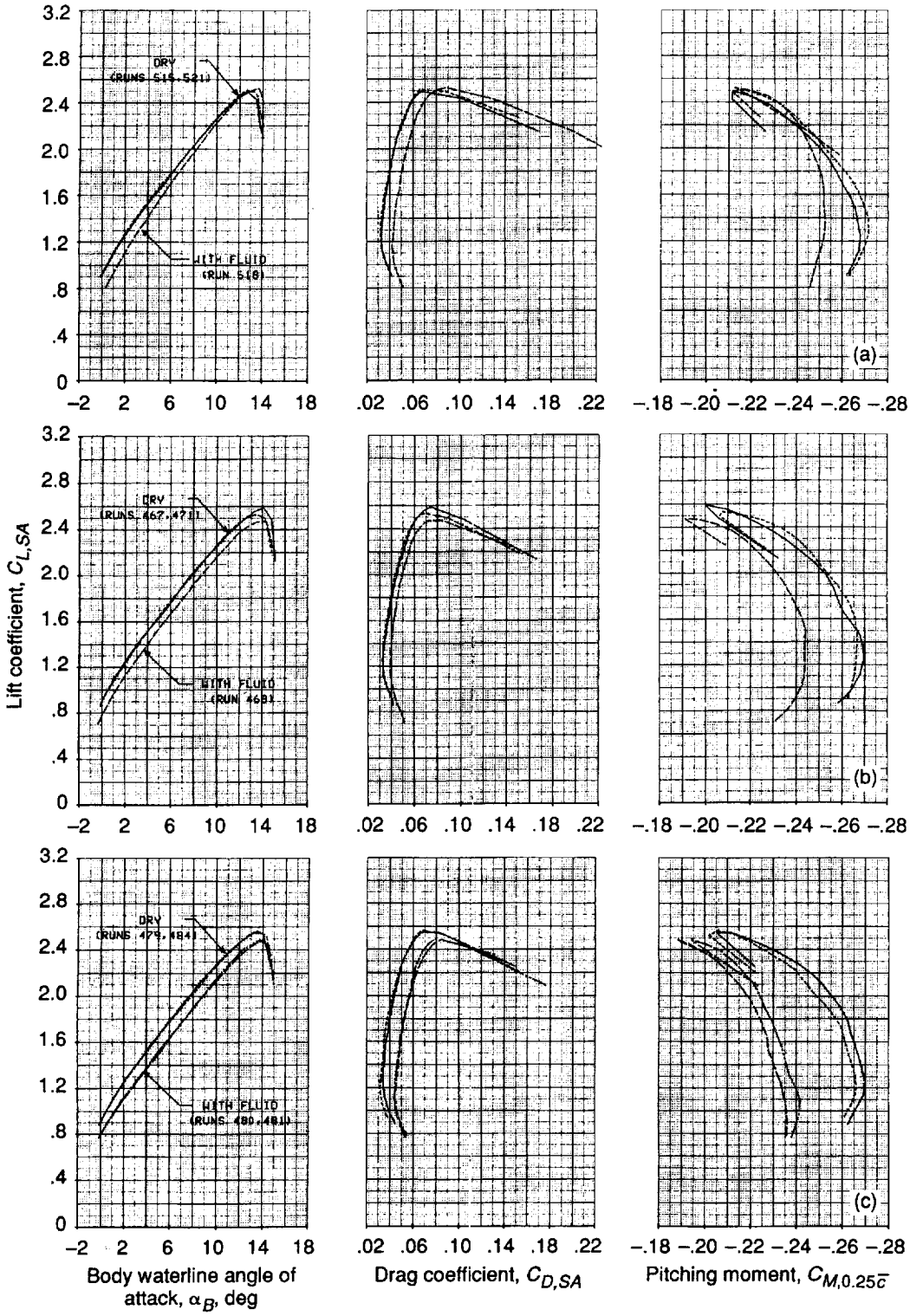

(a) Air temperature, 0 °C.
(b) Air temperature, −10 °C.
(c) Air temperature, −20 °C.

Figure 88.—Aerodynamic effects of fluid 4.1 on two-dimensional model in flaps 5, sealed-slat configuration. Data corrected for dynamic q effects.

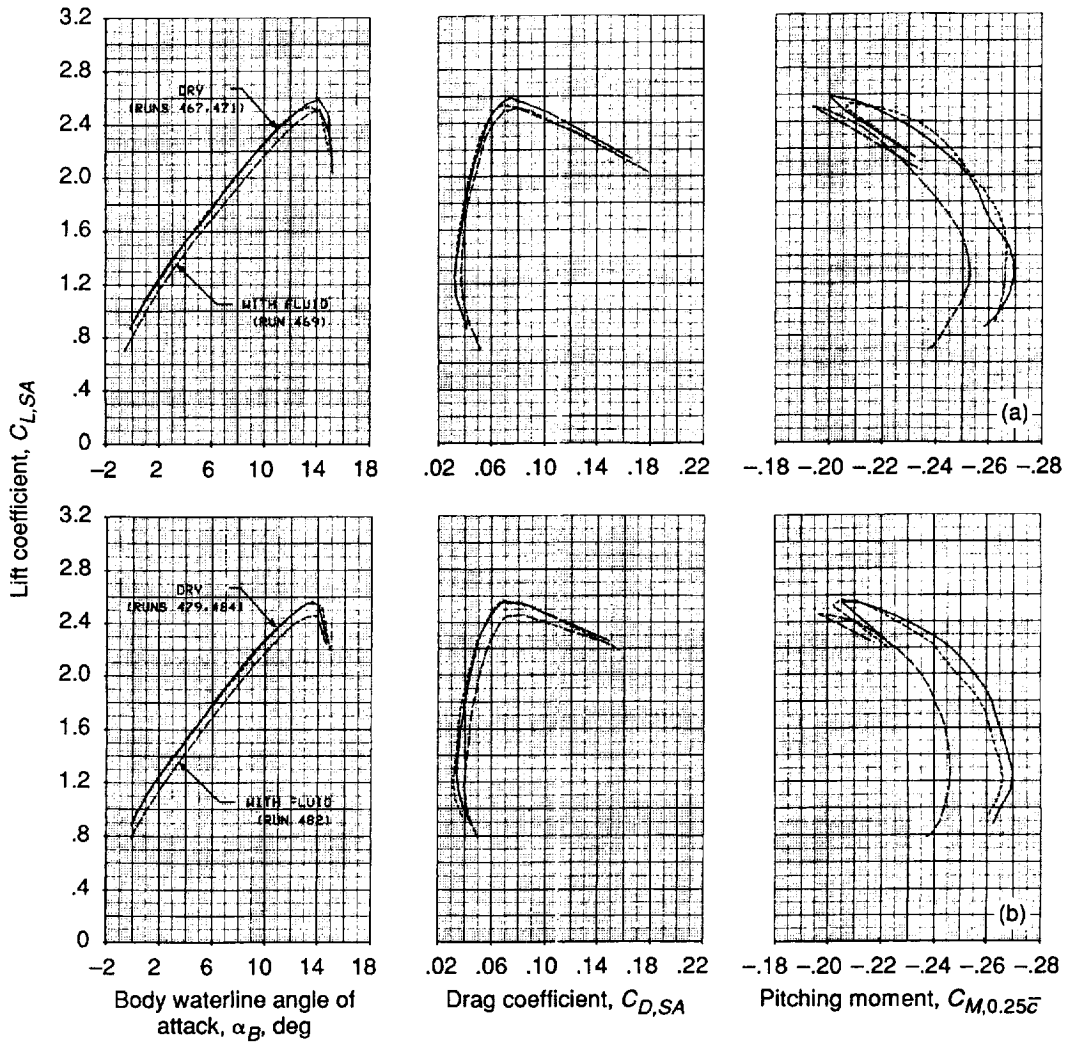

(a) Air temperature, –10 °C.

(b) Air temperature, –20 °C.

Figure 89.—Aerodynamic effects of fluid 4.2 on two-dimensional model in flaps 5, sealed-slat configuration. Data corrected for dynamic q effects.

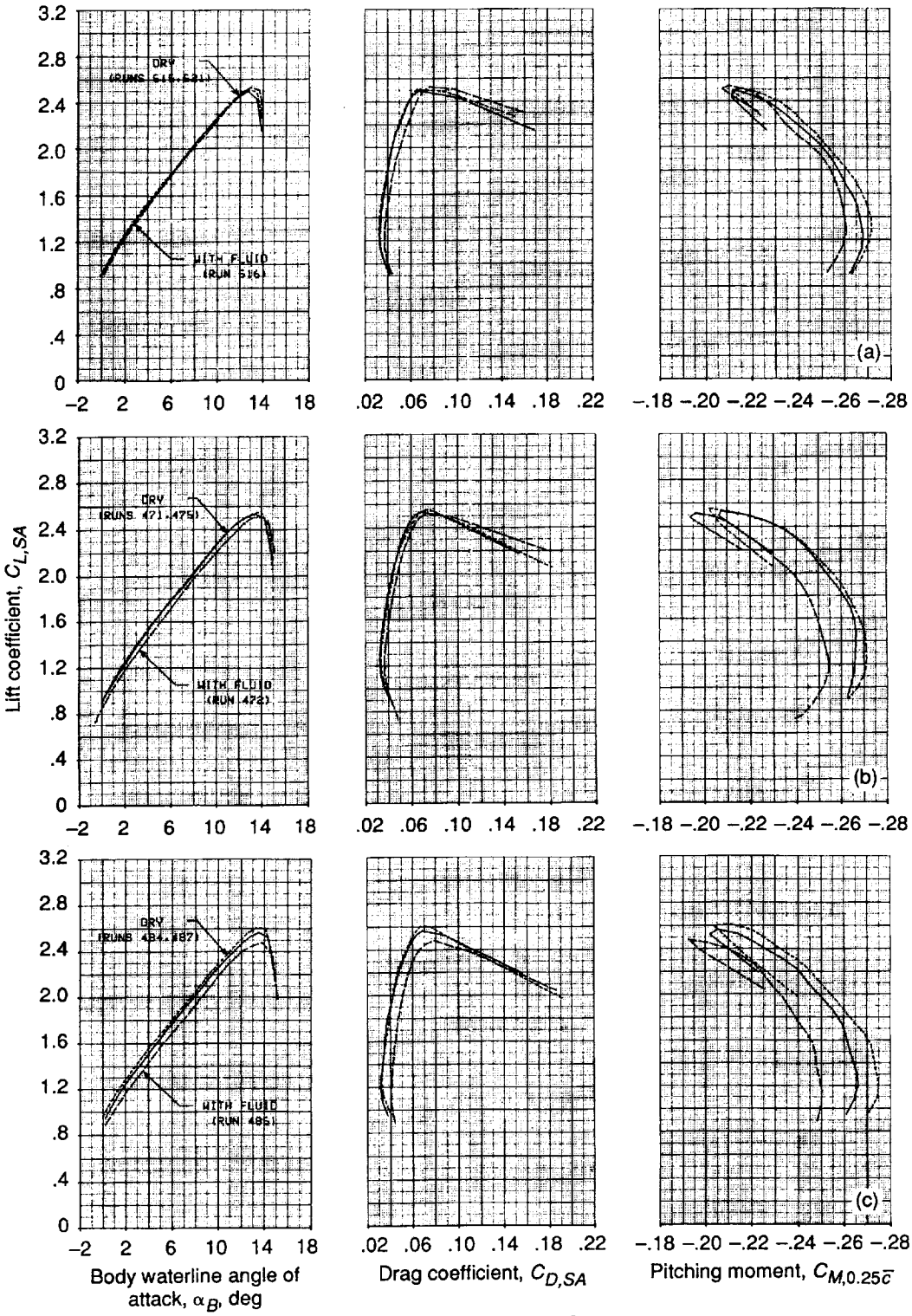

(a) Air temperature, 0 °C.
(b) Air temperature, –10 °C.
(c) Air temperature, –20 °C.

Figure 90.—Aerodynamic effects of fluid 5.1 on two-dimensional model in flaps 5, sealed-slat configuration. Data corrected for dynamic q effects.

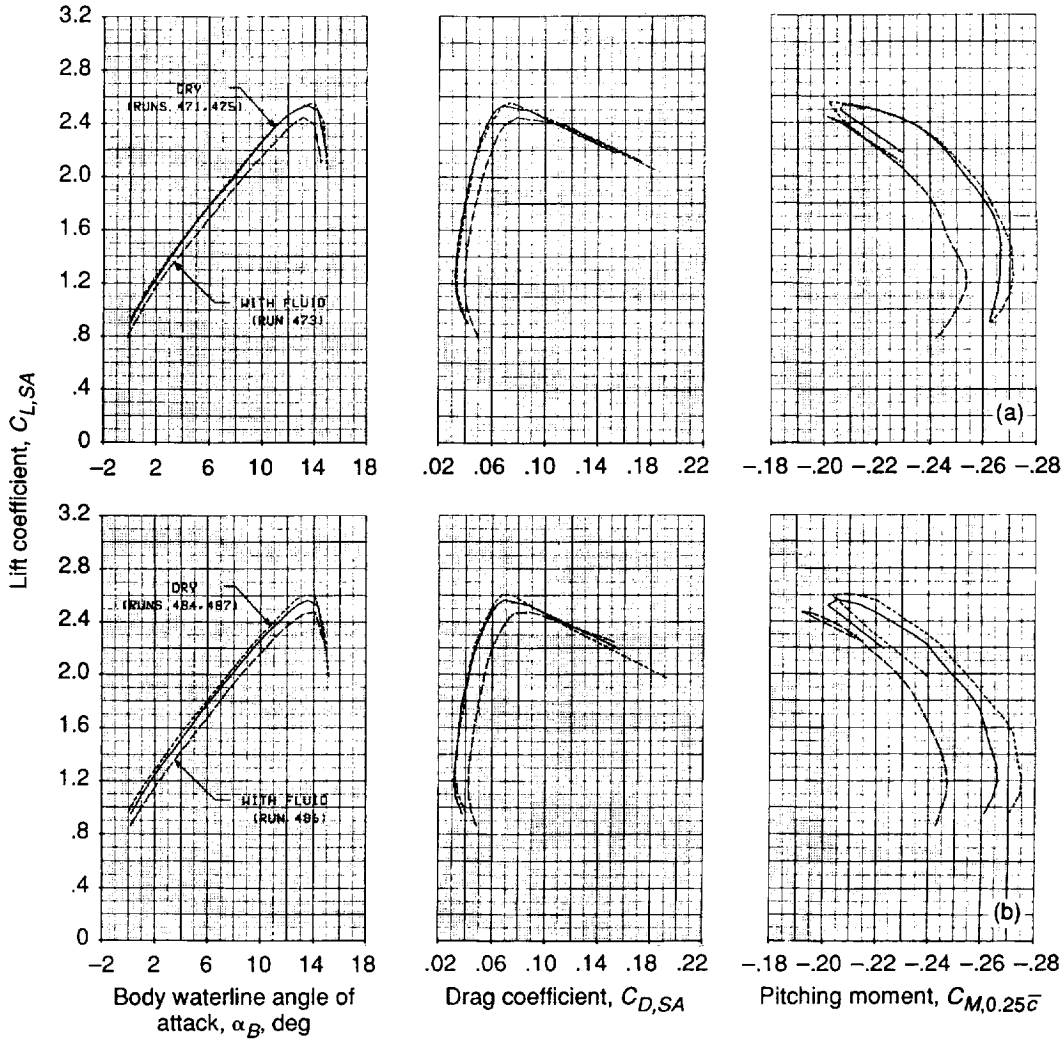

(a) Air temperature, −10 °C.

(b) Air temperature, −20 °C.

Figure 91.—Aerodynamic effects of fluid 5.2 on two-dimensional model in flaps 5, sealed-slat configuration. Data corrected for dynamic q effects.

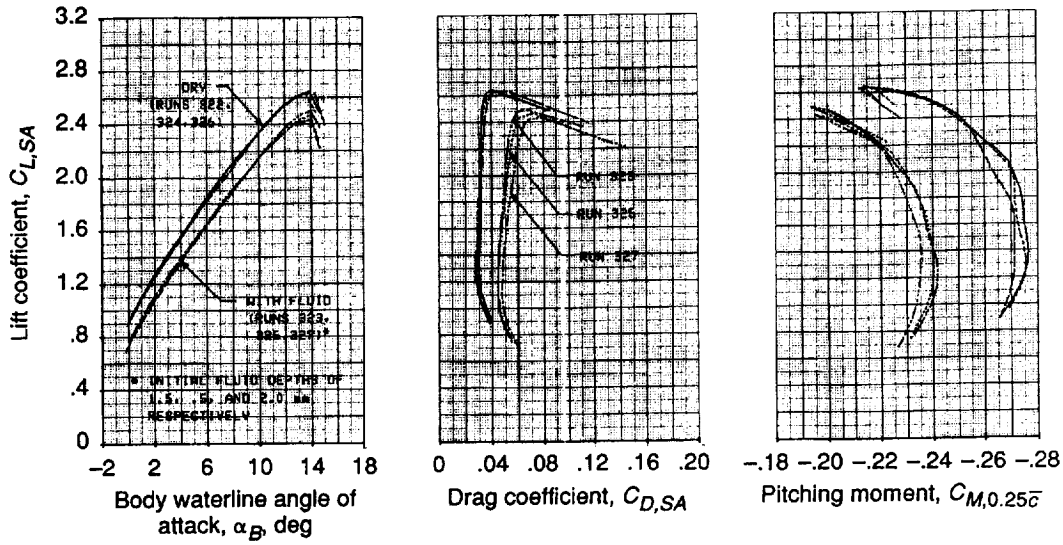

Figure 92.—Aerodynamic effects of initial fluid depth of fluid 3 on two-dimensional model in flaps 5, sealed-slat configuration. Air temperature, −20 °C; data corrected for dynamic q effects.

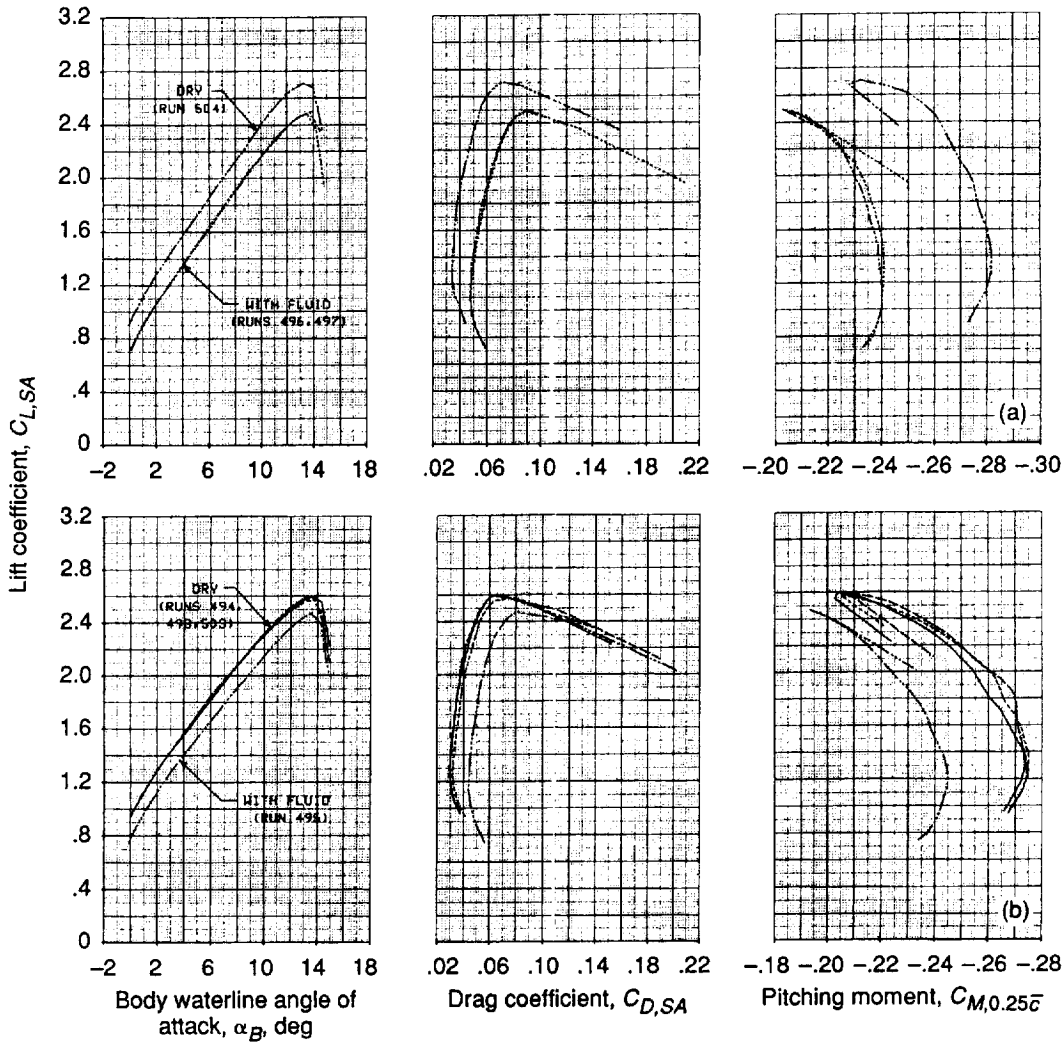

(a) Time to rotation, 20 sec.

(b) Time to rotation, 25 sec.

Figure 93.—Aerodynamic effects of time to rotation and fluid 3 on two-dimensional model in flaps 5, sealed-slat configuration. Data corrected for dynamic q effects.

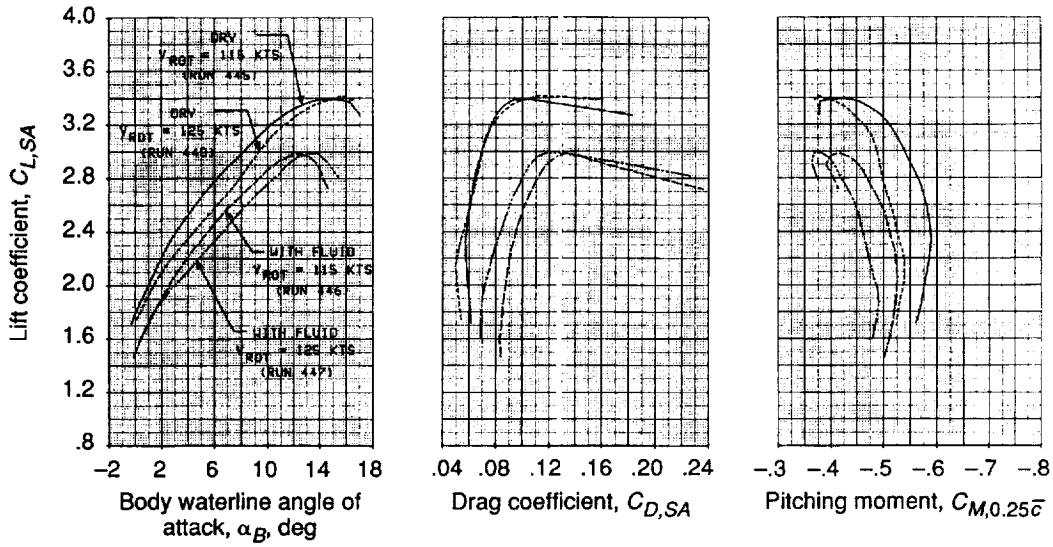

Figure 94.—Aerodynamic effects of velocity at rotation and fluid 3 on two-dimensional model in flaps 15, gapped-slat configuration. Air temperature, –20 °C; data corrected for dynamic q effects.

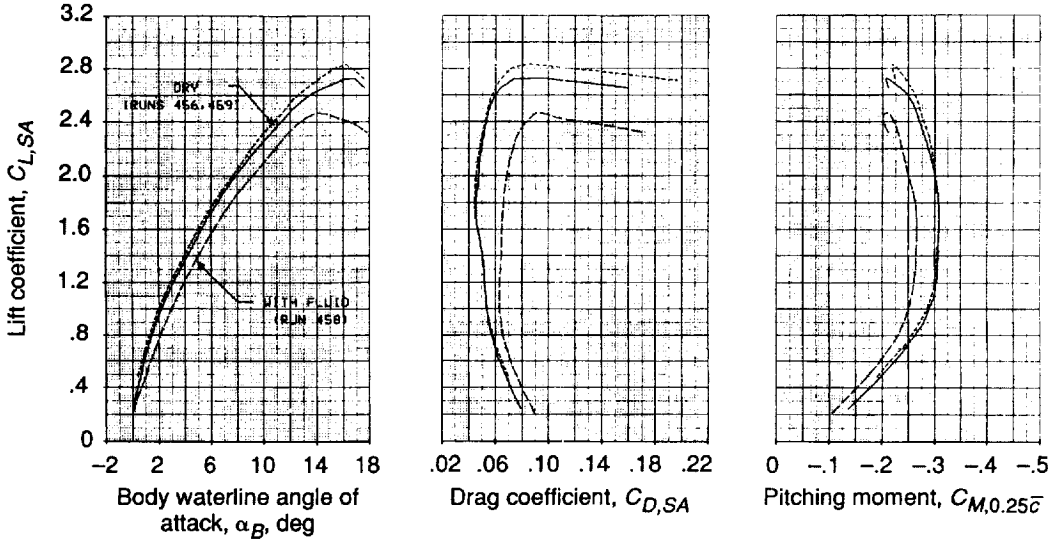

Figure 95.—Aerodynamic effects of fluid 3 on two-dimensional model in flaps 5, gapped-slats configuration. Air temperature, –20 °C; data corrected for dynamic q effects.

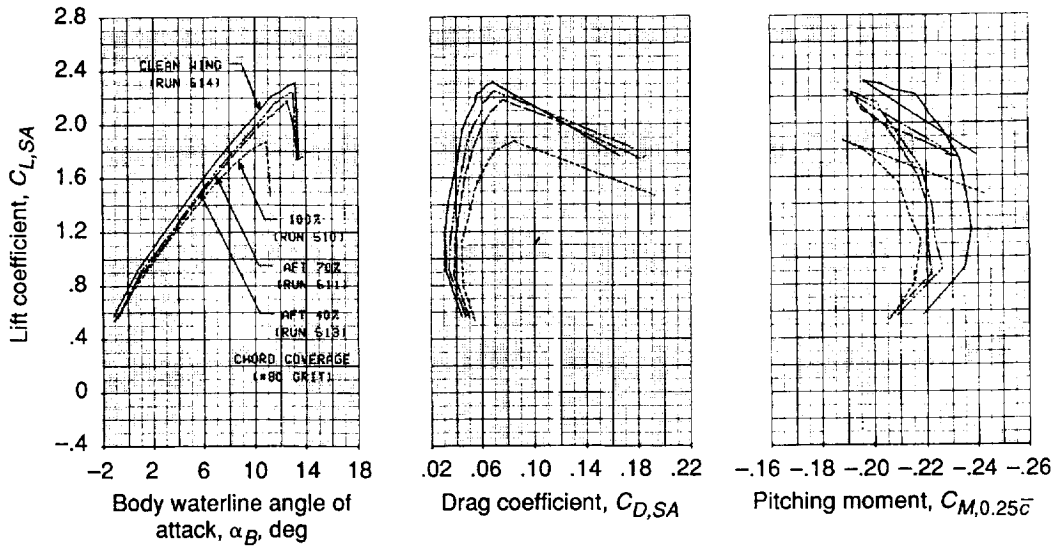

Figure 96.—Aerodynamic effects of simulated frost and chord coverage on two-dimensional model in flaps 5, sealed-slats configuration. Ambient temperature; data corrected for dynamic q effects.

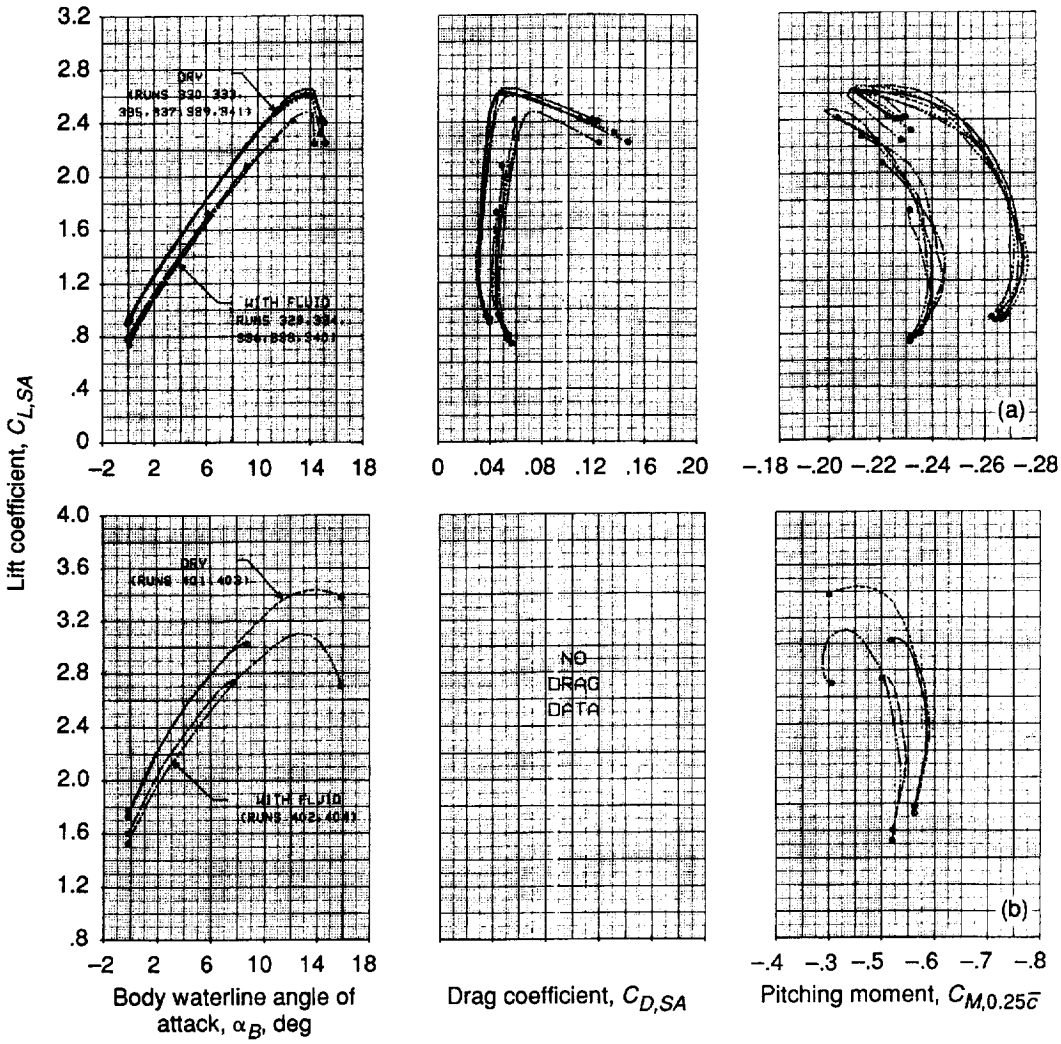

(a) Flaps 5, sealed-slat configuration; temperature, −20 °C.

(b) Flaps 15, gapped-slat configuration; temperature, −10 °C.

Figure 97.—Test technique verification for two-dimensional model with fluid 3. Data corrected for dynamic q effects.

Appendix D

Fluid Depth and Wave Data

This appendix contains the results of the ultraviolet fluorescence photography technique. The key features of the technique were as follows:

(1) A 0.005 percent concentration of Rhodamine 6G fluorescent dye was added to each of the fluids.

(2) A 70-mm Hasselblad camera with a Kodak Wratten 2E Ultraviolet barrier filter was mounted in the ceiling of the tunnel, directly above the model. Black and white film was used because it provides better resolution.

The ultraviolet barrier filter blocked out the ultraviolet light and admitted the fluorescent light emitted by the dye in the fluid. The brightness of the fluorescent light emitted by the fluid increases with increasing fluid depth, since the light is emitted by the fluid at all depths. This brightness was calibrated against fluid depth using the calibration plate discussed below.

(3) Two 2000-W sec strobe lights with ultraviolet exciter filters were mounted directly above the model, one at each end of the span.

(4) In order to get a continuous record of the fluid flowoff, a video camera was mounted in the tunnel ceiling above the model. Video tape recordings were made for each of the fluid runs.

(5) An ELC 4000 light source with an ultraviolet exciter filter was also mounted in the tunnel ceiling to provide a continuous source of ultraviolet light for the video camera. Figure 98 is a photograph (taken from above) of the lights and cameras mounted on the tunnel ceiling.

(6) Photographs were taken in synchronization with the ultraviolet strobe lights every 2 sec during each run.

(7) A calibration plate with grooves of various depths was filled with fluid and photographed before each run. The calibration plate details are shown in figure 99.

(8) After the test, a scanning microdensitometer was used to measure the optical density of the photographic negatives corresponding to a specified location on the model. By doing this also for the calibration plate photographic negative, the correspondence between optical density and fluid depth for a given run could be determined. In this manner, fluid depth (including waves) was determined as a function of model chordwise location.

Since photographs were taken every 2 sec during each run, a large number of photographs were taken for the entire test. Only key cases at certain times were analyzed on the microdensitometer. For most cases three times were chosen for analysis: (1) approximately 10 sec after the start of tunnel acceleration; (2) just before rotation; and (3) 2 to 4 sec after the start of rotation.

Two-dimensional Model Results

Fluids 1 to 4.—Figures 100 to 103 show the fluid depth profiles for all four of the basic fluids on the two-dimensional model in the flaps 5, sealed-slat configuration at −20 °C. The corresponding wave patterns were shown in figures 51 to 54. In figure 51 the photographs of fluid 1 are shown on the right and the corresponding fluid depth profiles are shown on the left. In the photographs, increased fluorescence corresponds to increased fluid depth. In some cases it may be noticed that the average fluid depth in the fluid depth profile at the earliest time shown (usually 10 sec) appears to be significantly deeper than the initial depth noted in the plot. This initial depth was measured manually at approximately 50 percent chord before the run. This apparent discrepancy is primarily a result of the details of the fluid distribution along the chord at the time the manual depth measurement was made. In some cases the single 50 percent chord depth measurement was not a good average value for the entire chord.

Figures 100(a) to (c) are larger scale versions of the three fluid depth profile plots shown in figure 51. Each contains an inset showing a blow-up of the region from approximately 50 to 55 percent chord. The noise level for this technique was estimated to be about 0.1 mm (0.004 in.). Therefore, fluid waves of this amplitude or smaller are not significant.

Effect of initial fluid depth.—Figures 53 and 104 show the fluid depth profiles and wave patterns for fluid 3 with initial fluid depths of 0.525 and 2.0 mm (0.02 and 0.08 in.) Though there are significant differences in the fluid depth profiles at the earliest time shown, there is very little difference between the two figures at 26 sec. This indicates that the fluid velocity is somewhat proportional to the fluid depth. The outer layers of the deeper fluid flow off more quickly than those of the shallow fluid.

Gapped slat versus sealed flat.—Figures 53 and 105 show results for the flaps 5 configuration with the slat sealed and gapped, respectively. Note that the differences between the velocities at rotation and times to rotation for these two runs. For the run shown in figure 53, rotation started at 22 sec. For the run shown in figure 105, rotation started at 25 sec. However, because of a slight delay in the start of the tunnel acceleration for the figure 105 case, rotation occurred at a velocity of about 57.6 m/sec (112 keas) in both cases. The differences between the fluid distributions for the two cases are mainly on the aft half of the model.

Flaps 15, gapped slat versus flaps 5, sealed slat.—Figures 106 and 103 show results for the flaps 15, gapped-slat configuration and the flaps 5, sealed slat configuration, respectively.

Although there are some differences in speeds and times to rotation for the two cases, the general indication is that the fluid flows off more slowly for the flaps 15 configuration than for the flaps 5 configuration.

Flaps 15 with cruise leading edge.—The results for the flaps 15, cruise leading-edge configuration are shown in figures 107 and 108. The tunnel acceleration and model rotation time were changed for this case in order to be representative of commuter aircraft.

Experimental fluids.—Results for the eight experimental fluids tested are shown in figures 109 to 120. Results are shown for 0 °C and for −20 °C for fluids 2.1, 3.1, 4.1, and 5.1. Results are shown for only −20 °C for fluids 2.2, 3.2, 4.2, and 5.2.

Three-dimensional Half Model Results

The three-dimensional half model ultraviolet fluorescence data are based on photographs of the 60- to 70-percent-span location. This region includes the spanwise station corresponding to the airfoil used for the two-dimensional model.

Flaps 5, fluid 3.—Flaps 5, fluid 3 results are shown in figures 121 to 127. Included are three runs at −20 °C and one each at −10 and 0 °C.

Flaps 5, fluid 4.—Results for flaps 5 with fluid 4 are shown in figure 132.

Flaps 15, gapped slat, fluid 3.—Results for the flaps 15, gapped-slat configuration are shown in figure 129. The secondary wave at $t = 22$ sec is very evident.

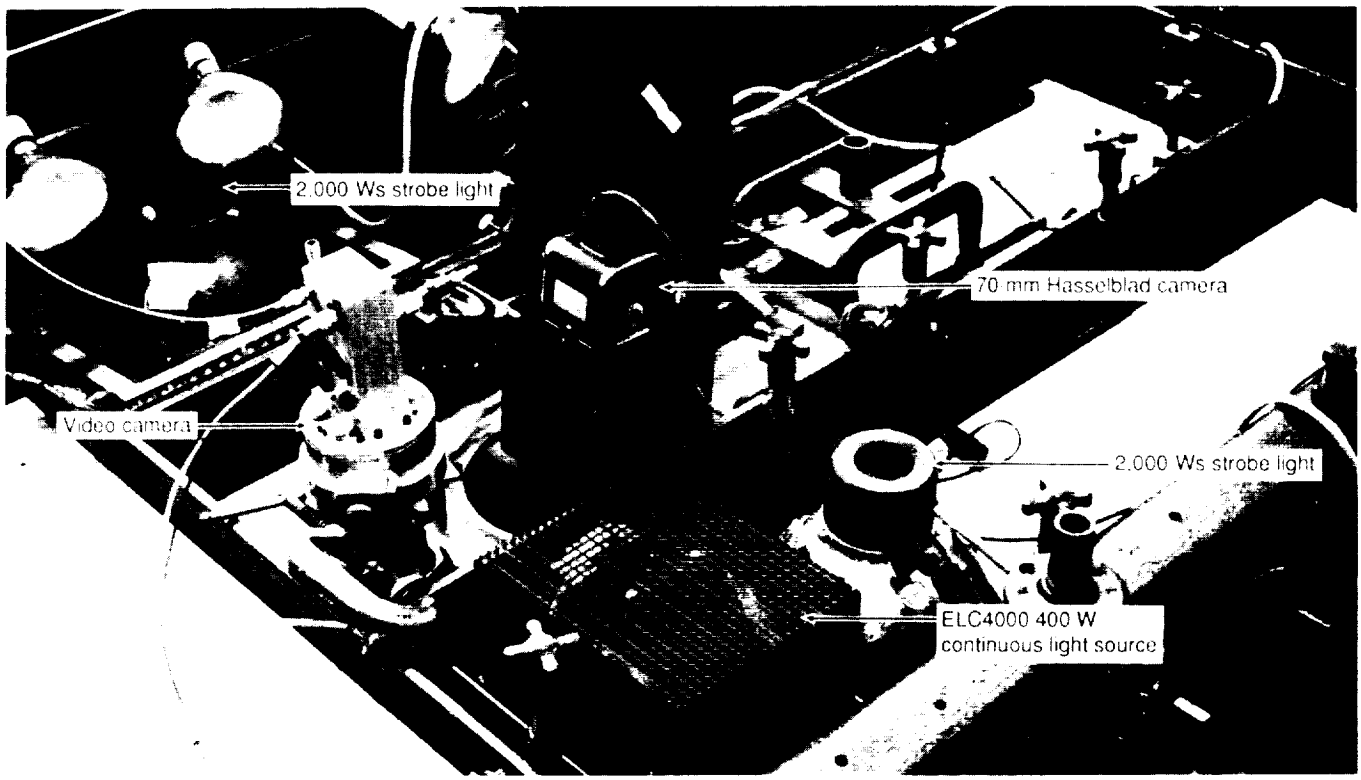

Figure 98.—Equipment setup for ultraviolet photographic technique.

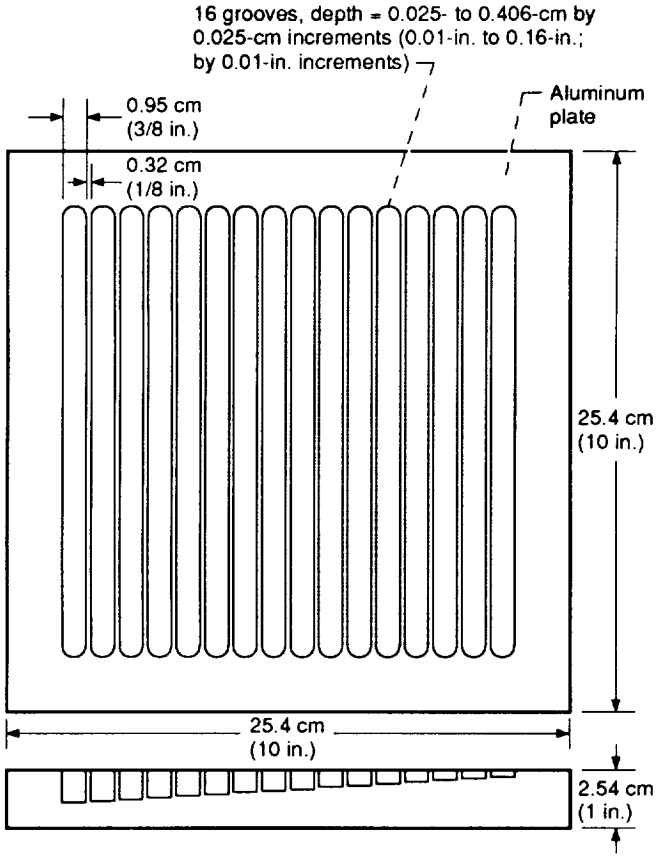

Figure 99.—Calibration plate.

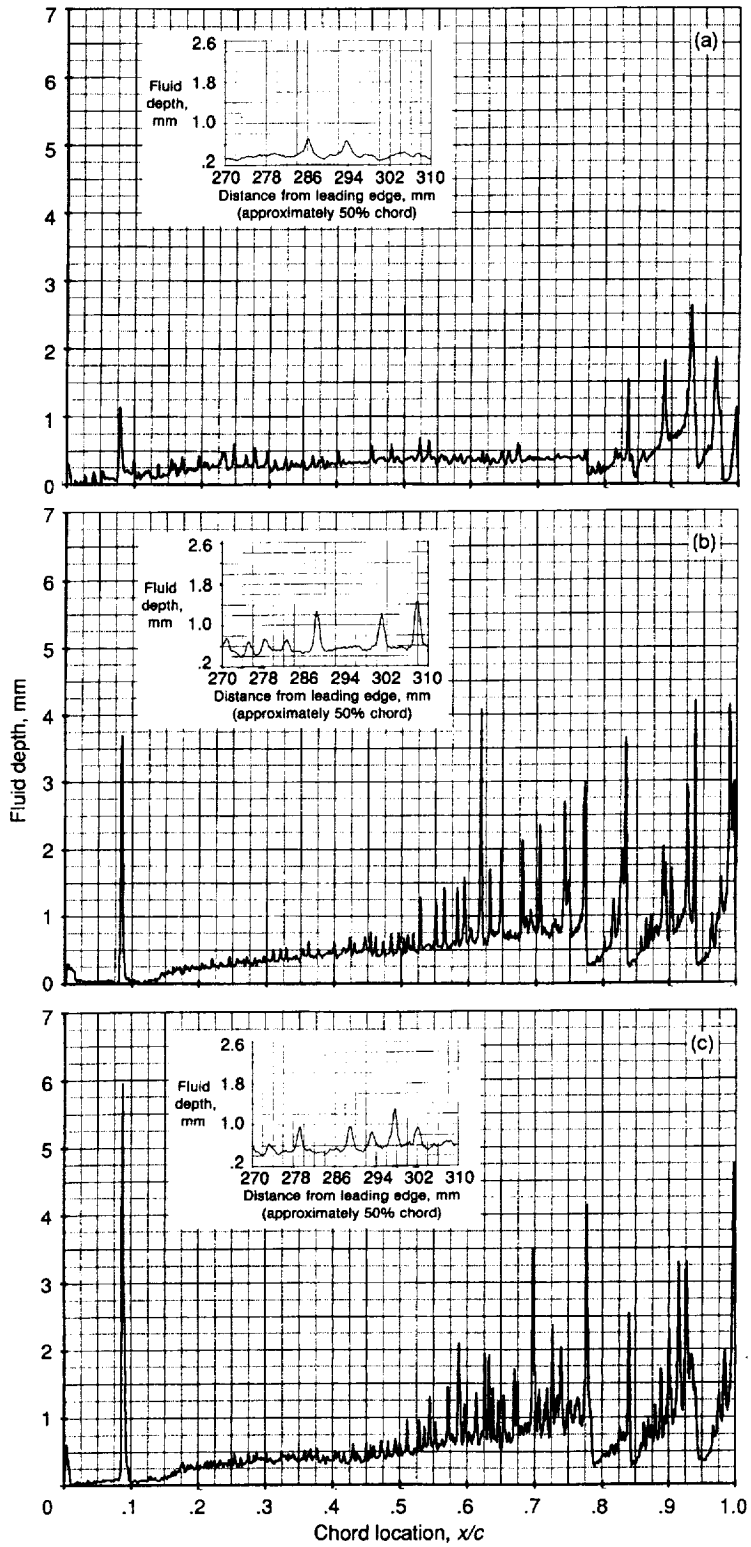

(a) Elapsed time, 10 sec; airspeed, 24.2 m/sec (47 keas); $\alpha_w = 0$; $h = 0.166$ mm.

(b) Elapsed time, 24 sec; airspeed, 61.2 m/sec (119 keas); $\alpha_w = -0.1°$; $h = 0.451$ mm.

(c) Elapsed time, 26 sec; airspeed, 66.3 m/sec (129 keas); $\alpha_w = 4.3°$; $h = 0.348$ mm.

Figure 100.—Fluid 1 depth profiles and detail roughness inset for two-dimensional model in flaps 5 configuration. Initial depth 0.750 mm; temperature, –20 °C. (See fig. 51 for wave patterns.)

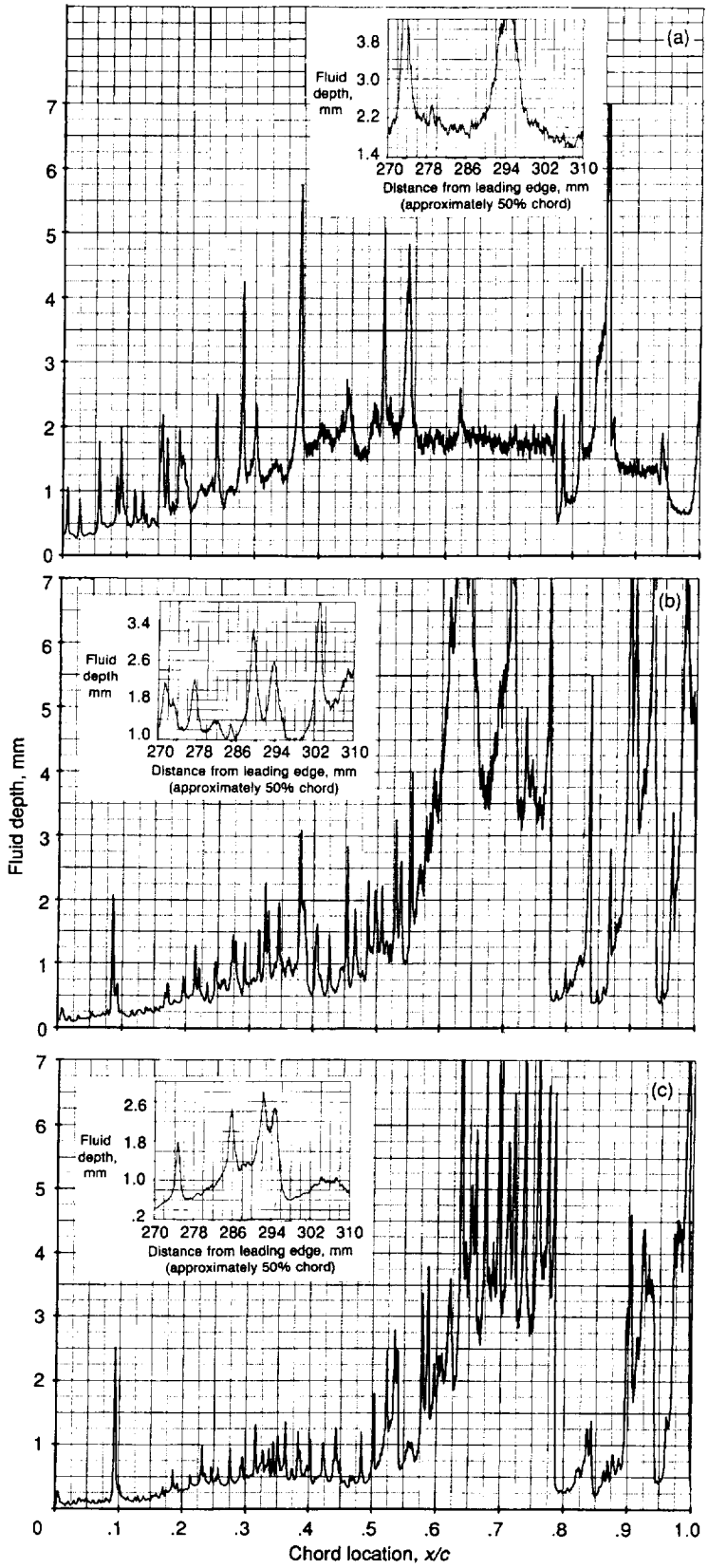

(a) Elapsed time, 10 sec; airspeed, 25.2 m/sec (49 keas); $\alpha_w = 0$; $h = 0.226$ mm.

(b) Elapsed time, 22 sec; airspeed, 57.6 m/sec (112 keas); $\alpha_w = -0.1°$; $h = 0.864$ mm.

(c) Elapsed time, 26 sec; airspeed, 67.9 m/sec (132 keas); $\alpha_w = 8.7°$; $h = 1.150$ mm.

Figure 101.—Fluid 2 depth profiles and detail roughness inset for two-dimensional model in flaps 5 configuration. Initial depth, 1.0 mm; temperature, –20 °C. (See fig. 52 for wave patterns.)

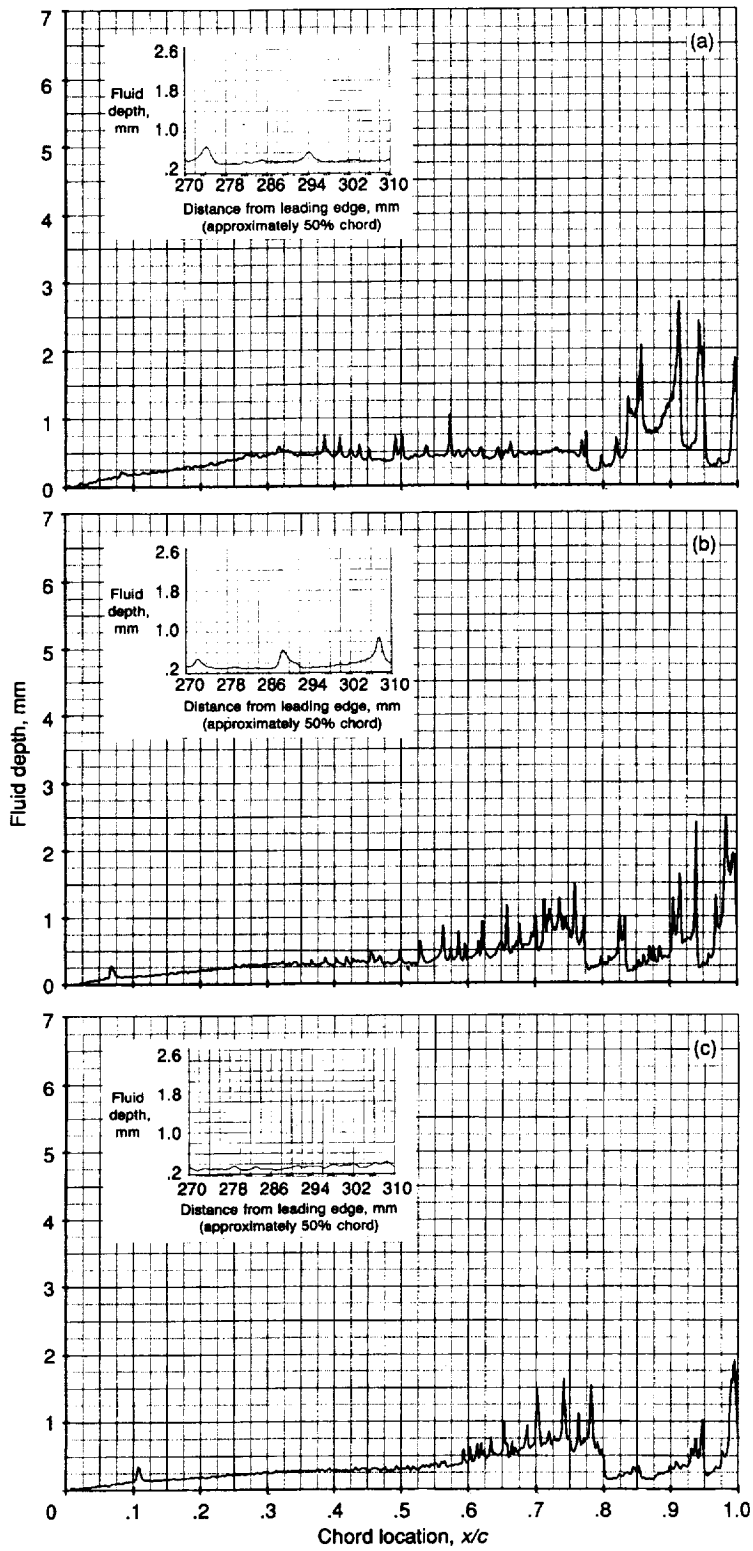

(a) Elapsed time, 10 sec; airspeed, 25.2 m/sec (49 keas); α_w = 0.1°; h = 0.15 mm.

(b) Elapsed time, 22 sec; airspeed, 57.6 m/sec (112 keas); α_w = 0.1°; h = 0.340 mm.

(c) Elapsed time, 26 sec; airspeed, 62.7 m/sec (122 keas); α_w = 12.1°; h = 0.928 mm.

Figure 102.—Fluid 3 depth profiles and detail roughness inset for two-dimensional model in flaps 5 configuration. Initial depth, 0.525 mm; temperature, –20 °C. (See fig. 53 for wave patterns.)

C-2

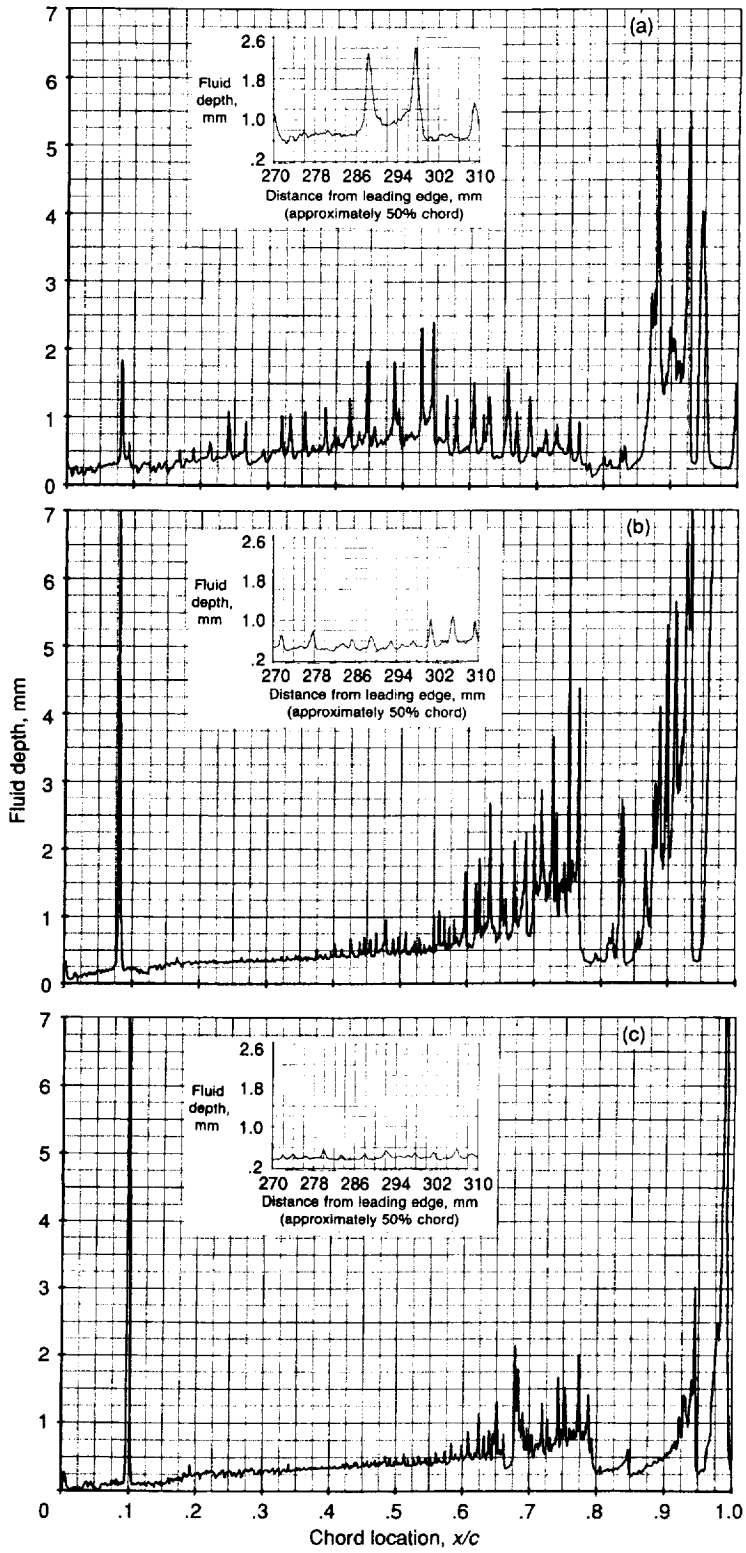

(a) Elapsed time, 10 sec; airspeed, 24.7 m/sec (48 keas); $\alpha_w = 0$; $h = 0.479$ mm.

(b) Elapsed time, 22 sec; airspeed, 56.5 m/sec (110 keas); $\alpha_w = -0.1°$; $h = 0.288$ mm.

(c) Elapsed time, 26 sec; airspeed, 66.8 m/sec (130 keas); $\alpha_w = 8.3°$; $h = 0.155$ mm.

Figure 103.—Fluid 4 depth profiles and detail roughness inset for two-dimensional model in flaps 5 configuration. Initial depth, 0.810 mm; temperature, –20 °C. (See fig. 54 for wave patterns.)

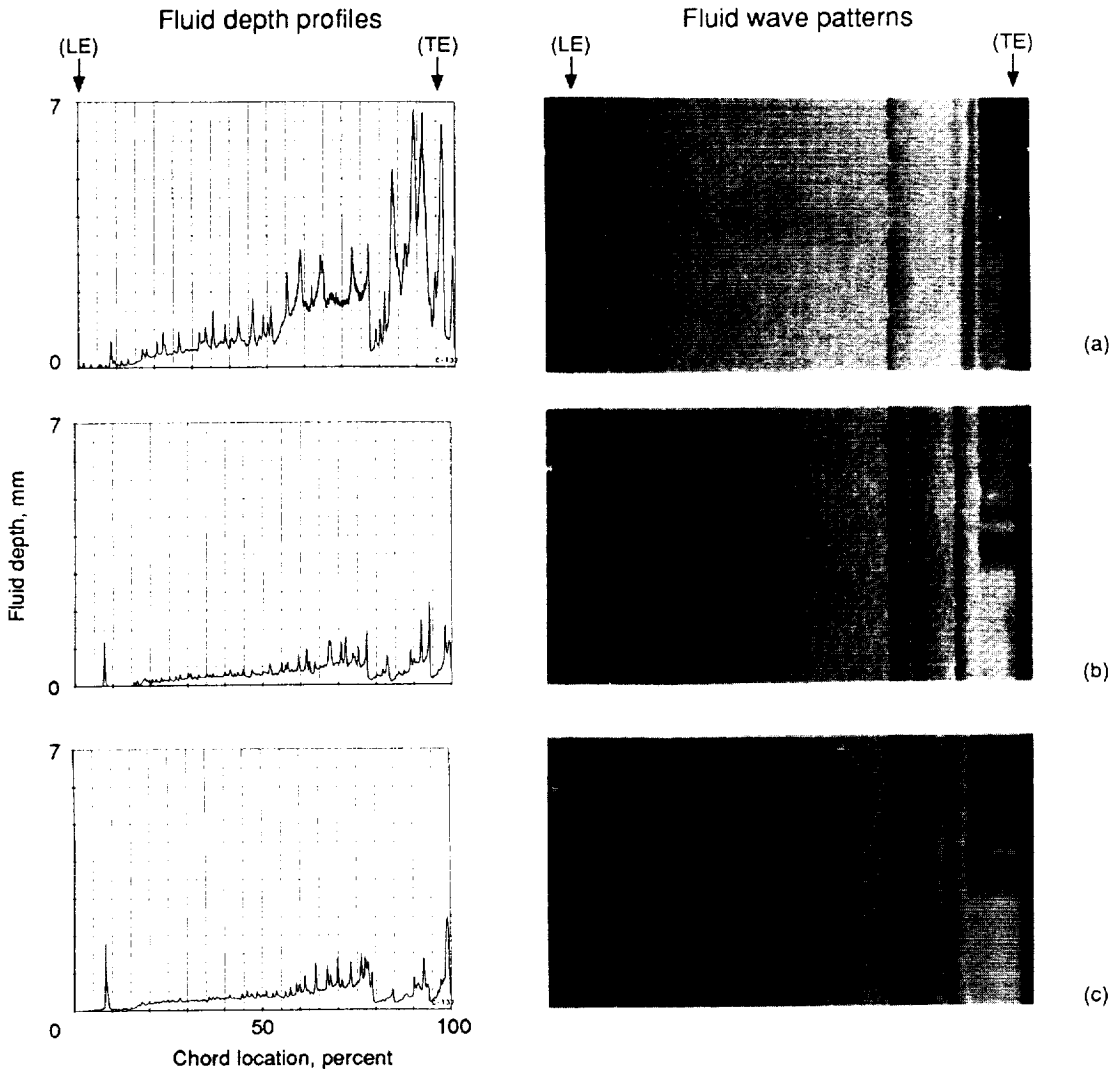

(a) Elapsed time, 12 sec; airspeed, 30.3 m/sec (59 keas); $\alpha_W = -0.2°$.

(b) Elapsed time, 22 sec; airspeed, 57.1 m/sec (111 keas); $\alpha_W = -0.3°$.

(c) Elapsed time, 26 sec; airspeed, 67.3 m/sec (131 keas); $\alpha_W = 10.1°$.

Figure 104.—Fluid 3 depth profiles and wave patterns for two-dimensional model in flaps 5 configuration. Initial depth, 2.0 mm; temperature, –20 °C; run 327.

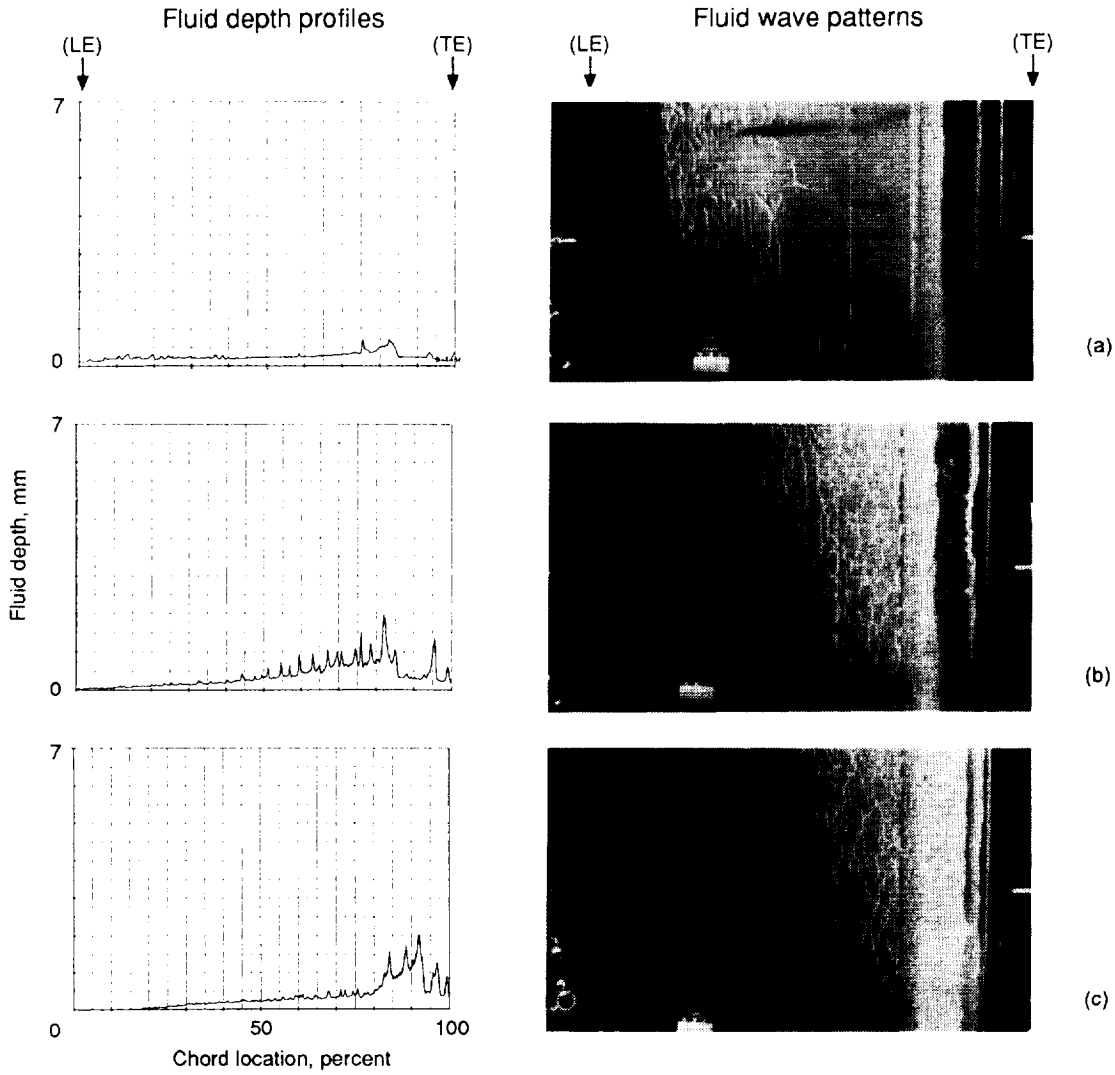

(a) Elapsed time, 10 sec; airspeed, 18.0 m/sec (35 keas); $\alpha_w = 0°$.

(b) Elapsed time, 24 sec; airspeed, 54.5 m/sec (106 keas); $\alpha_w = 0°$.

(c) Elapsed time, 28 sec; airspeed, 64.8 m/sec (126 keas); $\alpha_w = 7.6°$.

Figure 105.—Fluid 3 depth profiles and wave patterns for two-dimensional model in flaps 5, gapped slat configuration. Initial depth, 0.475 mm; temperature, –20 °C; run 458.

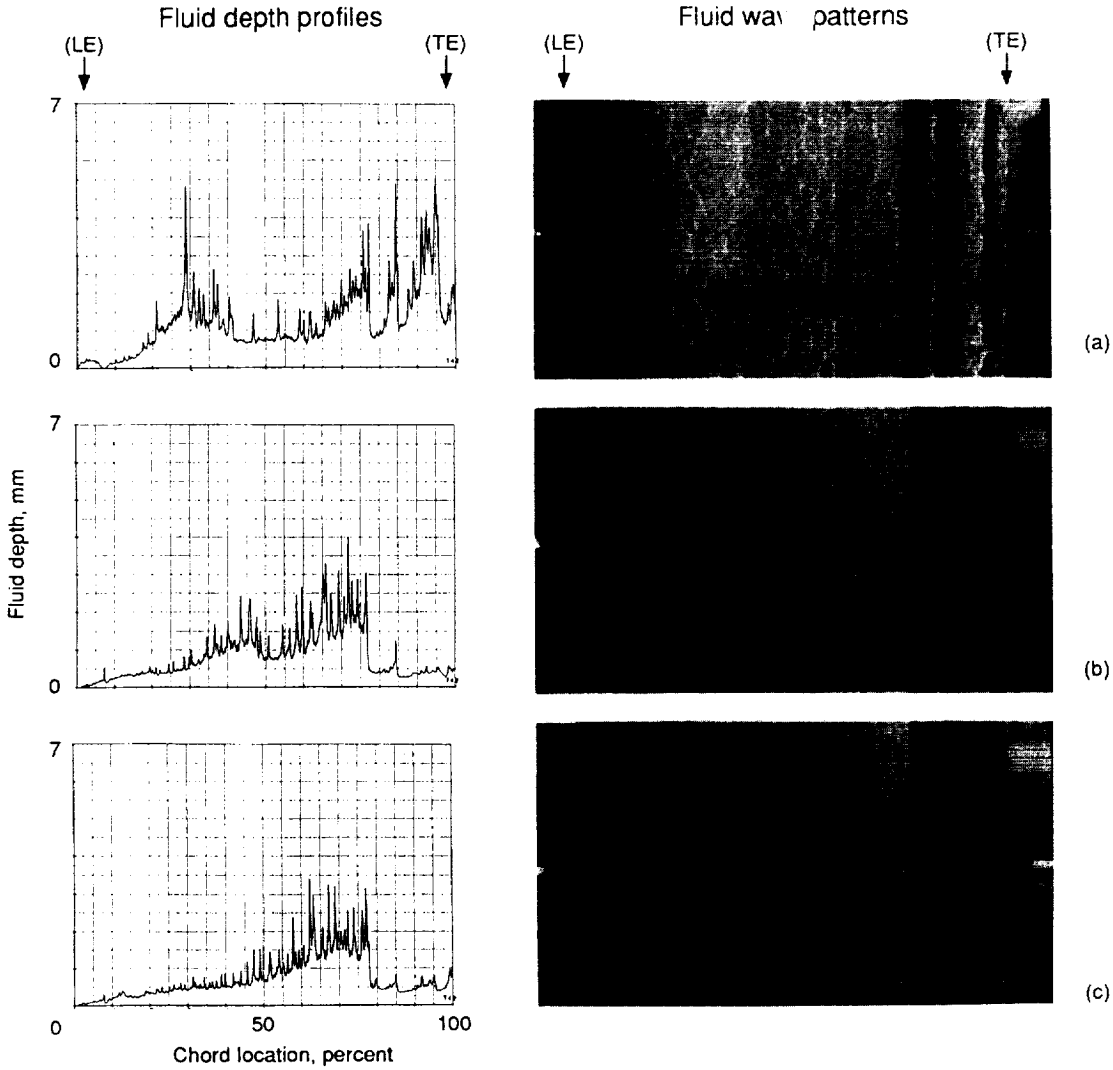

(a) Elapsed time, 10 sec; airspeed, 25.2 m/sec (49 keas); $\alpha_W = 0°$.

(b) Elapsed time, 20 sec; airspeed, 51.4 m/sec (100 keas); $\alpha_W = -0.1°$.

(c) Elapsed time, 22 sec; airspeed, 56.5 m/sec (110 keas); $\alpha_W = 4.9°$.

Figure 106.—Fluid 3 depth profiles and wave patterns for two-dimensional model in flaps 15, gapped slat configuration. Initial depth, 0.60 mm; temperature, –20 °C; run 422.

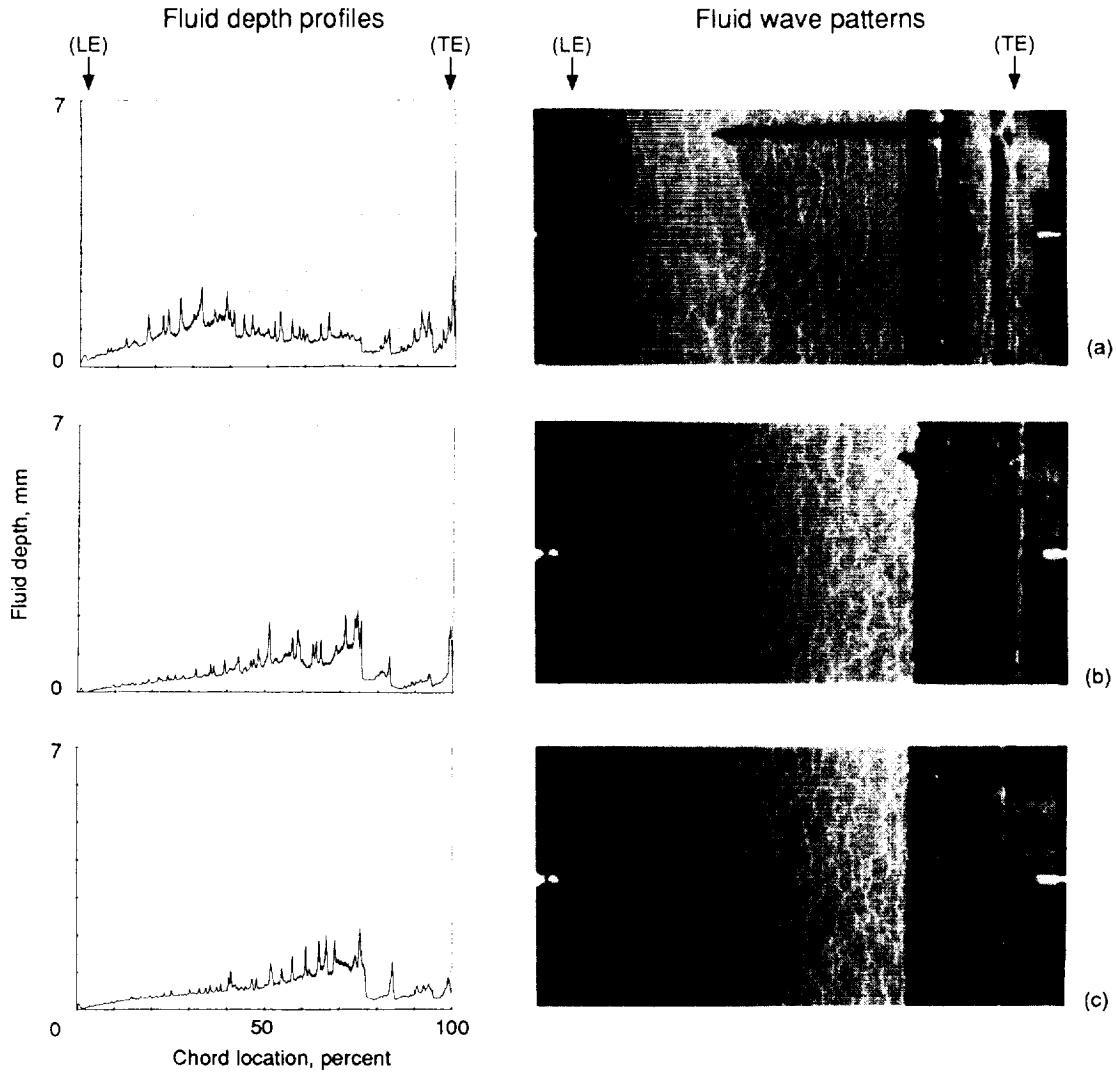

(a) Elapsed time, 10 sec; airspeed, 22.6 m/sec (44 keas); $\alpha_W = -0.1°$.

(b) Elapsed time, 16 sec; airspeed, 37.5 m/sec (73 keas); $\alpha_W = 1.0°$.

(c) Elapsed time, 18 sec; airspeed, 42.1 m/sec (82 keas); $\alpha_W = 7.3°$.

Figure 107.—Fluid 3 depth profiles and wave patterns for two-dimensional model in flaps 15, cruise leading edge configuration. Initial depth, 0.50 mm; temperature, –20 °C; run 442.

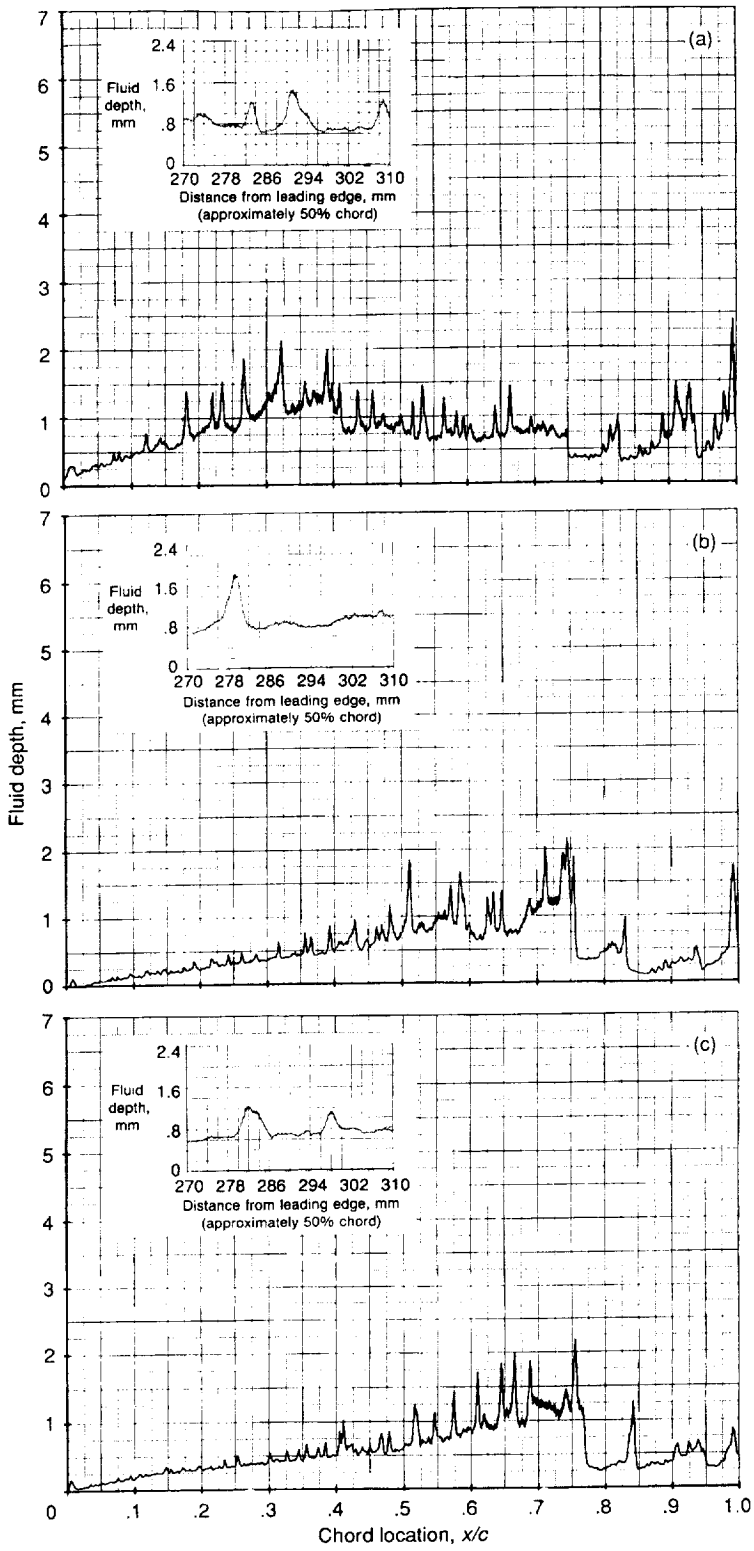

(a) Elapsed time, 10 sec; airspeed, 22.6 m/sec (44 keas); $\alpha_w = 0.1°$.

(b) Elapsed time, 16 sec; airspeed, 37.5 m/sec (73 keas); $\alpha_w = 1.0°$.

(c) Elapsed time, 18 sec; airspeed, 42.1 m/sec (82 keas); $\alpha_w = 7.3°$.

Figure 108.—Fluid 3 depth profiles and detail roughness inset for two-dimensional model in flaps 15, cruise leading edge configuration. Initial depth, 0.50 mm; temperature, −20 °C.

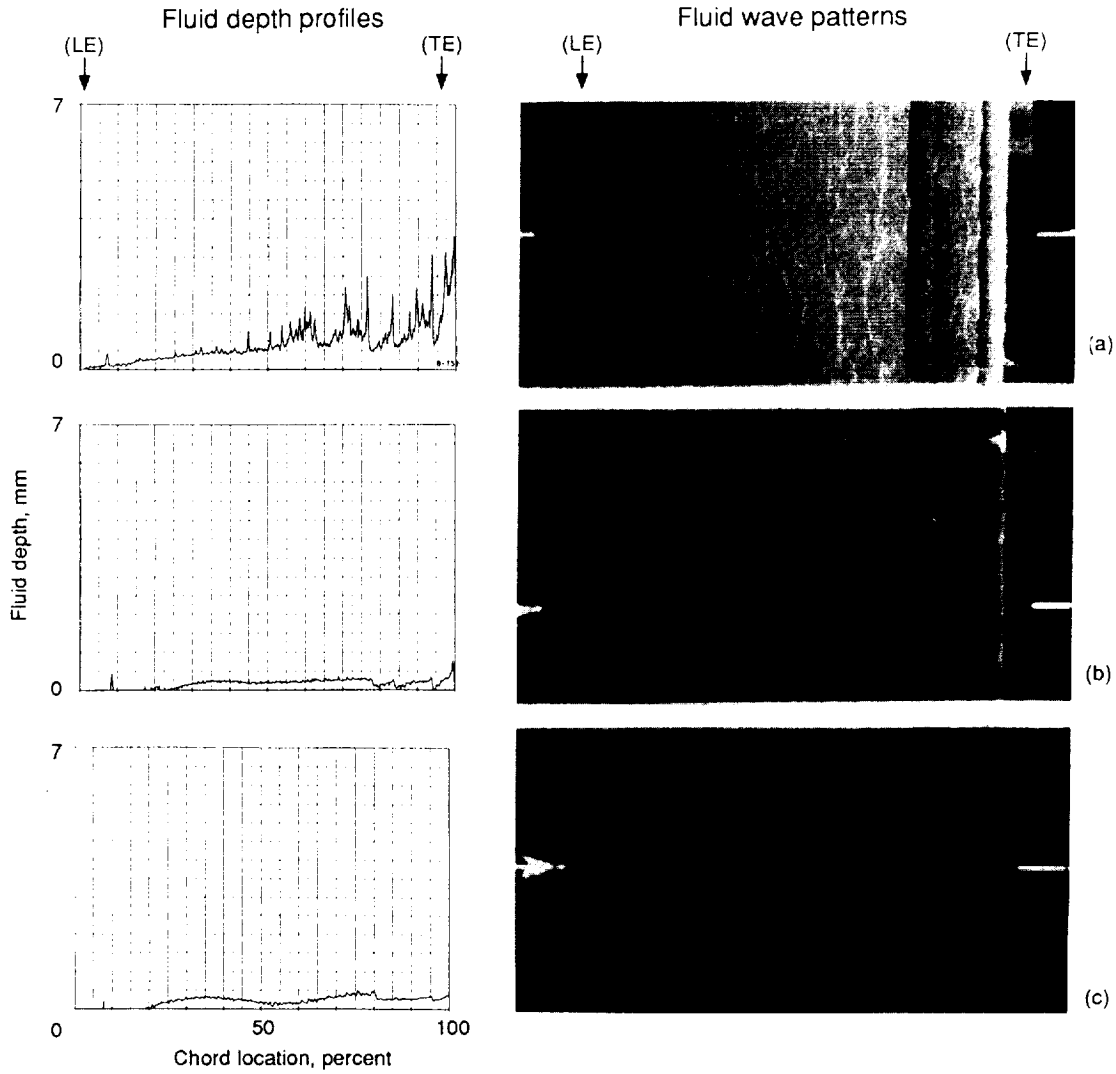

(a) Elapsed time, 12 sec; airspeed, 27.2 m/sec (53 keas); $\alpha_w = 0$.

(b) Elapsed time, 24 sec; airspeed, 57.6 m/sec (112 keas); $\alpha_w = 0$.

(c) Elapsed time, 28 sec; airspeed, 65.8 m/sec (128 keas); $\alpha_w = 9°$.

Figure 109.—Fluid 2.1 depth profiles and wave patterns for two-dimensional model in flaps 5 configuration. Initial depth, 0.500 mm; temperature, 0 °C; run 520.

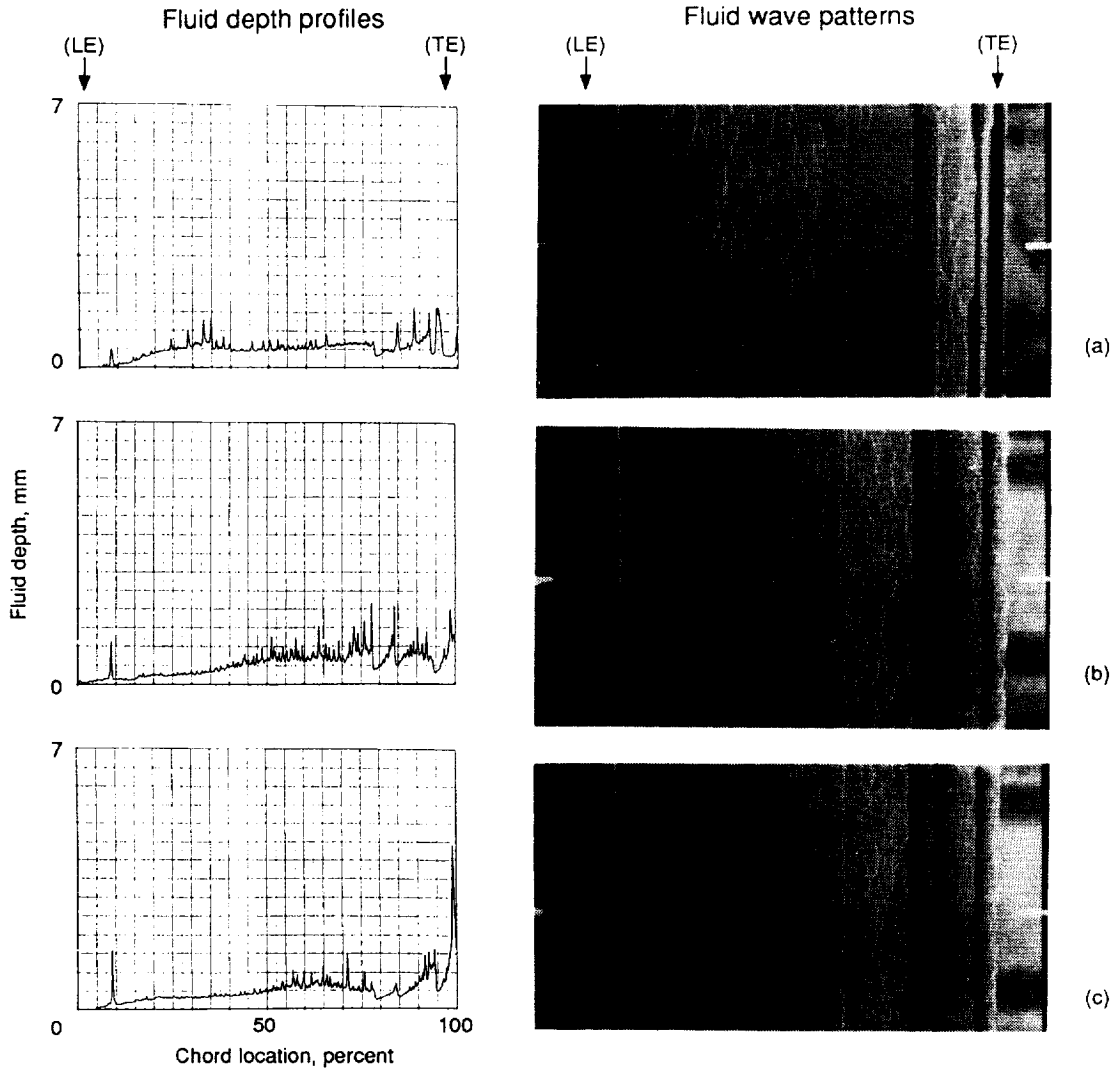

(a) Elapsed time, 10 sec; airspeed, 25.6 m/sec (49 keas); $\alpha_W = -0.1°$.

(b) Elapsed time, 24 sec; airspeed, 62.2 m/sec (121 keas); $\alpha_W = -0.2°$.

(c) Elapsed time, 26 sec; airspeed, 66.8 m/sec (130 keas); $\alpha_W = 3.4°$.

Figure 110.—Fluid 2.1 depth profiles and wave patterns for two-dimensional model in flaps 5 configuration. Initial depth, 0.55 mm; temperature, –20 °C; run 488.

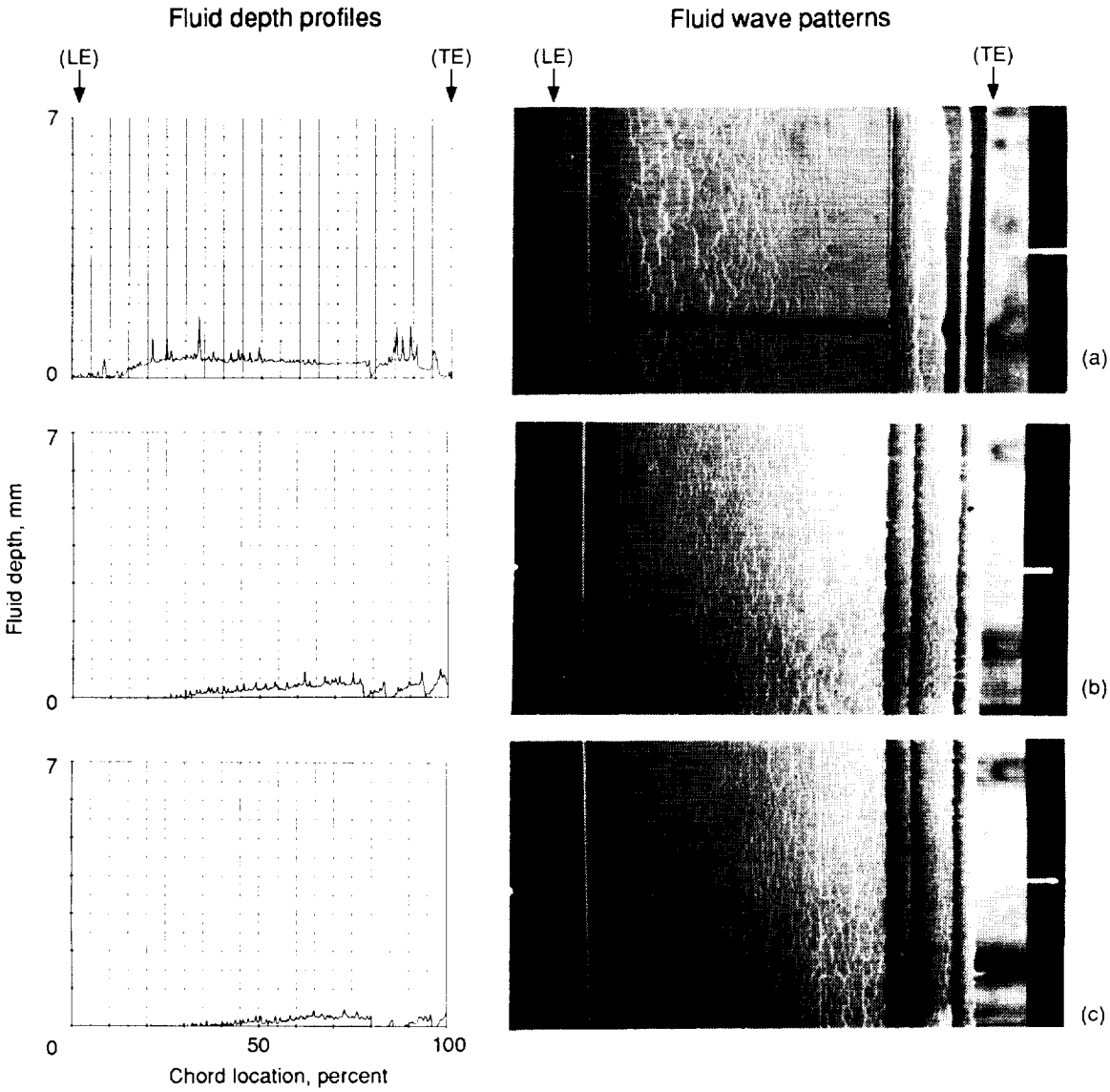

(a) Elapsed time, 10 sec; airspeed, 25.2 m/sec (49 keas); $\alpha_W = -0.2°$.

(b) Elapsed time, 24 sec; airspeed, 61.7 m/sec (120 keas); $\alpha_W = -0.3°$.

(c) Elapsed time, 28 sec; airspeed, 69.9 m/sec (136 keas); $\alpha_W = 9.3°$.

Figure 111.—Fluid 2.2 depth profiles and wave patterns for two-dimensional model in flaps 5 configuration. Initial depth, 0.525 mm; temperature, −20 °C; run 490.

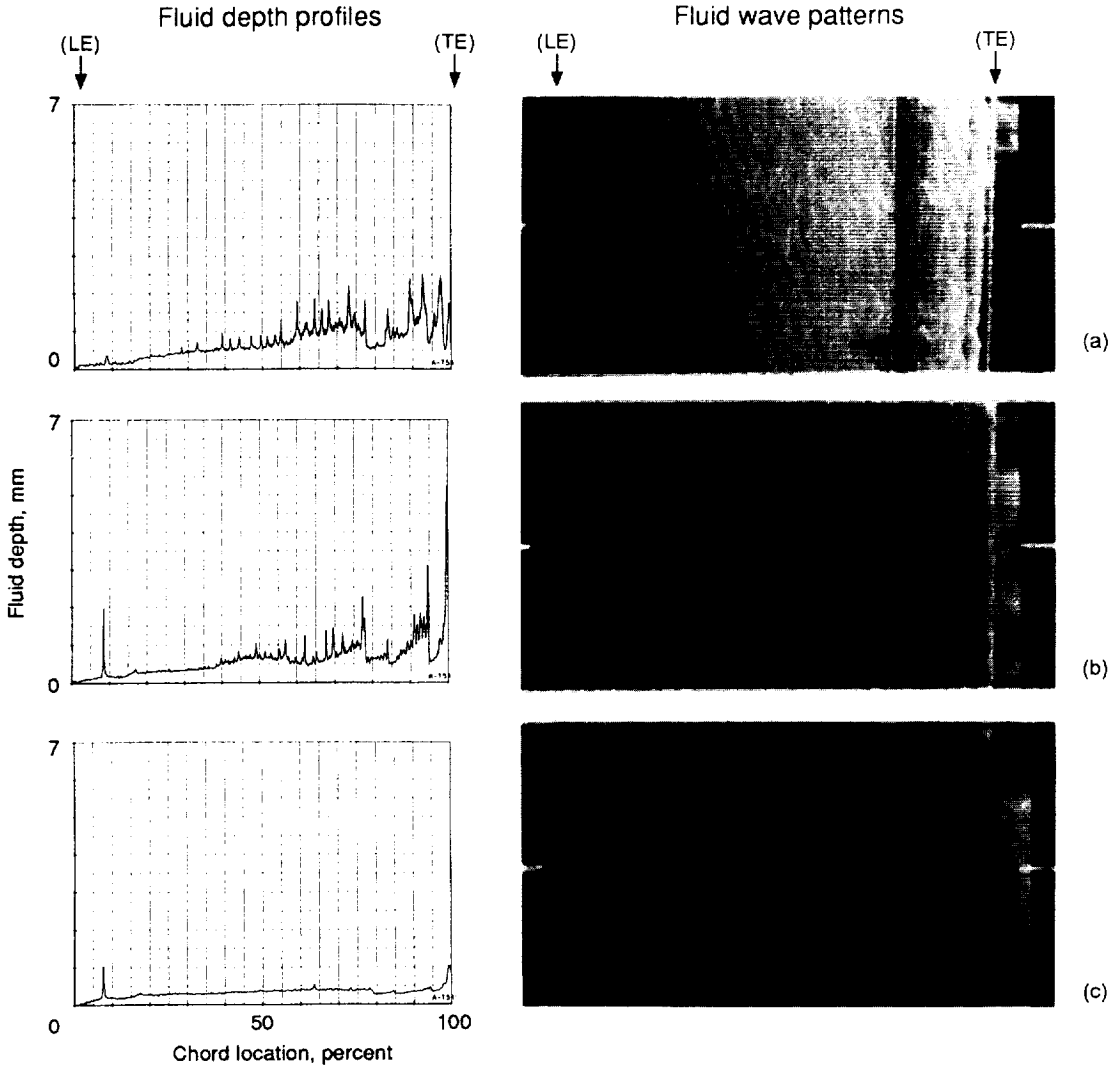

(a) Elapsed time, 12 sec; airspeed, 27.2 m/sec (53 keas); $\alpha_W = -0.8°$.

(b) Elapsed time, 24 sec; airspeed, 57.6 m/sec (112 keas); $\alpha_W = -0.8°$.

(c) Elapsed time, 28 sec; airspeed, 65.8 m/sec (128 keas); $\alpha_W = 8.4°$.

Figure 112.—Fluid 3.1 depth profiles and wave patterns for two-dimensional model in flaps 5 configuration. Initial depth, 0.500 mm; temperature, 0 °C; run 519.

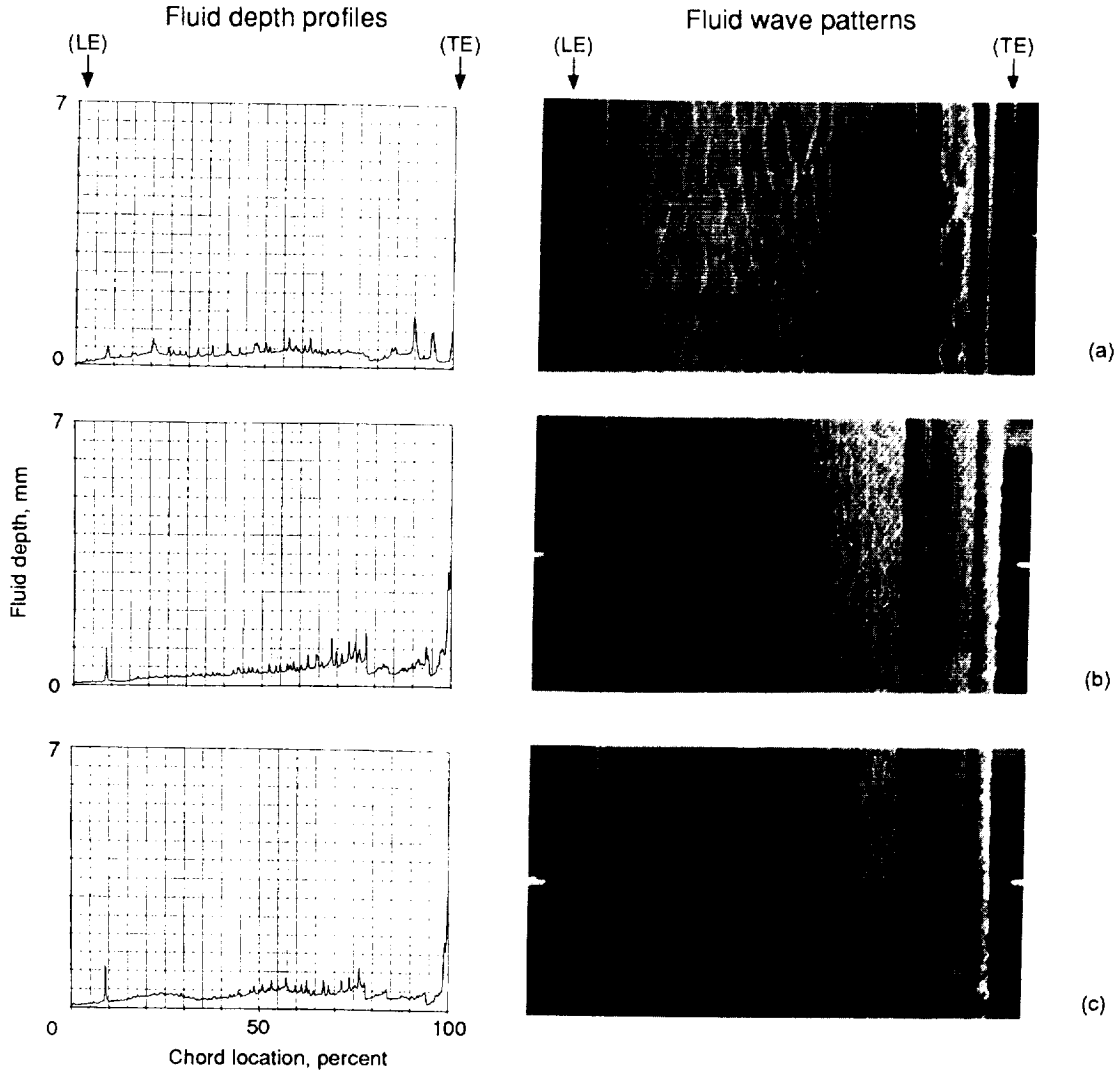

(a) Elapsed time, 10 sec; airspeed, 23.6 m/sec (46 keas); $\alpha_W = -0.4°$.

(b) Elapsed time, 24 sec; airspeed, 60.1 m/sec (117 keas); $\alpha_W = -0.4°$.

(c) Elapsed time, 26 sec; airspeed, 64.8 m/sec (126 keas); $\alpha_W = 1.9°$.

Figure 113.—Fluid 3.1 depth profiles and wave patterns for two-dimensional model in flaps 5 configuration. Initial depth, 0.530 mm; temperature, –20 °C; run 492.

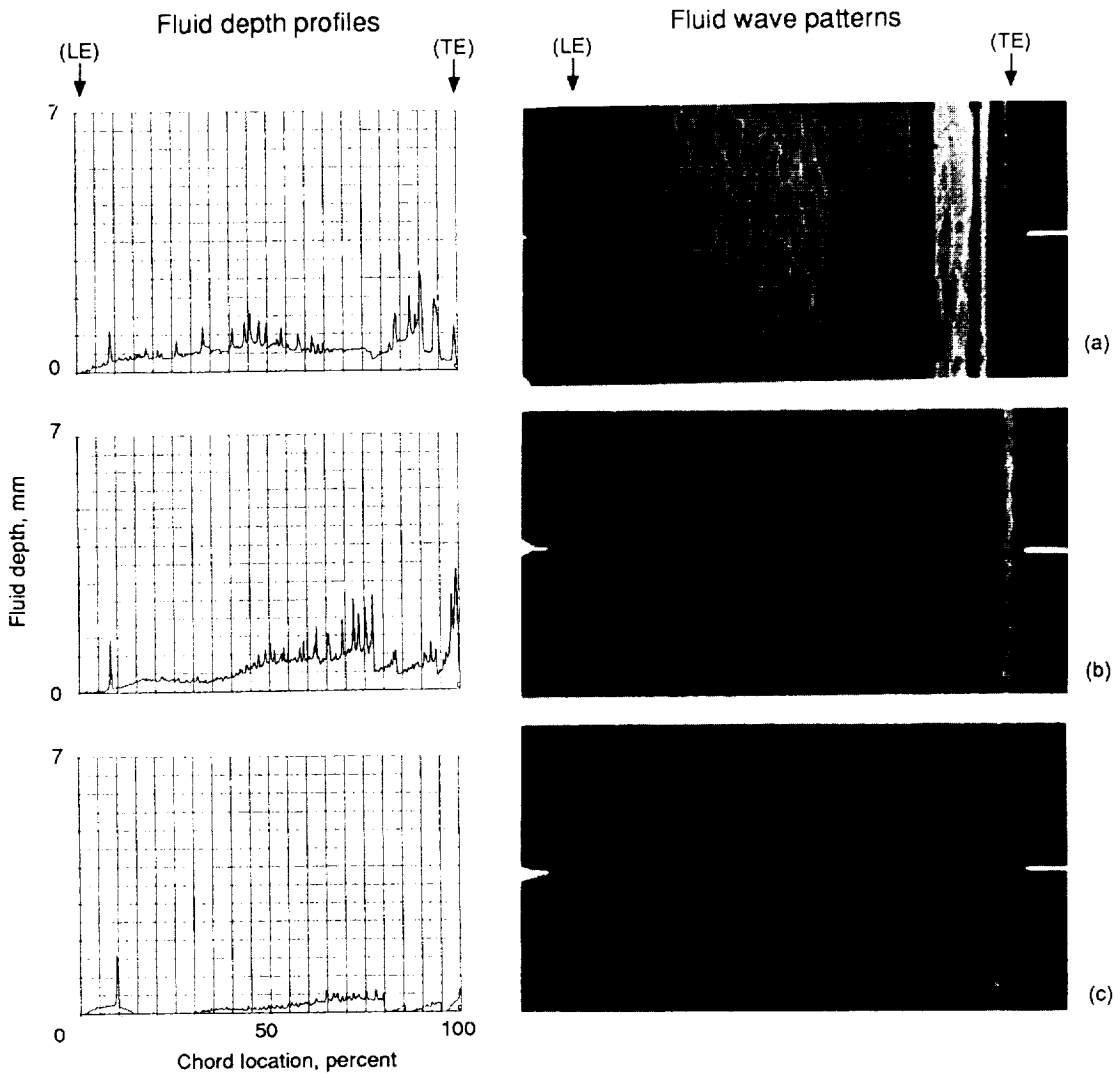

(a) Elapsed time, 10 sec; airspeed, 24.2 m/sec (47 keas); $\alpha_W = -0.2°$.

(b) Elapsed time, 24 sec; airspeed, 59.6 m/sec (116 keas); $\alpha_W = -0.3°$.

(c) Elapsed time, 28 sec; airspeed, 68.9 m/sec (134 keas); $\alpha_W = 8.4°$.

Figure 114.—Fluid 3.2 depth profiles and wave patterns for two-dimensional model in flaps 5 configuration. Initial depth, 0.500 mm; temperature, –20 °C; run 493.

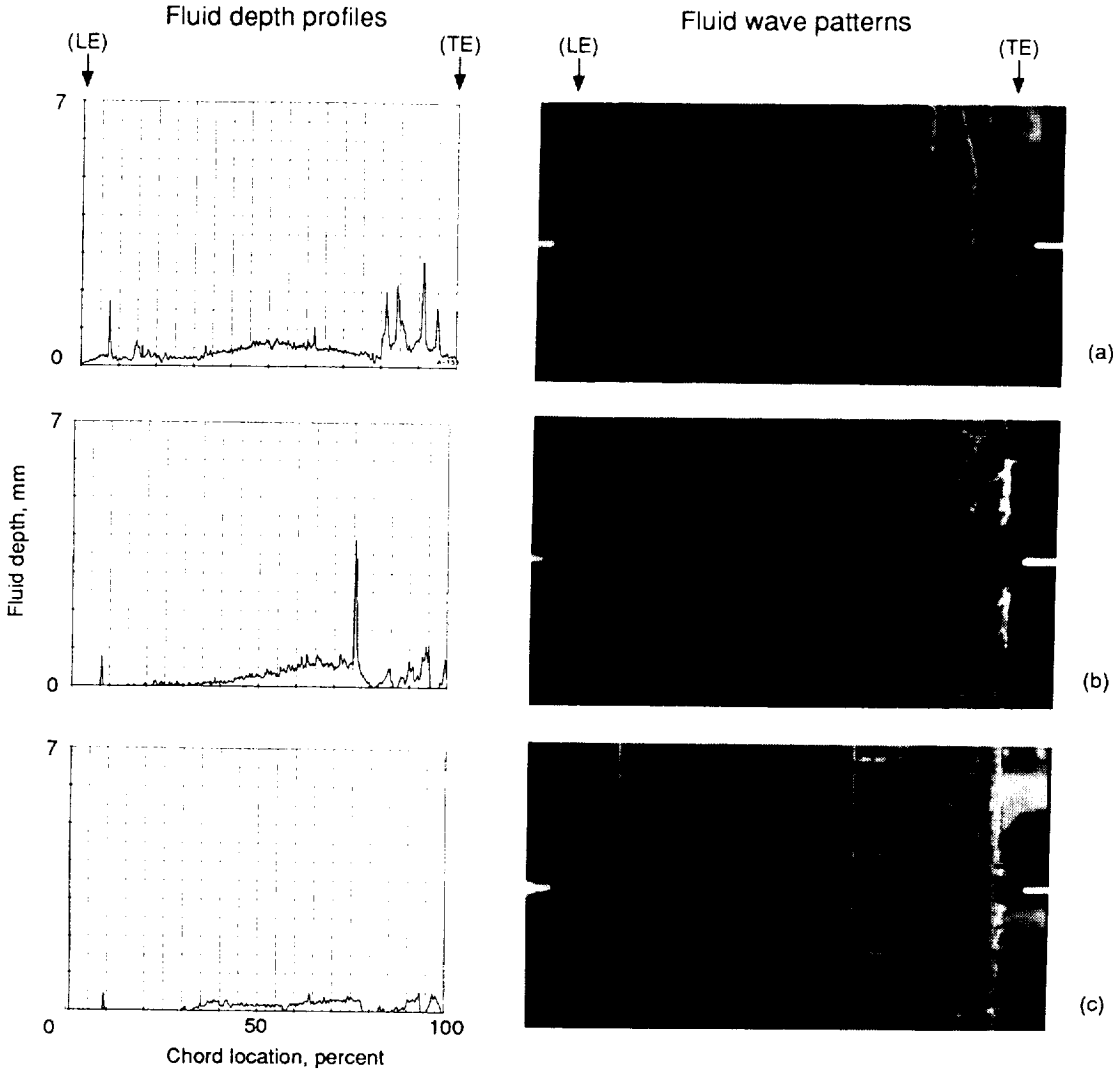

(a) Elapsed time, 12 sec; airspeed, 14.9 m/sec (29 keas); $\alpha_W = 0.3°$.

(b) Elapsed time, 24 sec; airspeed, 44.7 m/sec (87 keas); $\alpha_W = 0.2°$.

(c) Elapsed time, 28 sec; airspeed, 55.0 m/sec (107 keas); $\alpha_W = 9.7°$.

Figure 115.—Fluid 4.1 depth profiles and wave patterns for two-dimensional model in flaps 5 configuration. Initial depth, 0.425 mm; temperature, 0 °C; run 518.

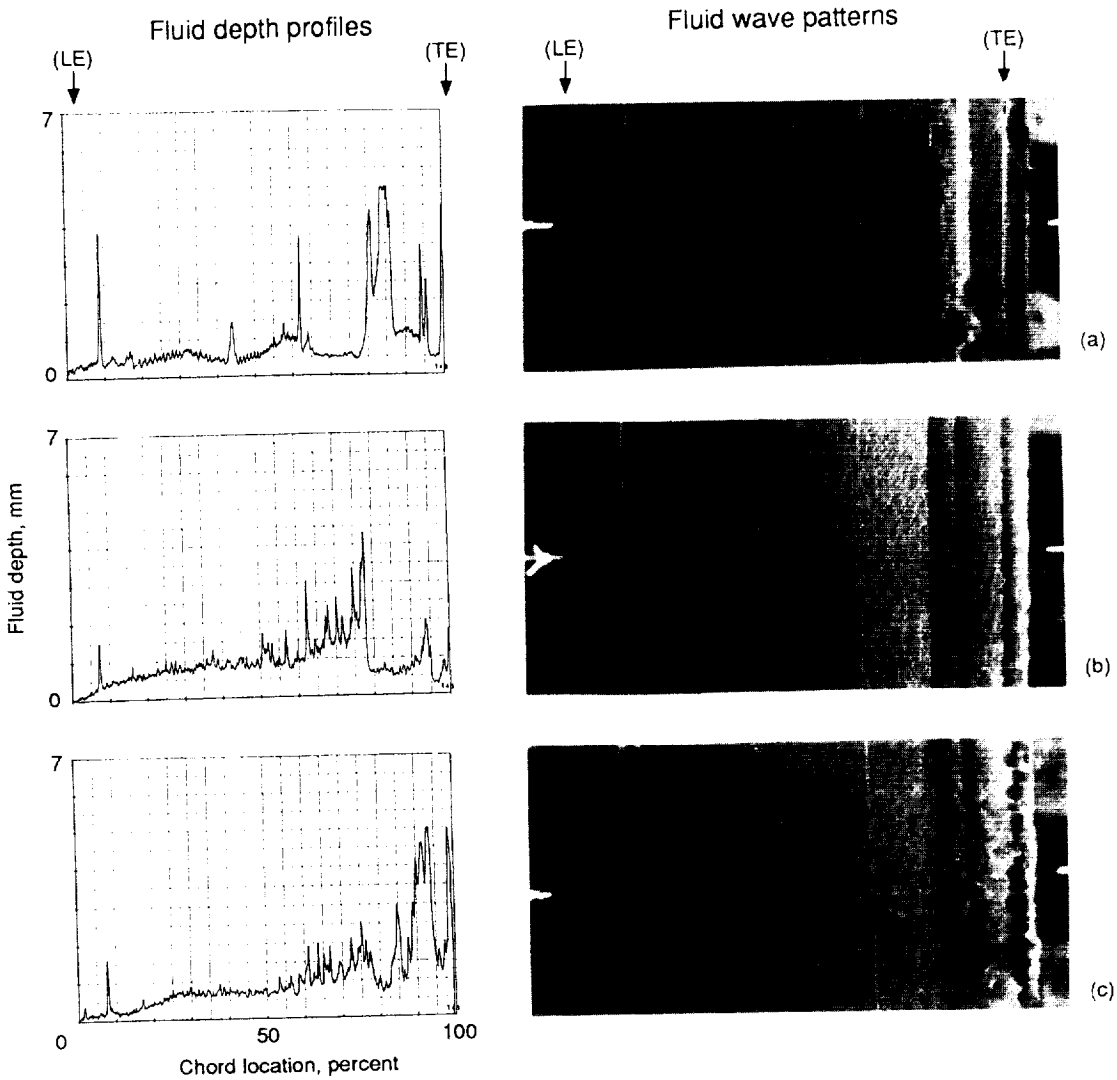

(a) Elapsed time, 10 sec; airspeed, 24.2 m/sec (47 keas); $\alpha_W = -0.3°$.

(b) Elapsed time, 24 sec; airspeed, 61.7 m/sec (120 keas); $\alpha_W = -0.4°$.

(c) Elapsed time, 26 sec; airspeed, 66.8 m/sec (130 keas); $\alpha_W = 4.2°$.

Figure 116.—Fluid 4.1 depth profiles and wave patterns for two-dimensional model in flaps 5 configuration. Initial depth, 0.450 mm; temperature, –20 °C; run 481.

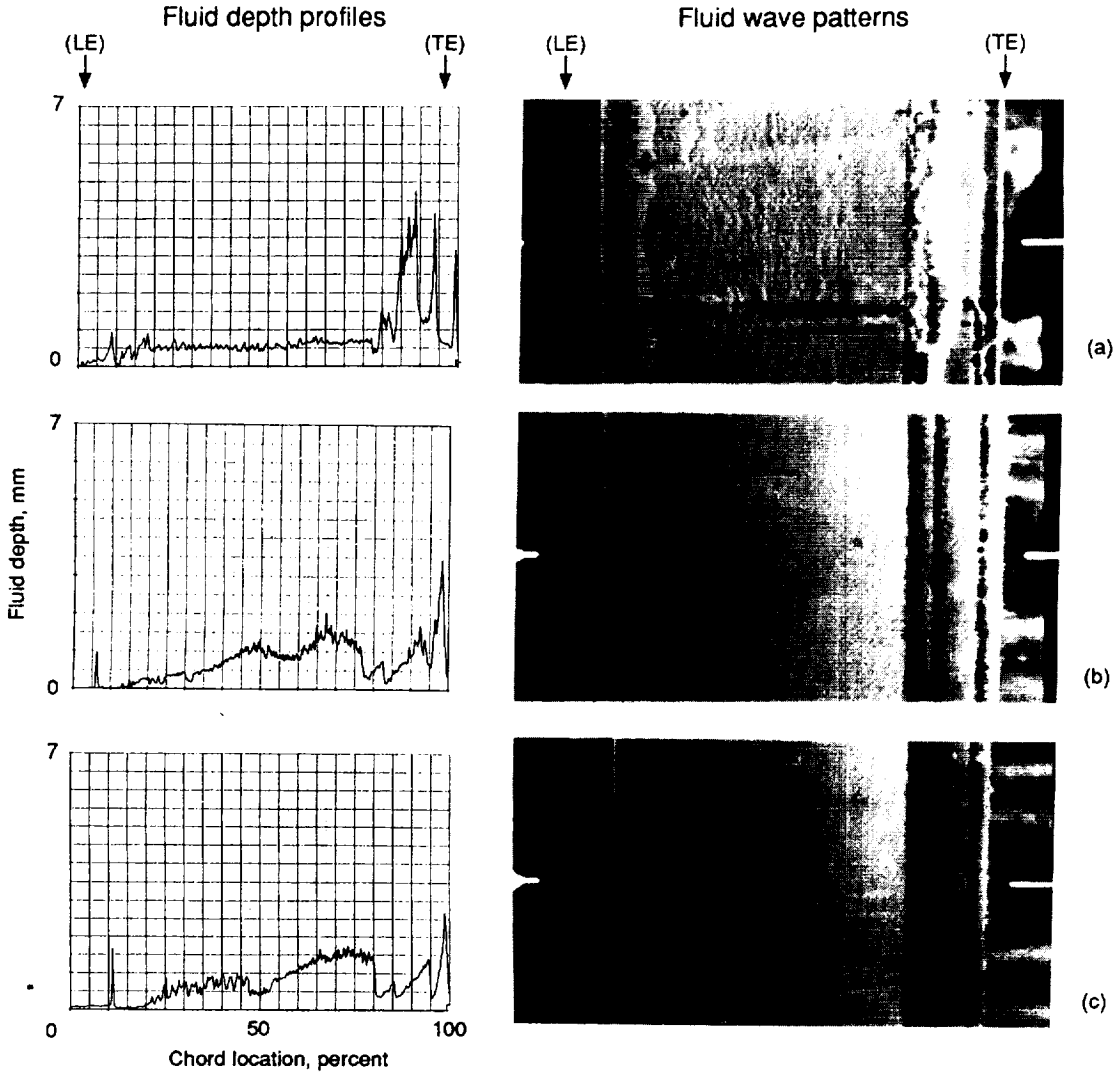

(a) Elapsed time, 10 sec; airspeed, 25.7 m/sec (50 keas); $\alpha_W = -0.1°$.

(b) Elapsed time, 24 sec; airspeed, 62.7 m/sec (122 keas); $\alpha_W = -0.1°$.

(c) Elapsed time, 28 sec; airspeed, 70.9 m/sec (138 keas); $\alpha_W = 11.6°$.

Figure 117.—Fluid 4.2 depth profiles and wave patterns for two-dimensional model in flaps 5 configuration. Initial depth, 0.475 mm; temperature, –20 °C; run 482.

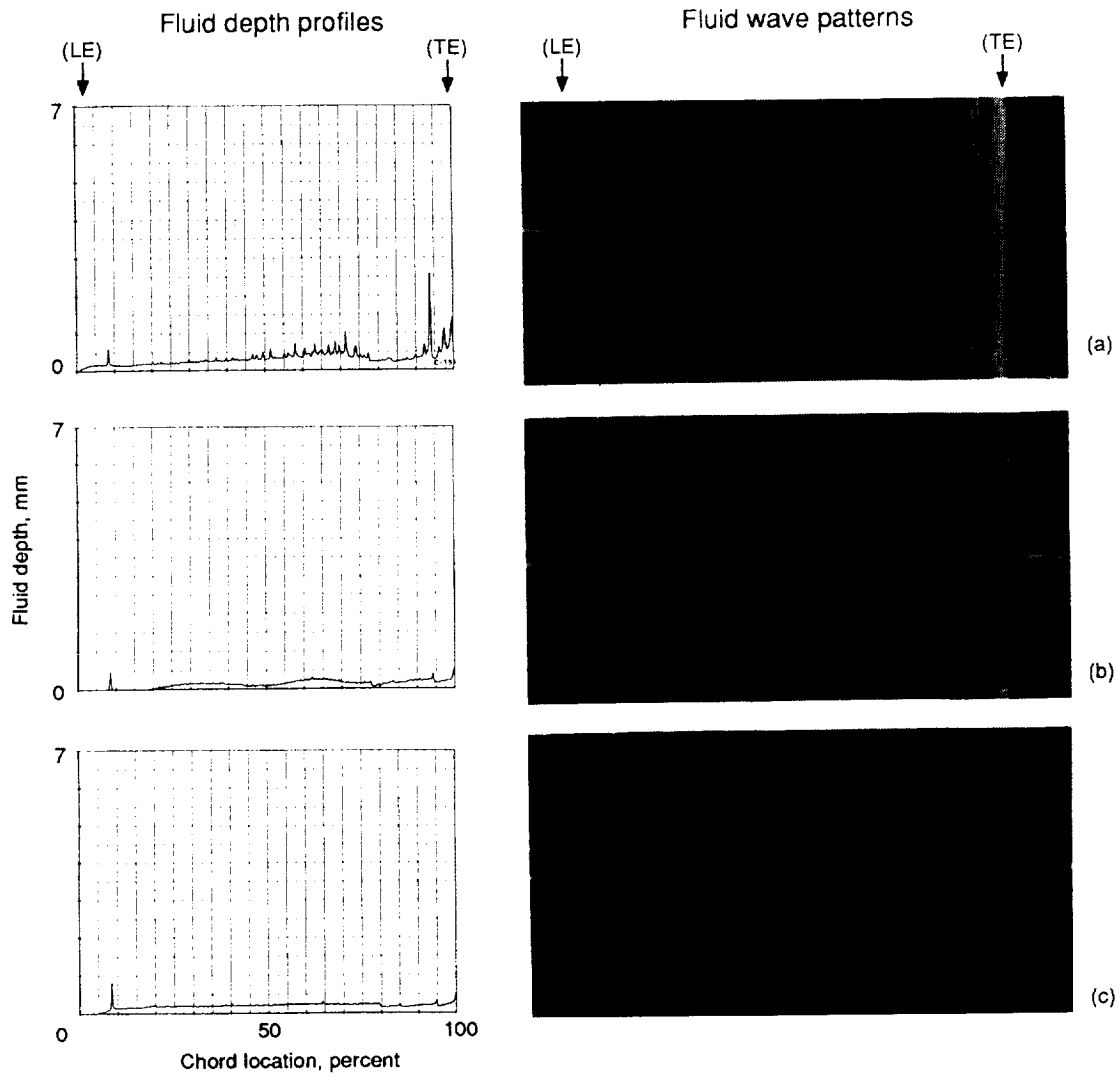

(a) Elapsed time, 12 sec; airspeed, 27.8 m/sec (54 keas); $\alpha_W = 0.1°$.

(b) Elapsed time, 24 sec; airspeed, 57.6 m/sec (112 keas); $\alpha_W = 0.1°$.

(c) Elapsed time, 28 sec; airspeed, 65.3 m/sec (127 keas); $\alpha_W = 9.7°$.

Figure 118.—Fluid 5.1 depth profiles and wave patterns for two-dimensional model in flaps 5 configuration. Initial depth, 0.475 mm; temperature, 0 °C; run 516.

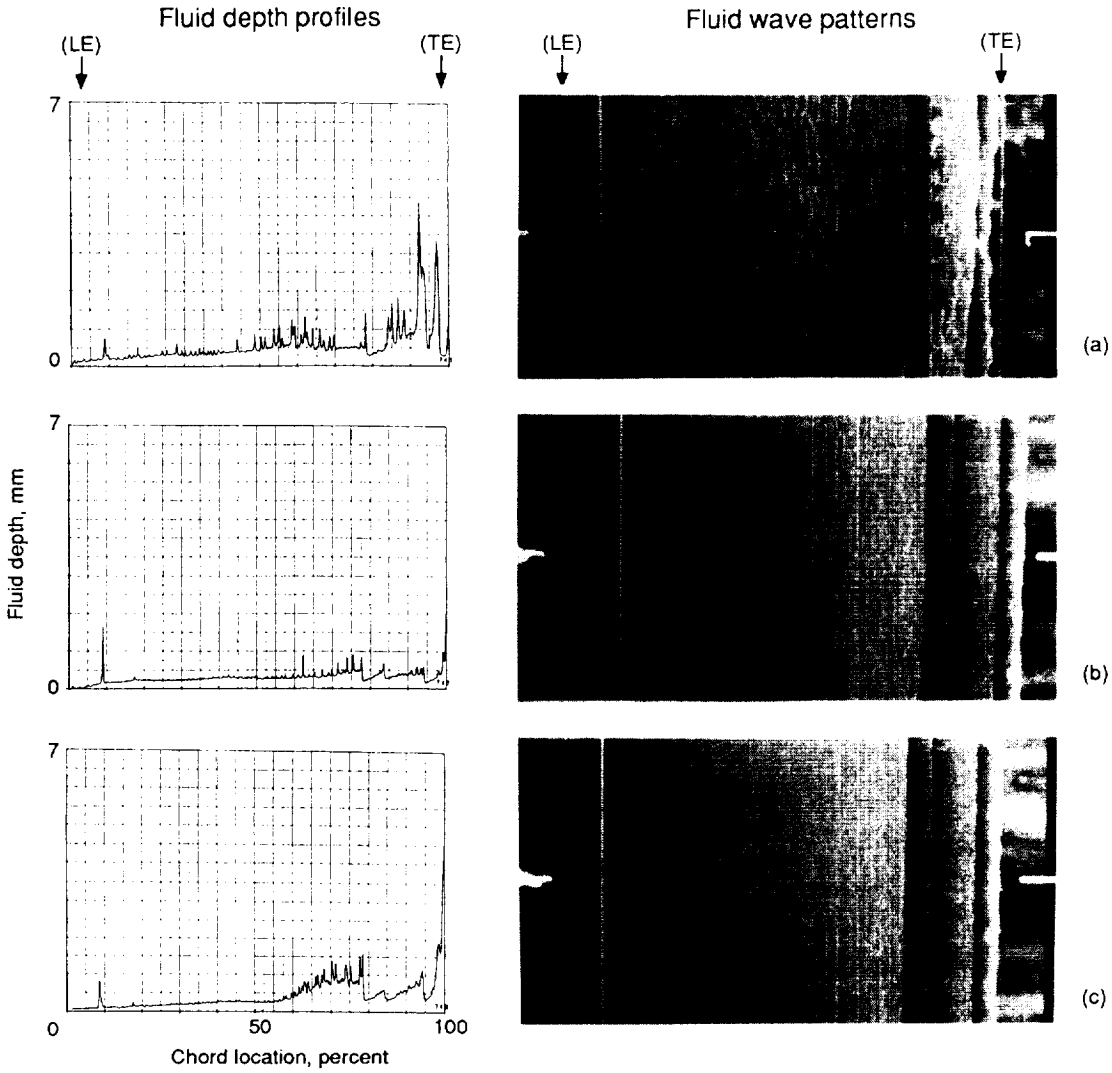

(a) Elapsed time, 10 sec; airspeed, 24.2 m/sec (47 keas); $\alpha_w = 0.3°$.

(b) Elapsed time, 24 sec; airspeed, 61.7 m/sec (120 keas); $\alpha_w = 0.2°$.

(c) Elapsed time, 26 sec; airspeed, 66.8 m/sec (130 keas); $\alpha_w = 4.4°$.

Figure 119.—Fluid 5.1 depth profiles and wave patterns for two-dimensional model in flaps 5 configuration. Initial depth, 0.500 mm; temperature, –20 °C; run 485.

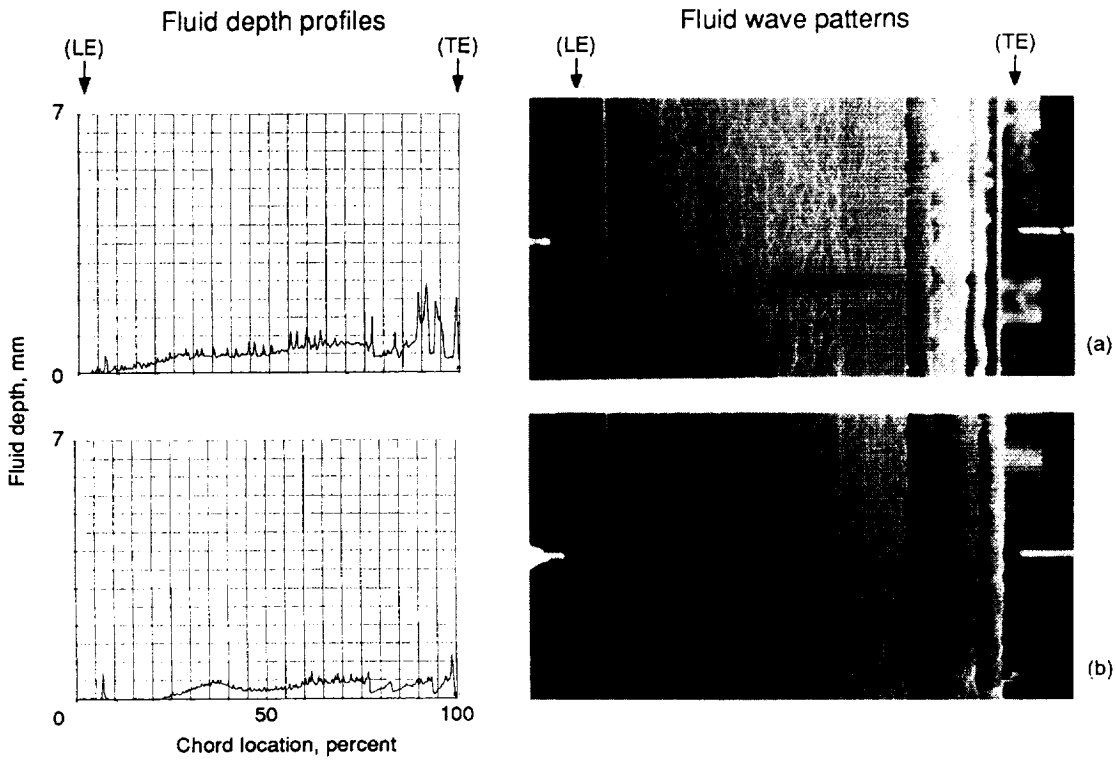

(a) Elapsed time, 10 sec; airspeed, 24.2 m/sec (47 keas); $\alpha_w = 0°$.

(b) Elapsed time, 24 sec; airspeed, 61.7 m/sec (120 keas); $\alpha_w = 0.1°$.

Figure 120.—Fluid 5.2 depth profiles and wave patterns for two-dimensional model in flaps 5 configuration. Initial depth, 0.500 mm; temperature, –20 °C; run 486.

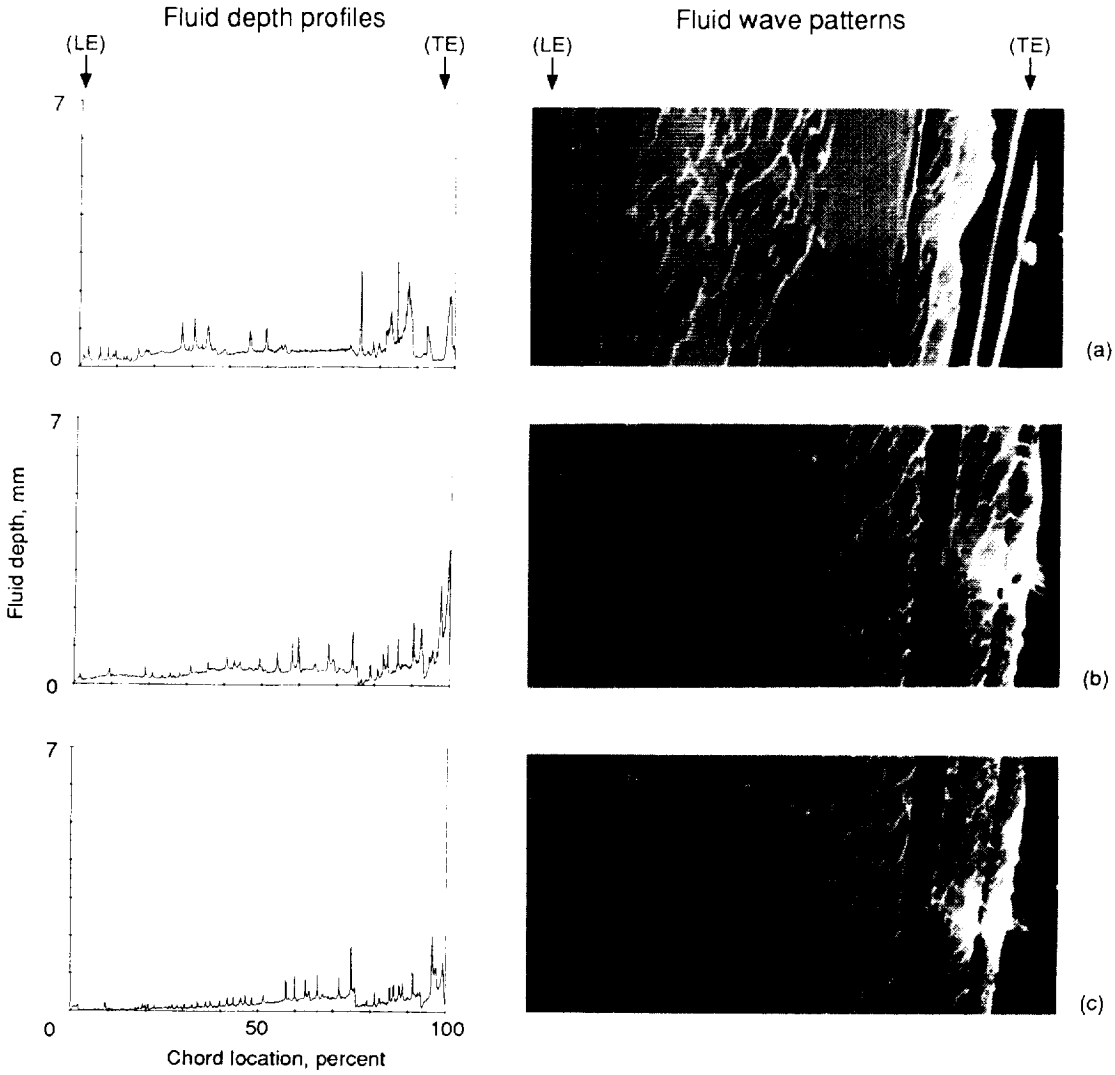

(a) Elapsed time, 9 sec; airspeed, 25.7 m/sec (50 keas); $\alpha_B = -0.1°$.

(b) Elapsed time, 21 sec; airspeed, 59.1 m/sec (115 keas); $\alpha_B = -0.1°$.

(c) Elapsed time, 24 sec; airspeed, 66.8 m/sec (130 keas); $\alpha_B = 4.4°$.

Figure 121.—Fluid 3 depth profiles and wave patterns for three-dimensional half model in flaps 5 configuration. Initial depth, 0.475 mm; temperature, –20 °C; run 149.

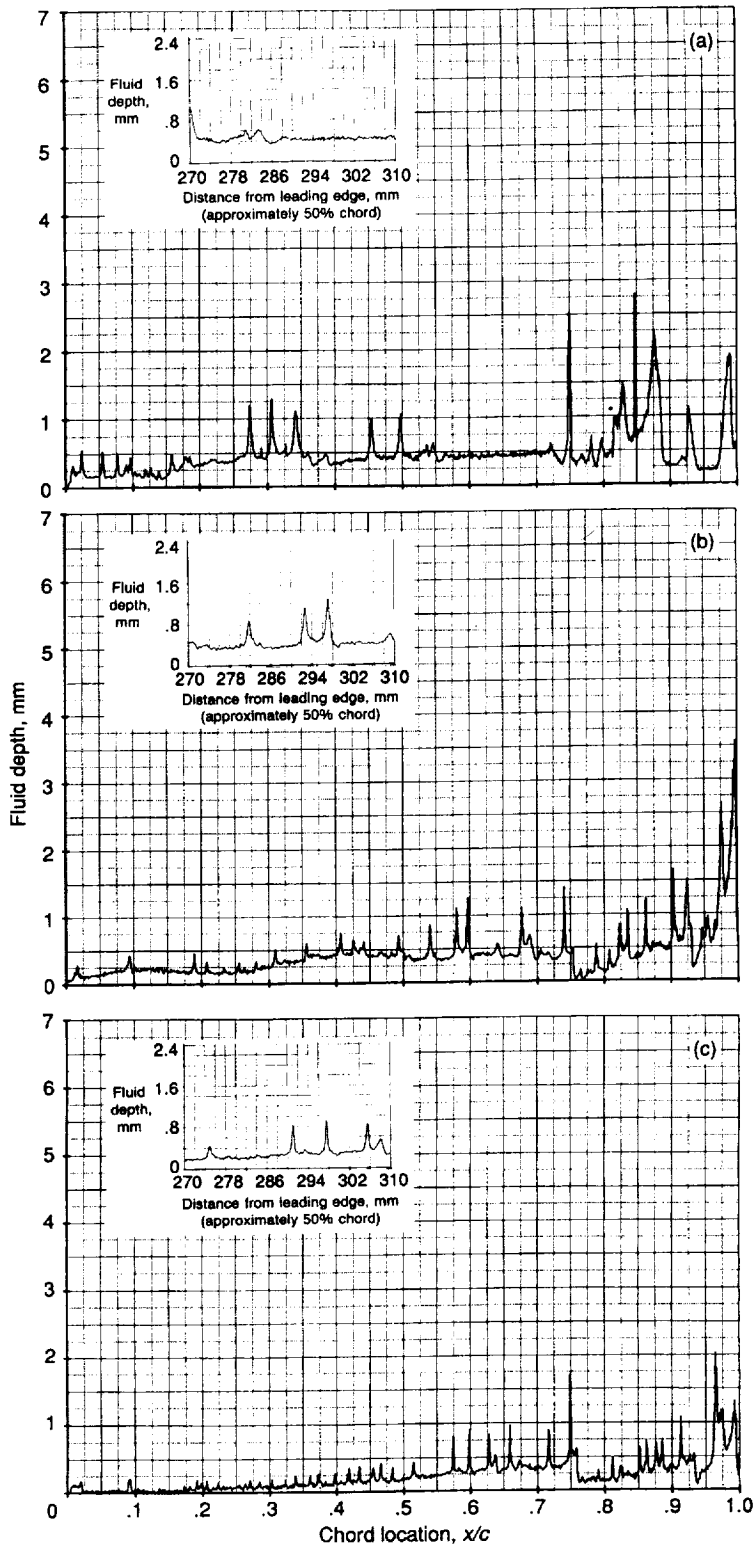

(a) Elapsed time, 9 sec; airspeed, 25.7 m/sec (50 keas); $\alpha_B = -0.1°$; $h = 0.238$ mm.

(b) Elapsed time, 21 sec; airspeed, 59.1 m/sec (115 keas); $\alpha_B = -0.1°$; $h = 0.422$ mm.

(c) Elapsed time, 24 sec; airspeed, 66.8 m/sec (130 keas); $\alpha_B = 4.4°$; $h = 0.436$ mm.

Figure 122.—Fluid 3 depth profiles and detail roughness inset for two-dimensional model in flaps 5 configuration. Initial depth, 0.475 mm; temperature, –20 °C.

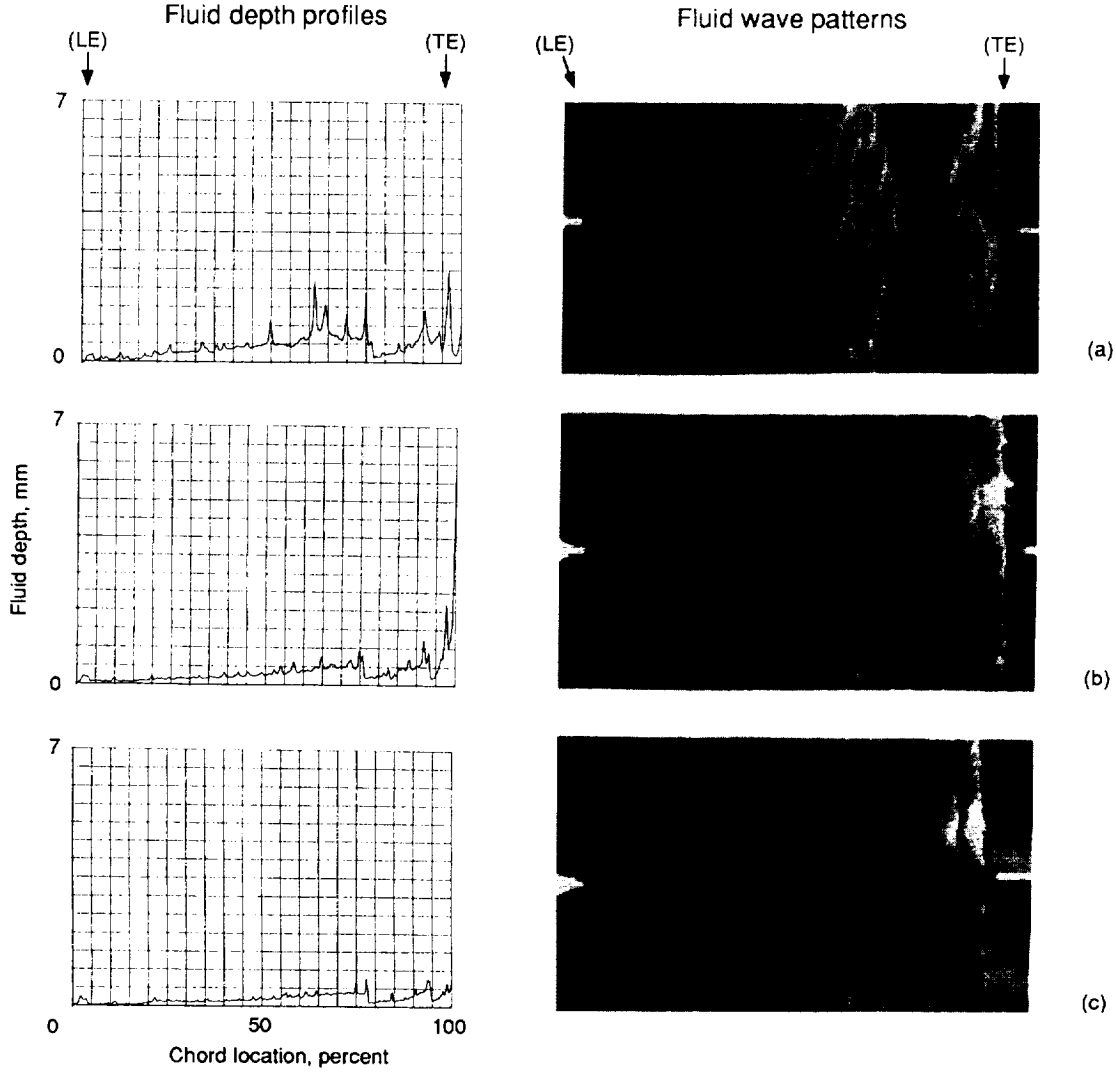

(a) Elapsed time, 12 sec; airspeed, 35.5 m/sec (69 keas); $\alpha_B = 0.1°$.

(b) Elapsed time, 20 sec; airspeed, 56.5 m/sec (110 keas); $\alpha_B = 0.1°$.

(c) Elapsed time, 24 sec; airspeed, 67.3 m/sec (131 keas); $\alpha_B = 8.1°$.

Figure 123.—Fluid 3 depth profiles and wave patterns for three-dimensional half model in flaps 5 configuration. Initial depth, 0.480 mm; temperature, –20 °C; run 230.

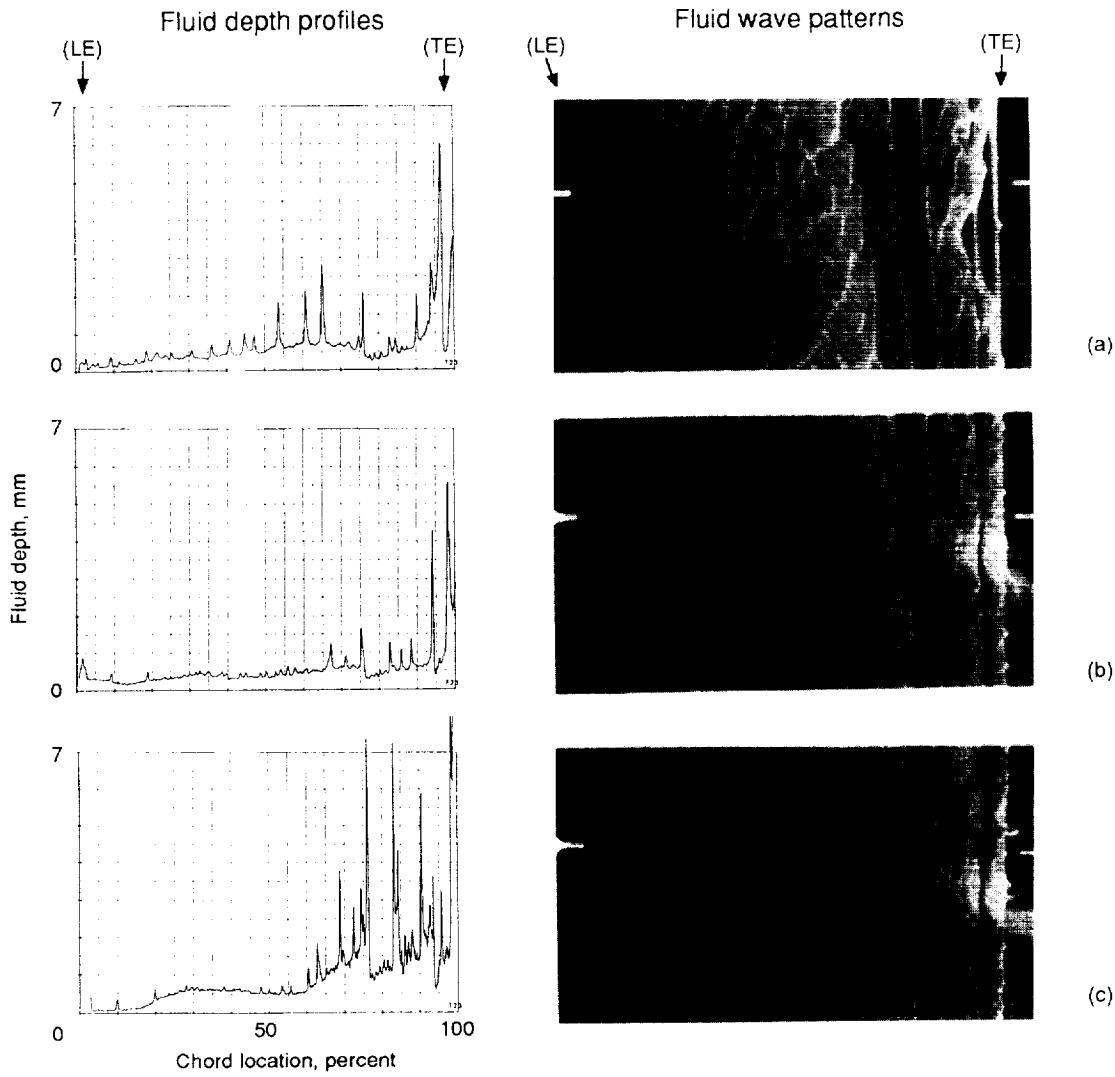

(a) Elapsed time, 12 sec; airspeed, 36.5 m/sec (71 keas); $\alpha_B = 0$.

(b) Elapsed time, 22 sec; airspeed, 62.7 m/sec (122 keas); $\alpha_B = 0$.

(c) Elapsed time, 24 sec; airspeed, 67.4 m/sec (131 keas); $\alpha_B = 5.9°$.

Figure 124.—Fluid 3 depth profiles and wave patterns for three-dimensional half model in flaps 5 configuration. Initial depth, 0.450 mm; temperature, –20 °C; run 232.

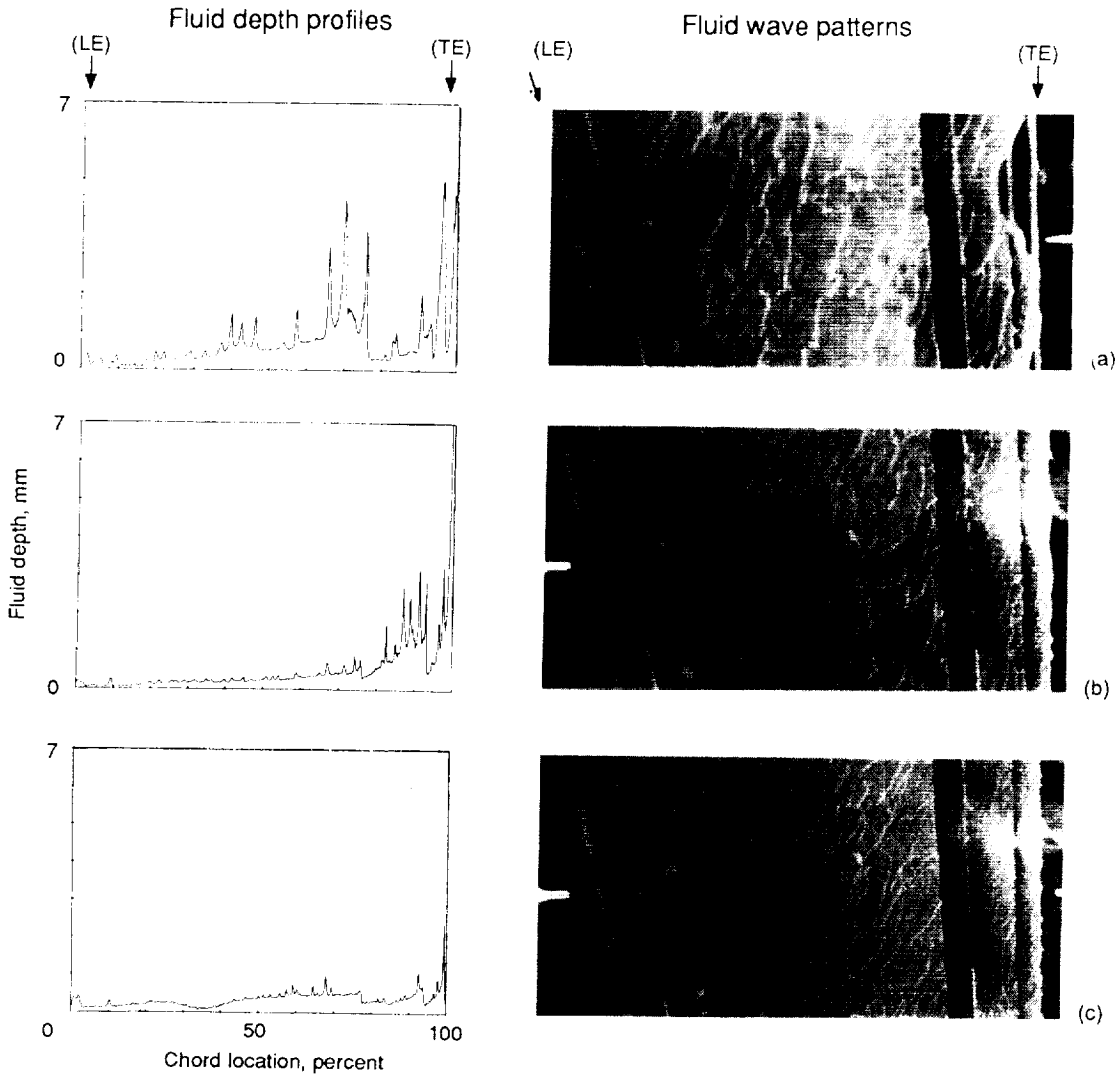

(a) Elapsed time, 12 sec; airspeed, 35.0 m/sec (68 keas); $\alpha_B = -0.2°$.

(b) Elapsed time, 22 sec; airspeed, 61.2 m/sec (119 keas); $\alpha_B = 1.5°$.

(c) Elapsed time, 24 sec; airspeed, 65.8 m/sec (128 keas); $\alpha_B = 8.6°$.

Figure 125.—Fluid 3 depth profiles and wave patterns for three-dimensional half model in flaps 5 configuration. Initial depth, 0.425 mm; temperature, −10 °C; run 180.

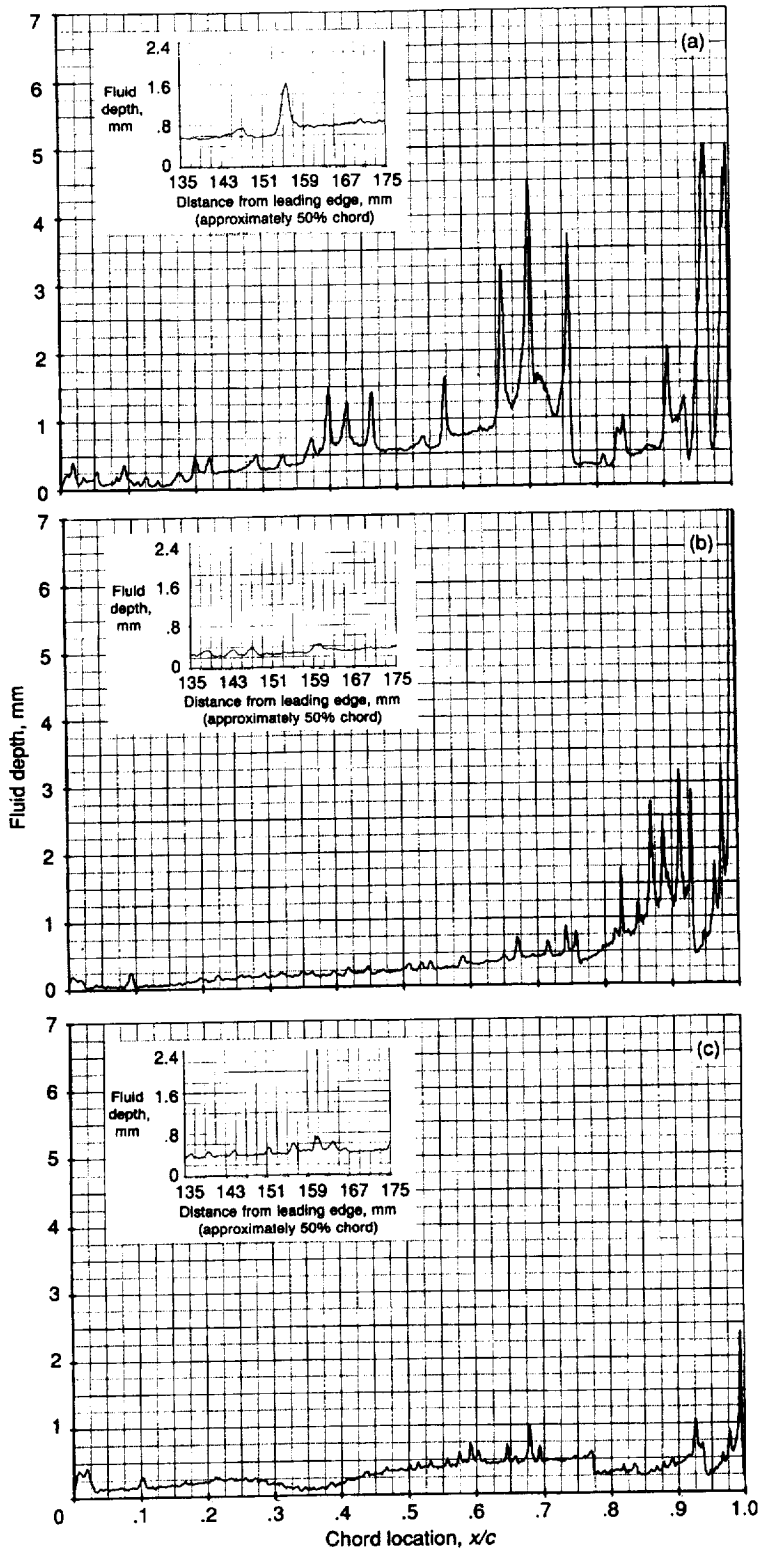

(a) Elapsed time, 12 sec; airspeed, 35.0 m/sec (68 keas); $\alpha_B = -0.2°$.

(b) Elapsed time, 22 sec; airspeed, 61.2 m/sec (119 keas); $\alpha_B = 1.5°$.

(c) Elapsed time, 24 sec; airspeed, 65.8 m/sec (128 keas); $\alpha_B = 8.6°$.

Figure 126.—Fluid 3 depth profiles and detail roughness inset for three-dimensional half model in flaps 5 configuration. Initial depth, 0.425 mm; temperature, –10 °C.

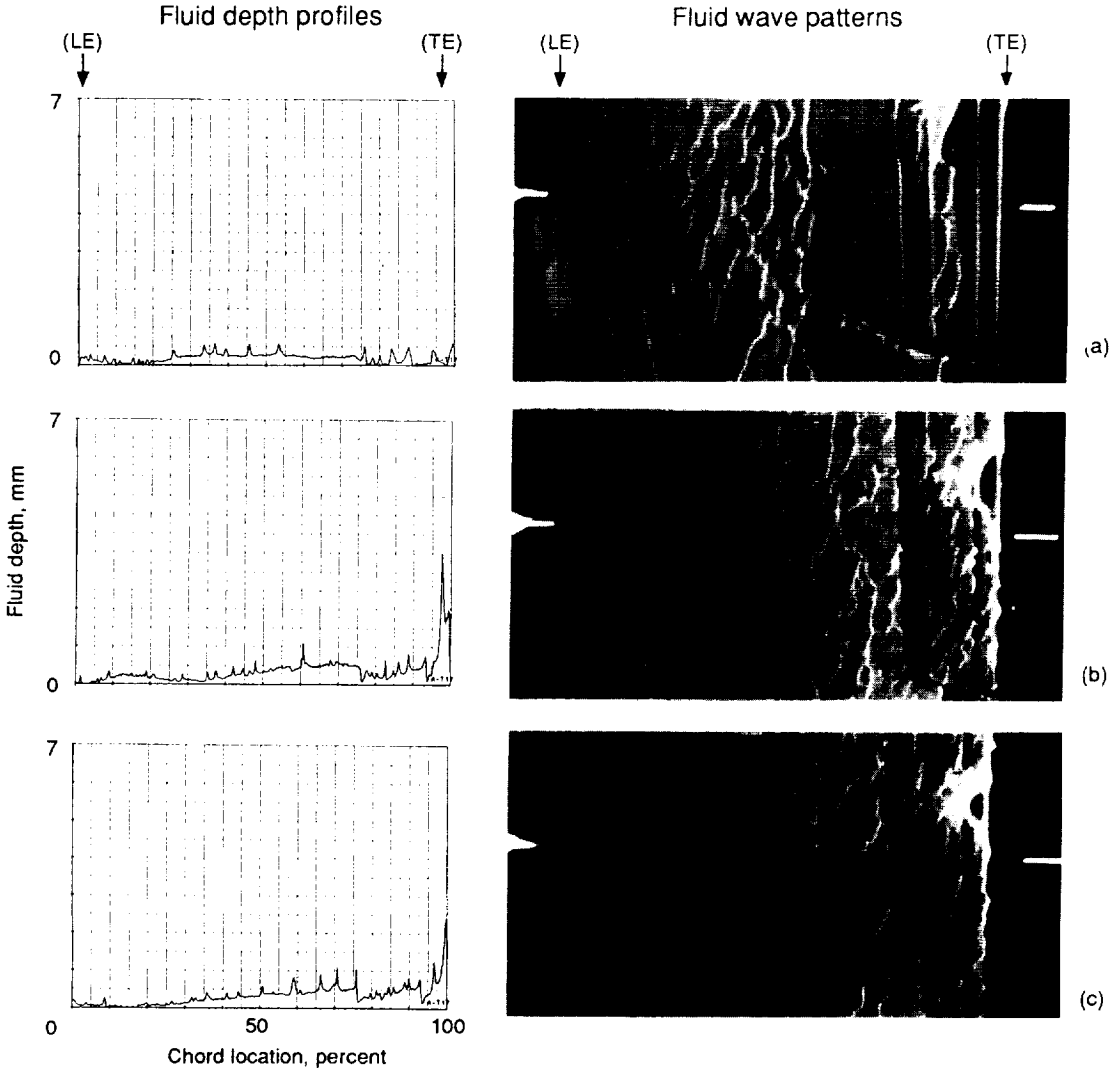

(a) Elapsed time, 12 sec; airspeed, 33.4 m/sec (65 keas); $\alpha_B = 0.1°$.

(b) Elapsed time, 21 sec; airspeed, 56.5 m/sec (110 keas); $\alpha_B = 0.1°$.

(c) Elapsed time, 24 sec; airspeed, 69.3 m/sec (125 keas); $\alpha_B = 9.4°$.

Figure 127.—Fluid 3 depth profiles and wave patterns for three-dimensional half model in flaps 5 configuration. Initial depth, 0.425 mm; temperature, 0 °C; run 172.

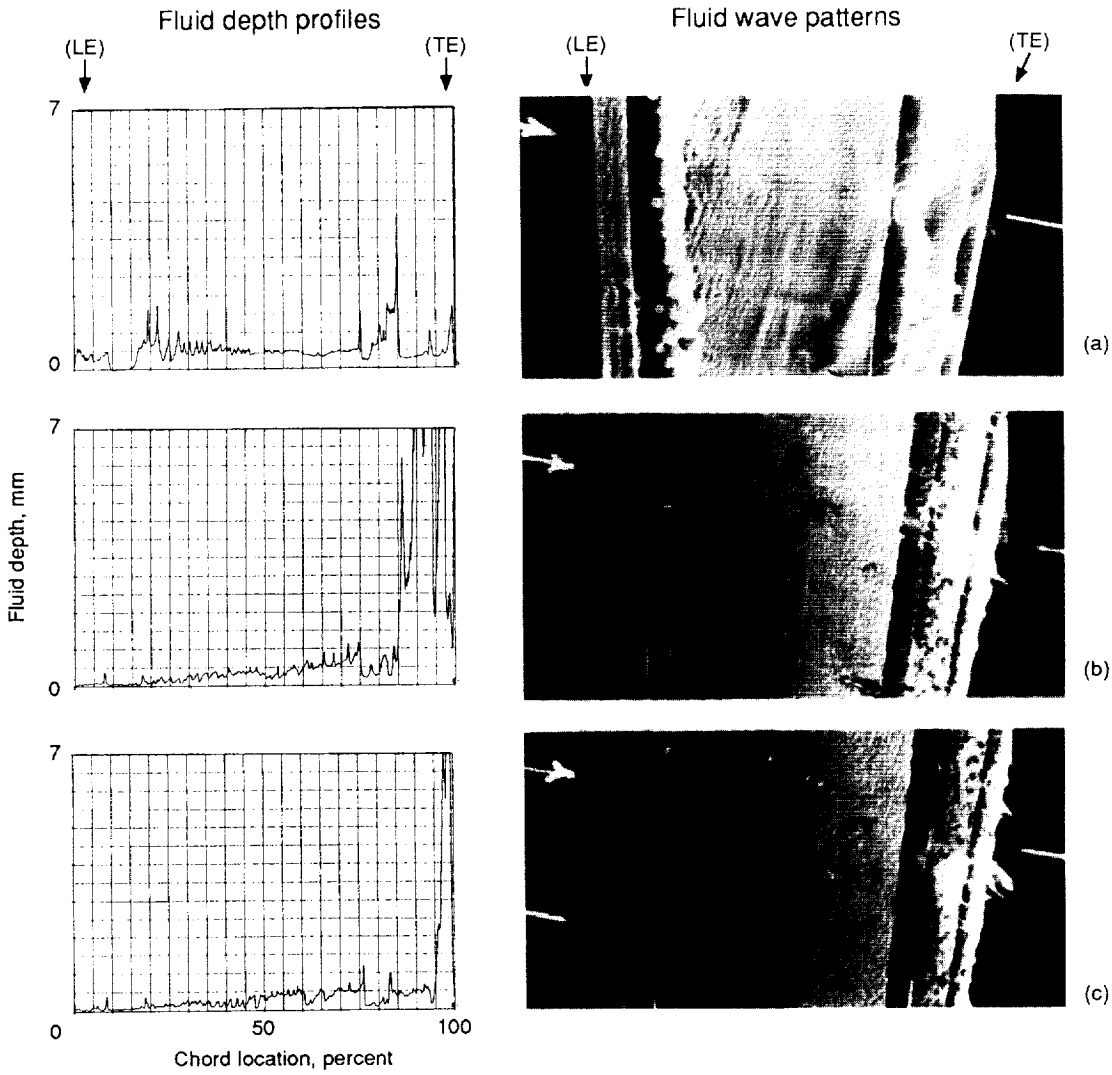

(a) Elapsed time, 9 sec; airspeed, 27.2 m/sec (53 keas); $\alpha_w = 0$.

(b) Elapsed time, 21 sec; airspeed, 60.1 m/sec (117 keas); $\alpha_w = 0$.

(c) Elapsed time, 24 sec; airspeed, 67.8 m/sec (132 keas); $\alpha_w = 7.0°$.

Figure 128.—Fluid 4 depth profiles and wave patterns for three-dimensional half model in flaps 5 configuration. Initial depth, 0.375 mm; temperature, –20 °C; run 155.

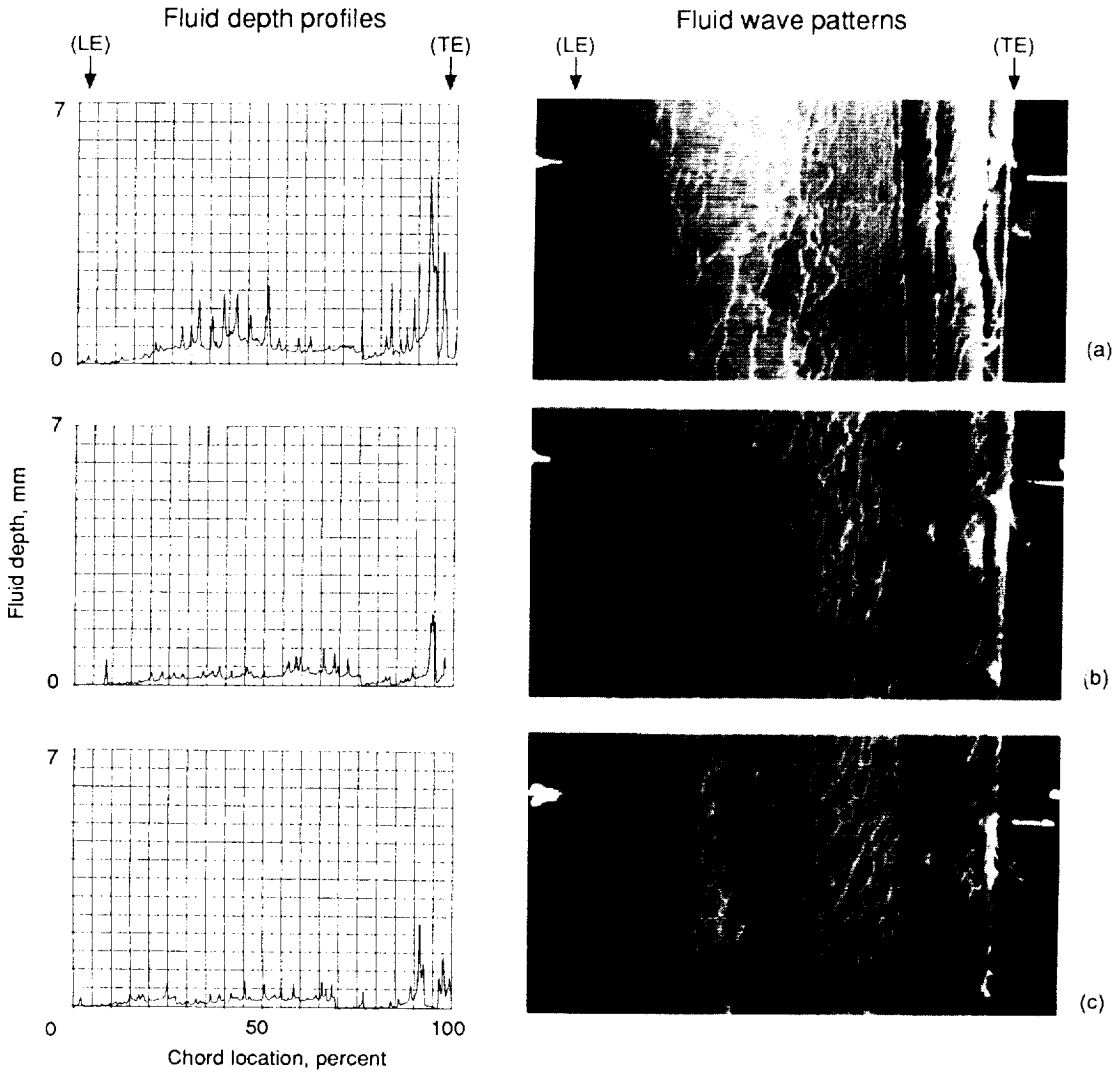

(a) Elapsed time, 10 sec; airspeed, 29.3 m/sec (57 keas); $\alpha_w = 0$.

(b) Elapsed time, 20 sec; airspeed, 56.5 m/sec (110 keas); $\alpha_w = 0.1°$.

(c) Elapsed time, 22 sec; airspeed, 61.7 m/sec (120 keas); $\alpha_w = 6.1°$.

Figure 129.—Fluid 3 depth profiles and wave patterns for three-dimensional half model in flaps 15, gapped slat configuration. Initial depth, 0.500 mm; temperature, –20 °C; run 205.

Appendix E

Data Repeatability, Tunnel Calibration, and Data Corrections

Data repeatability for both the two-dimensional model and the three-dimensional half model is summarized in this appendix. Also included is the calibration of the wind tunnel to account for the difference between the static pressure at the measurement station and that at the model location. Finally, the corrections applied to the raw wind tunnel data are discussed.

Data Repeatability

Three-dimensional half model lift repeatability.—The repeatability of the fully corrected three-dimensional half model lift coefficient is shown in figure 130. Data are shown for fluid 3 and for the dry wing at an angle of attack of 7°, at maximum lift and −10 °C. For the three cases with fluid 3 on the wing, the coefficient of variation is 2.1 percent at 7° and 1.3 percent at maximum lift. The repeatability is significantly better for the dry wing. At 7° the dry wing coefficient of variation is 1.0 percent, and at maximum lift it is 0.9 percent. The dry wing data for a given temperature were averaged to determine the baseline value to which the data with fluid at that temperature would be compared with determine the fluid effects.

Two-dimensional model lift repeatability.—The two-dimensional model fully corrected lift coefficient repeatability is shown in figure 131 for an angle of attack of 8°. All the data shown are for a temperature of −20 °C. The coefficient of variation for the dry baseline data is 0.9 percent. Only a single repeat run was made for fluids 1, 2, and 4, and two repeat runs were made for fluid 3. The repeatability of the fluid data is reasonably good. As was done with the three-dimensional half model, the dry wing data for a given temperature were averaged to determine the baseline value to which the data with fluid at that temperature would be compared to determine the fluid effects.

Figure 132 shows the repeatability of the fully corrected two-dimensional model maximum lift coefficient at a temperature of −20 °C. For the dry baseline data, the coefficient of variation is 1.2 percent. The repeatability of the fluid data is not as good as it was at an angle of attack of 8°.

Tunnel Calibration

The purpose of the tunnel calibration was to determine the difference in static pressure between the measurement station and the model location with the splitter wall(s) installed.

Three-dimensional half model.—For the three-dimensional half model, the tunnel was calibrated with only the right splitter wall installed. Separate calibrations were made with and without the ground plane installed. The standard IRT reference static source was used as the reference static pressure for the three-dimensional half model. The location of this static source is shown in figure 133. To determine the difference between the reference static and the static pressure at the model location, a temporary static port was located at the center of the turntable. The tunnel was then accelerated (model out) from 0 to 77.1 m/sec (0 to 150 keas), and the static pressure was measured at both locations as a function of tunnel q. The difference between the static pressure measured at the model location and that measured at the reference location at a given q was used in during data reduction to correct the measured reference static pressure.

Two-dimensional model.—For the two-dimensional model, the tunnel was calibrated with both of the splitter walls installed (model out). The standard IRT reference static was not used for this model because of the proximity of the leading edge of the left splitter wall to the IRT static source. There was some concern that the effect of the splitter wall on the reference static measurement would vary as a function of the model angle of attack because of the changing location of the splitter wall stagnation line. Therefore, the reference static source for the two-dimensional model was located 0.9 m (3 ft) from the leading edge of the right splitter wall (fig. 134). This location was chosen as a result of a potential flow panel method (program A502) analysis of the model pressure field and the splitter wall bullnose, or leading edge, pressure peak. As shown in figure 134, the location chosen was aft of the bullnose pressure peak about 0.9 m (3 ft) above the tunnel floor, which minimized the effect of the model. The tunnel calibration was, again, carried out by accelerating the tunnel (model out) from 77.1 m/sec (0 to 150 keas) and measuring the static pressure at the model location and at the reference static port as a function of tunnel q. The difference between these two pressures was then used in the subsequent data analysis to adjust the measured reference static to the model location as a function of q.

Standard Data Corrections

The following corrections were applied to the raw balance data for both the two-dimensional model and the three-dimensional half model: (1) balance interactions, (2) temperature corrections, (3) weight tare, and (4) balance deflections. Additional standard corrections for solid blockage, wake blockage, and wall interference were applied to the tunnel parameters and data coefficients for both models. The wall interference corrections were not applied to the three-dimensional half-model data when the ground plane was installed because the purpose of ground plane tests was to evaluate the constraint to the downwash.

Nonstandard Data Corrections

In addition to the standard data corrections, data from both the two-dimensional model and the three-dimensional half-model were corrected to account for effects specific to this test.

Initial balance offset correction—three-dimensional half model.—For five cases on the three-dimensional half model, an initial balance offset was large enough to affect the lift coefficient at the post rotation conditions. A negative initial balance offset is indicated by increasing C_N with increasing q, and a positive initial offset is indicated by decreasing C_N with increasing q, since, except for a very small Reynolds number effect, C_N should be approximately constant with q. Therefore, a correction was applied to the normal force at all q to make C_N at $q = 20$ equal to C_N at $q = 40$. These two values of q were chosen based on the following considerations: (1) They are high enough to be above the very low q region where small changes in normal force can have a large effect on C_N; (2) the two values are widely spaced; and (3) both values are before rotation. The correction was computed as follows:

$$C_{N20} + D_N/(20S_{ref}) = (C_{N40} + D_N/(40S_{ref})$$

$$D_N = (C_{N40} - C_{N20})S_{ref}/(1/20 - 1/40)$$

$$D_{CL} = D_N \cos \alpha_B/(qS_{ref})$$

This correction was computed for all angles of attack. The five cases that were corrected for initial balance offset (both the dry and with fluid runs) were

(1) Fluid 1, $T = -10$ °C, flaps 5, sealed slat
(2) Fluid 3, $T = 0$ °C, flaps 5, sealed slat
(3) Fluid 4, $T = -5$ °C, flaps 5, sealed slat
(4) Fluid 4, $T = -10$ °C, flaps 5, sealed slat
(5) Fluid 4, $T = -5$ °C, flaps 15, gapped slat

Dynamic q effects correction—two-dimensional model.—An additional correction was made to the two-dimensional model data for dynamic q effects. The dynamic q effect refers to a dependence of the lift coefficient on q (or run time, since q versus run time was constant from run to run), as shown in figure 135 for several runs. Notice that before rotation, c_l varies with run time (q). From 8 sec until rotation c_l is decreasing. Also notice that $c_{l,max}$ decreases from run to run as the run time at $c_{l,max}$ increases.

The cause of the dynamic q effect is not known. However, it may be an indication that there is an effect of the model on the static pressure at the reference location, and that this effect varies with q.

Since the time to rotation did vary somewhat from run to run throughout the course of the test, it was necessary to make a correction to account for the dynamic q effect. The correction used is based on the data shown in figure 136 from run 524. In that run the angle of attack was kept constant at 8.1. Thus, any change of c_l with time is due to the dynamic q effect. The first step in correcting each run consisted of adjusting the run time corresponding to a given angle of attack to a constant value for all runs. The lift at that angle of attack was then adjusted by the difference in lift for run 524 between the adjusted run time and the unadjusted run time.

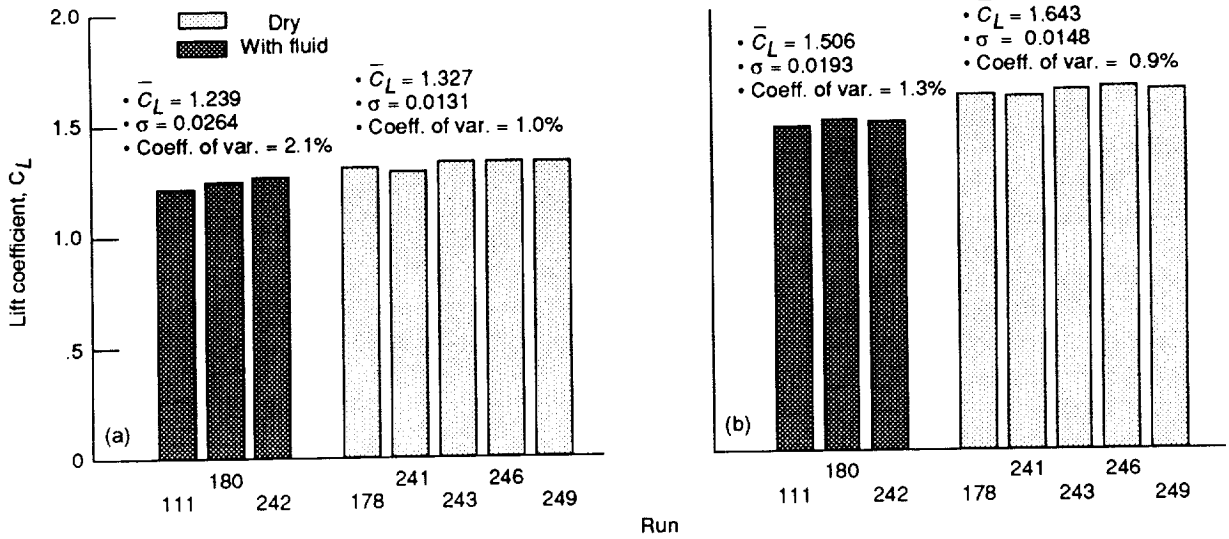

(a) At $\alpha_B = 7°$.
(b) At $C_{L,\ max}$.

Figure 130.—Lift repeatability for three-dimensional half model in flap 5, sealed slat configuration with ground plane in. Fluid 3; temperature, –10 °C.

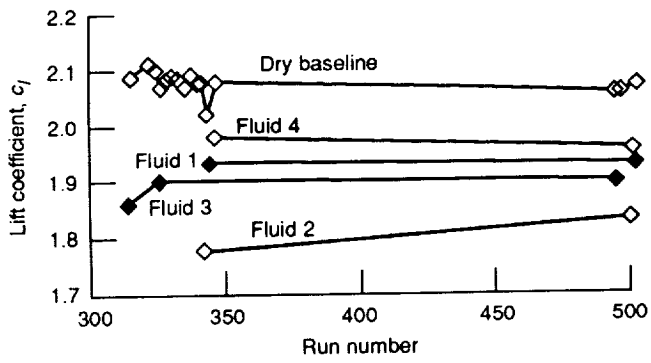

Figure 131.—Lift repeatability for two-dimensional model in flaps 5, sealed-slat configuration. Temperature, –20 °C; $\alpha_w = 8°$; data corrected for dynamic q effects. For dry (baseline) data: c_l = 2.087; σ = 0.019; coefficient of variability, 0.9 percent.

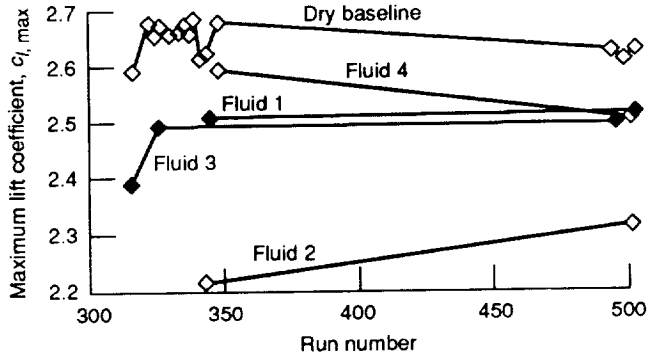

Figure 132.—Lift repeatability at maximum lift for two-dimensional model in flaps 5, sealed-slat configuration. Temperature, –20 °C; data corrected for dynamic q effects. For dry (baseline) data: $c_{l,\ max}$ = 2.646; σ = 0.031; coefficient of variability, 1.2 percent.

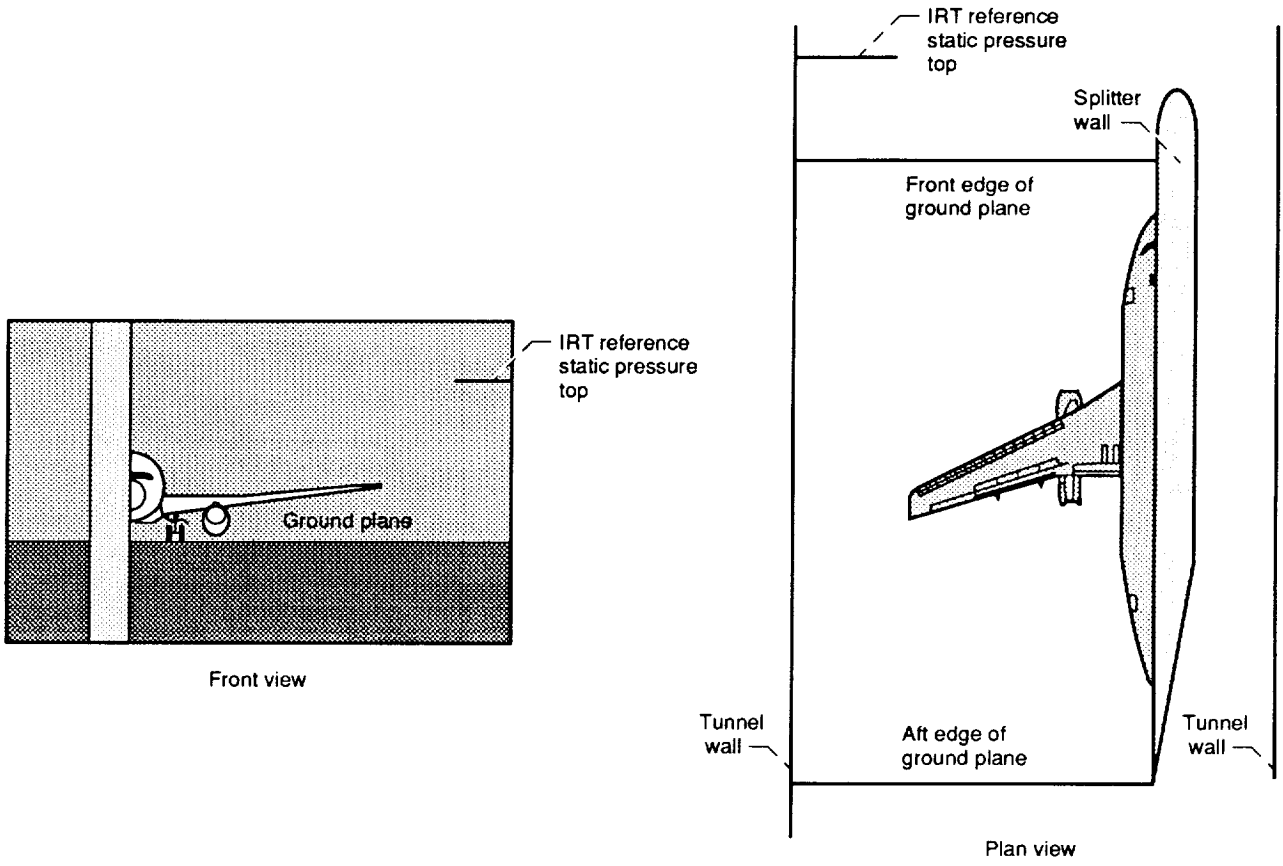

Figure 133.—Reference static for three-dimensional half model. Tunnel was calibrated with and without ground plane.

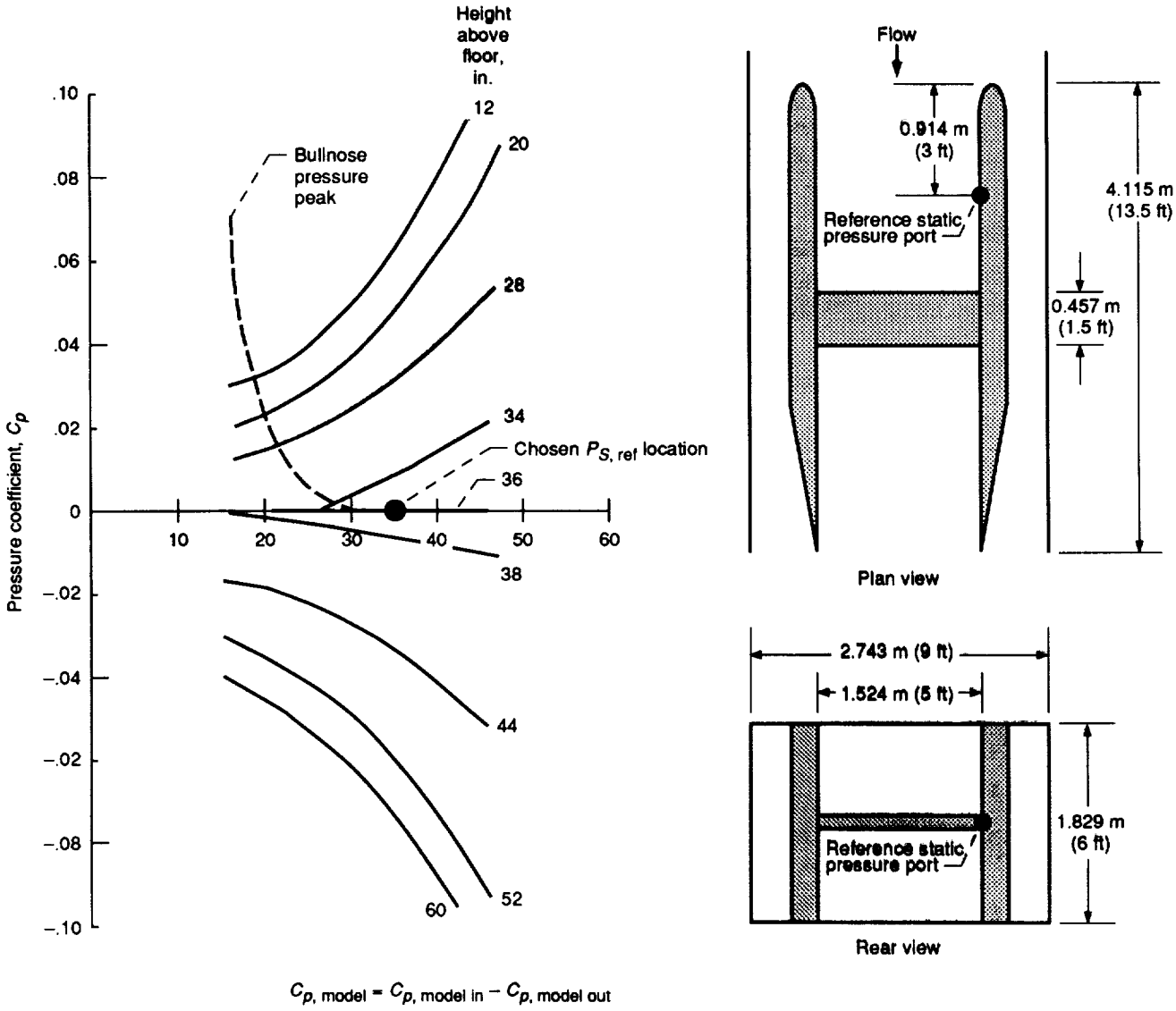

Figure 134.—Lines of change in model pressure coefficient showing reference static location chosen. Two-dimensional model. Potential flow panel method (A502) results.

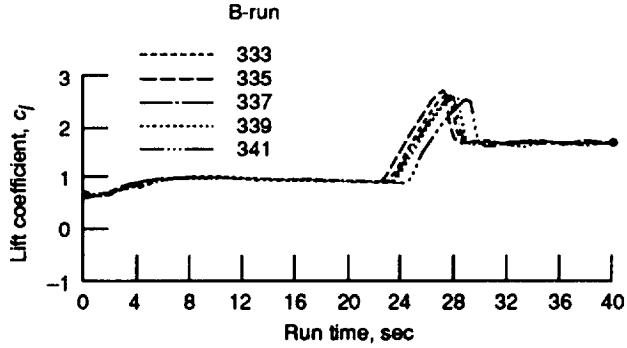

Figure 135.—Dependence of lift coefficient on run time for two-dimensional model in flaps 5, sealed-slat configuration: dynamic q effect. Dry wing, temperature, 20 °C.

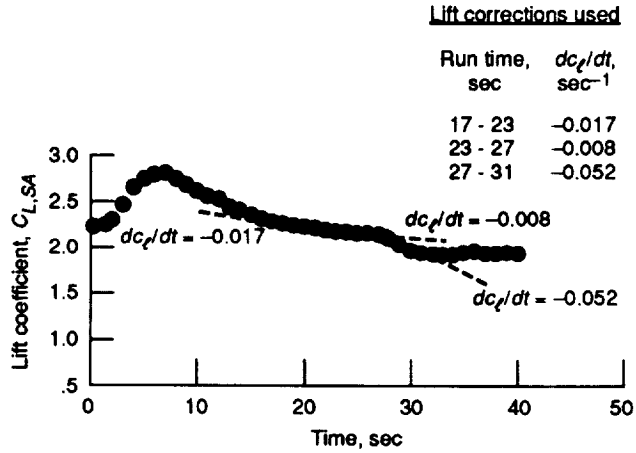

Figure 136.—Basis for dynamic q correction. Two-dimensional, flaps 5, sealed-slat configuration; dry wing; α_w = 8.1°; run 524.

Appendix F

Tabulations of Fluid Aerodynamic Effects

This appendix contains tabulations of the fluid aerodynamic effects (tables XVII to XXIV). For the three-dimensional half model, the lift loss, drag increase at takeoff safety speed, average takeoff acceleration drag increase, fluid effect on pitching moment, and fluid effect on rolling moment are tabulated. For the two-dimensional model, lift loss, drag increase at takeoff safety speed, and takeoff acceleration drag increase are tabulated.

TABLE XVII.—THREE-DIMENSIONAL HALF MODEL LIFT LOSS DATA
[All lift loss values in percent.]

(a) Flaps 5, sealed slat configuration, ground plane in

Fluid	T = 0 °C		T = -10 °C		T = -20 °C	
	ΔC_l (7°)	$\Delta C_{L,max}$	ΔC_l (7°)	$\Delta C_{L,max}$	ΔC_l (7°)	$\Delta C_{L,max}$
1	---	---	1.7	2.8	3.9	6.8
2	---	---	8.6	9.9	---	---
3	2.8	4.6	5.3	7.9	4.7	8.6
4	---	---	3.2	3.2	3.1	4.9

(b) Free air data; fluid 3; T = -20 °C

Configuration	At ΔC_l (7°)	At $\Delta C_{L,max}$
Flaps 5, sealed slat	7.6	7.2
Flaps 5, gapped slat	10.3	15.5
Flaps 5, sealed slat, 20° aileron	5.5	5.3
Flaps 15, gapped slat	9.9	11.3

(c) Flaps 15, gapped slat configuration, ground plane in

Fluid	T = 0 °C		T = -10 °C		T = -20 °C	
	ΔC_L (7°)	$\Delta C_{L,max}$	ΔC_l (7°)	$\Delta C_{L,max}$	ΔC_l (7°)	$\Delta C_{L,max}$
1	---	---	4.0	4.9	9.1	10.8
2	---	---	11.9	12.8	----	----
3	---	---	8.0	8.8	10.9	12.8
4	---	---	----	----	5.7	6.9

TABLE XVIII.—THREE-DIMENSIONAL MODEL DRAG INCREASE AT TAKEOFF SAFETY SPEED
[At C_L corresponding to $\alpha_{B,clean} = 7°$.]

Fluid	T = 0 °C	T = -10 °C	T = -20 °C
	Drag increase, ΔC_D, percent		
Flaps 5, sealed slats configuration			
1	----	0.9	7.0
2	----	18.2	------
3	10.0	14.2	11.3
4	----	4.0	8.1
Flaps 15, gapped slats configuration			
1	----	0.9	20.7
2	----	18.2	------
3	----	14.2	24.05
4	----	----	8.75

TABLE XIX.—AVERAGE TAKEOFF ACCELERATION DRAG INCREASE FOR THREE-DIMENSIONAL HALF MODEL
[$\alpha = 0°$; time = 15 sec; ground plane in.]

Fluid	T = 0 °C	T = -10 °C	T = -20 °C
	Drag increase, ΔC_D, percent		
Flaps 5, sealed slat configuration			
1	----	5.4	7.9
2	----	18.3	----
3	23.6	22.5	17.7
4	----	7.8	22.6
Flaps 15, gapped slat configuration			
1	----	0.8	9.4
2	----	14.0	----
3	----	8.0	15.4
4	----	----	6.4

TABLE XX.—FLUID EFFECT ON PITCHING MOMENT THREE-DIMENSIONAL HALF MODEL
[Temperature, -20 °C; ground plane in]

Fluid	At 7°	At $C_{L,max}$
	Pitching moment, C_M, 0.25C	
Flaps 5, sealed slat configuration		
1	-0.034	0.063
2	--------	-------
3	-.027	.053
4	-.034	.061
Dry	-.047	.087
Flaps 15, gapped slat configuration		
1	-0.134	-0.075
2	--------	-------
3	-.122	-.075
4	-.143	-.084
Dry	-.178	-.089

TABLE XXI.—FLUID EFFECT ON ROLLING MOMENT OF THREE-DIMENSIONAL HALF MODEL
[Temperature, -20 °C; ground plane in; fluid on left wing only.]

Fluid	At 7°	At $C_{L,max}$
	Rolling moment increment, Δc_l, percent	
Flaps 5, seal slats configuration		
1	-4.0	-7.6
2	------	------
3	-3.6	-9.9
4	-1.1	-4.7
Flaps 15, gapped slats configuration		
1	-7.9	-12.8
2	------	------
3	-10.8	-15.0
4	-5.6	-8.1

TABLE XXII.—TWO-DIMENSIONAL MODEL LIFT LOSS DATA

Fluid	T = 0 °C		T = -10 °C		T = -20 °C	
	Δc_l at 8°	$\Delta c_{l,max}$	Δc_l at 8°	$\Delta c_{l,max}$	Δc_l at 8°	$\Delta c_{l,max}$
	Lift loss, percent					
Flaps 5, sealed slat configuration						
1	---	---	4.8	2.7	7.0	5.1
2	---	---	11.4	6.9	13.2	14.4
3	4.8	5.9	7.1	5.1	9.4	7.0
4	---	---	2.5	1.3	5.3	3.9
2.1	---	---	4.2	1.2	6.3	4.8
2.2	---	---	6.2	1.8	7.1	4.9
3.1	5.1	0	4.4	3.5	5.9	2.9
3.2	---	---	5.3	5.2	5.7	4.4
4.1	3.4	0	5.0	2.8	7.5	3.3
4.2	---	---	4.6	1.4	5.2	4.5
5.1	1.0	0	2.4	1.4	5.5	3.8
5.2	---	---	4.4	4.7	5.5	3.8
Flaps 5, gapped slat configuration						
1	---	---	4.9	6.2	8.8	10.7
2	---	---	13.3	14.9	18.6	27.6
3	---	---	8.8	11.4	11.9	14.6
4	---	---	3.3	4.6	5.4	4.6

TABLE XXIII.—TWO-DIMENSIONAL MODEL DRAG INCREASE AT TAKEOFF SAFETY SPEED

[At C_l corresponding to $\alpha_{B,clean} = 6.5°$ except as noted.]

Fluid	T = 0 °C	T = -10 °C	T = -20 °C
	Model drag increase, ΔC_d		
Flaps 5, sealed slat configuration			
1	----	23.6	39.0
2	----	66.4	93.9
3	26.0	50.0	56.3
4	----	23.2	18.8
2.1	----	23.3	26.2
2.2	----	34.2	38.5
3.1	20.3	20.5	34.8
3.2	----	29.5	37.4
4.1	23.4	12.4	30.0
4.2	----	5.2	16.4
5.1	12.9	11.7	24.4
5.2	----	20.9	28.2
Flaps 15, gapped slat configuration			
1	----	16.3	26.8
2	----	65.2	83.1
3	----	32.9	51.1
4	----	8.8	19.4

TABLE XXIV.—AVERAGE TAKEOFF ACCELERATION DRAG INCREASE FOR TWO-DIMENSIONAL MODEL

Fluid	T = 0 °C	T = -10 °C	T = -20 °C
	Average takeoff acceleration drag increase, ΔC_{d_a}, percent		
Flaps 5, sealed slat configuration			
1	----	----	25.9
2	----	----	62.2
3	----	----	32.5
4	----	----	39.2
2.1	----	34.9	35.4
2.2	----	34.7	40.2
3.1	47.9	36.8	47.5
3.2	----	40.7	38.8
4.1	38.5	22.8	25.3
4.2	----	28.1	23.0
5.1	23.9	26.6	24.5
5.2	----	25.7	30.1
Flaps 15, gapped slat configuration			
1	----	----	----
2	----	----	----
3	----	----	----
4	----	----	----

REPORT DOCUMENTATION PAGE

Form Approved
OMB No. 0704-0188

1. AGENCY USE ONLY (*Leave blank*)	2. REPORT DATE	3. REPORT TYPE AND DATES COVERED
	August 1992	Technical Paper

4. TITLE AND SUBTITLE

Lewis Icing Research Tunnel Test of the Aerodynamic Effects of Aircraft Ground Deicing/Anti-Icing Fluids

5. FUNDING NUMBERS

WU-505-68-11

6. AUTHOR(S)

L. James Runyan, Thomas A. Zierten, Eugene G. Hill, and Harold E. Addy, Jr.

7. PERFORMING ORGANIZATION NAME(S) AND ADDRESS(ES)

National Aeronautics and Space Administration
Lewis Research Center
Cleveland, Ohio 44135-3191

8. PERFORMING ORGANIZATION REPORT NUMBER

E-5808

9. SPONSORING/MONITORING AGENCY NAMES(S) AND ADDRESS(ES)

National Aeronautics and Space Administration
Washington, D.C. 20546-0001

10. SPONSORING/MONITORING AGENCY REPORT NUMBER

NASA TP-3238

11. SUPPLEMENTARY NOTES

L. James Runyan, Thomas A. Zierten, and Eugene G. Hill, Boeing Commercial Airplanes, Seattle, Washington; Harold E. Addy, Jr., NASA Lewis Research Center.

12a. DISTRIBUTION/AVAILABILITY STATEMENT

Unclassified - Unlimited
Subject Category 03

12b. DISTRIBUTION CODE

13. ABSTRACT (*Maximum 200 words*)

A wind tunnel investigation of the effect of aircraft ground deicing/anti-icing fluids on the aerodynamic characteristics of a Boeing 737-200ADV airplane has been conducted. The test was carried out in the NASA Lewis Icing Research Tunnel. Fluids tested include a Newtonian deicing fluid, three non-Newtonian anti-icing fluids commercially available during or before 1988, and eight new experimental non-Newtonian fluids developed by four fluid manufacturers. The results show that fluids remain on the wing after liftoff and cause a measurable lift loss and drag increase. These effects are dependent on the high-lift configuration and on the temperature. For a configuration with a high-lift leading-edge device, the fluid effect is largest at the maximum lift condition. The fluid aerodynamic effects are related to the magnitude of the fluid surface roughness, particularly in the first 30 percent chord. The experimental fluids show a significant reduction in aerodynamic effects.

14. SUBJECT TERMS

Rheology; Non-Newtonian fluids; Deicing

15. NUMBER OF PAGES

136

16. PRICE CODE

A07

17. SECURITY CLASSIFICATION OF REPORT	18. SECURITY CLASSIFICATION OF THIS PAGE	19. SECURITY CLASSIFICATION OF ABSTRACT	20. LIMITATION OF ABSTRACT
Unclassified	Unclassified	Unclassified	

NASA-Langley, 1992